COMPUTATIONAL INVESTIGATION OF THE EFFECTS OF TURBULENCE, INERTIA, AND GRAVITY ON PARTICLE DYNAMICS

A Dissertation

Presented to the Faculty of the Graduate School

of Cornell University

in Partial Fulfillment of the Requirements for the Degree of

Doctor of Philosophy

by

Peter John Ireland

January 2015

COMPUTATIONAL INVESTIGATION OF THE EFFECTS OF TURBULENCE, INERTIA, AND GRAVITY ON PARTICLE DYNAMICS

Peter John Ireland, Ph.D.

Cornell University 2015

In this work, we examine the motion of particles which are subjected to varying levels of turbulence, inertia, and gravity, in both homogeneous and inhomogeneous turbulence. These investigations are performed through direct numerical simulation (DNS) of the Eulerian fluid velocity field combined with Lagrangian particle tracking. The primary motivation of these investigations is to better understand and model the dynamics and growth of water droplets in warm, cumulus clouds. In the first part of this work, we discuss the code we developed for these simulations, Highly Parallel Particle-laden flow Solver for Turbulence Research (HiPPSTR). HiPPSTR uses efficient parallelization strategies, time-integration techniques, and interpolation methods to enable massively parallel simulations of three-dimensional, particle-laden turbulence. In the second, third, and fourth sections of this work, we analyze simulations of particle-laden flows which are representative of those at the edges and cores of clouds. In the second section, we consider the mixing of droplets near interfaces with varying turbulence intensities and gravitational orientations, to provide insight into the dynamics near cloud edges. The simulations are parameterized to match wind-tunnel experiments of particle mixing which were conducted at Cornell, and the DNS and experimental results are compared and contrasted. Mixing is suppressed when turbulence intensities differ across the interface, and in all cases, the particle concentrations are subject to large fluctuations. In the third and

fourth sections, we use HiPPSTR to analyze droplet motion in isotropic turbulence, which we take to be representative of adiabatic cloud cores. The third section examines the Reynolds-number scaling of single-particle and particle-pair statistics without gravity, while the fourth section shows results when gravity is included. While weakly inertial particles preferentially sample certain regions of the flow, gravity reduces the degree of preferential sampling by limiting the time particles can spend interacting the underlying turbulence. We find that when particle inertia is small, the particle relative velocities and radial distribution functions (RDFs) are almost entirely insensitive to the flow Reynolds number, both with and without gravity. The relative velocities and RDFs for larger particles tend to weakly depend on the Reynolds number and to strongly depend on the degree of gravity. While non-local, path-history interactions significantly affect the relative velocities of moderate and large particles without gravity, these interactions are suppressed by gravity, reducing the relative velocities. We provide a physical explanation for the trends in the relative velocities with Reynolds number and gravity, and use the model of [198] to understand and predict how the trends in the relative velocities will affect the RDFs. The collision kernels for particles representative of those in atmospheric clouds are generally seen to be independent of Reynolds number, both with and without gravity, indicating relatively low Reynolds-number simulations are able to capture much of the physics responsible for droplet collisions in clouds. We conclude by discussing practical implications of this work for the cloud physics and turbulence communities and suggesting areas for future research.

BIOGRAPHICAL SKETCH

Peter J. Ireland was born on December 3, 1985, near Philadelphia, Pennsylvania, and moved to Clinton, Mississippi, at the age of 8. His interest in science, math, reading, and writing was instilled from an early age by many excellent teachers (including his mother) in both Pennsylvania and Mississippi. He graduated from Clinton High School in 2004, and majored in mechanical engineering as an undergraduate student at Mississippi State University (MSU) in Starkville, Mississippi. His interest in fluid dynamics was piqued by his work as an cooperative engineering student at Eaton Aerospace, Vickers Fluid Power, in Jackson, Mississippi, where he was involved in the design, analysis, testing, and documentation of hydraulic pumps. He became interested in computational fluid dynamics (CFD) when he was afforded the excellent opportunity to work as an undergraduate researcher for Professor Keith Walters at MSU. Under Professor Walters's guidance, he was motivated to pursue a PhD studying CFD, and decided to attend Cornell University and research under the guidance of Professor Lance Collins. He has spent the last five years at Cornell, using computational simulations to study particle-laden turbulent flows and their role in industrial and environmental phenomena.

ACKNOWLEDGEMENTS

Over the past five years, the struggles, disappointments, and triumphs on my road to a PhD have taught me more about what it means to be a researcher, a colleague, and a responsible member of society. I am grateful to the many people who have shared this journey with me and have guided and helped me along the way.

Days before the journey through graduate school began, I had to say goodbye to my grandmother Ethel 'Grammy' Ireland, who finally arrived at her true home at the age of 87. While her official occupation was one of a missionary and then a stepmother and pastor's wife, her kindness, generosity, selflessness, patience, and forgetfulness will forever endear her to me as the ideal professor for a curious young boy and a curious young researcher.

I am grateful to the many university professors who guided me along the way. Thank you, Professor Walters, for patiently teaching me what computational fluid dynamics is all about, and for surprising me by making this subject interesting and inspiring. Thank you for inspiring me to pursue a PhD, and for guiding me though the graduate school application process.

I am also grateful for my committee members, Professor Warhaft and Professor Diamessis, for their guidance in my work and personal development. In the competitive and sometimes impersonal world of academia, I am grateful to both of you for your relaxed attitudes and for your emphasis on the need for both personal and scientific growth. Professor Warhaft, thank you for teaching me that being a responsible scientist means making sure that our work has a positive impact on other people and on the environment we all must share, and not just that our sums are correct. Professor Diamessis, thank you for always being willing to take time out of your busy schedule to talk with me about how

to be a successful scientist who keeps relationships with others at the forefront of his life.

I am also deeply indebted to my PhD advisor Professor Lance Collins. Thank you, Professor Collins, for the time you have invested in my personal and professional growth, for the freedom and independence you have allowed me in the research, and for your pointed, accurate, and extremely helpful guidance along the way. I have been encouraged by your calm, patient demeanor, by your diplomacy with contentious academics, and by your understanding and guidance when things go wrong with the research (especially when it was my fault). I am continually amazed by your ability to make even the most technical of arguments accessible and engaging, and hope I have learned from you (at least in part) of what it means to craft a compelling and precise scientific argument. Your ability to produce meticulous, well-polished research while continually swamped with work as the Engineering Dean has taught me something of what it means to be a rigorous scientist under the toughest of conditions.

I would be remiss if I did not thank my colleagues, without whose help I would never have finished. Thank you, Garrett, for working with me on journal articles and conference presentations, and for teaching a computational scientist the value of experiments and the limits of his 16 digits of precision. Thank you, Ray, for patiently teaching me about DNS, and for always being relaxed, helpful, and cheerful. Thank you, Vaithi, for the deep insight into CFD which you willingly shared with me. Thank you, Parvez, for our many helpful discussions across the cubicles, and for your helpfulness in the many technical problems we solved together. Thank you, Andy, for sharing your deep physical insight with me and for teaching me some of the math I should have already known.

I thank U.S. National Science Foundation (NSF) for a Graduate Research Fellowship and for grants CBET 0756510 and 0967349, and the U.S. National Center for Atmospheric Research (NCAR) for providing high-performance computing support on Yellowstone (ark:/85065/d7wd3xhc), which is sponsored by NSF. I also acknowledge computing support that was provided by the Texas Advanced Computing Center and the Oak Ridge Leadership Computing Facility, and additional funding that was provided by Cornell University.

Finally, I would like to thank my friends and family for their invaluable role in this whole process. Thank you, Casey, David, Paul, Stephen, Stephen, Steven, and Theo, for making my time in Ithaca fun, meaningful, and encouraging, and for allowing me to share this stage of my life with you. Thank you, Mom and Dad, for your constant prayers and support (even if all you know is that I'm doing something about droplets in clouds), and Jeremy, Kristen, Lillie, Annie, Josh, and Tim for your help, encouragement, and advice. Finally, I would like to thank Michelle, for patiently listening to me talk about CFD after work (and only sometimes teasing me about it), for faithfully walking besides me through success and failure, and most of all, for teaching me what it means, both verbally and through example, to love other people and their Creator. I look forward to walking beside you through many longer and more joyful and frustrating journeys.

TABLE OF CONTENTS

LIST OF TABLES

LIST OF FIGURES

CHAPTER 1

INTRODUCTION

1.1 Particle-laden flows in industry and the environment

The focus of this dissertation is on understanding turbulent flows laden with inertial particles through computational simulations. Here, we use the term 'inertial particles' to denote particles which are more dense than their carrier flow. It is well-known that inertial particles can have dramatically different behavior in turbulence than inertialess fluid particles, and their dynamics can have a profound impact in a variety of different industrial and environmental settings. For example, to better design spray combustion chambers or aerosol drug delivery systems, engineers must understand the role of a turbulent field on particle clustering, collision, and coalescence. Inertial-particle interactions also affect such diverse natural phenomena as plankton distribution, cloud growth, and planetesimal formation.

While the research here is generally conducted from a fundamental perspective, the primary motivation of this work is to understand the role of turbulence on droplet motion and growth in warm, cumulus clouds. One long-standing question in the cloud physics community is why warm, cumulus clouds precipitate as quickly as they do. As discussed in [148, 45, 69], the smallest droplets in clouds tend to form around cloud condensation nuclei and initially grow as the surrounding humid air condenses around these droplets, increasing their size. However, as the size increases, the volumetric growth rates of the droplets induced by condensation must decrease. For droplets with diameters greater than $30\mu m$, the timescales on which condensational growth occurs become pro-

hibitively large, and condensational growth essentially stops. In the opposite limit (i.e., droplet diameters greater than about $80\mu m$), gravitational forces are significant, and droplet growth is driven by collisions between droplets with different settling speeds. While it is thought that droplet diameters must grow between $30\mu m$ and $80\mu m$ as a result of the underlying turbulence, it is still unclear the extent to which turbulence will alter these growth rates. In this dissertation, we seek to clarify this issue by means of computational simulations.

1.2 Simulating particle-laden flows

One of the most challenging problems in computational fluid dynamics is the study of a dispersed phase in a highly turbulent flow. We provide a summary of some of the challenges relevant to this work below. More information can be found in the review of [9].

In order to simulate a particle-laden flow, one must solve the relevant equations governing both the fluid and particle phases, and in some cases, account for the interaction between the two phases.

1.2.1 Fluid-phase simulation

There are three general ways to simulate the fluid phase of a turbulent flow. The first simulation method involves solving the Reynolds-averaged Navier Stokes (RANS) equations. These equations are constructed by taking the time average of the Navier Stokes equations and provide information about the mean velocity and pressure fields. While this approach is popular because of its simplicity

and the ease with which it can be applied to arbitrary geometries and large Reynolds numbers, it has a number of significant disadvantages which render it unsuitable for this research. The first disadvantage is that it contains no information about the fluctuations and coherent structures in the flow. We will show in this dissertation that these elements of the turbulence have a profound effect on the motion of inertial particles and thus cannot be neglected. The second disadvantage is that the RANS equations contain unclosed Reynolds-stress terms (i.e., terms which involve the covariance of the fluid velocity fluctuations), and models must be introduced to close these terms. In some cases, these closure models can lead to significant errors in the computed fluid field. Thus, even if particle motion could be attributed strictly to the averaged turbulent flow, there is no guarantee that RANS is able to solve for the average flow with sufficient fidelity to enable meaningful simulations of a dispersed particle phase.

Another commonly used simulation technique is Large Eddy Simulation (LES). In this approach, the large scales of the turbulence are computed, while the smaller scales are represented through a sub-grid model. LES has some of the advantages of RANS (e.g., the ability to simulate complex geometries and high Reynolds numbers with relative ease), but incurs considerably more computational expense. While LES is expected to be accurate for particles which are much larger than the grid size, in many flows of interest, the particles may be much smaller than the smallest resolved scales, and thus the accuracy of the simulation approach will be strongly tied to that of the sub-grid model. While promising work is underway in developing accurate sub-grid models for LES of particle-laden turbulence [135, 136], the field is not yet mature enough to justify using LES to predict the dynamics of small, dispersed particles.

For these reasons, we use a different computational approach, direct numerical simulation (DNS), to analyze particle dynamics in turbulence. While DNS provides an accurate description of the underlying flow field and does not require any sub-grid models, it is much more computationally demanding than both RANS and LES, and the computational expense increases dramatically both as the Reynolds number increases and as the geometric complexity of the domain increases. To achieve the maximum possible Reynolds numbers for our studies, we therefore consider turbulence on cubic, tri-periodic domains. Even with such simple geometries, however, the time needed to perform a simulation grows as R_λ^6 (as discussed in [130]), where R_λ is the Taylor-scale Reynolds-number. Sophisticated tools are therefore necessary to simulate the flow-field on highly parallel architectures in order to study flows at Reynolds numbers characteristic of those in the environment.

1.2.2 Particle-phase simulation

We now discuss the methodology for simulating the dispersed particle phase. A simple way to do so would be to treat the particle phase as a continuum and to solve the governing particle equations on an Eulerian grid. However, this approach has significant shortcomings which render it unsuitable for the studies in this dissertation. The first is that it involves closures, which (like RANS models) can cause leading-order errors in the particle motions. In addition, my investigations are primarily focused on particle motion near contact; for particles which are small, particle contact will occur at separations which are much less than the grid spacing, and an Eulerian model will be unable to provide information about the relative particle motion here. Finally, we will show that

when the particle inertia is large, the particle velocities are significantly affected by non-local, path-history interactions (i.e., caustics), which can cause the particle velocities to take on multiple values at a single point. An Eulerian field description of the particle motions is by construction unable to capture these effects.

We therefore adopt a Lagrangian description of the dispersed phase. While the most accurate way to simulate the particle phase is through a fully resolved particle-fluid DNS, the expense of such an approach renders it impractical for all but the lowest values of R_λ. We instead use a Lagrangian point-particle method based on the work of [109]. This approach assumes that particles are very small and dense, and can therefore be represented as infinitesimal points in the flow. Furthermore, We take the particle volume and mass loadings to be so low that the particle phase will not impact the flow itself, an approach known as 'one-way coupled simulation.' These conditions are generally reasonable for particle classes representative those in atmospheric clouds. We will discuss the accuracy of these approximations throughout this dissertation and will highlight any limitations in our numerics and the resulting particle statistics.

1.3 Organization of the dissertation

The first chapter of the dissertation (§2) discusses the code used to simulate particle-laden turbulence. In the following chapter (§3), we use an earlier version of this code to study particle motion across an interface with different levels of turbulence. This study is designed to mimic an experimental analysis and to provide insights into the motion of droplets near cloud boundaries. In

§4 and §5, We use this code to study droplet motion in homogeneous, isotropic turbulence (which we take to be representative of adiabatic cloud cores) at the highest Reynolds numbers to date. Section 4 focuses of the effect of Reynolds number on particle statistics without gravity, while §5 analyzes how gravity affects the particle motions at the different Reynolds numbers simulated. We conclude in §6 by discussing practical implications of the research for the cloud physics and turbulence communities, and by suggesting possible avenues for future research on particle-laden turbulent flows. To guide researchers who are undertaking large computational studies, we have included an appendix (Appendix C) discussing some of the challenges we faced and lessons we learned in running large-scale parallel computations.

CHAPTER 2

HIGHLY PARALLEL PARTICLE-LADEN FLOW SOLVER FOR TURBULENCE RESEARCH†

2.1 Abstract

In this paper, we present a Highly Parallel Particle-laden flow Solver for Turbulence Research (HiPPSTR). HiPPSTR is designed to perform three-dimensional direct numerical simulations of homogeneous turbulent flows using a pseudospectral algorithm with Lagrangian tracking of inertial point and/or fluid particles with one-way coupling on massively parallel architectures, and is the most general and efficient multiphase flow solver of its kind. We discuss the governing equations, parallelization strategies, time integration techniques, and interpolation methods used by HiPPSTR. By quantifying the errors in the numerical solution, we obtain optimal parameters for a given domain size and Reynolds number, and thereby achieve good parallel scaling on $O(10^4)$ processors.

2.2 Introduction

Turbulent flows laden with inertial particles (that is, particles denser than the carrier fluid) are ubiquitous in both industry and the environment. Natural

† P. J. Ireland, T. Vaithianathan, P. S. Sukheswalla, B. Ray, and L. R. Collins. Highly parallel particle-laden flow solver for turbulence research. *Comput. Fluids*, 76:170–177, 2013.

phenomena such as atmospheric cloud formation [55, 148, 179], plankton distributions in the sea [103], and planetesimal formation in the early universe [39, 38] are all influenced by particle-turbulence interactions. Inertial particle dynamics also impact engineered systems such as spray combustors [54], aerosol drug delivery systems [100], and powder manufacturing [132, 116], among many other systems [9]. Despite extensive research, however, open questions remain about the distribution of these particles in the flow, their settling speed due to gravity, and their collision rates. This is due in part to our incomplete understanding of the effect of the broad spectrum of flow scales that exists at intermediate or high Reynolds numbers.

Since inertial particle dynamics are strongly sensitive to the smallest scales in the flow [9], large-eddy simulation, with its associated small-scale modeling, has difficulties representing sub-filter particle dynamics accurately, including particle clustering that is driven by the Kolmogorov scales [57, 135]. Consequently, our investigations rely on the direct numerical simulation (DNS) of the three-dimensional Navier-Stokes equations and the Maxey & Riley equation for particle motion [109]. DNS has proven to be an extremely effective tool for investigating inertial particle dynamics, albeit at modest values of the Reynolds number due to the heavy computational demands of resolving all relevant temporal and spatial scales.

To extend the range of Reynolds numbers that can be simulated, we have developed a more advanced DNS code: the Highly Parallel, Particle-laden flow Solver for Turbulence Research (HiPPSTR). HiPPSTR is capable of simulating inertial particle motion in homogeneous turbulent flows on thousands of processors using a pseudospectral algorithm. The main objective of this paper is to

document the solution strategy and numerical algorithms involved in solving the relevant governing equations.

This paper is organized as follows. In §2.3, we show the equations governing the fluid and particle motion and the underlying assumptions of the flow solver. We discuss the time integration and interpolation techniques in §2.4 and §2.5, respectively, complete with an error analysis for optimizing code performance. Section 2.6 then describes the parallelization strategy, and §2.7 provides conclusions.

2.3 Governing equations

2.3.1 Fluid phase

The underlying flow solver is based on the algorithm presented in Ref. [30] and summarized below. It is capable of simulating both homogeneous isotropic turbulence (HIT) and homogeneous turbulent shear flow (HTSF) with a pseudospectral algorithm, while avoiding the troublesome remeshing step of earlier algorithms [140]. The governing equations for the flow of an incompressible fluid are the continuity and Navier-Stokes equations, here presented in rotational form

$$\frac{\partial u_i}{\partial x_i} = 0, \tag{2.1}$$

$$\frac{\partial u_i}{\partial t} + \epsilon_{ijk}\omega_j u_k = -\frac{\partial\left(p/\rho + \frac{1}{2}u^2\right)}{\partial x_i} + \nu\frac{\partial^2 u_i}{\partial x_j \partial x_j} + f_i, \tag{2.2}$$

where u_i is the velocity vector (with magnitude u), ϵ_{ijk} is the alternating unit symbol, ω_i is the vorticity, p is the pressure, ρ is the density, ν is the kinematic

viscosity, and f_i is a large-scale forcing function that is added to achieve stationary turbulence for HIT. Aside from the term $\frac{1}{2}u^2$, which ultimately will be subsumed into a modified pressure term—see Eq. (2.10) below, this form of the Navier-Stokes equation has only six nonlinear terms, as compared to nine in the standard form, which reduces the expense of computation and renders the solution method more stable.

Reynolds decomposition

We apply the standard Reynolds decomposition on the velocity, vorticity, and pressure, yielding

$$u_i = U_i + u_i', \tag{2.3}$$

$$\omega_i = \Omega_i + \omega_i', \tag{2.4}$$

$$p = P + p', \tag{2.5}$$

where capitalized variables denote mean quantities and primed variables denote fluctuating quantities.

Subtracting the ensemble average of Eqs. (2.1) and (2.2) from Eqs. (2.1) and (2.2), respectively, and specializing for the case of homogeneous turbulence (homogeneous turbulence implies all single-point statistics are independent of position, with the exception of the mean velocity U_i, which can vary linearly while still preserving homogeneity for all higher-order velocity statistics of the flow field) yields

$$\frac{\partial u_i'}{\partial x_i} = 0, \tag{2.6}$$

$$\frac{\partial u_i'}{\partial t} + \epsilon_{ijk}\left(\Omega_j u_k' + \omega_j' U_k + \omega_j' u_k'\right) = -\frac{\partial\left[p'/\rho + u_j' U_j + \frac{1}{2}u'^2\right]}{\partial x_i} + \nu\frac{\partial^2 u_i'}{\partial x_j \partial x_j} + f_i'. \tag{2.7}$$

We consider HTSF with a uniform mean shear rate $\mathcal{S}$, where coordinates x_1, x_2 and x_3 are the streamwise, spanwise and shear directions, respectively, without loss of generality. Under these conditions, the mean velocity and vorticity can be expressed as

$$\mathbf{U} = (\mathcal{S}x_3, 0, 0), \tag{2.8}$$

$$\mathbf{\Omega} = (0, \mathcal{S}, 0), \tag{2.9}$$

thus reducing Eq. (2.7) to

$$\frac{\partial u_i'}{\partial t} + u_3'\mathcal{S}\delta_{i1} + \mathcal{S}x_3\frac{\partial u_i'}{\partial x_1} + \epsilon_{ijk}\omega_j'u_k' = -\frac{\partial p^*}{\partial x_i} + \nu\frac{\partial^2 u_i'}{\partial x_j \partial x_j} + f_i', \tag{2.10}$$

where the modified pressure $p^* \equiv p'/\rho + \frac{1}{2}u'^2$. The above equations are written to encompass both HIT and HTSF; for HIT $\mathcal{S} = 0$ and $f_i' \neq 0$, while for HTSF $\mathcal{S} \neq 0$ and $f_i' = 0$.

Spectral transforms

Pseudospectral algorithms take advantage of the fact that the fluid velocity and pressure satisfy periodic boundary conditions. For HIT the period is simply the box domain, and so for a box of length $\mathcal{L}_1$, $\mathcal{L}_2$ and $\mathcal{L}_3$ in the x_1, x_2 and x_3 directions, respectively, the wavevector for the transforms takes the conventional form

$$\mathbf{k} \equiv \left(\frac{2\pi}{\mathcal{L}_1}n_1, \frac{2\pi}{\mathcal{L}_2}n_2, \frac{2\pi}{\mathcal{L}_3}n_3\right), \tag{2.11}$$

where the integers n_i vary between $-N_i/2 + 1$ and $N_i/2$ for N_i grid points in each direction [130]. Note that the code allows you to independently set the number of grid points N_i and the box length $\mathcal{L}_i$ in each direction.

For HTSF, the presence of the mean shear modifies this to a "shear-periodic boundary condition," as illustrated in Fig. 2.1. The classic Rogallo [140] al-

gorithm eliminated this complication by solving the equations of motion in a frame of reference that deforms with the mean shear, enabling standard fast Fourier transforms (FFTs) to be applied; however, in order to relieve the distortion of the physical space grid with time, the standard Rogallo algorithm maps the variables on the positively deformed mesh onto a mesh that is deformed in the opposite direction, a step known as "remeshing." Remeshing leads to sudden changes in the turbulent kinetic energy and dissipation rate as a consequence of zeroing out certain wavenumbers. The algorithm of Brucker et al. [30] eliminates this remeshing step by directly applying the spectral transform in a fixed frame of reference while incorporating the phase shift that results from the mean shear analytically. We begin by defining a modified wavevector as

$$k_i' \equiv k_i - \mathcal{S}tk_1\delta_{i3}, \tag{2.12}$$

and the Fourier decomposition of a variable $\phi(\mathbf{x}, t)$ as

$$\hat{\phi}(\mathbf{k}, t) \equiv \sum_{\mathbf{x}} \phi(\mathbf{x}, t) \exp\left(-Ik_i' x_i\right), \tag{2.13}$$

where $\hat{\phi}(\mathbf{k}, t)$ is the forward spectral transform of $\phi(\mathbf{x}, t)$, denoted as $\mathcal{F}\{\phi(\mathbf{x}, t)\}$, and I is the imaginary unit. The inclusion of the cross term $\mathcal{S}tk_1\delta_{i3}$ in the modified wavevector accounts for the shear-periodic boundary condition. We can similarly define a modified discrete backward spectral transform of $\hat{\phi}(\mathbf{k}, t)$ as

$$\phi(\mathbf{x}, t) = \frac{1}{N_1 N_2 N_3} \sum_{\mathbf{k}} \hat{\phi}(\mathbf{k}, t) \exp\left(Ik_i' x_i\right). \tag{2.14}$$

With these definitions, we can transform (2.6) and (2.10) to spectral space to obtain

$$k_i' \hat{u}_i' = 0, \tag{2.15}$$

$$\left[\frac{\partial}{\partial t} + \nu k'^2\right] \hat{u}_i' = \left(-\delta_{im} + \frac{k_i' k_m'}{k'^2}\right) \epsilon_{mjn} \mathcal{F}\left\{\omega_j' u_n'\right\} + 2\frac{k_i'}{k'^2} k_1' \mathcal{S}\hat{u}_3' - \delta_{i1}\mathcal{S}\hat{u}_3' + \hat{f}_i', \tag{2.16}$$

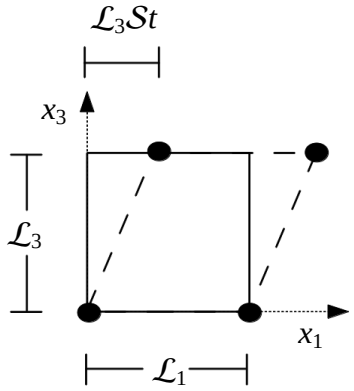

Figure 2.1: Shear-periodic boundary conditions due to the mean shear applied in the x_3 direction. The orthogonal domain is shown with the solid lines, while the shear-periodic boundary points are indicated by the black dots.

where $k'^2 = k'_i k'_i$. Note that we have used the incompressibility of the flow, as specified by Eq. (2.15), to project the pressure out of Eq. (2.16) (refer to Ref. [30] for a detailed derivation).

The direct evaluation of the convolution $\mathcal{F}\left\{\omega'_j u'_n\right\}$ would be computationally prohibitively expensive. The "pseudospectral approximation" is obtained by first transforming the velocity and vorticity into physical space, computing the product, then transforming the result back into spectral space [123]. The transformations between physical and spectral spaces are accomplished using modified fast Fourier transforms (FFTs) that are described in §2.6. The pseudospectral algorithm introduces aliasing errors that are eliminated by a combination of spherical truncation and phase-shifting (refer to Appendix A of Ref. [88] for details).

Low wavenumber forcing

To achieve stationary turbulence with HIT, we must introduce forcing to compensate for the energy that is dissipated [53]. The forcing is usually restricted to low wavenumbers (large scales) with the hope that the intermediate and high wavenumbers behave in a natural way that is not overly influenced by the forcing scheme. The two most widely used forcing schemes in the literature are "deterministic" and "random" forcing schemes. Both are described below.

The deterministic forcing scheme [184] first computes the amount of turbulent kinetic energy dissipated in a given time step h, $\Delta E_{\text{tot}}(h)$. This energy is restored at the end of each time step by augmenting the velocity over the forcing range between $k_{\text{f,min}}$ and $k_{\text{f,max}}$ so as to precisely compensate for the dissipated energy

$$\hat{\mathbf{u}}(\mathbf{k}, t_0 + h) = \hat{\mathbf{u}}(\mathbf{k}, t_0 + h) \sqrt{1 + \frac{\Delta E_{\text{tot}}(h)}{\int_{k_{\text{f,min}}}^{k_{\text{f,max}}} E(k, t_0 + h) dk}}, \tag{2.17}$$

where $E(k, t_0 + h)$ represents the turbulent kinetic energy in a wavenumber shell with magnitude k at time $t_0 + h$.

The alternative forcing scheme is based on introducing a stochastic forcing function, $\hat{f}_i'(\mathbf{k}, t)$ [53]. This function is non-zero only over the forcing range between $k_{\text{f,min}}$ and $k_{\text{f,max}}$ and evolves according to a vector-valued complex Ornstein-Uhlenbeck process [53], as shown below

$$d\hat{f}_i'(\mathbf{k}, t) = -\frac{\hat{f}_i'(\mathbf{k}, t)}{T_f} dt + \sqrt{\frac{2\sigma_f^2}{T_f}} dW_i(\mathbf{k}, t), \quad \forall k \ni (k_{\text{f,min}}, k_{\text{f,max}}], \tag{2.18}$$

where T_f is the integral time-scale of the random forcing, σ_f^2 denotes its strength, and $W_i(\mathbf{k}, t)$ is the Wiener process whose increment dW_i is defined to be a joint-

normal, with zero mean, and covariance given by

$$\langle dW_i dW_j^* \rangle = h\delta_{ij}. \tag{2.19}$$

While implementing on a computer, we set the increment $dW_i = (\alpha_i + I\beta_i)\sqrt{h/2}$, where α_i and β_i are two independent random numbers drawn from a standard normal distribution.

2.3.2 Particle phase

The Maxey & Riley equation [109] is used for simulating spherical, non-deforming particles in the flow. We take the particles to be small (i.e., $d/\eta \ll 1$, where d is the particle diameter, $\eta \equiv \nu^{3/4}/\epsilon^{1/4}$ is the Kolmogorov length scale, and ϵ is the average turbulent kinetic energy dissipation rate) and heavy (i.e., $\rho_p/\rho \gg 1$, where ρ_p and ρ are the densities of the particles and fluid, respectively). We also assume that the particles are subjected to only linear drag forces, which is valid when the particle Reynolds number $Re_p \equiv \|\mathbf{u}(\mathbf{x}) - \mathbf{v}\|d/\nu < 1$. Here, $\mathbf{u}(\mathbf{x})$ denotes the undisturbed fluid velocity at the particle position, and $\mathbf{v}$ denotes the particle velocity. For HTSF, we express $\mathbf{u}(\mathbf{x})$ as

$$u_i(\mathbf{x}) = u_i'(\mathbf{x}) + \mathcal{S}x_3\delta_{i1}, \tag{2.20}$$

and for HIT, $u_i(\mathbf{x}) = u_i'(\mathbf{x})$.

Under these assumptions, the Maxey & Riley equation simplifies to a system of ordinary differential equations for the position and velocity of a given particle

$$\frac{d\mathbf{x}}{dt} = \mathbf{v}, \tag{2.21}$$

$$\frac{d\mathbf{v}}{dt} = \frac{\mathbf{u}(\mathbf{x}) - \mathbf{v}}{\tau_p} + \mathbf{g}, \tag{2.22}$$

where $\tau_p \equiv \frac{\rho_p}{\rho}\frac{d^2}{18\nu}$ is the particle response time and $\mathbf{g}$ is the gravitational acceleration vector. Note that the numerical solution of (2.21) and (2.22) requires an interpolation of grid values of the fluid velocity to the location at the center of each particle. The interpolation methods used are discussed in §2.5.

The influence of particles on the continuity and momentum equations is neglected due to the low volume ($O(10^{-6})$) and mass ($O(10^{-3})$) loadings [50, 162], and therefore we consider only one-way coupling between the flow field and the particles. All particles are represented as point-particles, and collisions are neglected [161, 137].

2.4 Time integration

2.4.1 Fluid update

To calculate the temporal evolution of the fluid, we introduce the integrating factor

$$A_{ij}(t') \equiv \exp\left[\int_0^{t'}\left(\nu k'^2\delta_{ij} - 2\delta_{i3}\delta_{j3}\mathcal{S}\frac{k'_1k'_3}{k'^2}\right)dt\right] \tag{2.23}$$

into (2.16), yielding

$$\frac{\partial}{\partial t}\left[A_{ij}(t)\hat{u}'_j\right] = A_{ij}(t)RHS_{\,j}(t), \tag{2.24}$$

where for ease of notation, we have defined

$$RHS_{\,j} \equiv \left(-\delta_{jm} + \frac{k'_jk'_m}{k'^2}\right)\epsilon_{m\ell n}\mathcal{F}\left\{\omega'_\ell u'_n\right\} + 2\frac{k'_j}{k'^2}k'_1\mathcal{S}\hat{u}'_3 - \delta_{j1}\mathcal{S}\hat{u}'_3. \tag{2.25}$$

Integrating (2.24) from time t_0 to time $t_0 + h$, we obtain

$$A_{ij}(t_0+h)\hat{u}'_j(t_0+h) = \hat{u}'_j(t_0)A_{ij}(t_0) + \int_{t_0}^{t_0+h} RHS_{\,j}(t)A_{ij}(t)dt. \tag{2.26}$$

The trapezoid rule is used to approximate the integral on the RHS of (2.26), yielding

$$\int_{t_0}^{t_0+h} RHS_j(t)A_{ij}(t)dt \approx \frac{h}{2}RHS_j(t_0)A_{ij}(t_0) + \frac{h}{2}RHS_j(t_0+h)A_{ij}(t_0+h). \tag{2.27}$$

As the integrand in Eq. (2.23) is a rational function of time, we can evaluate $A_{ij}(t')$ analytically, substitute the result into Eq. (2.26), and apply the approximation in Eq. (2.27) to formulate a second-order Runge-Kutta method (RK2) for Eq. (2.26) as follows

$$\begin{aligned}\hat{u}_i'(t_0+h) = \hat{u}_j'(t_0)\exp\left[-\int_{t_0}^{t_0+h}\left(\nu k'^2\delta_{ij} - 2\delta_{i3}\delta_{j3}\mathcal{S}\frac{k_1'k_3'}{k'^2}\right)dt\right] \\ + \frac{h}{2}RHS_j(t_0)\exp\left[-\int_{t_0}^{t_0+h}\left(\nu k'^2\delta_{ij} - 2\delta_{i3}\delta_{j3}\mathcal{S}\frac{k_1'k_3'}{k'^2}\right)dt\right] \\ + \frac{h}{2}RHS_i(t_0+h).\end{aligned} \tag{2.28}$$

To avoid convective instabilities, the time step h is chosen to satisfy the Courant condition [133]

$$\frac{u'_{\max}h\sqrt{3}}{\min(\Delta x_1, \Delta x_2, \Delta x_3)} \lesssim 0.5, \tag{2.29}$$

where $u'_{\max}$ is the maximum velocity fluctuation in the domain, and Δx_i is the grid spacing in the i^{th} coordinate direction.

2.4.2 Particle update

Inertial particles introduce another time scale into the simulation, namely the particle response time τ_p, which is a parameter that is independent of the fluid time step h. For the case where $\tau_p \ll h$, the system defined by (2.21) and (2.22) is stiff, and traditional explicit Runge-Kutta schemes require an extremely small time step for numerical accuracy and stability. Note that updating the particle

equations implicitly would be prohibitively expensive, as it necessarily would involve multiple interpolations of the fluid velocity to the particle location. An alternative scheme we have used in the past is known as "subcycling," whereby the time step used to update the particle field is chosen so as to ensure $h/\tau_p \leq 0.1$. The fluid velocity field is linearly interpolated between the values at consecutive fluid time steps. While this method improves the accuracy of the RK2 method, it is computationally expensive, particularly for particles with low values of τ_p. Additionally, subcycling can degrade the parallel scaling of the code for simulations with a distribution of values of τ_p. The distribution of τ_p may vary from processor to processor, causing the entire calculation to run at the speed of the slowest processor (i.e., the processor with the highest load).

We have overcome these limitations by formulating an alternative second-order scheme that is uniformly effective over the entire range of τ_p, including the challenging case of $\tau_p \ll h$. The numerical scheme is based on "exponential integrators" [75]. Exponential integrators are a broad class of methods that treat the linear term in (2.22) exactly and the inhomogeneous part using an exponential quadrature.

The starting point for all of the updates is as follows

$$\mathbf{v}(t_0 + h) = e^{-h/\tau_p}\mathbf{v}(t_0) + w_1\mathbf{u}[\mathbf{x}(t_0)] + w_2\mathbf{u}[\mathbf{x}(t_0) + \mathbf{v}(t_0)h] + (1 - e^{-h/\tau_p})\tau_p\mathbf{g}, \quad (2.30)$$

where the weights w_1 and w_2 define the method. In our standard RK2 implementation, the weights are defined by

$$w_1^{RK} = 0.5\left(h/\tau_p\right)e^{-h/\tau_p}, \; w_2^{RK} = 0.5\left(h/\tau_p\right), \quad (2.31)$$

where the superscript "RK" indicates the standard RK method. In the new formulation based on the exponential quadrature, we redefine the weights as fol-

lows

$$w_1 \equiv \left(\frac{h}{\tau_p}\right)\left[\varphi_1\left(-\frac{h}{\tau_p}\right) - \varphi_2\left(-\frac{h}{\tau_p}\right)\right],\ w_2 \equiv \left(\frac{h}{\tau_p}\right)\varphi_2\left(-\frac{h}{\tau_p}\right), \tag{2.32}$$

and

$$\varphi_1(z) \equiv \frac{e^z - 1}{z},\ \varphi_2(z) \equiv \frac{e^z - z - 1}{z^2}. \tag{2.33}$$

Figure 2.2 compares the behavior of the RK weights with the newly defined exponential weights as a function of h/τ_p for particles with Stokes numbers $St \equiv \tau_p/\tau_\eta \leq 0.1$, where $\tau_\eta \equiv (\nu/\epsilon)^{1/2}$ is the Kolmogorov time scale. In the limit $h/\tau_p \to 0$, we see all the weights converge, implying consistency between the RK and exponential-quadrature methods in the limit of a highly resolved simulation, and confirming the new method's second-order accuracy. In the other limit, that is $St \to 0$ (or equivalently $h/\tau_p \to \infty$), we see the standard RK weights diverge, which clearly will lead to large numerical errors. In contrast, the exponential-quadrature weights have limits $w_1 \to 0$ and $w_2 \to 1$, implying from Eq. (2.30) that the particle velocity smoothly approaches $\mathbf{u}[\mathbf{x}(t_0) + \mathbf{v}(t_0)h] + \tau_p\mathbf{g}$ in this limit, which is the fluid velocity (corrected for gravitational settling) at the anticipated particle position at time $t_0 + h$ based on an Euler time step, i.e., the correct limit. Furthermore, the truncation error per step (as $\tau_p \to 0$) for the RK2 scheme is $O\left(h^3\tau_p^{-3}\mathbf{u}\right)$ while that of the new scheme is $O\left(h^3\tau_p^{-1}\frac{d^2\mathbf{u}}{dt^2}\right)$, indicating that the error constant for the RK2 is $O\left(\tau_p^{-2}\right)$ greater than that of the exponential integrator.

We quantify the integration errors in the two schemes by performing a numerical experiment on a domain with 512^3 grid points, $2,097,152$ particles, and small scale resolution $k_{\max}\eta = 2$ (where $k_{\max} = N\sqrt{2}/3$ is the maximum resolved wavenumber magnitude). We first use a Courant number of 0.5 to advance the particle field for one time step, with both the RK2 scheme and the exponential integrator scheme. To reduce time-stepping errors and attain a baseline case for quantifying these errors, we perform a set of low-Courant-number simula-

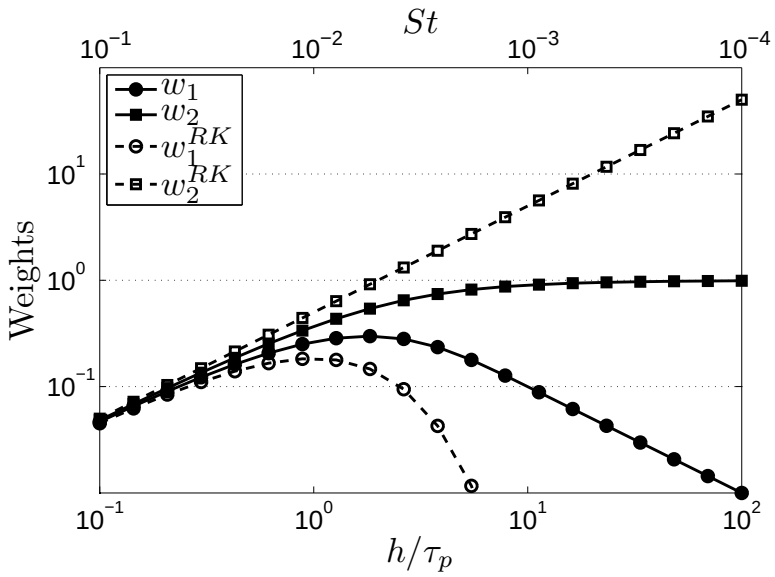

Figure 2.2: Functional behavior of weights for the exponential integrator (denoted as solid lines with closed symbols) and the Runge-Kutta scheme (denoted as dashed lines with open symbols) in a Stokes number range of interest.

tions, starting from the same initial condition as the simultations with a Courant number of 0.5. We advance the particle field for 1000 time steps using the exponential integrator scheme with the Courant number of 0.0005 (i.e., a time step equal to $1/1000^{\text{th}}$ that of the other simulations) and $h/\tau_p \leq 0.1$. The estimated root-mean-square (RMS) velocity errors incurred during numerical integration for the exponential integrator and RK2 schemes are plotted in figure 2.3(a). The time to update the positions and velocities of the particles for each of the two schemes is plotted in figure 2.3(b), normalized by the time to complete one step of the Navier-Stokes solver, which remains constant for all the cases. From figures 2.3(a) and (b), it is evident that the exponential integrator outperforms the RK2 scheme, both in terms of numerical accuracy and computational expense, particularly for high values of h/τ_p (i.e., low values of St).

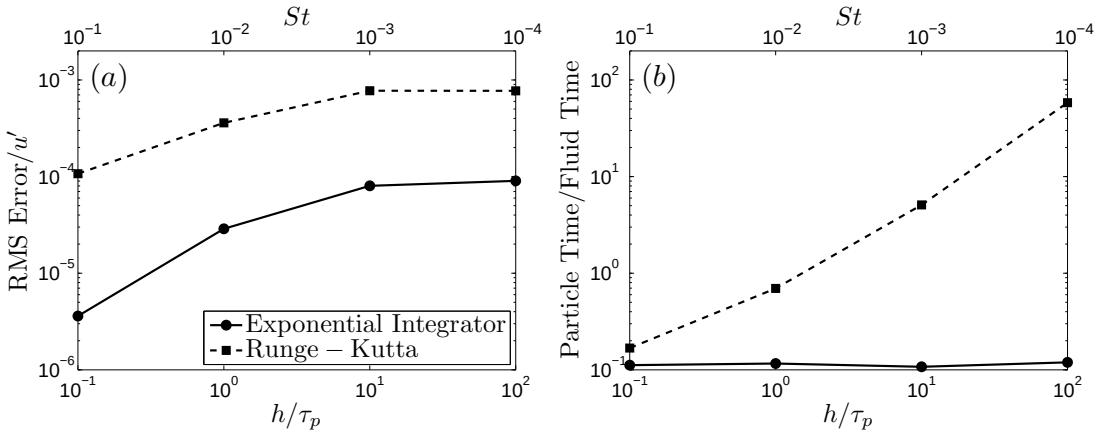

Figure 2.3: (a) RMS velocity integration errors in the particle update (normalized by the RMS fluid velocity) as a function of h/τ_p and St for both the exponential integrator and RK2 schemes. (b) Time to update the positions and velocities of $2,097,152$ particles for both schemes, normalized by the time to complete one step of the Navier-Stokes solver.

2.5 Interpolation

2.5.1 Interpolation Methods

As discussed in §2.3.2, the solution of (2.21) and (2.22) requires an interpolation of grid values of the fluid velocity to the particle centers. In principle, this interpolation could be performed exactly (provided that the grid is sufficiently fine to capture all scales of motion) using a spectral interpolation [10]. For a typical simulation involving at least a million particles, however, such an interpolation technique is prohibitively expensive.

To compute the fluid velocities at the particle centers, we have embedded several different interpolation methods into our code. They include linear, Lagrangian [19], Hermite [99], shape function method (SFM) [10], and B-spline interpolation [169]. For the Lagrangian and B-spline interpolations, we use 4,

6, 8, and 10 interpolation points (denoted as Lag$P$ and BSpline$P$, where P is the number of interpolation points). These interpolation methods are compared in figure 2.4, both in terms of accuracy and computational expense. All data in figure 2.4 is from a simulation with 512^3 grid points, $2,097,152$ particles, and $k_{\max}\eta = 2$. In all cases, we determined the "exact" values of the particle velocities from a spectral interpolation, and defined the velocity error of a particular scheme as the RMS difference between the velocities obtained from that scheme and the spectral interpolation at a given time.

Based on figure 2.4, the B-spline interpolation scheme, which is optimized for spectral simulations [169], provides the best trade-off between computational expense and accuracy. To determine the optimal number of spline points, we compare the interpolation error to the local time-stepping error, as given in figure 2.3(a). From these results, for a given run, we choose the number of spline points so that the interpolation and time-stepping errors are of the same order of magnitude.

2.5.2 Interpolation in shear flow

All our interpolation methods are designed for velocities which are stored on an orthogonal grid in physical space. As discussed in §2.3.1, the Brucker et al. [30] algorithm for the fluid velocity stores the physical-space velocity on an orthogonal mesh that is shear periodic. Consequently, the interpolation methods must be adapted to accommodate particles that require data from shear-periodic grid points. As an example, consider linear interpolation for the particle shown in figure 2.5. The schematic is shown in two dimensions on a 4×4 grid for clarity.

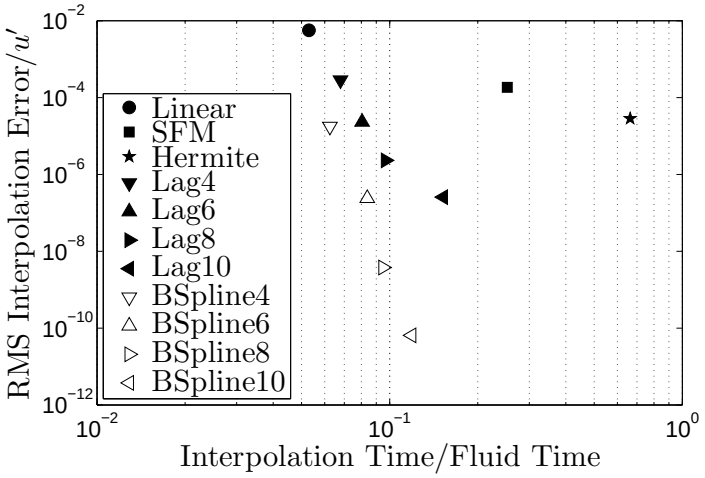

Figure 2.4: Interpolation error for different methods as a function of computation time, which is normalized by the time for one step of the Navier-Stokes solver. All errors are normalized by the RMS fluid velocity, u'.

Grid values of velocity are stored at the filled circles, and periodic points are shown as squares: standard periodic points are filled squares and shear-periodic points are open squares. The dotted lines in the figure illustrate the phase shift that occurs between points A, B, C and D on the bottom surface and the shear-periodic points on the top surface. To complete the interpolation, the data on the top surface must be phase shifted back to the orthogonal mesh points A′, B′, C′ and D′. This is accomplished by applying a one-dimensional spectral transform along the x_1-direction

$$\check{\mathbf{u}}'_{\text{boundary}}(k_1, x_2, x_3) \equiv \sum_{x_1} \mathbf{u}'_{\text{boundary}}(x_1, x_2, x_3)\exp\left(-Ik_1x_1\right), \tag{2.34}$$

multiplying by the following factor to shift the points in the x_1-direction

$$\check{\mathbf{u}}''_{\text{boundary}}(k_1, x_2, x_3) \equiv \check{\mathbf{u}}'_{\text{boundary}}(k_1, x_2, x_3)\exp\left(-Ik_1\mathcal{S}t\mathcal{L}_3\right), \tag{2.35}$$

and converting back to physical space to recover the values at the open squares

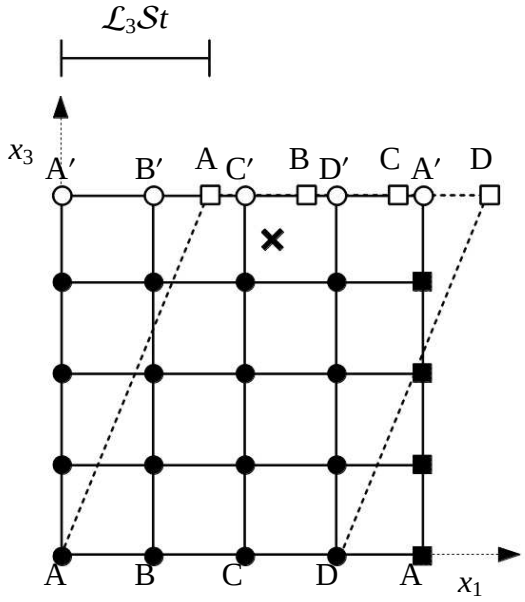

Figure 2.5: Example to demonstrate the interpolation approach for shear-periodic boundary conditions on a 4×4 grid. The particle is indicated by the symbol $\times$, the stored grid values by filled circles, the standard periodic boundary points by filled squares, and the shear-periodic boundary points by open squares. Corresponding boundary points are labeled A, B, C, D to illustrate the shear-periodic boundary condition. We determine the velocity values at the open circles (A′, B′, C′, D′) to complete the interpolation.

A′, B′, C′ and D′ (denoted $\mathbf{u}''_{\text{boundary}}$ below)

$$\mathbf{u}''_{\text{boundary}}(x_1, x_2, x_3) \equiv \frac{1}{N_1} \sum_{k_1} \check{\mathbf{u}}''_{\text{boundary}}(k_1, x_2, x_3) \exp\left(Ik_1 x_1\right). \tag{2.36}$$

Given these velocity values, we can complete the interpolation using the standard approaches for orthogonal grids.

2.6 Parallelization

2.6.1 Fluid update

As the Reynolds number increases, the range of spatial and temporal scales also increases, resulting in the approximate scaling $N_T \sim R_\lambda^{9/2}$, where N_T is the total number of grid points, $R_\lambda \equiv 2K\sqrt{5/(3\nu\epsilon)}$ is the Reynolds number based on the Taylor microscale, and K is the average turbulent kinetic energy. The rapid increase in the computational load with Reynolds number has limited DNS to relatively modest values of this parameter. Furthermore, with the slowing of processor speeds from Moore's Law over the past decade, the strategy for advancing supercomputer speeds has shifted toward increasing the number of accessible processors on the system. Exploiting these massively parallel architectures requires a new class of algorithms.

The previous version of the code utilized one-dimensional ("plane") parallel domain decomposition. Using this parallelization strategy, a domain with N^3 grid points can be parallelized on at most N processors, which realistically can accommodate a maximum simulation size of 1024^3 grid points or Reynolds numbers in the range $R_\lambda \lesssim 400$.

To increase the granularity of the parallelization, we have modified the code to allow two-dimensional ("pencil") domain decomposition. With pencil decomposition, we are able to parallelize a domain with N^3 grid points on up to N^2 processors. Figure 2.6 illustrates the difference between the plane and pencil domain decompositions.

While the Message Passing Interface (MPI) is used as the communication en-

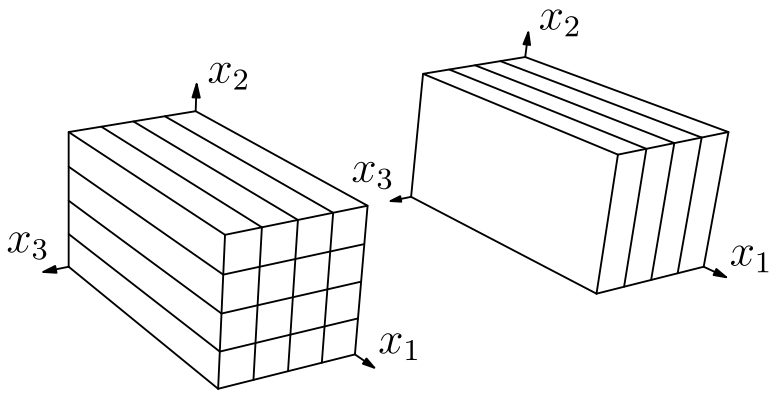

Figure 2.6: A representative two-dimensional ('pencil') decomposition (left) and one-dimensional ('plane') decomposition (right).

vironment, the detailed bookkeeping for the FFTs with pencil decomposition is performed using the P3DFFT library [128]. P3DFFT uses standard FFT libraries (such as FFTW [60] or ESSL [1]) to compute the three-dimensional FFT of the velocity or pressure distributed over the two-dimensional array of processors. The FFTs are necessary for computing the nonlinear convolution sums described in §2.3.1 and constitute the bulk of the computational expense of the overall fluid solver. They are performed as a series of one-dimensional FFTs in each of the three coordinate dimensions. Starting from a spectral-space variable $\hat{\phi}(k_1, k_2, k_3)$, where the entire k_3-dimension is stored on each pencil, we first perform $N_1 \times N_2$ one-dimensional complex-to-complex pencil transforms in the x_3 direction to obtain

$$\check{\phi}(k_1, k_2, x_3) \equiv \frac{1}{N_3} \sum_{k_3} \hat{\phi}(k_1, k_2, k_3) \exp\left(I k_3 x_3\right). \tag{2.37}$$

For HTSF only, we phase shift $\check{\phi}(k_1, k_2, x_3)$ to account for the shear-periodic boundary conditions, as discussed in §2.3.1

$$\tilde{\phi}(k_1, k_2, x_3) \equiv \check{\phi}(k_1, k_2, x_3) \exp\left(-I k_1 \mathcal{S}t x_3\right). \tag{2.38}$$

The data in the second and third dimensions is then transposed using the P3DFFT column communicator, so that all the data from the second dimension

is now contiguous. Next, $N_1 \times N_3$ one-dimensional complex-to-complex FFTs are performed on the second dimension

$$\breve{\phi}(k_1, x_2, x_3) \equiv \frac{1}{N_2} \sum_{k_2} \tilde{\phi}(k_1, k_2, x_3) \exp\left(I k_2 x_2\right). \tag{2.39}$$

The data in the first and second dimensions is then transposed using the P3DFFT row communicator, after which $N_2 \times N_3$ complex-to-real one-dimensional transforms are performed on the first dimension, to obtain

$$\phi(x_1, x_2, x_3) = \frac{1}{N_1} \sum_{k_1} \breve{\phi}(k_1, x_2, x_3) \exp\left(I k_1 x_1\right). \tag{2.40}$$

The forward transform follows by analogy. Starting from a real-space variable $\phi(x_1, x_2, x_3)$, we first perform $N_2 \times N_3$ real-to-complex one-dimensional transforms on the first dimension

$$\breve{\phi}(k_1, x_2, x_3) = \sum_{x_1} \phi(x_1, x_2, x_3) \exp\left(-I k_1 x_1\right). \tag{2.41}$$

The data in the first and second dimensions is transposed using the P3DFFT row communicator, and $N_1 \times N_3$ complex-to-complex one-dimensional transforms are performed on the second dimension

$$\tilde{\phi}(k_1, k_2, x_3) = \sum_{x_2} \breve{\phi}(k_1, x_2, x_3) \exp\left(-I k_2 x_2\right). \tag{2.42}$$

We then perform a transpose of the second and third dimensions using the P3DFFT column communicator, and phase shift to account for the shear-periodic boundary conditions

$$\breve{\phi}(k_1, k_2, x_3) = \tilde{\phi}(k_1, k_2, x_3) \exp\left(-I k_1 \mathcal{S}t x_3\right). \tag{2.43}$$

We complete the transformation by calling $N_1 \times N_2$ complex-to-complex one-dimensional transforms

$$\hat{\phi}(k_1, k_2, k_3) = \sum_{x_3} \breve{\phi}(k_1, k_2, x_3) \exp\left(-I k_3 x_3\right). \tag{2.44}$$

2.6.2 Particle update

The scale separation between the largest and smallest turbulent flow features increases with the flow Reynolds number. Therefore, an increase in Reynolds number requires an increase in the number of Lagrangian particles, to ensure that the particles sample the flow with sufficient resolution. The flow Reynolds number we achieve is determined by both the number of grid points and the small-scale resolution $k_{\max}\eta$. From experience, for $k_{\max}\eta \approx 2$, we have found that a population of $(N/4)^3$ particles (where N is the number of grid points in each direction) for a given St provides a good balance between statistical convergence and computational expense.

At the start of a simulation, particles are placed randomly throughout the solution domain with a uniform distribution. These random initial positions are generated efficiently in parallel using version 2.0 of the SPRNG library [104]. Each particle is assigned to a processor based on its physical location in the flow. Some of the grid values of the fluid velocity needed for the interpolation discussed in §2.5 may reside outside of that processor's memory, however. We therefore pad the processor's velocity field with ghost cells, as illustrated in figure 2.7. The unshaded grid cells represent fluid velocities that are local to a given processor, and the shaded grid cells represent ghost cell values from adjacent processors. The cells are numbered to indicate the correspondence between standard grid cells and ghost cells. The ghost cell exchanges are performed using two-sided, nonblocking MPI. As the simulation progresses, particles travel throughout the simulation domain under the influence of the turbulent flow. Particles which cross processor boundaries are exchanged at the end of every time step, also using two-sided, nonblocking MPI.

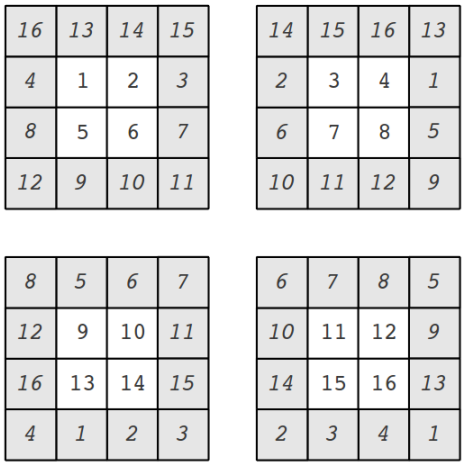

Figure 2.7: Ghost cell communication for interpolation for a representative two-dimensional parallel domain decomposition over four processors. The unshaded grid cells are fluid velocities which are local to each processor, and the shaded grid cells are ghost cells from adjacent processors. The cells are numbered to indicate the correspondence between standard grid cells and ghost cells.

2.6.3 Parallel scaling

In figure 2.8, we show timing data for simulations with a total of N^3 grid points and $(N/4)^3$ particles as a function of the number of processors M. The wall-clock time per step t is normalized by $N^3 log_2 N$, the expected scaling for a three-dimensional FFT. The ideal scaling case (slope -1 line) is shown for comparison. All timings were performed on the computing cluster "Jaguar" at Oak Ridge National Laboratory (ORNL).

We achieve good scaling on ORNL Jaguar for the largest problem sizes. For a domain with 2048^3 grid points, for example, we observe 85% strong scaling when moving from 1024 processors to 4096 processors, and nearly 60% strong scaling on up to $16,384$ processors.

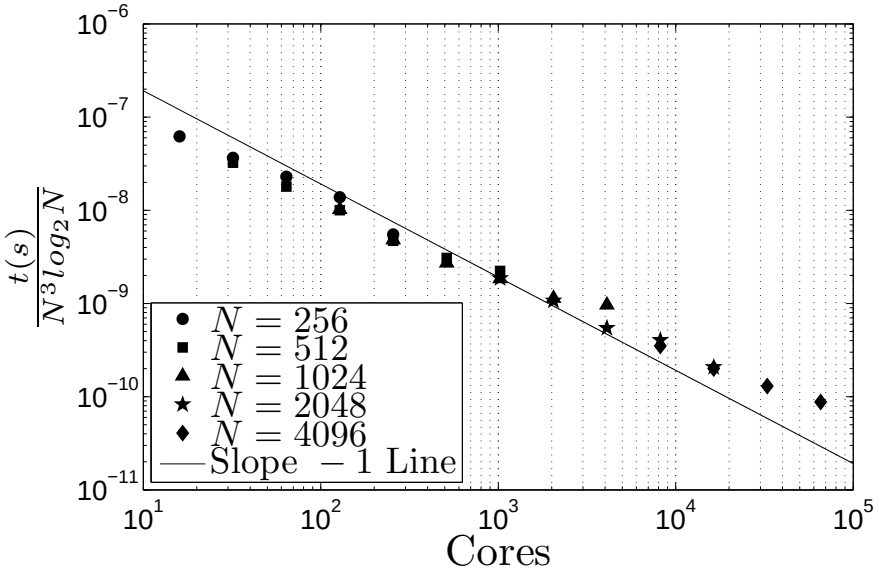

Figure 2.8: Parallel scaling on ORNL Jaguar for grids of size N^3 with $(N/4)^3$ particles on M processors. The wall-clock time per step t is normalized by $N^3 log_2 N$, the expected scaling for a three-dimensional FFT.

2.7 Conclusion

We have presented a highly parallel, pseudospectral code ideally suited for the direct numerical simulation of particle-laden turbulence. HiPPSTR, the most efficient and general multiphase flow code of its kind, utilizes two-dimensional parallel domain decomposition, Runge-Kutta and exponential-integral time-stepping, and accurate and efficient B-spline velocity interpolation methods. All of these methods are selected and tuned for optimal performance on massively parallel architectures. HiPPSTR thus achieves good parallel scaling on $O(10^4)$ cores, making it ideal for high-Reynolds-number simulations of particle-laden turbulence.

Acknowledgments

This article is a revised and expanded version of a conference proceeding for the Seventh International Conference on Computational Fluid Dynamics (ICCFD7) [83]. We are grateful to M. van Hinsberg and Professor P.-K. Yeung for helpful discussions during the code development. The authors acknowledge financial support from the National Science Foundation through Grant CBET-0967349 and through the Graduate Research Fellowship awarded to PJI. Additionally, the authors are indebted to several organizations for computational time used in developing and optimizing HiPPSTR. We would like to acknowledge high-performance computing support provided by the Extreme Science and Engineering Discovery Environment (supported by National Science Foundation grant number OCI-1053575), NCAR's Computational and Information Systems Laboratory (sponsored by the National Science Foundation), and the resources of the Oak Ridge Leadership Computing Facility at the Oak Ridge National Laboratory (supported by the Office of Science of the U. S. Department of Energy under Contract No. DE-AC05-00OR22725).

CHAPTER 3

DIRECT NUMERICAL SIMULATION OF INERTIAL PARTICLE ENTRAINMENT IN A SHEARLESS MIXING LAYER†

3.1 Abstract

We present the first computational study of the dynamics of inertial particles in a shearless turbulence mixing layer. We parameterize our direct numerical simulations to isolate the effects of turbulence, Reynolds number, particle inertia, and gravity on the entrainment process. By analyzing particle concentrations, particle and fluid velocities, particle size distributions, and higher-order velocity moments, we explore the impact of particle inertia and gravity on the mechanism of turbulent mixing. We neglect thermodynamic processes, including phase changes between the drops and surrounding air, which is equivalent to assuming the air is saturated (i.e., 100% humidity). Entrainment is found to be governed by the large scales of the flow and is relatively insensitive to the Reynolds number over the range considered. Our results show that both fluid and particle velocities exhibit intermittency and that gravity and turbulent diffusion interact in unexpected ways to dictate particle dynamics. An analysis of the temporal evolution of fluid and particle statistics suggests that particle concentration profiles and velocities are self-similar under certain circumstances. We also observe large fluctuations in particle concentrations resulting from entrainment and introduce a model to estimate the impact these fluctuations have

† P. J. Ireland and L. R. Collins. Direct numerical simulation of inertial particle entrainment in a shearless mixing layer. *J. Fluid Mech*, 704:301–332, 2012.

on the radial distribution function, a statistic that is often used to quantify inertial particle clustering. Our study is both a computational counterpart to and an extension of the wind-tunnel experiments by [62] and [65]. We find good agreement between these experimental studies and our computational results. We anticipate that a better understanding of the role of gravity and turbulence on inertial particle entrainment will lead to improved cloud evolution predictions.

3.2 Introduction

Entrainment, the drawing in of external fluid by a turbulent flow, is ubiquitous to both industrial and natural turbulent processes. In jets, plumes, and mixing layers, entrainment results from the turbulent diffusion of momentum from a central core region [130]. There have been a number of experimental and numerical investigations of the fluid mechanics and mixing characteristics of tracer species convected by these flows [41, 171, 21, 105, 181, 180, 77, 78]. In particular, the connection of tracer species to a wide range of combustion processes has led to a broad literature on the mixing characteristics of entraining flows [11, 27, 29, 117, 96, 131].

Entrainment also has been recognized as an important process in atmospheric clouds. In particular, entrainment of dry air near cloud boundaries by turbulence can affect precipitation mechanisms, yet still little is known about the fundamental parameters and mechanisms that control the entrainment process [134, 148]. Indeed, the observation of [22] still remains relevant today, 'It is even possible that if cumulus clouds did not entrain, many problems in cloud physics would have been more-or-less solved.' Clouds, aside from their role in

weather, are responsible for the greatest uncertainty in global climate models [148, 160].

In the meantime, our understanding of the motion of inertial particles in turbulence has advanced considerably. A number of numerical studies demonstrate inertial particle clustering outside of vortices due to a centrifugal effect [106, 159, 48, 137, 178, 61, 14]. Recent experimental measurements with sufficient precision show clustering levels that are similar to the numerical simulations [186, 145, 146, 43]. Clustering has been shown to affect aerosol processes such as particle collisions and coalescence [161, 178, 138, 200], particle sedimentation [108, 106, 175, 118, 4, 91], the modulation of turbulence by particles [157, 50, 162, 46, 79], and particle acceleration statistics [12, 8, 7, 63, 98].

That understanding, however, has not been extended to the entrainment of inertial particles across interfaces by turbulence, as is found at the boundaries of atmospheric clouds; that is, the impact of inertia and gravity on the mixing process is not well understood. In two recent studies, [62] and [65] investigated this issue by examining the motion of droplets across a 'shearless mixing layer,' which is simply an interface between flows with the same mean velocity but different turbulence levels [170, 28, 93, 166, 90, 167]. These studies are particularly relevant to entrainment in cumulus clouds, where a sharp interface exists between the highly turbulent cloud and the less turbulent ambient air [148]. By eliminating mean shear in their flow, they were able to focus on the intrinsic turbulence effects. Both experiments [170, 90, 62, 65] and simulations [28, 93, 166, 90] show that the fluid velocity field is marked by high intermittency near the interface, characteristic of turbulent bursts penetrating the low turbulence region. Prior numerical studies of the shearless mixing layer have

not considered the effect of particle inertia, and thus one of the goals of this study is to determine how inertial particles behave differently from the passive scalars or inertialess 'tracer' particles in this flow.

Gravity also plays an unexpected role on inertial particle dynamics. Some experiments [4] and simulations [175] have shown that inertial particles fall faster through turbulence than through a quiescent fluid. The enhancement is due to 'preferential sweeping,' whereby inertial particles are preferentially swept toward downward-moving fluid by the vortices. Other studies [118, 91, 65] have shown that for certain parameters, sedimentation can be inhibited by turbulence. [118] postulated that large particles are subject to a 'loitering' effect, whereby they spend more time (on average) in fluid moving opposite to the direction of gravity.

In this paper, we analyze the entrainment of inertial particles across a shearless mixing layer using direct numerical simulations (DNS). In contrast to several previous studies which focus on the thermodynamics of entrainment at cloud boundaries (e.g., see [101, 151, 112]), our objective is to understand more fully the underlying turbulent processes in the absense of thermodynamics. The simulations thus neglect phase changes between the drops and the surrounding air, corresponding to the limit of perfectly saturated air (i.e., 100% humidity). The shearless mixing layer is perhaps the simplest inhomogeneous turbulent flow to consider because of its lack of any mean velocity gradients, and hence production, making it ideal for isolating the various mechanisms involved in the entrainment process. Our DNS conditions have been chosen to mimic (to the extent possible) the parameters in the recent wind-tunnel experiments of [62] and [65]. As with the experiments, we too consider two turbulent flow

conditions. The turbulence–turbulence interface (TTI) case considers particle entrainment across an interface with uniform turbulence parameters, and the turbulence–non-turbulence interface (TNI) case considers particle entrainment across an interface with a step change in the turbulence parameters. By varying particle inertia, flow Reynolds number, gravitational orientation, and turbulence intensity, we are able to explore the role of each parameter on the overall mixing process. We provide comparisons with the experiments where applicable. The overall goal of this study is to develop new insight into the entrainment process for inertial particles that can be used to improve existing cloud models.

The paper is organized in the following manner. We explain the methods, equations, assumptions, and relevant parameters in the DNS in §3.3. Fluid statistics are discussed in §3.4 with reference to previous studies of turbulent fluid in a shearless mixing layer, and particle dynamics are analyzed in §3.5 through profiles of particle concentration, velocity, and inertia. Finally, in §3.6, we summarize our work and suggest practical implications for cloud physics and other fields.

3.3 Numerical methods

3.3.1 Governing equations and numerical methods

The governing equations for an incompressible fluid in a three-dimensional periodic cube are the continuity equation and the Navier-Stokes equations, here presented in rotational form

$$\nabla \cdot \mathbf{u} = 0 \,, \tag{3.1}$$

$$\frac{\partial \mathbf{u}}{\partial t} + \omega \times \mathbf{u} + \nabla\left(\frac{p}{\rho_f} + \frac{u^2}{2}\right) = \nu \nabla^2 \mathbf{u} \,, \tag{3.2}$$

where $\mathbf{u}$ is the fluid velocity, $\boldsymbol{\omega} \equiv \nabla \times \mathbf{u}$ is the vorticity, p is the pressure, ρ_f is the fluid density, and ν is the kinematic viscosity. We employ a pseudospectral method to advance these equations on a 512^3 grid using a second-order, explicit Runge-Kutta scheme with aliasing errors removed by means of a combination of spherical truncation and phase-shifting. Further details of the fluid update are given in [30].

Non-evaporating, solid particles in the flow field are advanced according to the equation of [109], which in the limit of small, heavy particles (i.e., $d/\eta \ll 1$, where d is the particle diameter and η is the Kolmogorov lengthscale, and $\rho_p/\rho_f \gg 1$, where ρ_p is the particle density) reduces to the following set of linear ordinary differential equations for the i^{th} particle

$$\frac{d\mathbf{X}_i}{dt} = \begin{cases} \mathbf{u}(\mathbf{X}_i) & \text{passive tracers} \\ \mathbf{v}_i & \text{inertial particles} \end{cases} \tag{3.3}$$

$$\frac{d\mathbf{v}_i}{dt} = \frac{\mathbf{u}(\mathbf{X}_i) - \mathbf{v}_i}{\tau_{p_i}} + (1 - \rho_f/\rho_p)\mathbf{g}, \tag{3.4}$$

where $\mathbf{X}_i$ and $\mathbf{v}_i$ are the instantaneous position and velocity of the i^{th} particle respectively, $\mathbf{u}(\mathbf{X}_i)$ is the undisturbed fluid velocity at the particle center, $\tau_{p_i} \equiv d_i^2 \rho_p / (18 \rho_f \nu)$ is the particle response time, and $\mathbf{g}$ is the gravitational acceleration. Equations (3.3) and (3.4) have the additional restriction that the particle Reynolds number must be small, i.e., $Re_p \equiv \|\mathbf{u}(\mathbf{X}) - \mathbf{v}\| d/\nu < 0.5$ [49]. This condition is met by over 99.8% of the particles at a given time in the simulation. To obtain $\mathbf{u}(\mathbf{X}_i)$, we employ an 8^{th} order Lagrange polynomial interpolation in three dimensions. The influence of particles on the continuity and momentum equations is negligible for low volume ($\Phi_v \sim 10^{-6}$) and mass ($\Phi_m \sim 10^{-3}$) loadings (e.g., see [50, 162]), and we therefore consider only one-way coupling between

the flow field and the particles. All particles are represented as point particles, and collisions are neglected [137].

3.3.2 Initialization

For the isotropic velocity field, we first generate a random phase velocity with components that are scaled to match the following prescribed energy spectrum [85]

$$E_0(k) = C_\kappa \epsilon_0^{2/3} k^{-5/3} \begin{cases} (k/\kappa_0)^2 & k < \kappa_0 \\ (k/\kappa_0)^{-5/3} & \kappa_0 \le k \le \kappa_\eta \\ 0 & k > \kappa_\eta \end{cases}, \tag{3.5}$$

where k is the wavenumber, $C_\kappa \approx 1.5$ is the Kolmogorov constant, ϵ_0 is the initial energy dissipation rate, κ_0 is the initial location of the peak in the energy spectrum, and κ_η is the maximum energy-containing wavenumber. We select these parameters to give good resolution of both large- and small-scale motions. For adequate large-scale resolution, we require that $\mathcal{L}/\ell \gtrsim 8$, where $\mathcal{L} = 2\pi$ is the length of one side the computational domain, and ℓ is the longitudinal integral lengthscale [130]. Small-scale resolution is maintained by ensuring that $k_{max}\eta > 1$, where k_{max} is the maximum resolved wavenumber [52]. After generating a random phase velocity field, we let the flow evolve according to (3.1) and (3.2) until the skewness of the velocity derivatives $\langle(\partial u/\partial x)^3\rangle / \left[\langle(\partial u/\partial x)^2\rangle^{3/2}\right]$ converged to the accepted value of about -0.4 [164]. This then was the initial velocity field for all of the turbulence–turbulence interface (TTI) studies.

The turbulence–non-turbulence interface (TNI) simulations require that we generate turbulence with strong spatial variation (i.e., the 'shearless' mixing layer). Our approach is based on the initialization procedure used by [28], [93],

and [166]. We first create two separate isotropic velocity fields according to the algorithm described above, each with different turbulence characteristics. We shall refer to the low and high turbulence velocity fields, respectively, as $\mathbf{u}_{\text{low}}$ and $\mathbf{u}_{\text{high}}$. The two velocities are combined to generate a provisional mixing layer velocity $\breve{\mathbf{u}}$ as follows

$$\breve{\mathbf{u}}(\mathbf{x}) = [1 - \mathcal{G}(\mathbf{x})]\, \mathbf{u}_{\mathbf{low}}(\mathbf{x}) + \mathcal{G}(\mathbf{x})\mathbf{u}_{\mathbf{high}}(\mathbf{x}) \,, \tag{3.6}$$

where the smoothing function $\mathcal{G}(\mathbf{x})$ is defined as [93]

$$\mathcal{G}(\mathbf{x}) = \begin{cases} 0 & \text{if } 0 \le y < 5\pi/12 \\ \frac{1}{2}(\sin(6(y - \frac{\pi}{2})) + 1) & \text{if } 5\pi/12 \le y < 7\pi/12 \\ 1 & \text{if } 7\pi/12 \le y < 17\pi/12 \\ \frac{1}{2}(\sin(6(y - \frac{4\pi}{3})) + 1) & \text{if } 17\pi/12 \le y < 19\pi/12 \\ 0 & \text{if } 19\pi/12 \le y \le 2\pi \end{cases} . \tag{3.7}$$

In this way, we establish variation of the turbulence intensity in the y–direction, with a slab of high intensity turbulence in the center of the cube surrounded by low-intensity turbulence on either side. The blending region between high and low turbulence intensities comprises 1/6 of the total width of the periodic cube.

The resulting velocity $\breve{\mathbf{u}}(\mathbf{x})$ has the correct turbulence levels; however, as a consequence of the filter, it no longer satisfies continuity (i.e., $\nabla \cdot \breve{\mathbf{u}} \neq 0$). To correct this, we take the Fourier transform of $\breve{\mathbf{u}}(\mathbf{x})$, say $\hat{\breve{\mathbf{u}}}(\mathbf{k})$, and form the inner product with the 'projection tensor' $P_{ij}(k_i) = \delta_{ij} - k_i k_j / k^2$ [130]

$$\hat{\mathbf{u}}(\mathbf{k}) \equiv \mathbf{P}(\mathbf{k}) \cdot \hat{\breve{\mathbf{u}}}(\mathbf{k}) \,. \tag{3.8}$$

The resulting velocity field $\hat{\mathbf{u}}(\mathbf{k})$ in Fourier space or $\mathbf{u}(\mathbf{x})$ in physical space is, by definition, divergence-free. This procedure, however, diminishes the ratio of the intensity of the high and low turbulence regions. By iteratively rescaling

the velocity components and projecting to satisfy continuity, we can converge the divergence-free velocity field arbitrarily close to the intended turbulence intensity ratio.

The particles are placed randomly throughout the central slab of the cube (the one corresponding to the high turbulence region in the TNI simulations). They are initialized with the fluid velocity at their location plus a Stokes' drift term to account for gravitational settling. It should be noted that other simulations performed with the Stokes' drift omitted at initialization showed no discernible difference in particle statistics at later times, suggesting that the effect of the initial velocity is quickly forgotten.

The periodic boundary conditions require that we use this slab configuration, where the two interfaces are statistically equivalent and can be analyzed together. We define $y = 0$ as the location of the initial interfaces, with the particle injection side (the initial high energy side for the TNI) given by $y < 0$ and the non-injection side (the initial low energy side for the TNI) given by $y > 0$. Thus, by our sign convention, particle velocities directed toward the non-injection side are positive. All statistics are presented as a function of the inhomogeneous coordinate y and are averaged over the statistically homogeneous x–z plane corresponding to that value of y. Properties such as the energy and dissipation spectra, the large-eddy turnover time, the Stokes numbers, and the settling velocities, which are presented without regard to their spatial location, are defined based on fluid properties in the center of the high energy region, where the flow is approximately isotropic.

Parameter	High Turbulence Side			Low Turbulence Side		
	I	II	III	I	II	III
ν	0.001	0.0012	0.002	0.001	0.0012	0.002
ϵ_0	6	6	6	0.048	0.048	0.048
κ_0	4	4	4	4	4	4
κ_η	152	152	152	152	152	152

Table 3.1: Initialization parameters for the DNS for the high turbulence side (TTI and TNI) and low turbulence side (TNI only). The initial fields are created according to the procedure given in §3.3.2. Parameters are in arbitrary units.

3.3.3 Parameters

The parameters in the simulations are chosen to match those of the wind-tunnel experiments described in [62] and [65]. One complication is our inability in the simulations to match the Reynolds numbers in the experiments. On a 512^3 grid the Taylor microscale Reynolds number $R_\lambda \equiv 2K\sqrt{5/(3\nu\epsilon)}$ is less than half that of [62] and [65] ($R_\lambda = 275$), where K is the turbulent kinetic energy and ϵ is the turbulent energy dissipation rate. We perform three different simulations at Reynolds numbers R_λ ranging from 75 to 111 at initialization and from 54 to 71 at $t/\tau = 0.7$, where $\tau \equiv K_0/\epsilon_0$ is the initial large-eddy turnover time (as defined in previous studies of the shearless mixing layer, e.g., [28, 93, 166, 90], to study the effect of the Reynolds number on fluid and particle statistics over the range we could access. As is evident from table 3.1, the three flow fields corresponding to the three different Reynolds numbers are created to have similar large scales, but different dissipation (small) scales. Normalized energy and dissipation spectra for the TTI for the three fields are shown in figure 3.1.

Because we are unable to match the Reynolds number in the experiment, we are forced to choose whether to match the large or small scales to the experi-

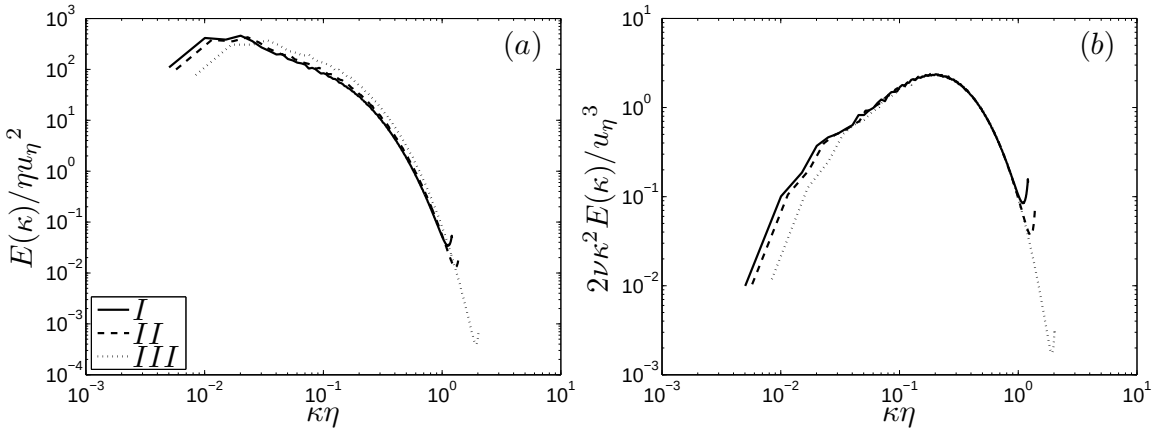

Figure 3.1: Normalized (a) energy and (b) dissipation spectra at 0.7 large-eddy turnover times for the three TTI cases defined in table 3.2.

ments (since both could not be matched simultaneously). As we will demonstrate, the overall fluid and particle dynamics are a strong function of the large-scale turbulence, and hence we choose to match those statistics.

We attempt to match the turbulent energy ratio between the high and low turbulence sides to the TNI wind-tunnel experiments. Their initial energy ratio was estimated to be 27; however, the uncertainty is large due to the large error in the intensity measurement on the low turbulence side. The energy ratio was approximately 27 at the test section, corresponding to $t/\tau = 0.7$. This ratio in the simulation was approximately 33 initially and 17 at $t/\tau = 0.7$. We attribute the difference in energy decay rates between the experiment and DNS to the discrepancy in the Reynolds numbers and the large uncertainties in the experiment at the entrance. Nevertheless, in both cases the turbulent energy ratio is sufficiently large that the turbulence dynamics are controlled by the high turbulence side of the flow.

To avoid additional complexities in the mixing process, we match the inte-

gral length scales ℓ in the high and low turbulence regions. These scales differ by no more than 20% at the start of the simulations. Accurate measurements of ℓ in the low turbulence side in [62] and [65] were not available. To learn more about the effect of the length scale ratio, the interested reader is referred to the study by [166] that varied the length scale ratio ℓ_{high}/ℓ_{low}.

Following convention (e.g., see [158, 159]), we define the particle Stokes number as $St_\ell \equiv \tau_p/\tau_\ell$, where $\tau_\ell \equiv \ell/u'$ is the large-eddy turnover time, and $u' \equiv \sqrt{2K/3}$ is the turbulence intensity. τ_ℓ was defined in [62] based on the the homogeneous velocity component u, i.e., $\tau_\ell = \ell/u_{\text{rms}}$. However, turbulence in the wind-tunnel is inherently anisotropic as compared to the DNS, and consequently, τ_ℓ/τ is larger in the experiment than in the DNS. As there is no unique way to reconcile this discrepancy, we adopt the convention of using τ to define the dimensionless time (i.e., t/τ) and τ_ℓ to define the particle Stokes number.

The parameters in the simulations and the corresponding values in the experiment (where applicable) are given in table 3.2. The particle Stokes number distributions at $t/\tau = 0.7$ are shown in figure 3.2 for both (a) St_ℓ and (b) St_η. As you can see, there is very close agreement in St_ℓ but not in St_η due to the difference in Reynolds numbers.

For the cases with gravity, a key dimensionless number is the settling parameter $Sv_\ell \equiv \tau_p g/u'$, which is the ratio of the particle terminal velocity $\tau_p g$ to the turbulence intensity u' (e.g., see [188]). Note that for given values of St_ℓ and Sv_ℓ we can form a large-scale Froude number ($Fr_\ell \equiv Sv_\ell/St_\ell = \frac{g}{u'/\tau_\ell}$) which depends only on fluid parameters. Fr_ℓ can be viewed as the ratio between the gravitational acceleration g and the large-eddy acceleration u'/τ_ℓ.

Parameter	DNS			Experiment
	I	II	III	
Kinematic viscosity ν	0.001	0.0012	0.002	1.5×10^{-5} m^2/s
Turbulent kinetic energy K	1.09	1.11	1.18	0.106 m^2/s^2
Energy dissipation rate ϵ	1.57	1.58	1.59	0.138 m^2/s^3
Integral lengthscale ℓ	0.385	0.387	0.404	0.24 m
Kolmogorov lengthscale η	0.00503	0.00575	0.00843	0.397 mm
Kolmogorov timescale τ_η	0.0253	0.0276	0.0355	0.0105 s
Large-eddy timescale τ_ℓ	0.452	0.450	0.456	0.774 s
Large-eddy turnover time τ	0.794	0.789	0.732	0.764 s
Reynolds number R_λ	71	66	54	275
$k_{max}\eta$ (minimum)	1.04	1.18	1.71	-
CFL (maximum)	0.301	0.295	0.283	-

Table 3.2: Parameters in DNS and experiment. All DNS values correspond to the high turbulence region and are in arbitrary units. The 'experiment' refers to data from the wind-tunnel tests of [62] and [65]. All data, with the exception of the large-eddy turnover time τ, are taken at $t/\tau = 0.7$. For the experiment, τ was computed based on values at the test section since no accurate initial values were available; for the DNS, τ was computed from values at initialization as was done in previous shearless mixing layer studies [28, 93, 166, 90]. DNS values of τ calculated at $t/\tau = 0.7$ differ from the initial value by less than 15%.

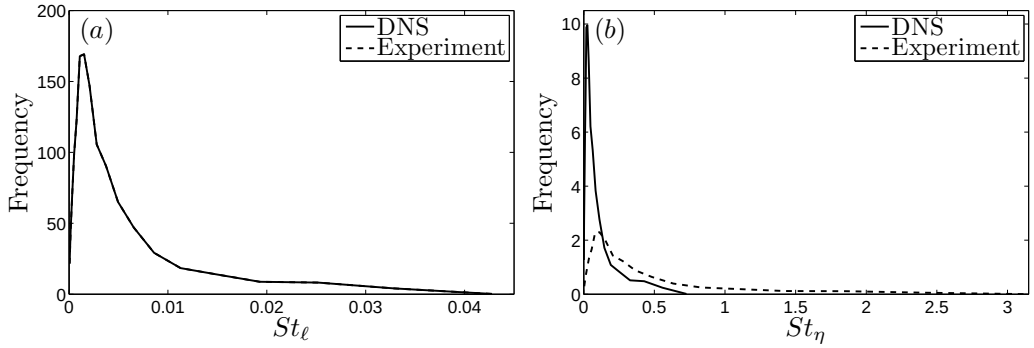

Figure 3.2: Stokes number distribution at $t/\tau = 0.7$ for DNS and experiment of [62] in terms of (a) St_ℓ and (b) St_η. All timescales are defined by the turbulence characteristics at the center of the high turbulence region. Frequencies are normalized by the area under the PDF. The values for St_η in (b) are for case I (the highest Reynolds number case).

We set the gravitational acceleration in the DNS to $g = 50$ (arbitrary units) so that the settling parameters for the particles in the DNS match those of the experiment (and hence $Fr_\ell \approx 25$ is the same in both the experiment and DNS). Since there is little variation in the large scales among the three Reynolds number cases, g was fixed for all three flow fields.

3.4 TNI Fluid Statistics

As was done in previous shearless mixing layer studies, we present fluid statistics for the TNI flow as a function of the inhomogeneous coordinate y normalized by a mixing layer half-width $L_{1/2}^{u_i}$ [170, 28, 93, 166, 90, 167]. We define $L_{1/2}^{u_i}$ by mapping the variance of velocity component u_i (u_i^2) in high energy side to 1 and in the low energy side to 0, and calculating the distance between the scaled velocity variances of 0.25 and 0.75, as was first proposed by [170]. We define $L_{1/2}^{u_y}$ as the half-width based on the inhomogeneous component u_y and $L_{1/2}^{u_x,u_z}$ as the half-width based on the homogeneous velocity components u_x and u_z that are statistically equivalent and therefore averaged together.

In figure 3.3, we show profiles of the spatial variation of turbulent kinetic energy for TNI for three different Reynolds numbers at $t/\tau = 0.7$, normalized by the kinetic energy in the high turbulence region of the flow. Experimental results from [62] at the same dimensionless time are included for comparison. The good agreement between energy levels in the experiment and DNS at this time confirms that the blending parameters chosen in §3.3.2 are appropriate.

Two-dimensional contours of the turbulent kinetic energy field in figure 3.4 show pockets of high turbulence in what initially was the low-turbulence re-

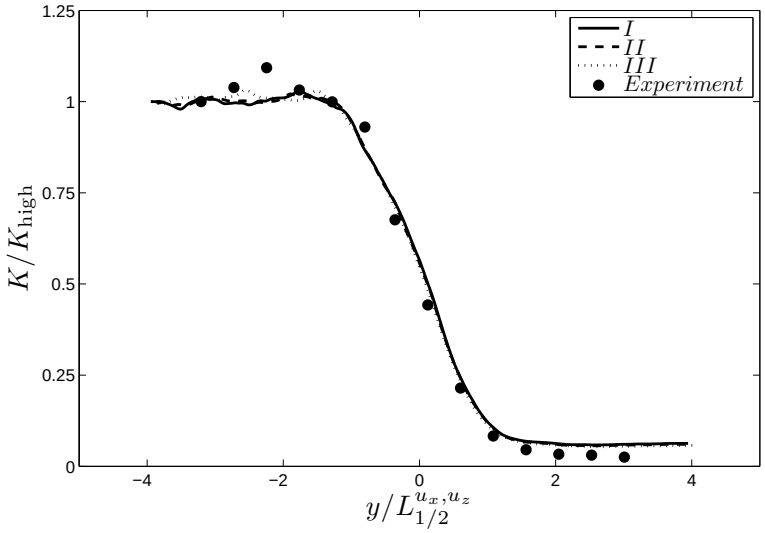

Figure 3.3: Profiles of turbulent kinetic energy for TNI at $t/\tau = 0.7$. DNS profiles are shown for the three different Reynolds number cases defined in table 3.2. Experimental results from [62] are shown for comparison. The energy levels are scaled by the energy in the high turbulence region, and the coordinate y is normalized by the mixing layer half-width $L_{1/2}^{u_x,u_z}$ computed from the variances of the homogeneous velocity components.

gion. We expect that these pockets of high turbulence will lead to increased intermittency across the mixing layer.

We consider the normalized third-order (skewness, $S_{u_x} = \langle u_x^3 \rangle / \langle u_x^2 \rangle^{3/2}$) and fourth-order (kurtosis, $K_{u_x} = \langle u_x^4 \rangle / \langle u_x^2 \rangle^2$) moments of each velocity component (where S_{u_y}, S_{u_z}, K_{u_y} and K_{u_z} are defined by analogy) to quantify the degree of intermittency of the flow. Note that $S \equiv 0$ and $K \equiv 3$ for a Gaussian field. To improve statistics, skewness and kurtosis values for the two statistically equivalent, homogeneous velocity components u_x and u_z are averaged together.

Figure 3.5 gives skewness and kurtosis profiles for the TNI at $t/\tau = 0.7$. The results for each velocity component are presented as a function of the inhomogeneous coordinate y normalized by the half-width $L_{1/2}^{u_i}$ corresponding to that

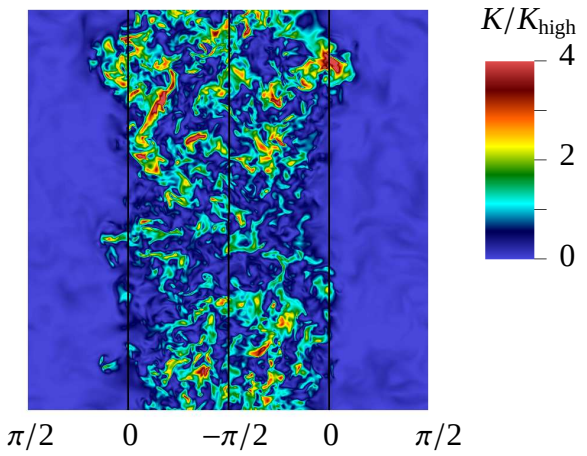

Figure 3.4: Contours of turbulent kinetic energy levels K (scaled by the average energy in the high turbulence region) in a two-dimensional x–y plane for the TNI at $t/\tau = 0.7$.

velocity component. Experimental data from [62] show similar trends. As is evident from figure 3.5(a), S_{u_y} is positive near the interface, indicative of high intensity turbulent bursts which preferentially are directed toward the low-turbulence region. The skewness of the homogeneous velocity components (not shown) is close to zero throughout the entire domain.

Figure 3.5 indicates strong departures from Gaussian behavior in the mixing region. Notice that $K_{u_y} > K_{u_x,u_z}$, which implies that u_y is the most highly intermittent component of the fluid velocity. The reason for this stronger intermittency is explained in detail in [170]. Again, we see similar trends between our DNS and [62]. The location and magnitude of the K_{u_y} peaks are slightly different, possibly due to differences in the Reynolds numbers or the imperfect match of the initial conditions of the two flows. All velocity components for the TTI are nearly Gaussian throughout the entire domain.

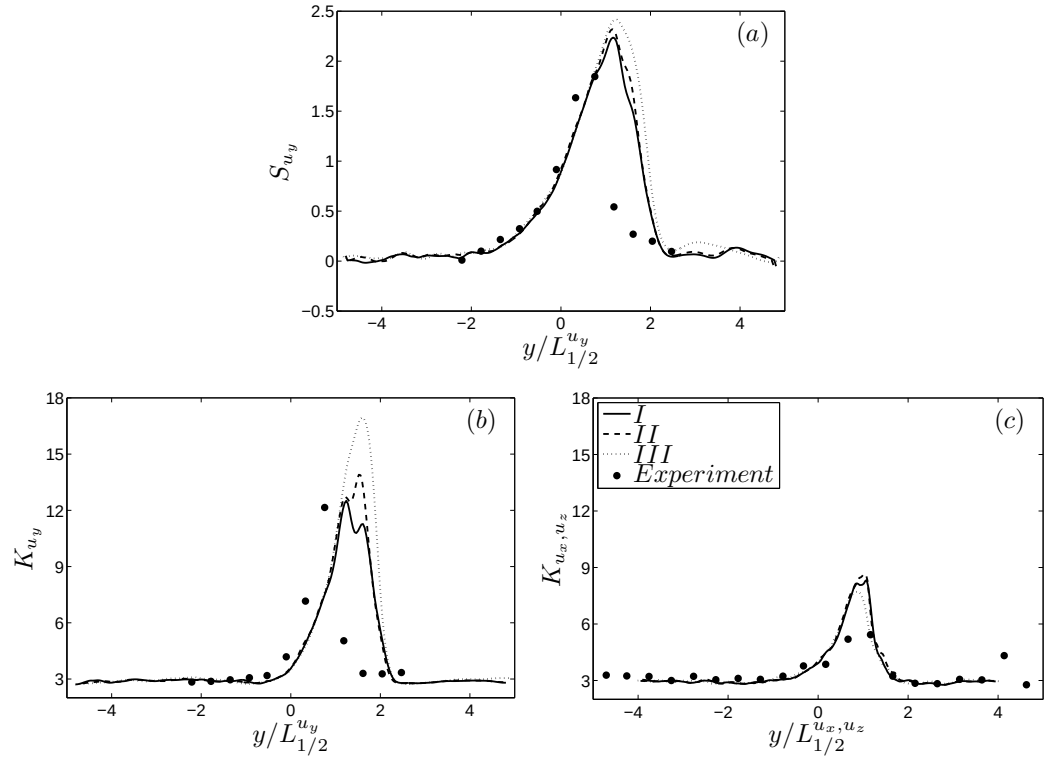

Figure 3.5: (a) Skewness and (b) kurtosis of the inhomogeneous velocity component u_y at $t/\tau = 0.7$ for the three TNI cases defined in table 3.2. Also shown, (c) kurtosis of the homogeneous velocity components u_x and u_z. Experimental results from [62] are included for comparison. Since experimental measurements for u_z were not made, the experimental statistics in (c) are only for the component u_x.

3.5 Particle statistics

We now consider the motion of inertial particles that are convected by both the TTI and TNI flow fields. The particles initially are seeded randomly throughout the centre slab (for the TNI, this corresponds to the high turbulence region) with two different mean concentration profiles between the particle-rich and particle-lean regions (see figure 3.6). The first is a step change and the second has a gradual transition based on the smoothing function $\mathcal{G}(\mathbf{x})$ defined in (3.7).

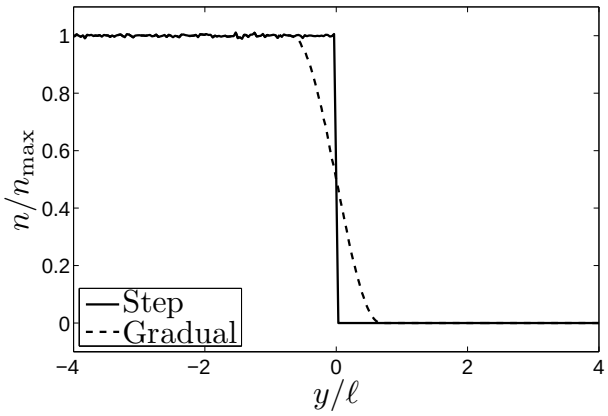

Figure 3.6: Two initial mean concentration profiles for the particle field. The solid line is a step change at the interface and the dashed line uses the smoothing function $\mathcal{G}(\mathbf{x})$ as defined in (3.7) to provide a more gradual transition between the high- and low-concentration regions.

We advance the particle positions and velocities according to (3.3) and (3.4). Statistics are gathered by averaging over the homogeneous x–z plane and are treated as a function of the inhomogeneous coordinate, y.

3.5.1 Mean particle concentrations

Figure 3.7 plots the number of particles at a given y–coordinate normalized by the number of particles in the particle injection side (here taken to be the initial concentration in the central slab) at a dimensionless time $t/\tau = 0.7$ equal to the time in the experiment that corresponds to the test section and for both initial particle concentration profiles. It is evident that the initial particle distribution only weakly affects the particle distributions at later times for both the TTI and TNI. Moreover, the choice of the initial distribution does not resolve the discrepancies between the DNS and experimental measurements presented later in the

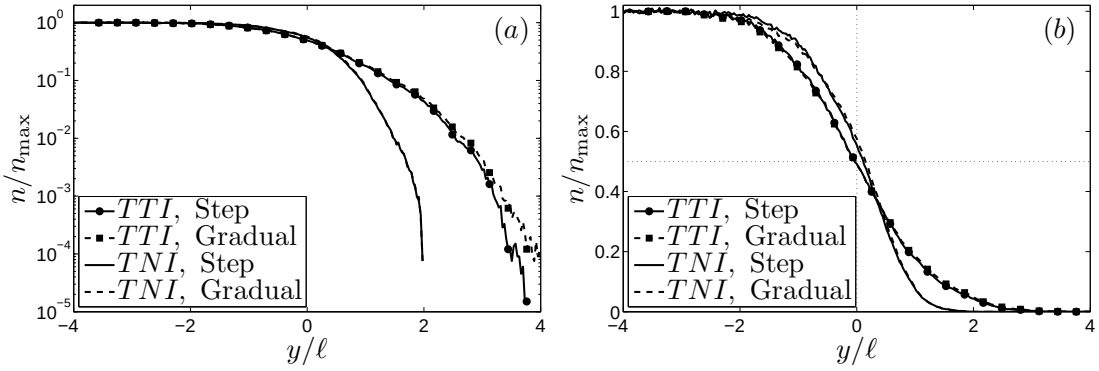

Figure 3.7: Particle concentration profiles at $t/\tau = 0.7$ for the TTI and TNI for the two different initial particle distributions shown in figure 3.6 on (a) a semilog scale and (b) a linear scale. The results are for the highest Reynolds number case (I).

paper (cf. figure 3.12). As the gradual distribution introduces parameters that were not measured in the experiments [62, 65], and the impact on the results is relatively weak, we hereafter present only the results from the step distribution.

Figure 3.8(a) shows the velocity measures of the half-width for the TNI ($L_{1/2}^{u_x,u_z}$ and $L_{1/2}^{u_y}$) and $\tilde{L}_{1/2}$ for both the TNI and the TTI. Notice that all measures of the half-width are of the same order of magnitude for the duration of the simulation. The half-width $\tilde{L}_{1/2}$ is greater for the TTI case than that for the TNI case at all times, indicating that the TTI mixes more quickly than the TNI. In figure 3.8(b), we plot least-squares power-law fits for $\tilde{L}_{1/2}$ of the form $\tilde{L}_{1/2}/\ell = c_0(t/\tau)^{c_1}$ (where ℓ is the integral length scale at $t/\tau = 0.7$). (We are unable to simulate past $t/\tau \approx 0.7$ for the TTI and $t/\tau \approx 0.9$ for the TNI, because after this point the particles will reach the y-boundary of our domain and periodic boundary conditions in y will contaminate the results.) For the TTI, we calculate $c_0 = 2.03 \pm 0.16$ and $c_1 = 0.774 \pm 0.064$, while for the TNI, we obtain $c_0 = 1.47 \pm 0.071$ and $c_1 = 0.854 \pm 0.045$. Due to the uncertainties on the power-law fits for c_1 (which represent 95% confidence intervals), we cannot de-

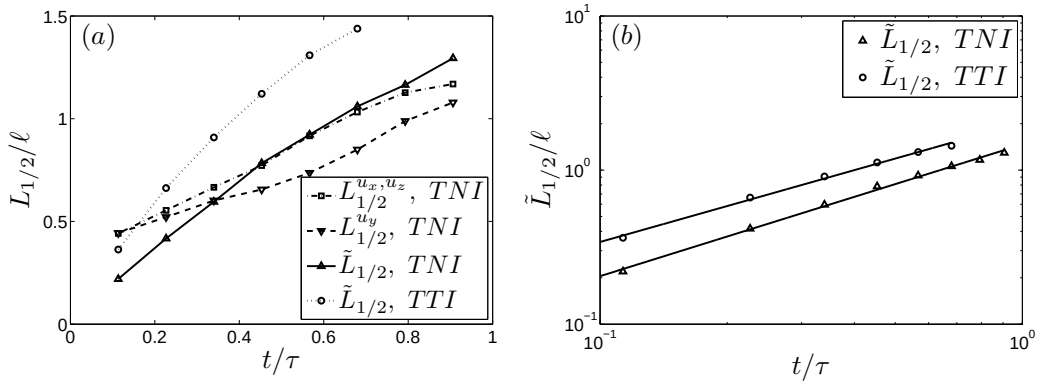

Figure 3.8: Time evolution of the mixing layer half-width. Different measures of $L_{1/2}$ are shown in (a), and power-law fits for $\tilde{L}_{1/2}$ are given in (b). All measures of $L_{1/2}$ are normalized by ℓ, the integral length scale at $t/\tau = 0.7$. We observe very similar results when $L_{1/2}$ is normalized by the instantaneous integral length scale.

termine whether the $\tilde{L}_{1/2}$ grows more quickly for the TTI or the TNI. c_1 in our DNS agrees well with the value of 0.83 presented in [171], which was computed from the mean concentration profiles of a passive scalar line source mixing in a TNI.

Figure 3.9 shows the particle concentration profiles for the case without gravity (hereafter referred to as 'g^0'). As we are interested in making an absolute comparison between the TTI and TNI which have different values of $\tilde{L}_{1/2}$, we normalize the inhomogeneous coordinate by the longitudinal integral length scale ℓ in the homogeneous region of the flow, which is identical for both cases. From these profiles, we again see that the TTI is much more effective at transporting the particles than the TNI. This finding is consistent with the observation that the boundaries between cumulus clouds (generally more turbulent) and the ambient air (generally less turbulent) are sharp and well-defined (e.g., see [148]). From figure 3.9(b), we also note the symmetry in the TTI profile but the asymmetry in the TNI profile, a consequence of the gradient in mean tur-

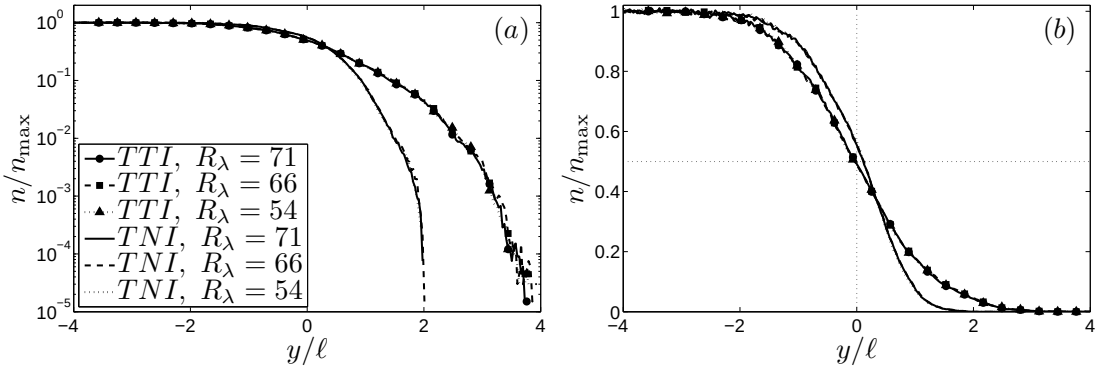

Figure 3.9: Particle concentration profiles for the TTI and TNI at the three indicated Reynolds numbers and $t/\tau = 0.7$ on (a) a semilog scale and (b) a linear scale. Negative values of y correspond to regions initially laden with particles, while positive values of y correspond to regions initially void of particles.

bulent kinetic energy in the TNI. Symmetric TTI profiles and asymmetric TNI profiles were observed by [171] for passive scalar dispersion and are discussed in detail there.

This difference between the TTI and TNI cases can be explained by a simple eddy diffusivity argument. If we approximate the transport of particles as that of passive scalars, we expect the particle concentration plots to take the form of error functions, and the turbulent diffusivity to scale with u' [97, 102, 156]. Since u' is smaller in the low turbulence region, we expect a lower diffusivity there and fewer particles to be mixed. [62] and [65] showed that the particle concentration profiles can be well represented by an error function with a diffusivity that varies based on the local turbulence intensity u', which is consistent with our findings.

Figure 3.9 also shows the variation in the mean particle concentration with Reynolds number (see §3.3.3 for the description of the three cases). Over the limited range of Reynolds numbers achieved in our simulations ($R_\lambda = 54 - 71$

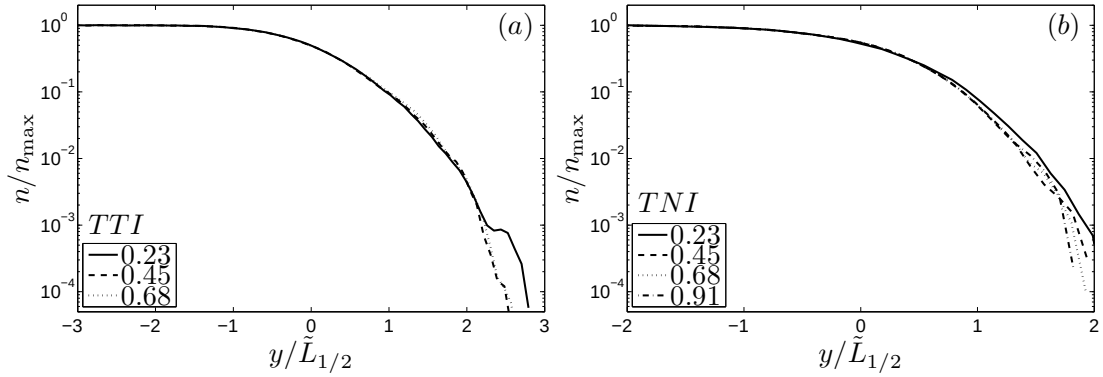

Figure 3.10: Particle concentration plots for the (a) TTI and (b) TNI at the indicated times, t/τ.

at $t/\tau = 0.7$), we observe no discernible Reynolds number dependence in these profiles. We similarly find no Reynolds number dependence when gravitational effects are included. Hence for the remaining figures we only show the highest Reynolds number case (I). (We also found no Reynolds number dependence in the statistics of particle concentration fluctuations, mean velocities, and higher-order velocity moments presented in the following sections.)

Figure 3.10 shows the temporal evolution of the TTI and TNI mean particle concentration profiles using the half-width $\tilde{L}_{1/2}$ to normalize the y coordinate. In these coordinates, the TTI profiles appear to be self-similar, with only a slight deviation far into the non-injection side of the first profile at $t/\tau = 0.23$. The TNI profiles also approach self-similarity after an initial transient period indicated by the first profile. The approximate self-similarity of these profiles, combined with the power-law relation for $\tilde{L}_{1/2}$, suggests that particle concentration profiles at different times can be estimated from data at a given time, at least for $t/\tau \lesssim 1$.

We examine the role of particle inertia on the mean concentration profiles at $t/\tau = 0.7$ by splitting the particles into two classes. Following the binning procedure of [65], we define 'large' particles as those with a response time τ_p

greater than $2.4\overline{\tau}_p$ (where $\overline{\tau}_p$ is the arithmetic mean response time), and 'small' particles as those with a response time τ_p less than $0.6\overline{\tau}_p$. Concentration profiles for large and small particles, without gravity, are compared in figure 3.11. Also shown are concentration profiles for inertialess (tracer) particles. Figure 3.11 shows that in the absence of gravity, particle inertia plays a negligible role on the mean concentration profiles. From figure 3.2(b) we see the particles span a relatively large range of Stokes numbers defined based on the Kolmogorov scales ($0 < St_\eta \lesssim 0.7$), so we would expect an appreciable effect of inertia if the small scales were playing a significant role in the mixing process. Since all particles have large-scale Stokes numbers St_ℓ close to zero, we would expect a relatively weak effect of inertia if particle dynamics are a function of the large-scale turbulence. The relatively weak effect of inertia that is observed is consistent with the large scales being dominant and further justifies the use of the large-scale Stokes number St_ℓ as the appropriate measure of particle inertia. To test this hypothesis further, we performed additional simulations with a broader small-scale Stokes number distribution ($0 < St_\eta \lesssim 3$) to match the experimental values of St_η in figure 3.2(b). Even with this wider range, the concentration profiles without gravity (not shown) exhibit no appreciable dependence on Stokes number.

Next we examine the effect of gravity on particle transport by considering gravity acting either favorably or adversely to the mixing process (hereafter referred to as 'g^+' and 'g^-,' respectively). The particle concentration profiles for each case at $t/\tau = 0.7$ are shown in figure 3.12. The first-order effect of gravity is to shift the concentration profiles from their position without gravity, resulting in more (less) particles deeper into the non-injection side for g^+ (g^-). Experimental data from [62] are included in figure 3.12 for comparison. Note that the experimental data have been shifted slightly (5.5 cm for the TTI and 7.5 cm for

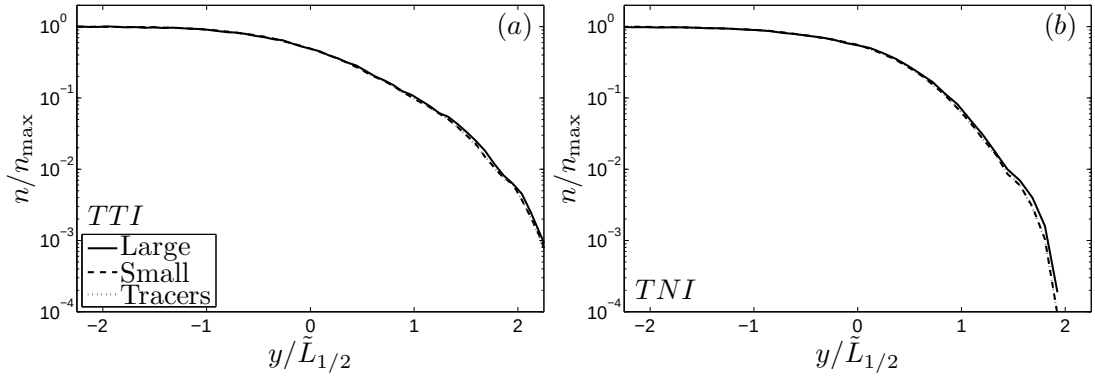

Figure 3.11: Effect of particle inertia on the (a) TTI and (b) TNI concentration profiles at $t/\tau = 0.7$ and without gravity.

the TNI) toward the non-injection side for two reasons. First, in both the TTI and TNI experiments, the streamwise velocity component exhibits a boundary layer near the splitter plate. This momentum deficit leads to a decrease in the particle flux on the particle injection side, effectively shifting the particle concentration profiles towards the particle injection side. We are able to generate a qualitatively similar shift in our DNS by initializing the particle distribution with a deficit of particles near the interface. Second, the experimental studies have shown that an asymmetric wake is formed past the splitter plate for the TNI due to the difference in turbulence intensity on each side of the plate. The center of the wake is shifted approximately 3 cm into the high turbulence region. For more information about these shifts, refer to [65].

The particle concentration profiles in figure 3.13 indicate that the particle response time τ_p is an important parameter when gravity is present. Gravity preferentially acts on the particles with the largest particle response time. Thus, when gravity assists particle transport (g^+), larger particles are transported farther from their initial location than smaller particles; the reverse is true when gravity hinders particle transport (g^-). These trends can be observed in the vi-

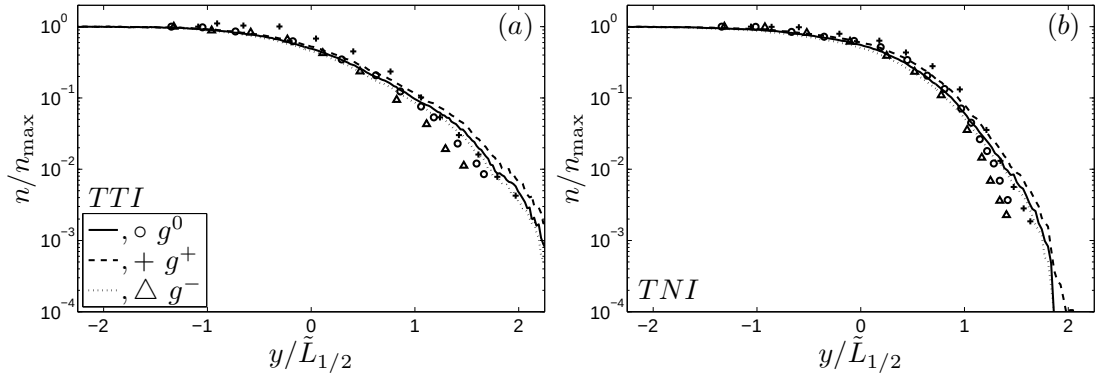

Figure 3.12: Effect of gravity on the (a) TTI and (b) TNI concentration profiles at $t/\tau = 0.7$. Lines correspond to DNS and symbols are the experimental data from [62].

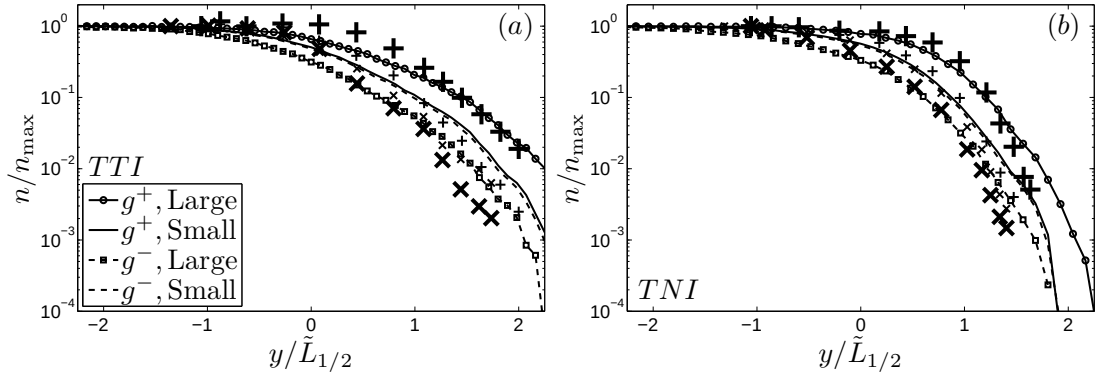

Figure 3.13: Effect of particle inertia on the (a) TTI and (b) TNI concentration profiles at $t/\tau = 0.7$, with the indicated particle size and direction of gravity. Experimental data from [65] are shown for comparison, where + corresponds to g^+ and $\times$ to g^-. Large symbols are for large particles, and small symbols are for small particles.

sualizations of particles in the non-injection side in figure 3.14, where we see that the g^+ case has larger particles in the non-injection side than the g^0 case. Our data in figure 3.13 agree well with the results of [65] (shown for comparison).

The results presented thus far have been focused on the mean particle con-

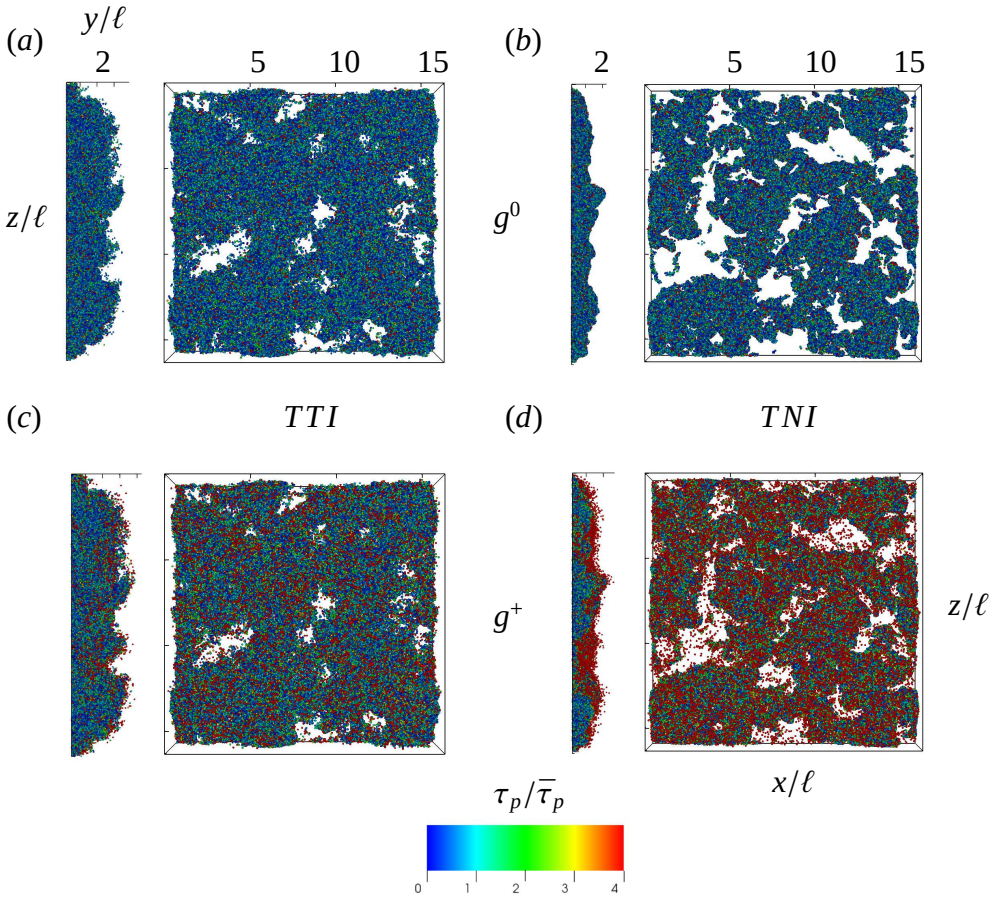

Figure 3.14: Instantaneous particle field on the non-injection side (positive y) at $t/\tau = 0.7$ for the (a) TTI with g^0, (b) TNI with g^0, (c) TTI with g^+, and (d) TNI with g^+.

centration. In the next section, we look more closely at the impact of gravity and particle inertia on particle concentration fluctuations.

3.5.2 Apparent 'clustering' due to particle entrainment

As discussed in §3.2, inertia can cause an initially uniform distribution of particles to cluster outside the vortices of the flow. The mechanism responsible for inertial clustering is completely unrelated to the entrainment process that

is the focus of this study. Inertial clustering occurs when inertial particles are 'centrifuged' out of regions of high vorticity and accumulate in regions of high strain (e.g., [9]). The nonuniform particle concentrations we observe, however, are due to the mixing of particles from one region of flow to the other. This is apparent in figure 3.14, which shows particle positions in the non-injection side of the TTI and TNI flows, with and without gravity. The nonuniform particle concentration field is present in both flows, with the degree of the fluctuations being higher for the TNI. Note that this nonuniform distribution occurs even for inertialess (tracer) particles. The connection between the large eddies and high concentration regions is apparent in figure 3.15, which shows isocontours of the turbulent kinetic energy (left) and particle concentrations (right) along a x–y slice. From these figures, we see that highly turbulent regions are particularly effective at transporting particles. For example, the turbulent patch in the upper right corner of the mixing layer drives a protrusion of particle-rich fluid that advances into the non-injection side of the box with time. We believe intermittent 'bursts' such as these play a critical role in mixing the particles, particularly for the TNI case. As a consequence, we see that regions of high turbulence and high particle flux are closely correlated. The spatial coherence and intermittency of the turbulence (and hence the flux) leads to high concentration regions on scales on the order of the integral length scale.

Both inertial clustering and particle entrainment impact statistical measures of the particle concentration fluctuations. For example, the statistic most commonly used to quantify inertial clustering is the radial distribution function (RDF, e.g., see [161]). As noted in the experimental study by [146], spatial inhomogeneities resulting from incomplete mixing impact the RDF. In particular, they observed an extended 'shoulder' at separation distances well into the in-

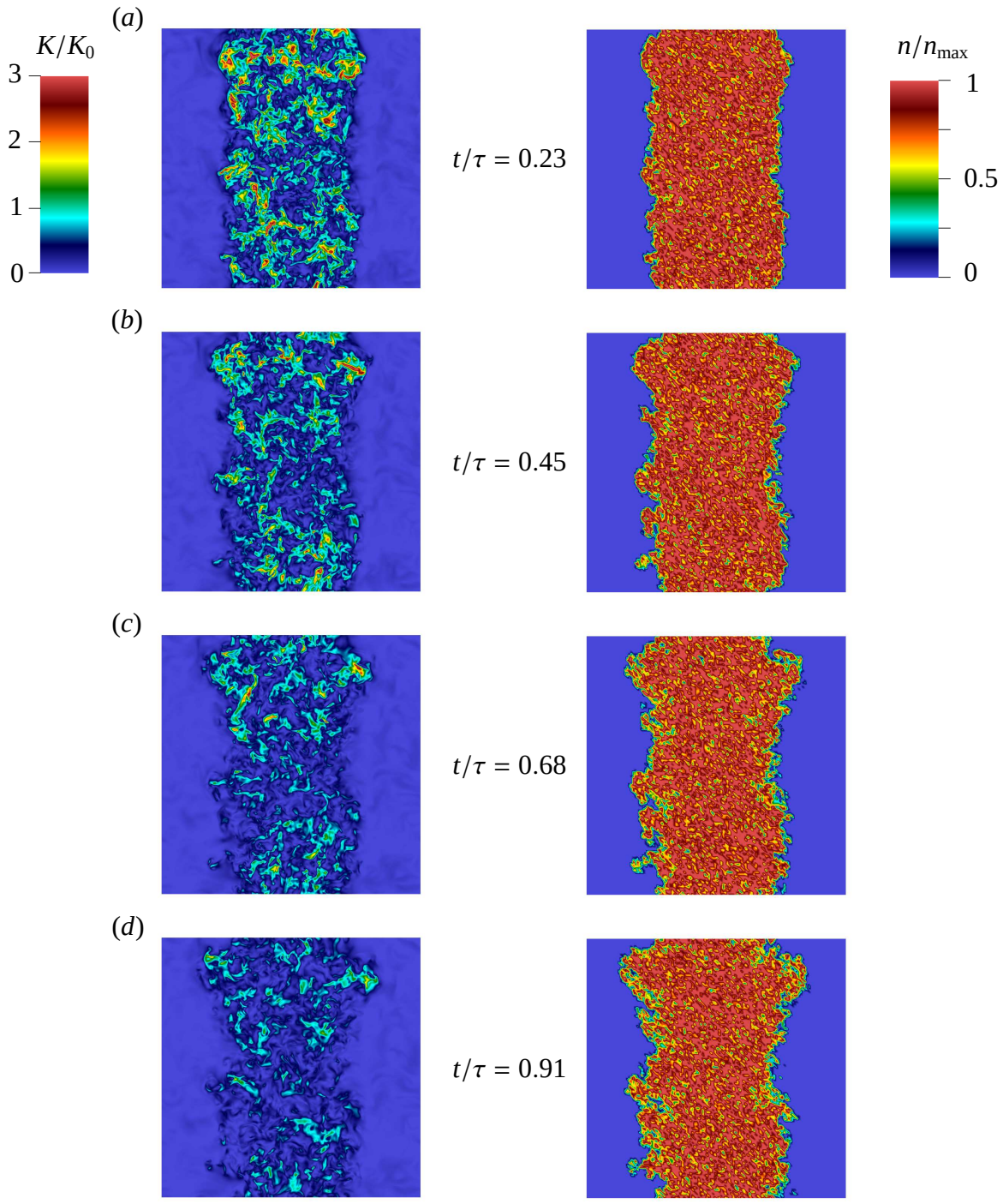

Figure 3.15: Isocontours of normalized turbulent kinetic energy (left) and particle concentration (right) in a two-dimensional x–y plane for the TNI case with g^0 at the indicated times.

ertial range (i.e., beyond the separation distance where inertial clustering is expected to be important). To investigate this phenomenon in the present system, we evaluate the two-dimensional RDF (2D RDF) measured along the x–z plane for a fixed value of y. We define the 2D RDF as follows

$$g_{2D}(r_i) \equiv \frac{N_i/A_i}{N/A}\,, \tag{3.9}$$

where N_i is the number of particle *pairs* that lie within a shell with an average radius of r_i and radial width Δr, A_i is the area of the shell, and N is the total number of particle pairs located in the total cross-sectional area, A. Note the 2D RDF is *not* equivalent to the 3D RDF, but instead involves a projection of the 3D RDF onto the 2D plane, introducing a loss of information [76]. Nevertheless, it is the highest measure we can consider in this inhomogeneous particle field.

Figure 3.16 shows the 2D RDF at $t/\tau = 0.7$ for g^0, g^+, and g^- at $y/\ell = -1$, 0 and +1. We observe that the degree of nonuniformity is consistently greater for the TNI than for the TTI, increases with distance towards the non-injection side, and is enhanced for g^- and suppressed for g^+. To better understand the competing processes controlling the particle concentration fluctuations, we plot the temporal evolution of $g_{2D}(r_i)$ in figure 3.17. At $y/\ell = 0$ and $y/\ell = 1$, the degree of nonuniformity decreases with time, while at $y/\ell = -1$ it increases slightly with time. Turbulent transport of particles from regions of higher concentration to regions of lower concentration forms apparent 'clusters' of variable sizes that scale with the integral length scale of the turbulence, causing $g_{2D}(r_i)$ to increase. Turbulent mixing within the x–z plane tends to break up these 'clusters,' reducing $g_{2D}(r_i)$. The lower turbulence levels on the non-injection side in the TNI flow weaken the homogenization process, leading to larger values of $g_{2D}(r_i)$ than for the TTI flow. Particles that reach deeper into the non-injection side must necessarily be transported by the most energetic turbulent fluctuations, and therefore

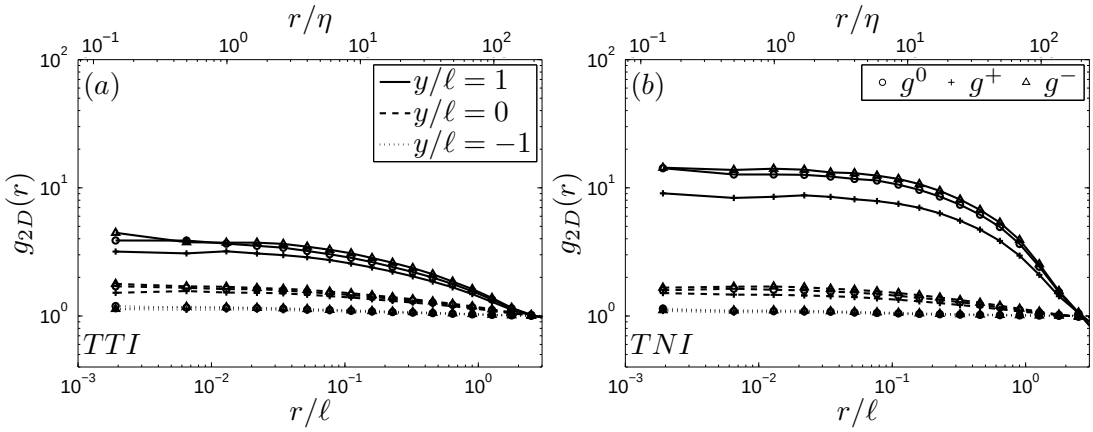

Figure 3.16: 2D RDFs for the (a) TTI and (b) TNI at $t/\tau = 0.7$ and at the indicated y–location (line type) and direction of gravity (symbol).

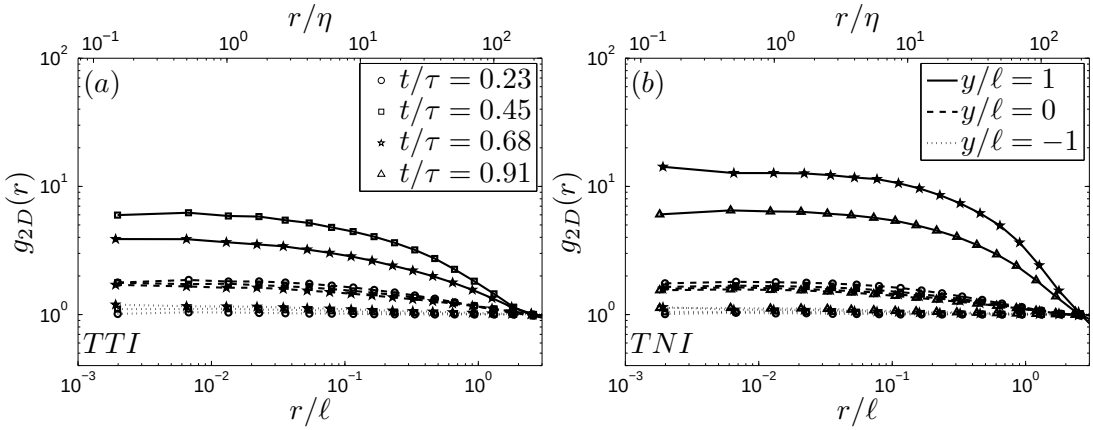

Figure 3.17: Temporal evolution of the 2D RDFs for the (a) TTI and (b) TNI at the indicated y–location (line type) and time (symbol). Note some curves are not shown due to inadequate statistics.

they are the most densely concentrated. When gravity assists transport (g^+), the particles are less dependent on the turbulent fluctuation, and therefore they exhibit lower levels of nonuniformity relative to the g^- case.

As already noted, the apparent 'clustering' observed in this mixing study is qualitatively different than inertial clustering. For example, the length scale of inertial clustering is of the order 10η [4], whereas the nonuniformity in the

particle distribution here scales with the integral length scale. Additionally, inertial clustering is very sensitive to the particle Stokes number, whereas mixing-driven concentration inhomogeneities are only weakly dependent on the particle Stokes number. Indeed, simulations performed with inertialess (tracer) particles have similar 2D RDFs to the inertial cases without gravity.

We can estimate the degree of nonuniformity by assuming the particle concentration within each 'cluster' is approximately equal to the maximum particle concentration, and the particle concentration outside each 'cluster' is zero. If we analyze this idealized case, in the limit $r/\ell \to 0$ the 2D RDF approaches the asymptote A/A_c, where A_c is the cross-sectional area of the clusters per total cross-section, A. Furthermore, the same assumption implies $n/n_{\max} = (A/A_c)^{-1}$. Hence if this assumption were valid, we would expect the product $n/n_{\max} \times g_{2D}(r_i)$ to approach unity at small separations. Figure 3.18 shows the rescaled 2D RDF as a function of r/ℓ. We see that while the asymptote is not precisely unity, it is reasonably close for the variety of conditions shown. Indeed, the above analysis represents an upper bound for mixing-driven concentration nonuniformity, as it neglects the effect of mixing in the x–z plane, which tends to reduce the 2D RDF.

[65] include one-dimensional RDFs for g^+ at different values of y/ℓ. Their plots of $g_{1D}(r_i)$ and $n/n_{\max} \times g_{1D}(r_i)$ show similar qualitative trends.

3.5.3 Particle velocity statistics

To investigate the dynamics of the mixing process further, we present in this section an analysis of the particle velocity statistics. We first examine the av-

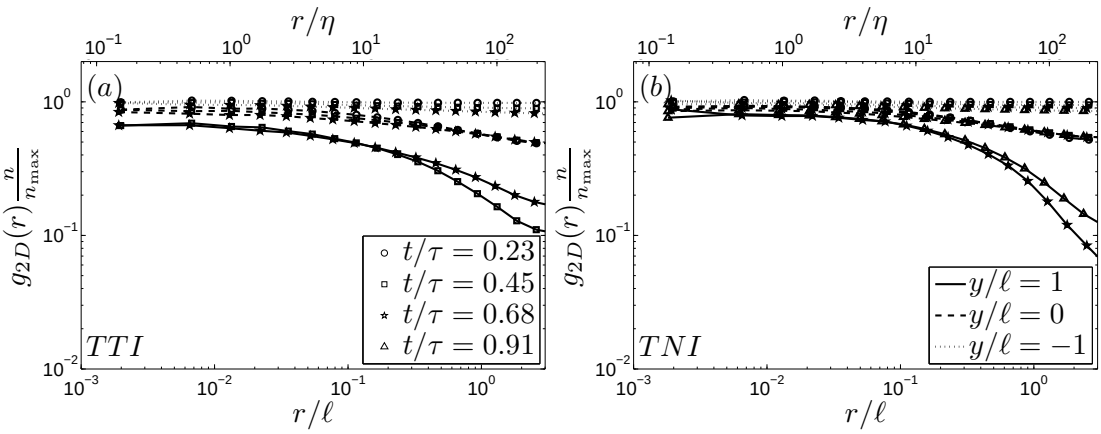

Figure 3.18: 2D RDFs multiplied by $n/n_{\max}$ for the (a) TTI and (b) TNI at the indicated y–location (line type) and time (symbol).

erage velocities of particles in the shearless mixing layer. Then, to investigate discrepancies between DNS and experiments in the particle injection side, we study particle settling in isotropic turbulence with uniformly seeded particles. Finally, we examine second- and third-order moments of the particle velocity field in the shearless mixing layer.

Average particle velocities in the shearless mixing layer

We plot the average y–component of the velocity for the case without gravity in figure 3.19, separating small and large particles. Consistent with the results shown in figure 3.11, we see no discernible effect of the particle size on the mean velocity. The increase in the average velocity with increasing y is due to the turbulent flux of particles. For the TNI flow, we notice that the average velocity reaches a maximum far into the non-injection side and then decreases. This trend is greater than the 95% confidence interval and so is statistically significant. Particles that are carried the farthest into the non-injection side are generally carried by fluid experiencing the largest turbulent fluctuations. As this

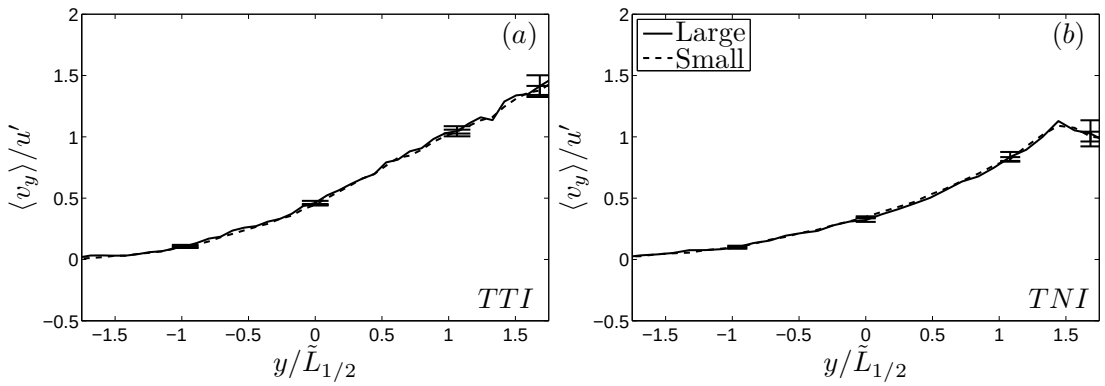

Figure 3.19: Profiles of the average particle velocity $\langle v_y \rangle$ for the (a) TTI and (b) TNI at $t/\tau = 0.7$, g^0, and the indicated particle size. Error bars are 95% confidence intervals.

fluid penetrates the low- turbulence region of the TNI flow, its kinetic energy is diminished by the surrounding fluid, causing the mean particle velocity to decrease far into the non-injection side.

Figure 3.20 gives the temporal evolution of the average particle transport velocities for the case without gravity. For the TTI, this scaling does not produce a self-similar behavior, suggesting the average particle velocity spreads more quickly than does the half-width $\tilde{L}_{1/2}$. For the TNI, in contrast, we see that the four lines collapse well in these coordinates, up to $y/\tilde{L}_{1/2} \approx 1$. Therefore, as with the particle concentration profiles, there is good potential for a model for the TNI case based on the turbulence intensity of the carrier fluid u', the half-width $\tilde{L}_{1/2}$, and a velocity profile at a given time t/τ.

We consider gravitational effects on the mean particle velocity in figure 3.21. Experimental data from [65] are shown for comparison. We expect both turbulent diffusion and gravity to contribute to particle transport velocities for g^+ and g^-. As expected, when gravity acts in the same direction as turbulent diffusion, we have larger transport velocities, and when gravity acts opposite to turbulent

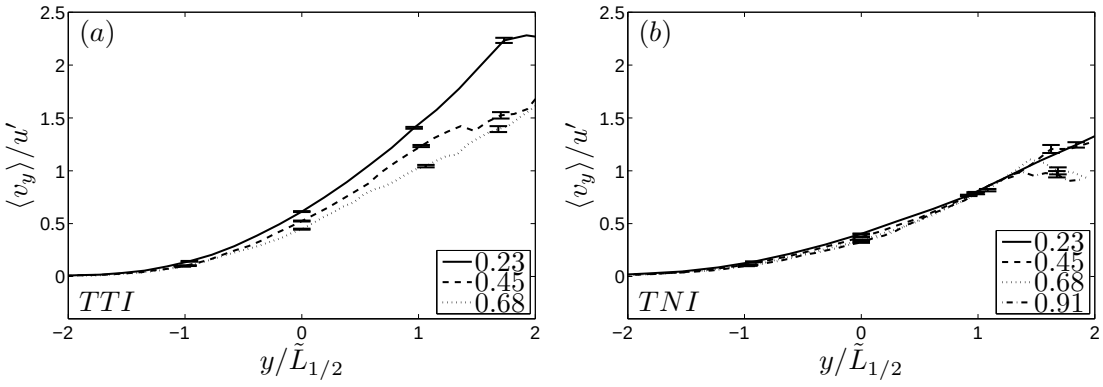

Figure 3.20: Evolution of the average particle velocity $\langle v_y \rangle$ profiles for the (a) TTI and (b) TNI with g^0, and the indicated dimensionless times t/τ.

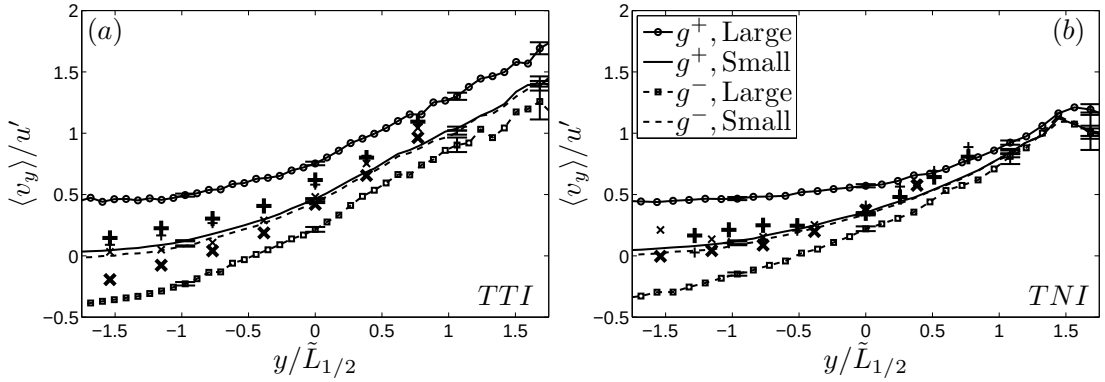

Figure 3.21: Profiles of the average particle velocity $\langle v_y \rangle$ for the (a) TTI and (b) TNI at $t/\tau = 0.7$ and the indicated particle size and direction of gravity. Experimental data from [65] are shown for comparison, where + corresponds to g^+ and × to g^-. Large symbols are for large particles, and small symbols are for small particles.

diffusion, we have smaller transport velocities. Both the experiment and DNS indicate that the large particles are more strongly affected by gravity than the small particles. In the DNS, however, the particle velocity is a much stronger function of particle size than in the experiment, particularly in the injection side ($y < 0$). We will discuss this further in §3.5.3.

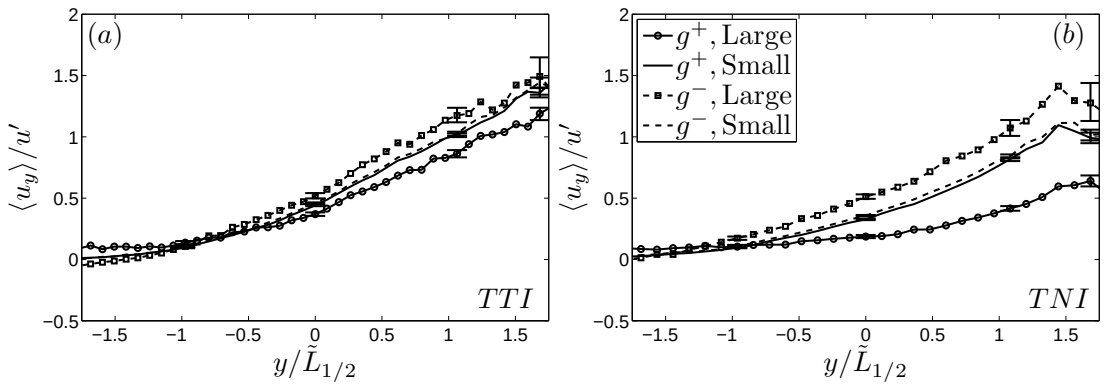

Figure 3.22: Average *fluid* velocity $\langle u_y \rangle$ at the particle centers for the (a) TTI and (b) TNI at $t/\tau = 0.7$, and the indicated particle size and direction of gravity.

We also see in figure 3.21 that the g^+ and g^- curves for the large particles converge with increased y, particularly for the TNI. This convergence is essentially a sampling effect. Far into the non-injection side, for a given value of y, the sample only contains particles that have transport velocities $\langle v_y \rangle$ above a certain threshold, as particles with velocities below this threshold will not reach this value of y. Therefore for g^-, the particles sampled at a given location on the non-injection side generally come from turbulent fluid with an even larger velocity fluctuation than for g^+, since this fluid is acting in opposition to gravity. Plots of the average fluid velocity at the particle centers $\langle u_y \rangle$ in figure 3.22 confirm this hypothesis. This trend in $\langle u_y \rangle$ is strongest for the largest particles, which experience the largest gravitational effect. The increased values of $\langle u_y \rangle$ in the non-injection side for g^- counter the decrease due to gravitational settling, causing the g^+ and g^- particle transport velocity curves in figure 3.21 to converge. This convergence is more pronounced for the TNI than for the TTI, since gravitational effects are even more significant. ($S\, v_\ell$, a non-dimensional measure of gravitational effects, scales with $K^{-1/2}$.) Indeed for the TNI, at $y/\tilde{L}_{1/2} \approx 1.5$, $\langle v_y \rangle$ is the same for g^+ and g^-.

Average velocities with uniform particle seeding

To separate the effects of turbulent diffusion from gravity, we performed additional simulations with the same turbulence parameters as the homogeneous TTI flow, but now with uniform particle seeding throughout the entire domain. We used a series of monodisperse particles (400,000 particles for each Stokes number) over a wider Stokes number range than in the mixing layer DNS. To remain consistent with the mixing layer study, we used the same value for gravitational acceleration, and hence $Fr_\ell \equiv S v_\ell / S t_\ell$ is matched to the shearless mixing layer.

To investigate the effects of nonlinear drag on particle motion, we introduce a drag coefficient into the equation for the particle velocity

$$\frac{d\mathbf{v}_i}{dt} = C_D \frac{\mathbf{u}(\mathbf{X}_i) - \mathbf{v}_i}{\tau_{p_i}} + (1 - \rho_f/\rho_p)\mathbf{g} \,, \tag{3.10}$$

where $C_D = 1$ for linear drag, and the nonlinear drag coefficient is given by [33, 175, 111]

$$C_D = 1 + 0.15 Re_p^{0.687} \,. \tag{3.11}$$

The simulations were run in decaying isotropic turbulence for the same duration ($t/\tau = 0.7$) as for the mixing layer simulations.

We plot in figure 3.23(a) DNS and experimental results for the average settling velocity $\langle v_y \rangle$ as a function of $S t_\ell$. Also shown for comparison is $\tau_p g$, the settling velocity in a quiescent fluid with linear Stokes' drag. To more clearly show the enhancement or reduction of the settling velocity in the DNS due to turbulence, we subtract the nonlinear settling velocity in a quiescent fluid $v_{y_{lam}}$ from $\langle v_y \rangle$ and normalize by u' (e.g., see [175]) in figure 3.23(b). Consistent with [175] and the experiments of [65], we observe preferential sweeping at modest

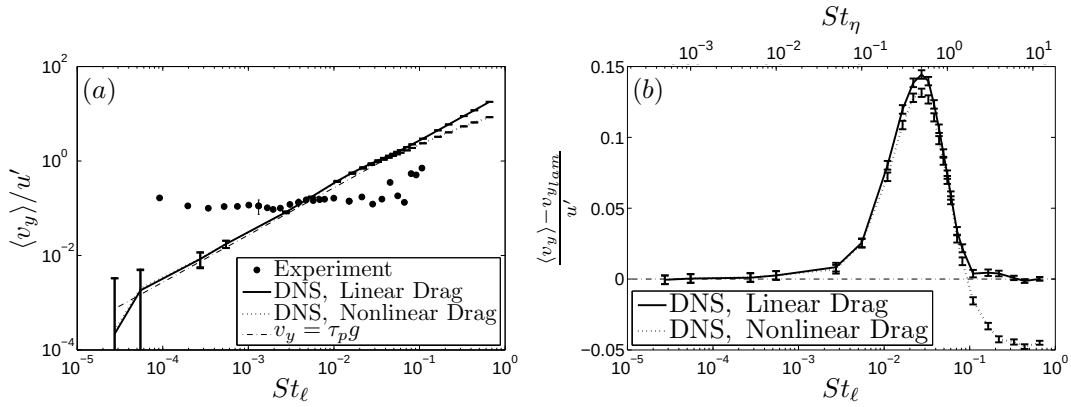

Figure 3.23: (a) Average particle settling velocity with uniform particle seeding for the DNS (with linear and nonlinear drag) and the experiment of [65]. (b) Settling velocity enhancement (compared to the settling velocity in a quiescent fluid $v_{y_{lam}}$) for the DNS (with linear and nonlinear drag).

Stokes numbers and loitering at high Stokes numbers, but the magnitudes of the two effects differ significantly from the experiment.

For the smallest St_ℓ particles, [65] show settling speeds in excess of $\tau_p g$. They attribute this velocity enhancement to the 'preferential sweeping' mechanism identified by [175] and [118], whereby a particle is more likely to reside in fluid traveling in the same direction of gravity. The findings in [65] are consistent with the experimental results of [118] and [91], which also show preferential sweeping at very low values of Stokes number. For the DNS, we observe preferential sweeping only at much larger Stokes numbers, consistent with earlier DNS [175, 188, 23] and some experiments [4, 189, 190]. Since we would expect inertial particles with $St_\ell \to 0$ to behave like tracers (with $v_y \to 0$), the reason for this deviation in the experiment is unclear.

For the largest St_ℓ particles, [65] show settling speeds which are considerably slower than predicted by Stokes' drag. They argue that this reduction is

not caused by nonlinear drag, since the majority of the particles with reduced settling speeds are still in the linear drag regime. Citing [118], [65] attribute this reduction to the 'loitering effect.' [118] reasoned that heavy particles bisect turbulent eddies and spend more time (on average) in fluid that is moving opposite to the direction of gravity. He argued that loitering still could occur even in the linear drag regime. Our DNS (figure 3.23(b)) shows only a modest loitering with nonlinear drag. The explanation for loitering due to nonlinear drag is given by [175]. Particles falling in the nonlinear drag regime will experience higher drag when traveling in fluid that is moving opposite to gravity (due to higher slip velocities) and lower drag in fluid that is moving in the same direction as gravity (due to lower slip velocities). Hence, on average, particles will loiter in fluid that is traveling opposite to gravity. This loitering, however, is relatively modest in our DNS–about 5% for the largest particles.

In summary, while the DNS with nonlinear drag show both preferential sweeping and loitering at moderate and high Stokes numbers, respectively, the magnitude of the deviations are considerably smaller than those observed in the experiments of [65]. This deviation cannot be explained by nonlinear drag. Turbulence modulation by the particles in the experiment and other collective effects are also unlikely due to the low volume and mass loadings (e.g., [50, 162, 4]). Some possible explanations are the difference in Reynolds numbers between the experiment and simulations, and possible effects due to the mean flow and anisotropy of the turbulence in the wind tunnel, but this is purely speculative since none of these effects have been systematically explored in the literature. Finally, we note that while there are significant differences in the settling speeds as a function of Stokes number, the trends with respect to particle concentrations, particle concentration fluctuations, and higher-order particle

velocity moments (presented below) agree well.

Higher-order particle velocity moments

Returning to the shearless mixing layer with nonuniform particle seeding, we consider the variance of particle velocities across the mixing layer. The higher-order moments for the small particles are very weak functions of gravity, and therefore we show g^0 for all particles and g^+ and g^- only for the large particles. Figure 3.24 shows the particle velocity variance of the x and z (homogeneous direction) components and y (inhomogeneous direction) component as a function of position for the TTI and TNI, scaled by the average fluid velocity variance of that component in the injection side $\langle u_i^2 \rangle$. The variance for the fluid field (dotted line) as well as experimental data from [65] (symbols) are shown for comparison. The variances of the homogeneous velocity components for the TTI (figure 3.24(a)) are nearly identical to those of the underlying fluid velocity, suggesting that the particles in those directions are simply responding to the fluid. On the other hand, $\sigma_{v_y}^2$ decreases in the non-injection side of the TTI (figure 3.24(c)), relative to the underlying fluid velocity. Moreover, we observe a slightly higher variance for g^+ than for g^0 or g^- over most of the domain. The experiments of [65] show the same qualitative trend, although their spatial variation is much greater than the DNS. We hypothesize that for g^0 and g^-, particles are transported by relatively large, intermittent fluctuations that are comparatively coherent and strongly correlated. These fluctuations lead to large mean fluxes of particles, but somewhat less variance because of their coherence. In contrast, g^+ allows somewhat weaker fluctuations to carry the particles the same distance, and these weaker events are more randomized, leading to a slightly

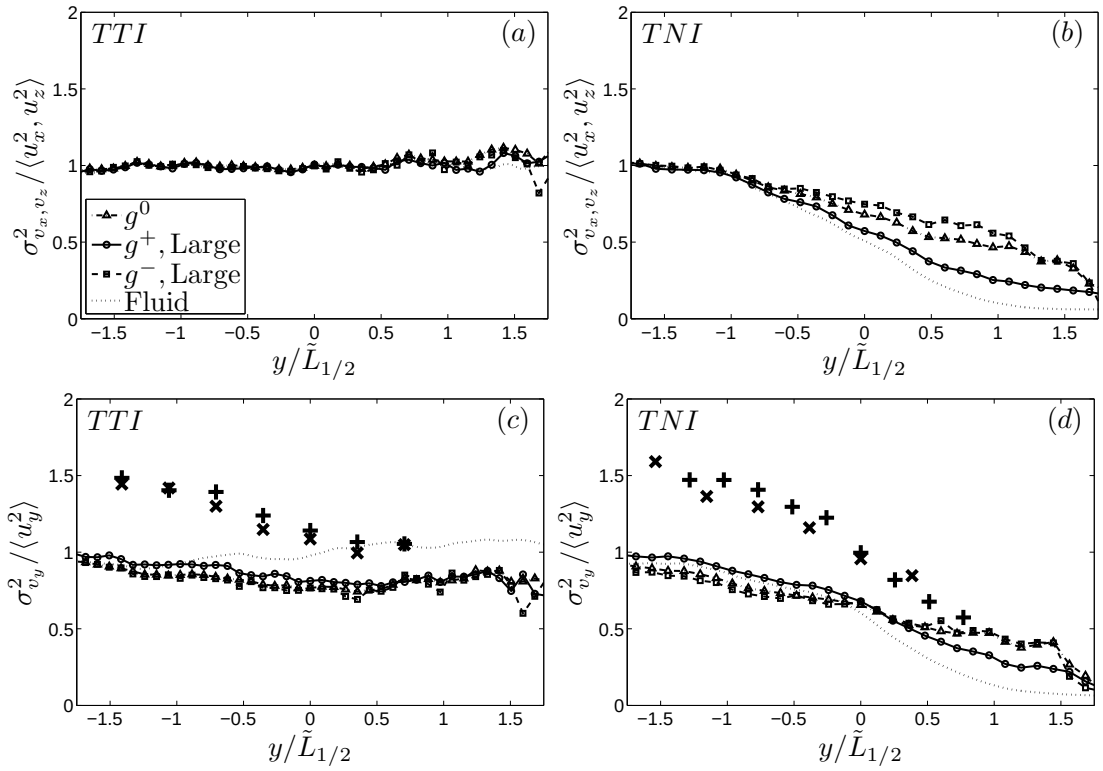

Figure 3.24: Profiles of the particle velocity variance of the components in the homogeneous directions for the (a) TTI and (b) TNI, and component in the inhomogeneous direction for the (c) TTI and (d) TNI, at $t/\tau = 0.7$. As indicated in the legend, we consider all particles for g^0 and only large particles for g^+ and g^-. The variances are scaled by the average fluid velocity variance of that component in the injection side, $\langle u_i^2 \rangle$. Experimental data from [65] for large particles are shown for comparison, where + corresponds to g^+ and $\times$ to g^-.

higher variance. Farther into the non-injection side, however, this effect disappears as the memory of the fluid from which the particles originated decays and the variances for all three cases approach each other.

For the TNI cases (figures 3.24(b) and 3.24(d)), we observe a much stronger spatial variation in the velocity variance of all three velocity components, reflecting the spatial variation in the underlying fluid. In addition to the physics described above for the TTI, the particles on the non-injection side are also equi-

librating with surrounding fluid that is at a lower turbulent kinetic energy. We observe that the dependencies on the injection side are qualitatively the same as for the TTI; however, on the non-injection side there is a reversal, with the variances for g^0 and g^- exceeding that for g^+. We believe this results from a memory effect, whereby particles overcoming gravity (g^-) must initially have larger velocity fluctuations, relative to the g^+ case, to overcome gravity. As the particles equilibrate their energy with the surrounding fluid, they retain some memory of the fluctuation that brought them there, causing the g^- case to achieve a higher variance than the g^+ case.

Our trends are qualitatively consistent with those of [65], although the magnitudes differ. One surprising experimental result in figures 3.24(c) and 3.24(d) is the high particle y-velocity variances for $y < 0$. We observe particle velocity variances from the experiment which are about 50% greater than the corresponding fluid velocity variances. A recent DNS study in isotropic turbulence [144] yielded the same unexpected trend over a range of Stokes numbers, and attributed it to biased sampling of the fluid flow due to particle inertia. However, the relative amount of the overshoot by the particles was well below 5% and hence cannot explain the experiment. The much larger discrepancy in the particle statistics in the experiment may be due to the inherent difference in the underlying flows, which is caused, at least in part, by the anisotropy in the wind-tunnel flow and the difference in Reynolds numbers.

The final higher-order moment we consider is the standardized third-order moment, or skewness, of the velocity fluctuations. Skewness provides information about the asymmetry of the underlying velocity PDF, which is indirectly related to its intermittency. Note that the homogeneous velocity components

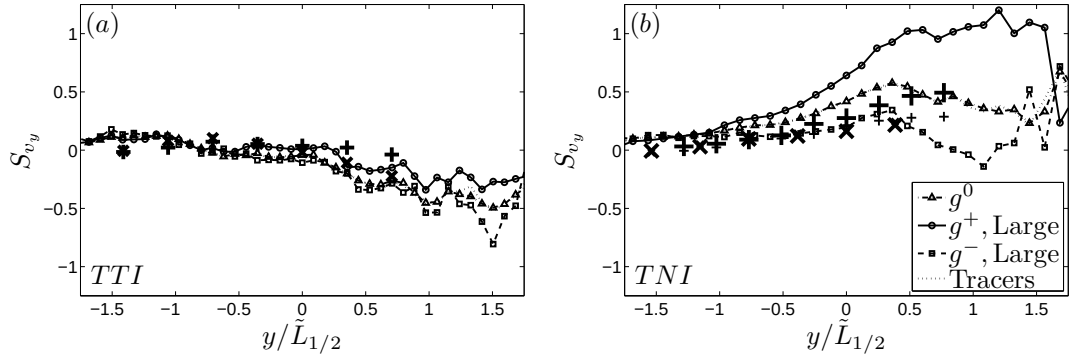

Figure 3.25: Profiles of skewness of the particle velocity component in the inhomogeneous direction for the (a) TTI and (b) TNI at t/τ = 0.7. As indicated in the legend, we consider all particles for g^0 and only large particles for g^+ and g^-. Experimental data from [65] for large particles are shown for comparison, where + corresponds to g^+ and $\times$ to g^-.

(not shown) have essentially no skewness, and so we focus our attention on the y–component of velocity. Figure 3.25 shows the skewness profiles for (a) the TTI and (b) the TNI. On the injection side of the TTI, the skewness values are negligible; however, on the non-injection side, we see strongly negative skewness, with the largest magnitude associated with g^- and smallest magnitude associated with g^+. The skewness in the velocity of the underlying fluid is approximately zero throughout, suggesting this effect must be related to the particle flux, particle inertia, or both. The effect of the biased sampling is observed by considering the fluid skewness along tracer particle trajectories (dotted line). We see almost identical results for tracer particles and inertial particles without gravity, indicating that the negative skewness results almost entirely from the biased sampling introduced by the particle flux. Gravity acting in the adverse direction (g^-) further enhances negative velocity fluctuations, which decreases the skewness even further, while the opposite is true for favorable gravity (g^+).

In contrast to the TTI, we observe positive skewness for the TNI over nearly

the entire mixing region (cf. figure 3.25(b)). Recall that the underlying fluid velocity is also highly positively skewed due to the inhomogeneous turbulent kinetic energy (cf. figure 3.5(a)). Undoubtedly the particle velocity is responding to this forcing from the fluid velocity field. However, the degree of skewness of the particle velocity is less than that for the fluid for the same reasons described above for the TTI. That is, biased sampling and adverse gravity tend to reduce the skewness. The qualitative trends for the TNI are the same as for the TTI, but shifted due to the underlying skewness in the fluid velocity.

All of these trends are qualitatively consistent with the experimental results of [65], which are shown for comparison in figure 3.25. Again, the differences in magnitudes are likely an effect (at least in part) of anisotropy and differences in the Reynolds numbers.

3.6 Conclusions

We investigated the entrainment of inertial, non-evaporating particles across a shearless mixing layer in the absense of thermodynamic processes with the goal of understanding the fundamental turbulence mechanisms involved and their dependence on parameters such as particle inertia (Stokes number), gravity (acting in both a favorable and adverse direction) and the Reynolds number. The studies were carried out with two flow configurations, the turbulence–turbulence interface (TTI) and the turbulence–non-turbulence interface (TNI), so that the effect of the inhomogeneous turbulent field in the latter could be isolated. The entire study was motivated by recent experiments by [62] and [65] of the equivalent system carried out in a wind-tunnel that built off of earlier

experiments of the shearless mixing layer [170].

Consistent with the experiments, we find that the TTI is more effective at mixing the inertial particles than the TNI. Over the limited range of Reynolds numbers we could achieve in these 512^3 DNS ($R_\lambda = 54 - 71$ at $t/\tau = 0.7$), we find little dependence on Reynolds number, and moreover clear evidence that the inertial particle mixing is dominated by the largest scales of the turbulence, confirming our use of $S\,t_\ell$ as the appropriate measure of inertia. Note that $S\,t_\ell \lesssim 0.04$ for all the particles and hence in general inertial effects are negligible, in the absence of gravity. With gravity present, however, the mixing process is either enhanced (favorable gravity, g^+) or inhibited (adverse gravity, g^-), with larger particles experiencing the stronger effect. Gravity therefore causes the distribution of particle response times across the layer to go from uniform for no gravity to an enrichment (favorable) or depletion (adverse) of larger particles deep into the non-injection side. The explanation for these effects could be found from a simple analysis of the settling speed of the particles for each condition, and hence the mean concentration statistics are quite similar to the well-studied case of passive scalars undergoing gravitational settling.

One contribution of this work is to demonstrate the impact of mixing on the 2D RDF. To gain a further understanding of the nonuniform particle concentrations, we examined the 2D RDF computed along x–z planes at fixed y. Both visual evidence and the 2D RDF show evidence of apparent 'clustering' resulting from the mixing process. Particles swept into a particular plane would be locally concentrated by the coherent bursts of turbulence that carried them. Mixing along the plane would tend to break up the high concentration regions and hence diminish the 2D RDF. The 2D RDFs increase with decreasing r/ℓ, ap-

proaching a constant for $r/\ell \ll 1$. This constant is found to be related to the ratio A/A_c, where A_c is the cross-sectional area of the 'clusters' within the total cross section, A. This analysis assumes the concentration within the 'cluster' is fixed to the maximum particle concentration, and hence represents an upper bound. Under the assumptions of this model, we expect the product $n/n_{\max} \times g_{2D}(r_i)$ to approach unity as $r/\ell \to 0$. Plots of this rescaled 2D RDF approach constants that are at or below unity most likely because of mixing in the homogeneous directions. This part of the study highlights the role inhomogeneous mixing plays in the 'clustering' process. Note these issues previously have been raised by [146], who found evidence of apparent 'clustering' due to spatial inhomogeneities in the particle concentration field in their wind-tunnel measurements.

We then went on to study different moments of the particle velocity statistics across the mixing layer. Our findings show that when gravity assists particle transport (g^+), particles are less dependent on the highly turbulent fluid for transport, and particle velocities have higher-order moments that are closer to the underlying flow. For g^- the opposite is true (though the differences are not simply monotonic), as particles have higher-order moments farther from the underlying flow due to an increased dependence on the high turbulence fluid for transport. We observe good qualitative agreement between the experiments of [65] and our DNS with regard to higher-order moments. The intermittency of the particle velocity distributions and non-montonic trends in particle velocity moments with gravity show that inertial particles undergoing entrainment exhibit much more complex and unexpected dynamics than passive scalars with gravitational settling.

An important discrepancy between our DNS and [65] involves the gravi-

tational settling velocity of the particles. In simulations with uniform particle seeding and both linear and nonlinear drag forces on the particles, we find enhanced settling for moderate Stokes numbers, consistent with the 'preferential sweeping' mechanism described by [175]. [65], however, observed enhanced settling for particles with very small Stokes numbers. They also found reduced settling for large Stokes number particles that they claim were still in the linear drag regime. We only observe reduced settling in our DNS for large Stokes number particles with nonlinear drag, consistent with [175]. The reason for these discrepancies is unclear, and further experimental and computational studies which analyze the effect of scale separation, anisotropy, and the mean flow on particle settling are needed.

This study is relevant for industrial and environmental processes with inertial particles that are subject to entrainment, including exhaust plumes, the atmospheric boundary layer, and the oceanic thermocline. In particular, we are interested in better understanding the impact of entrainment on cloud growth and evolution. Our particle parameters are all within the range of those in cumulus clouds, though the flow Reynolds number is considerably lower [153]. Since much of our results show a very weak dependence on the Reynolds number (though this hypothesis remains to be tested at the higher Reynolds numbers characteristic of environmental flows), computational simulations may be able to predict the dynamics of particle entrainment accurately in cumulus clouds. Furthermore, since particle dynamics are dependent mostly on the large scales on the flow, it is possible that LES can reproduce the essential flow dynamics at realistic Reynolds numbers. We hope that this paper will lead to improved understanding and modeling of inertial particle entrainment and thereby advance cloud and climate modeling.

The authors would like to thank Zellman Warhaft, Garrett Good, and Sergiy Gerashchenko for discussions and for providing us with their experimental data. This work was supported by the National Science Foundation through CBET grants 0756510 and 0967349, and a graduate research fellowship to Peter Ireland. We also would like to acknowledge the TeraGrid resources provided by the Texas Advanced Computing Center under grants TG-CTS100052 and TG-CTS100062.

CHAPTER 4

THE EFFECT OF REYNOLDS NUMBER ON INERTIAL PARTICLE DYNAMICS IN ISOTROPIC TURBULENCE. PART I: SIMULATIONS WITHOUT GRAVITATIONAL EFFECTS.†

4.1 Abstract

In this study, we analyze the statistics of both individual inertial particles and inertial particle pairs in direct numerical simulations of homogeneous isotropic turbulence in the absence of gravity. The effect of the Taylor microscale Reynolds number R_λ on the particle statistics is examined over the largest range to date (from $R_\lambda = 88 - 597$), at small, intermediate, and large Kolmogorov-scale Stokes numbers St. We first explore the effect of preferential sampling on the single-particle statistics and find that low-St inertial particles are ejected from both vortex tubes and vortex sheets (the latter becoming increasingly prevalent at higher Reynolds numbers) and preferentially accumulate in regions of irrotational dissipation. We use this understanding of preferential sampling to provide a physical explanation for many of the trends in the particle velocity gradients, kinetic energies, and accelerations at low St, which are well-represented by the model of [32]. As St increases, inertial filtering effects become more important, causing the particle kinetic energies and accelerations to decrease. The effect of inertial filtering on the particle kinetic energies and accelerations di-

† P. J. Ireland, A. D. Bragg, and L. R. Collins. The effect of Reynolds number on inertial particle dynamics in isotropic turbulence. Part I: Simulations without gravitational effects. 2014. In preparation.

minishes with increasing Reynolds number and is well-captured by the models of [2] and [197], respectively.

We then consider particle-pair statistics, and focus our attention on the relative velocities and radial distribution functions (RDFs) of the particles, with the aim of understanding the underlying physical mechanisms contributing to particle collisions. The relative velocity statistics indicate that preferential-sampling effects are important for $St \lesssim 0.1$ and that path-history/non-local effects become increasingly important for $St \gtrsim 0.2$. While higher-order relative velocity statistics are influenced by the increased intermittency of the turbulence at high Reynolds numbers, the lower-order relative velocity statistics are only weakly sensitive to changes in Reynolds number at low St. The Reynolds-number trends in these quantities at intermediate and large St are explained based on the influence of the available flow scales on the path-history and inertial filtering effects. We find that the RDFs peak near St of order unity, that they exhibit power-law scaling for low and intermediate St, and that they are largely independent of Reynolds number for low and intermediate St. We use the model of [198] to explain the physical mechanisms responsible for these trends, and find that this model is able to capture the quantitative behavior of the RDFs extremely well when DNS data for the structure functions are specified, in agreement with [24]. We also observe that at large St, changes in the RDF are related to changes the scaling exponents of the relative velocity variances. The particle collision kernel closely matches that computed by [141] and is found to be largely insensitive to the flow Reynolds number. This suggests that relatively low-Reynolds-number simulations may be able to capture much of the relevant physics of droplet collisions and growth in the adiabatic cores of atmospheric clouds.

4.2 Introduction

Since the pioneering study of [122] over forty years ago, direct numerical simulation (DNS) has been widely used to study turbulent flows. Previous DNS studies have provided a wealth of information about the underlying turbulent flow field, much of which is very difficult to obtain experimentally, including Lagrangian statistics [192], pressure fluctuations [155], and velocity gradient tensors [5].

Only within the last ten years, however, with the advent of tera- and petascale computing, have DNS at Reynolds numbers comparable to those in the largest laboratory experiments become possible. The highest-Reynolds-number simulations to date (with Taylor microscale Reynolds numbers $R_\lambda \sim 1000$) have been of isotropic turbulence in tri-periodic domains and have considered both the Eulerian dynamics of the turbulent flow field and the Lagrangian dynamics of inertialess tracer (i.e., fluid) particles advected by the flow [89, 86, 87, 191].

Many industrial and environmental turbulent flows, however, are laden with dense, inertial particles, which can display profoundly different dynamics than inertialess fluid particles. The degree to which the dynamics of inertial particles differ from those of fluid particles depends on their Stokes number St, a non-dimensional measure of particle inertia, which we define based on Kolmogorov-scale turbulence. We summarize the relevant physical mechanisms at small, intermediate, and large values of St below.

It is well-known from both computational and experimental studies that inertial particles preferentially concentrate in certain regions of the flow (e.g., see [9]). This preferential concentration is often attributed to the fact that heavy par-

ticles are centrifuged out of vortex cores and accumulate in low-vorticity and high-strain regions [107, 159, 48], leading to higher collision rates [161]. However, this centrifuge mechanism is mainly important for small-St particles which are strongly coupled to the underlying flow. As St is increased, the particle dynamics become less coupled to the local fluid velocity field and the influence of their path-history interactions with the turbulence becomes increasingly important (e.g., see [25]). Particles with sufficiently large St can therefore come together from different regions of the flow with large relative velocities, increasing their collision rate [183, 56]. Such a process is referred to as 'caustics' [183] and the 'sling effect' [56]. At high values of St, several studies (e.g., [12, 7]) have shown that particles have a modulated response to the underlying turbulence as they filter out high-frequency flow features (i.e., features with timescales significantly below the particle response time), and they therefore have lower kinetic energies and lower accelerations.

Despite recent advances in simulating high-Reynolds-number turbulent flows, current studies of inertial particles in turbulence are primarily at low and moderate Reynolds numbers ($R_\lambda \lesssim 500$), and only recently have DNSs been conducted of inertial particles in turbulence with a well-defined inertial range [15, 16, 126, 135, 141, 125]. It is vital to understand the effect of Reynolds number on the mechanisms above (preferential accumulation, path-history interactions, and inertial filtering), particularly at higher Reynolds numbers which are more representative of those in nature. We give two examples to emphasize the importance of developing such an understanding.

The first example, cloud formation, is the primary motivation for this work. For reviews on this subject, see [148, 45, 69]; here we provide a brief overview.

It is well-known that standard microphysical cloud models over-predict the time required for the onset of precipitation in warm cumulus clouds (e.g., see [148]). At early stages of cloud formation, particles experience condensational growth. This process slows down quickly with increasing droplet diameter, making condensational growth effective only for droplets with diameters less than about $30\mu m$ [69]. Moreover, gravity is only able to significantly enhance collisional growth for particles with diameters above $80\mu m$ [134, 69], leaving a 'size gap' where neither condensational growth nor gravitational coalescence is very effective. For particles between these two limits, it has been proposed that turbulence-induced collisions are primarily responsible for droplet growth.

It is unclear, however, the extent to which particle collision rates are affected by changes in Reynolds number at conditions representative of those in cumulus clouds (which have $R_\lambda \sim 10,000$, see [152]). [161] showed that particle collision rates depend on both the degree of clustering and on the relative velocities between particles, and thus many subsequent analyses have considered the Reynolds-number dependence of both of these statistics. While the early study of [178] suggested that clustering increases with R_λ, later investigations [34, 15, 135, 141] indicate that clustering saturates at higher Reynolds numbers. Other researchers have suggested that caustics become more prevalent at high Reynolds numbers, leading to larger relative velocities and thus more frequent particle collisions [55, 183]. The findings of [15] and [141], however, do not seem to support that trend. In all cases, the Reynolds-number range ($R_\lambda \lesssim 500$) leaves open the question of whether the results apply to atmospheric conditions at much higher Reynolds numbers.

The second example relates to planetesimal formation. Planetesimals begin

to form when small dust grains collide and coalesce in turbulent protoplanetary nebulae [124]. [40] estimated that the turbulence in such nebulae is characterized by $R_\lambda \sim 10^4 - 10^6$. It is unclear to what extent the rate of coalescence depends on the Reynolds number, and studies at progressively higher Reynolds numbers are necessary to develop scaling relations for particle collision rates at conditions representative of nebula turbulence. [124] noted that the range of relevant particle sizes in the planetesimal formation process spans about nine orders of magnitude, and therefore we expect that the collision rates will be affected by preferential accumulation (for small, medium, and large particles), path-history interactions (for medium and large particles), and inertial filtering (for the largest particles).

In this study, we use high-performance computing resources provided by the U. S. National Center for Atmospheric Research [35] to simulate inertial particles in isotropic turbulence over the range $88 \leq R_\lambda \leq 597$. To our knowledge, the top value represents the highest Reynolds-number flow with particles simulated to date. The overall goal is to improve predictions for the collision kernel at Reynolds numbers more representative of those in atmospheric clouds. Gravitational forces are neglected in this study, but will be considered in detail in Part II of this study [82].

The paper is organized as follows: §4.3 provides a summary of the numerical methods used and the relevant fluid and particle parameters. In §4.4, we study single-particle statistics (small-scale velocity gradients, large-scale velocity fluctuations, and accelerations). Many of the results from this section help explain the particle-pair statistics presented in §4.5. These statistics include the particle relative velocities, radial distribution functions, and collision kernels.

Finally, in §4.6, we summarize our results and suggest practical implications for the turbulence and cloud physics communities.

4.3 Overview of simulations

A brief summary of the simulation parameters and numerical methods is provided below. Refer to [84] for a more detailed description of the code, including integration techniques, parallelization strategies, and interpolation methods.

4.3.1 Fluid phase

We perform DNS of isotropic turbulence on a cubic, tri-periodic domain of length $\mathcal{L} = 2\pi$ with N^3 grid points. A pseudospectral method [123] is used to evaluate the continuity and momentum equations for an incompressible flow,

$$\nabla \cdot \boldsymbol{u} = 0, \tag{4.1}$$

$$\frac{\partial \boldsymbol{u}}{\partial t} + \boldsymbol{\omega} \times \boldsymbol{u} + \nabla \left(\frac{p}{\rho_f} + \frac{u^2}{2} \right) = \nu \nabla^2 \boldsymbol{u} + \boldsymbol{f}. \tag{4.2}$$

Here, $\boldsymbol{u}$ is the fluid velocity, $\boldsymbol{\omega} \equiv \nabla \times \boldsymbol{u}$ is the vorticity, p is the pressure, ρ_f is the fluid density, ν is the kinematic viscosity, and $\boldsymbol{f}$ is a large-scale forcing term that is added to make the flow field statistically stationary. For our simulations, we added forcing to wavenumbers with magnitude $\kappa = \sqrt{2}$ in Fourier space in a deterministic fashion to compensate precisely for the energy lost to viscous dissipation [184].

We perform a series of five different simulations, with Taylor microscale Reynolds numbers $R_\lambda \equiv 2k\sqrt{5/(3\nu\epsilon)}$ ranging from 88 to 597, where k denotes

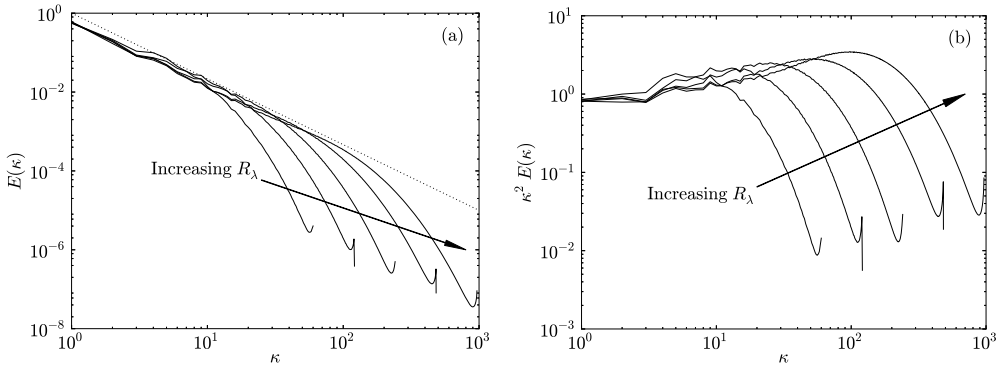

Figure 4.1: (a) Energy (a) and (b) dissipation spectra for the different simulations described in table 4.1. The diagonal dotted line in (a) has a slope of $-5/3$, the expected spectral scaling in the inertial subrange. All values are in arbitrary units.

the turbulent kinetic energy and ϵ the turbulent energy dissipation rate. Details of the simulations are given in table 4.1. The simulations are parameterized to have similar large scales, but different dissipation (small) scales. The small-scale resolution for the simulations was held constant, with $\kappa_{\max}\eta \approx 1.6 - 1.7$, where $\kappa_{\max} \equiv \sqrt{2}N/3$ is the maximum resolved wavenumber and $\eta \equiv \left(\nu^3/\epsilon\right)^{1/4}$ is the Kolmogorov lengthscale. Time-averaged energy and dissipation spectra for all five simulations are shown in figure 4.1. A clear $-5/3$ spectral slope is evident for the three highest Reynolds-number cases ($R_\lambda \geq 224$), indicating the presence of a well-defined inertial subrange. The simulations are performed in parallel on N_{proc} processors, and the P3DFFT library [128] is used for efficient parallel computation of three-dimensional fast Fourier transforms.

4.3.2 Particle phase

We simulate the motion of small ($d/\eta \ll 1$, where d is the particle diameter), heavy ($\rho_p/\rho_f \gg 1$, where ρ_p is the particle density), spherical particles. 18 dif-

Table 4.1: Flow parameters for the DNS study. All dimensional parameters are in arbitrary units, and all statistics are averaged over time T. All quantities are defined in the text in §4.3.1 and §4.3.2.

Simulation	I	II	III	IV	V
R_λ	88	140	224	398	597
ν	0.005	0.002	0.0008289	0.0003	0.00013
ϵ	0.270	0.267	0.253	0.223	0.228
ℓ	1.46	1.41	1.40	1.45	1.43
ℓ/η	55.8	107	204	436	812
u'	0.914	0.914	0.915	0.915	0.915
u'/u_η	4.77	6.01	7.60	10.1	12.4
T_L	1.60	1.54	1.53	1.58	1.57
T_L/τ_η	11.7	17.7	26.8	43.0	65.4
T/T_L	15.0	10.4	11.4	11.1	5.75
$k_{\max}\eta$	1.59	1.59	1.66	1.60	1.70
N	128	256	512	1024	2048
N_p	262,144	262,144	2,097,152	16,777,216	134,217,728
N_{tracked}	32,768	32,768	262,144	2,097,152	16,777,216
N_{proc}	16	16	64	1024	16,384

ferent particle classes are simulated with Stokes numbers St ranging from 0 to 30. $St \equiv \tau_p/\tau_\eta$ is a non-dimensional measure of a particle's inertia, comparing the response time of the particle $\tau_p \equiv \rho_p d^2/\left(18\rho_f\nu\right)$ to the Kolmogorov timescale $\tau_\eta \equiv (\nu/\epsilon)^{1/2}$.

We assume that the particles are subjected to only linear drag forces, which is a reasonable approximation when the particle Reynolds number $Re_p \equiv |\boldsymbol{u}(\boldsymbol{x}^p(t),t) - \boldsymbol{v}^p(t)|/\nu < 0.5$ [49]. Here, $\boldsymbol{u}(\boldsymbol{x}^p(t),t)$ denotes the undisturbed fluid

velocity at the particle position $\boldsymbol{x}^p(t)$, and $\boldsymbol{v}^p(t)$ denotes the velocity of the particle. (Throughout this study, we use the superscript p on $\boldsymbol{x}$, $\boldsymbol{u}$, and $\boldsymbol{v}$ to denote time-dependent, Lagrangian variables defined along particle trajectories. Phase-space positions and velocities are denoted without the superscript p.) Though particles with large St experience non-negligible nonlinear drag forces (e.g., see [175]), the use of a linear drag model for large-St particles provides a useful first approximation and facilitates comparison between several theoretical models that make the same assumption (e.g., [32, 198, 71]). The present study also neglects the influence of gravity. Part II of this study [82] will address the combined effects of gravity and turbulence on particle motion. Finally, since a primary motivation is to understand droplet dynamics in atmospheric clouds, where the particle mass and volume loadings are low [148], we assume that the particle loadings are sufficiently dilute such that inter-particle interactions and two-way coupling between the phases are negligible [50, 162].

Under these assumptions, each inertial particle obeys a simplified Maxey-Riley equation [109],

$$\frac{d^2\boldsymbol{x}^p}{dt^2} = \frac{d\boldsymbol{v}^p}{dt} = \frac{\boldsymbol{u}\left(\boldsymbol{x}^p(t), t\right) - \boldsymbol{v}^p(t)}{\tau_p}, \tag{4.3}$$

and each fluid (i.e., inertialess) particle is tracked by solving

$$\frac{d\boldsymbol{x}^p}{dt} = \boldsymbol{u}(\boldsymbol{x}^p(t), t). \tag{4.4}$$

To compute $\boldsymbol{u}^p(t) = \boldsymbol{u}(\boldsymbol{x}^p(t), t)$, we need to interpolate from the Eulerian grid to the particle location. While other studies (e.g., see [15, 47]) have done so using tri-linear interpolation, [84] showed that such an approach can lead to errors in the interpolated velocity which are orders of magnitude above the local time-stepping error. In addition, [168] demonstrated that tri-linear interpolation, which possesses only C^0 continuity, leads to artificial high frequency os-

cillations in the computed particle accelerations. [136] noted that the relative motion of particles at small separations will depend strongly on the interpolation scheme. Since a main focus of this paper is particle motion near-contact and its influence on particle collisions, it is crucial to calculate $\boldsymbol{u}(\boldsymbol{x}^p(t), t)$ as accurately as possible. To that end, we use an eight-point B-spline interpolation scheme (with C^6 continuity) based on the algorithm in [169].

The particles were initially placed in the flow with a uniform distribution and velocities $\boldsymbol{v}^p$ equal to the underlying fluid velocity $\boldsymbol{u}^p$. We began computing particle statistics once the particle distributions and velocities became statistically stationary, usually about 5 large-eddy turnover times $T_L \equiv \ell/u'$ (where ℓ is the integral lengthscale and $u' \equiv \sqrt{2k/3}$) after the particles were introduced into the flow. Particle statistics were calculated at a frequency of 2-3 times per T_L and were time-averaged over the duration of the run T.

For a subset N_{tracked} of the total number of particles in each class N_p, we stored particle positions, velocities, and velocity gradients every $0.1\tau_\eta$ for a duration of about $100\tau_\eta$. These data are used to compute Lagrangian correlations, accelerations, and timescales of the particles.

4.4 Single-particle statistics

We first consider single-particle statistics from our simulations. These statistics will provide a basis for our understanding of the two-particle statistics presented in §4.5. We explore velocity gradient (i.e., small-scale velocity) statistics in §4.4.1, kinetic energy (i.e., large-scale velocity) statistics in §4.4.2, and acceleration statistics in §4.4.3. In each case, we study the effect of the underlying flow

topology on these statistics.

4.4.1 Velocity gradient statistics

We consider the gradients of the underlying fluid velocity at the particle locations, $\boldsymbol{A}(\boldsymbol{x}^p(t),t) \equiv \nabla \boldsymbol{u}(\boldsymbol{x}^p(t),t)$. These statistics provide us with information about the small-scale velocity field experienced by the particles. (Refer to [114] for a recent review on this subject.) In particular, to understand the interaction of particles with specific topological features of the turbulence, we decompose $\boldsymbol{A}(\boldsymbol{x}^p(t),t)$ into a symmetric strain rate tensor $\boldsymbol{\mathcal{S}}(\boldsymbol{x}^p(t),t) \equiv [\boldsymbol{A}(\boldsymbol{x}^p(t),t)+\boldsymbol{A}^\intercal(\boldsymbol{x}^p(t),t)]/2$ and an antisymmetric rotation rate tensor $\boldsymbol{\mathcal{R}}(\boldsymbol{x}^p(t),t) \equiv [\boldsymbol{A}(\boldsymbol{x}^p(t),t) - \boldsymbol{A}^\intercal(\boldsymbol{x}^p(t),t)]/2$.

Due to their inertia, heavy particles are ejected out of regions of high rotation rate and accumulate in regions of high strain rate (e.g., [107, 159, 48]), and this is associated with a 'preferential sampling' of $\boldsymbol{A}(\boldsymbol{x},t)$. For particles with low inertia ($St \ll 1$), preferential sampling is the dominant clustering mechanism (e.g., see [32]). As the particle inertia increases, the particle motion becomes increasingly decoupled from the local fluid turbulence, and the effect of the preferential sampling on the particle dynamics decreases. At the other limit ($St \gg 1$), preferential sampling vanishes and the particles have a damped response to the underlying flow which leads them to sample the turbulence more uniformly (e.g., see [12]).

We first consider the average of the second invariants of the strain rate and rotation rate tensors evaluated at the inertial particle positions

$$\langle \mathcal{S}^2 \rangle^p \equiv \langle \boldsymbol{\mathcal{S}}(\boldsymbol{x}^p(t),t) : \boldsymbol{\mathcal{S}}(\boldsymbol{x}^p(t),t) \rangle, \tag{4.5}$$

and

$$\langle \mathcal{R}^2 \rangle^p \equiv \langle \boldsymbol{\mathcal{R}}(\boldsymbol{x}^p(t), t) : \boldsymbol{\mathcal{R}}(\boldsymbol{x}^p(t), t) \rangle. \tag{4.6}$$

By definition, for fully mixed fluid particles ($St = 0$) in homogeneous turbulence, $\tau_\eta^2 \langle \mathcal{S}^2 \rangle^p = \tau_\eta^2 \langle \mathcal{R}^2 \rangle^p = 0.5$.

Since small-St particles are centrifuged out of regions of high rotation, we expect that $\tau_\eta^2 \langle \mathcal{R}^2 \rangle^p$ will decrease with increasing St; their accumulation in high strain regions would also lead to the expectation that $\tau_\eta^2 \langle \mathcal{S}^2 \rangle^p$ will increase with increasing St. In figure 4.2 we see that while $\tau_\eta^2 \langle \mathcal{R}^2 \rangle^p$ is more strongly affected by changes in R_λ than is $\tau_\eta^2 \langle \mathcal{S}^2 \rangle^p$, both quantities decrease with increasing St (for $St \ll 1$). This surprising result is consistent with other DNS [34, 32, 143]. Our data also show that both $\tau_\eta^2 \langle \mathcal{S}^2 \rangle^p$ and $\tau_\eta^2 \langle \mathcal{R}^2 \rangle^p$ decrease with increasing R_λ for $St \ll 1$, in agreement with [34].

We use the formulation given in [32] (and re-derived in [143]) to model the effect of biased sampling on $\tau_\eta^2 \langle \mathcal{S}^2 \rangle^p$ and $\tau_\eta^2 \langle \mathcal{R}^2 \rangle^p$ in limit of $St \ll 1$. [32, 143] showed that for an arbitrary quantity ϕ, the average value of ϕ sampled along a particle trajectory $\langle \phi \rangle^p$ can be reconstructed entirely from fluid particle statistics using the relation,

$$\langle \phi(St) \rangle^p = \langle \phi(St = 0) \rangle^p + \tau_\eta \sigma_\phi^p St \left(\rho^p_{\mathcal{S}^2 \phi} \sigma^p_{\mathcal{S}^2} T^p_{\mathcal{S}^2 \phi} - \rho^p_{\mathcal{R}^2 \phi} \sigma^p_{\mathcal{R}^2} T^p_{\mathcal{R}^2 \phi} \right). \tag{4.7}$$

Here, σ_Y^p denotes the standard deviation of a variable Y along a fluid particle trajectory, ρ^p_{YZ} is the correlation coefficient between Y and Z,

$$\rho^p_{YZ} \equiv \frac{\left\langle \left[Y(\boldsymbol{x}^p(t), t) - \langle Y(\boldsymbol{x}^p(t), t) \rangle \right] \left[Z(\boldsymbol{x}^p(t), t) - \langle Z(\boldsymbol{x}^p(t), t) \rangle \right] \right\rangle}{\sigma_Y^p \sigma_Z^p}, \tag{4.8}$$

and T^p_{YZ} is the Lagrangian correlation time,

$$T^p_{YZ} \equiv \frac{\displaystyle\int_0^\infty \left\langle [Y(\boldsymbol{x}^p(0), 0) - \langle Y(\boldsymbol{x}^p(t), t) \rangle][Z(\boldsymbol{x}^p(t'), t') - \langle Z(\boldsymbol{x}^p(t), t) \rangle] \right\rangle dt'}{\left\langle [Y(\boldsymbol{x}^p(t), t) - \langle Y(\boldsymbol{x}^p(t), t) \rangle][Z(\boldsymbol{x}^p(t), t) - \langle Z(\boldsymbol{x}^p(t), t) \rangle] \right\rangle}. \tag{4.9}$$

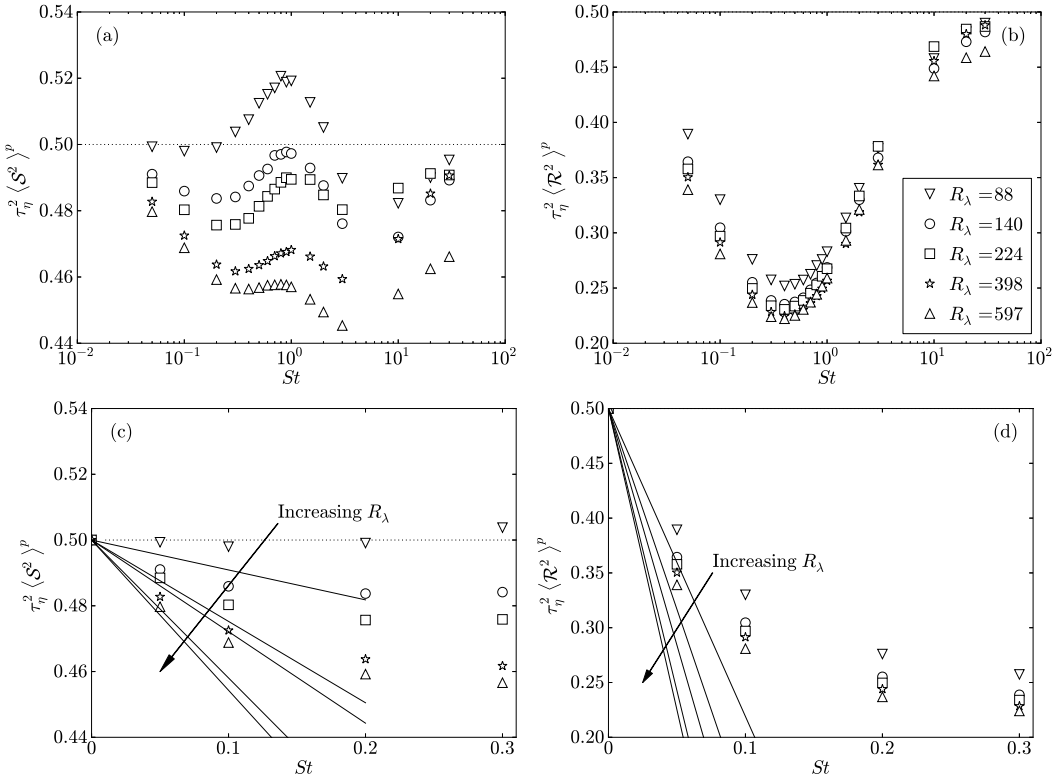

Figure 4.2: Data for $\langle \mathcal{S}^2 \rangle^p$ (a,c) and $\langle \mathcal{R}^2 \rangle^p$ (b,d) sampled at inertial particle positions as function of St for different values of R_λ. The data are shown at low St in (c,d) to highlight the effect of biased sampling in this regime. The solid lines in (c) and (d) are the predictions from Eq. (4.7) for $St \ll 1$. DNS data are shown with symbols.

The predictions from Eq. (4.7) for small St are shown by the solid lines in figure 4.2(c) and figure 4.2(d). In the limit of small St, this model is able to capture the decrease in both $\tau_\eta^2 \langle \mathcal{S}^2 \rangle^p$ and $\tau_\eta^2 \langle \mathcal{R}^2 \rangle^p$ with increasing St, and also the decrease in these quantities with increasing R_λ. It is uncertain whether the quantitative differences between the DNS data and the model are due to shortcomings of the model or the fact that the smallest inertial particles ($St = 0.05$) are too large for the model (which assumes $St \ll 1$) to hold.

Despite the success of the model of [32] in reproducing the trends in the

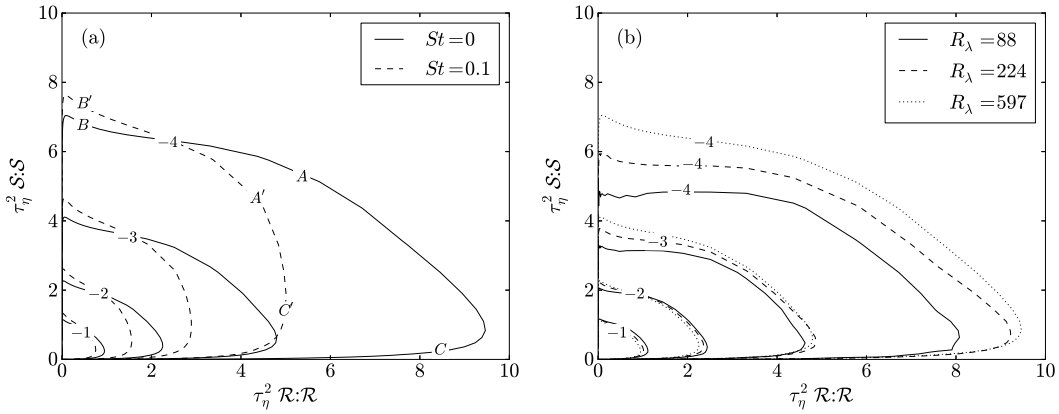

Figure 4.3: (a) Joint PDFs of τ_η^2: $\boldsymbol{\mathcal{S}}$: $\boldsymbol{\mathcal{S}}$ and $\tau_\eta^2\boldsymbol{\mathcal{R}}$: $\boldsymbol{\mathcal{R}}$ for $R_\lambda = 597$ for $St = 0$ and $St = 0.1$ particles. Certain regions of the flow are labeled to aid in the discussion of the trends. (b) Joint PDFs of $\tau_\eta^2\boldsymbol{\mathcal{S}}$: $\boldsymbol{\mathcal{S}}$ and $\tau_\eta^2\boldsymbol{\mathcal{R}}$: $\boldsymbol{\mathcal{R}}$ for different R_λ for $St = 0$ particles. In both plots, the exponents of the decade are indicated on the contour lines.

DNS, the physical explanation for the changes in the mean strain and rotation rates remains unclear. In figure 4.3(a), we plot joint PDFs of the strain and rotation rates sampled by both $St = 0$ and $St = 0.1$ particles to better understand the specific topological features of the regions of the flow contributing to these changes. Following the designations given in [154], we refer to regions with high strain and high rotation (indicated by 'A' in figure 4.3(a)) as 'vortex sheets,' regions of low rotation and high strain (indicated by 'B') as 'irrotational dissipation' areas, and regions of high rotation and low strain (indicated by 'C') as 'vortex tubes.'

Our results show three main trends in the particle concentrations. First, inertial particles are ejected from vortex sheets (A) into regions of moderate rotation and moderate strain (A'). This ejection from vortex sheets has only recently been discussed in the literature [143]. Second, they move from irrotational dissipation regions (B) to regions of comparable rotation and even higher strain (B'). Third, the particles move out of vortex tubes (C) into regions of lower rotation

and higher strain (C'). Evidently, this first effect is primarily responsible for the decrease in $\tau_\eta^2\langle\mathcal{S}^2\rangle^p$ at small St, as suggested in [143], and the first and third effects both contribute to the decrease in $\tau_\eta^2\langle\mathcal{R}^2\rangle^p$. We will revisit these three trends in relation to the particle kinetic energies (§4.4.2) and the particle accelerations (§4.4.3).

Figure 4.3(b) shows the PDF map for fluid particles at three values of the Reynolds number. Notice that as R_λ increases, the probability of encountering a vortex sheet (overlapping high strain and high rotation) increases. This finding is consistent with the results of [191], who observed that high strain and rotation events increasingly overlap in isotropic turbulence as the Reynolds number increases. It is thus likely that with increasing Reynolds number, rotation and strain events become increasingly intense, and the resulting vortex sheets become increasingly efficient at expelling particles, causing both $\tau_\eta^2\langle\mathcal{S}^2\rangle^p$ and $\tau_\eta^2\langle\mathcal{R}^2\rangle^p$ to decrease (cf. figure 4.2).

[107] noted that at low St, the compressibility of the particle field (and hence the degree of particle clustering) is directly related to the difference between the rates of strain and rotation sampled by the particles, $\tau_\eta^2\langle\mathcal{S}^2\rangle^p - \tau_\eta^2\langle\mathcal{R}^2\rangle^p$. From figure 4.4, we see that at low St, $\tau_\eta^2\langle\mathcal{S}^2\rangle^p - \tau_\eta^2\langle\mathcal{R}^2\rangle^p$ increases with increasing R_λ, suggesting that the degree of clustering may also increase here. We will test this hypothesis in §4.5.2 when we directly measure particle clustering at different values of St and R_λ.

We finally consider the Lagrangian strain and rotation timescales, which will be useful for understanding the trends in particle clustering in §4.5.2. Since the fluid and particle phases are isotropic, we will have nine statistically equivalent strain timescales: $T^p_{\mathcal{S}_{11}\mathcal{S}_{11}}$, $T^p_{\mathcal{S}_{11}\mathcal{S}_{22}}$, $T^p_{\mathcal{S}_{11}\mathcal{S}_{33}}$, $T^p_{\mathcal{S}_{12}\mathcal{S}_{12}}$, $T^p_{\mathcal{S}_{13}\mathcal{S}_{13}}$, $T^p_{\mathcal{S}_{22}\mathcal{S}_{22}}$, $T^p_{\mathcal{S}_{22}\mathcal{S}_{33}}$, $T^p_{\mathcal{S}_{23}\mathcal{S}_{23}}$, and

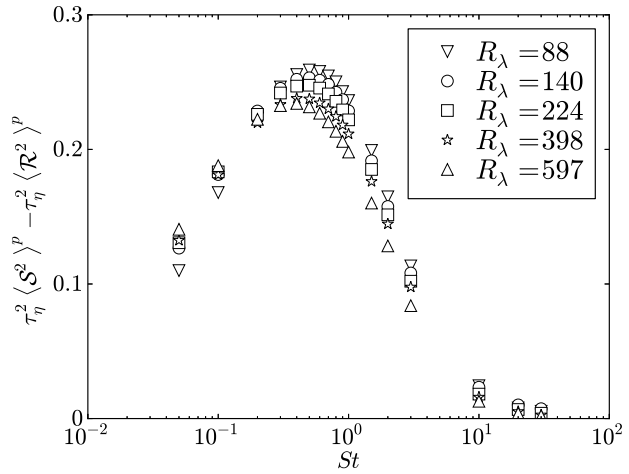

Figure 4.4: The difference between the mean rates of strain and rotation sampled by the particles as a function of St for different values of R_λ.

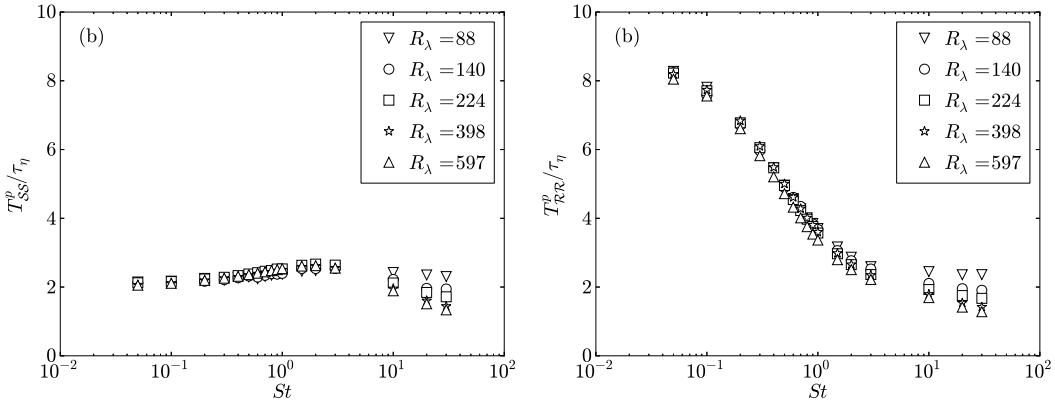

Figure 4.5: Lagrangian timescales of a single component of the strain rate (a) and rotation rate (b) tensors, plotted as a function of St for different values of R_λ.

$T^p_{\mathcal{S}_{33}\mathcal{S}_{33}}$. We take the strain timescale $T^p_{\mathcal{SS}}$ to be the average of these nine components. We similarly take the rotation timescale $T^p_{\mathcal{RR}}$ to be the average of three statistically equivalent components: $T^p_{\mathcal{R}_{12}\mathcal{R}_{12}}$, $T^p_{\mathcal{R}_{13}\mathcal{R}_{13}}$, and $T^p_{\mathcal{R}_{23}\mathcal{R}_{23}}$.

We see that $T^p_{\mathcal{SS}}/\tau_\eta$ is independent of R_λ for $St < 10$, and decreases weakly with increasing R_λ for $St \geq 10$. On the other hand, $T^p_{\mathcal{RR}}/\tau_\eta$ tends to decrease with

increasing R_λ for all values of St, and this decrease becomes more pronounced as St increases. We also see that $T^p_{\mathcal{RR}}$ is much more sensitive to changes in St than $T^p_{\mathcal{SS}}$, suggesting that the dominant effect of inertia is to cause particles to spend less time in strongly rotating regions. As a result, the particles will generally have less time to respond to fluctuations in the rotation rate, causing $\langle \mathcal{R}^2 \rangle^p$ to be strongly reduced with increasing St, as was seen above.

4.4.2 Particle kinetic energy

We now move from small-scale velocity statistics to large-scale velocity statistics. Figure 4.6 shows the average particle kinetic energy $k^p(St) \equiv \frac{1}{2}\langle \boldsymbol{v}^p(t) \cdot \boldsymbol{v}^p(t) \rangle$ (normalized by the average fluid kinetic energy k) for different values of R_λ.

We first consider the effect of inertial filtering on this statistic, and then examine the effect of biased sampling. It is well-known that filtering leads to a reduction in the particle turbulent kinetic energy for large values of St. This reduction is the strongest (weakest) for the lowest (highest) Reynolds numbers, as seen in figure 4.6(a). These trends are captured by the model in [2], which assumes an exponential decorrelation of the Lagrangian fluid velocity. Under this assumption, the ratio between the particle and fluid kinetic energies can be expressed as

$$\frac{k^p(St)}{k} \approx \frac{1}{1+\tau_p/\tau_\ell} = \frac{1}{1+St\left(\tau_\eta/\tau_\ell\right)}, \tag{4.10}$$

where τ_ℓ is the Lagrangian correlation time of the fluid, which we approximate using the relation given in [199]. The model predictions of $k^p(St)/k$ are included in figure 4.6(a) and are in good agreement with the DNS at large St, where filtering is dominant. The trends with R_λ are also reproduced well.

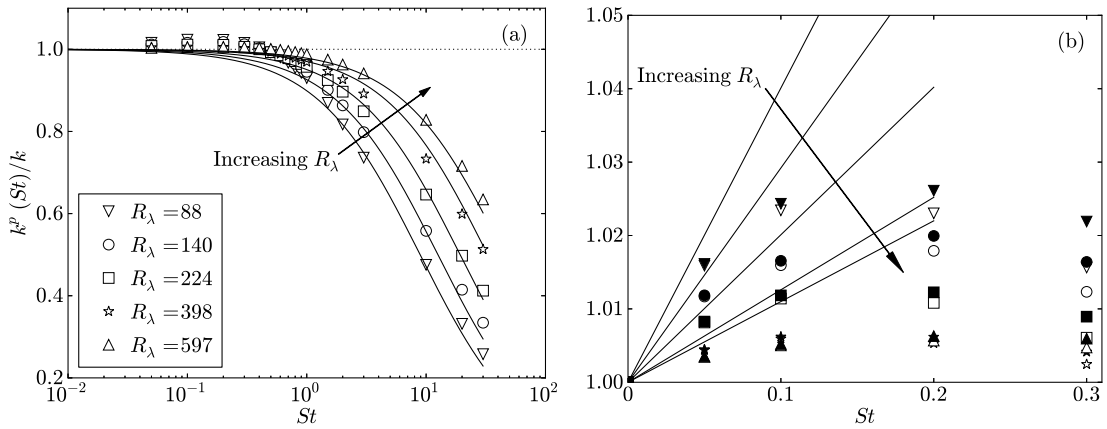

Figure 4.6: (a) The ratio between the average particle kinetic energy $k^p(St)$ and the average fluid kinetic energy k for different values of R_λ. DNS data are shown with symbols, and the predictions of the filtering model in Eq. (4.10) are shown with solid lines. (b) The ratio between $k^p(St)$ and k (open symbols), and the ratio between the average fluid kinetic energy at the particle locations $k^{fp}(St)$ and k (filled symbols), shown at low St to highlight the effects of biased sampling. Also shown is the prediction from the biased sampling model given in Eq. (4.7) (solid lines).

We thus have the following physical explanation of inertial filtering on the particle kinetic energies: for low-Reynolds-number flows, the response time of the largest particles exceeds the timescales of many large-scale flow features. The result is a filtered response to the large-scale turbulence and an overall reduction in the particle kinetic energy. As the Reynolds number is increased (and the particle response time is fixed with respect to the small-scale turbulence), more flow features are present with timescales that exceed the particle response time, and hence the effect of inertial filtering is diminished with increasing R_λ, as predicted by Eq. (4.10).

To highlight the effect of biased sampling on the particle kinetic energy, figure 4.6(b) shows both the average particle kinetic energy $k^p(St)$ and the av-

erage kinetic energy of the fluid sampled along an inertial particle trajectory, $k^{fp}(St) \equiv \frac{1}{2}\langle \boldsymbol{u}(\boldsymbol{x}^p(t),t) \cdot \boldsymbol{u}(\boldsymbol{x}^p(t),t)\rangle$. As is evident in figure 4.6(b), the particle kinetic energy exceeds k for low values of St. By comparing k^p to k^{fp}, we see that the increased kinetic energy of the smallest particles is due almost entirely to biased sampling of the flow field. While [144] were the first to show an increase in $k^p(St)/k$ for low St (which they attributed to biased sampling), this trend is also suggested by the early study of [159], in which the authors observed that small inertial particles preferentially sample certain high kinetic energy regions they referred to as 'streaming zones.' Figure 4.6(b) also shows that at small values of St, $k^p(St)/k$ decreases with increasing Reynolds number.

The solid lines in figure 4.6(b) show the predictions of the particle kinetic energy from Eq. (4.7). In the limit of small St, the model of [32] is able to capture qualitatively both the increase in $k^p(St)/k$ with increasing St and the decrease in $k^p(St)/k$ with increasing R_λ.

To further elucidate the physical mechanisms leading to these trends, we plot the mean kinetic energy of the fluid conditioned on $\mathcal{S}^2$ and $\mathcal{R}^2$, $k_{\mathcal{S}^2,\mathcal{R}^2}$, in figure 4.7. Isocontours of the concentrations of $St = 0$ and $St = 0.1$ particles are shown for comparison. While the data contain considerable statistical noise, we can draw a few conclusions about the qualitative trends.

From figure 4.7(a), we see that the change in kinetic energy at $R_\lambda = 88$ can be divided into the three mechanisms discussed in §4.4.1. First, particles are ejected from vortex sheets (A) into moderate rotation and moderate strain regions (A'), which generally tends to decrease the particle kinetic energy. Second, as St increases, particles in irrotational straining regions (B) travel into regions of higher strain (B'), which are characterized by higher kinetic energy.

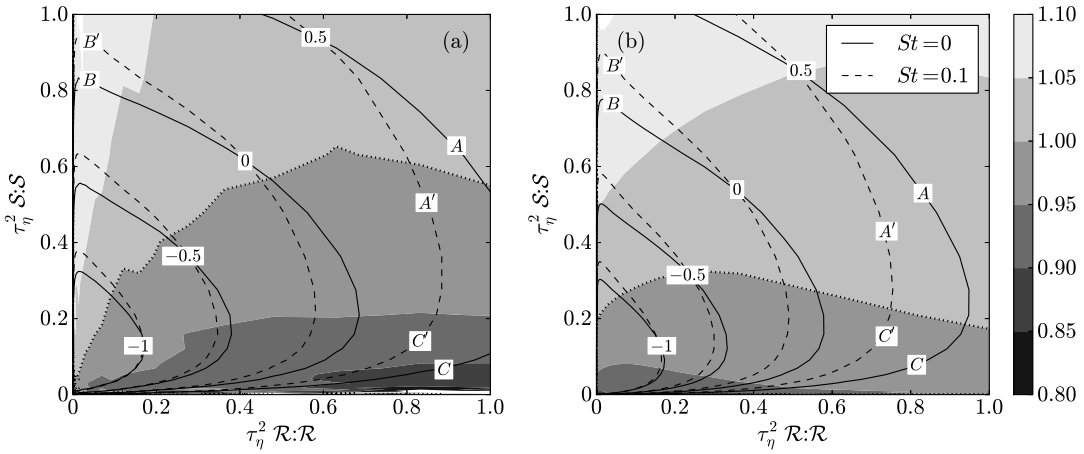

Figure 4.7: Filled contours of the fluid kinetic energy conditioned on $\mathcal{S}^2$ and $\mathcal{R}^2$, $k_{\mathcal{S}^2,\mathcal{R}^2}$, normalized by the unconditioned mean fluid kinetic energy k at (a) the lowest Reynolds number and (b) the highest Reynolds number. The dotted contour lines indicate $k_{\mathcal{S}^2,\mathcal{R}^2}/k = 1$. Isocontours of particle concentration for $St = 0$ and $St = 0.1$ particles are included for reference, with the exponents of the decade indicated on the contour lines. Certain regions of the flow are labeled to aid in the discussion of the trends.

Third, some inertial particles are ejected from vortex tubes (C), which are characterized by lower kinetic energies, and travel into lower rotation and higher strain regions (C'), which have higher kinetic energies. The observed increase in $k^p(St)/k$ must therefore be due to the second and third mechanisms.

At high Reynolds numbers (figure 4.7(b)), however, a larger portion of the flow is occupied by regions of overlapping high strain and high rotation from which particles are ejected (see §4.4.1). The first mechanism (which tends to decrease the kinetic energy) therefore plays a larger role. Also, at $R_\lambda = 597$, high rotation and low strain regions (C) are no longer associated with very low kinetic energies, causing the third mechanism to be less effective at increasing the particle kinetic energy. The overall result is a decrease in $k^p(St)/k$ with increasing Reynolds number at small values of St.

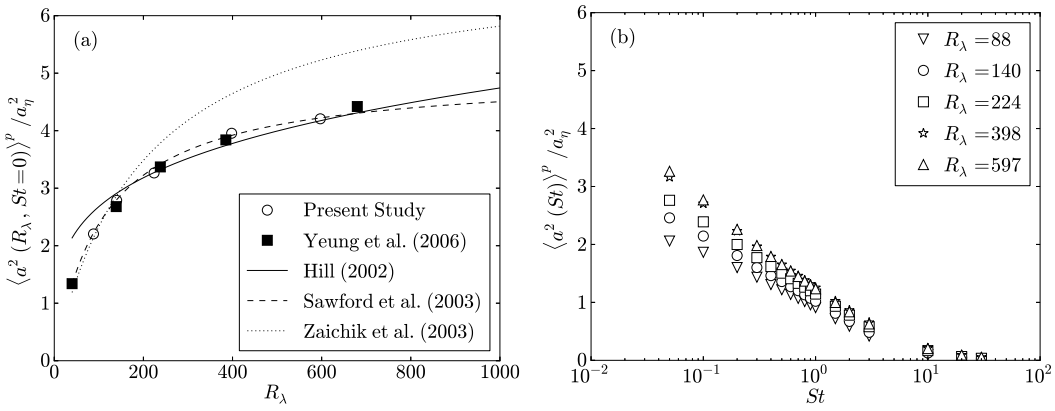

Figure 4.8: (a) The acceleration variance of Lagrangian fluid particles as a function of R_λ. The results from the present study (open circles) are compared to DNS data from [193] (filled squares) and several theoretical predictions (lines). (b) The acceleration variance of inertial particles as a function of St for different values of R_λ.

4.4.3 Particle accelerations

In this section, we analyze fluid and inertial particle accelerations $\boldsymbol{a}^p(t) \equiv d\boldsymbol{v}^p(t)/dt$. Fluid particle accelerations are known to be strongly intermittent (e.g., see [173, 86]), with the probability of intense acceleration events increasing with the Reynolds number. Before accounting for inertial effects, we consider the effect of R_λ on the acceleration variance $\langle a^2\rangle^p \equiv \langle \boldsymbol{a}^p(t) \cdot \boldsymbol{a}^p(t)\rangle/3$ of Lagrangian fluid particles in figure 4.8(a). To facilitate comparison between the different Reynolds numbers, we have normalized $\langle a^2\rangle^p$ by the Kolmogorov acceleration variance $a_\eta^2 \equiv \sqrt{\epsilon^3/\nu}$. The DNS data from [193] and the theoretical predictions of [74], [147], and [199] are shown for comparison. We see that our DNS data agrees well with [193], and that the model of [147] best reproduces the trends in the DNS. [74] breaks down at low R_λ, while [199] fails at high R_λ.

We turn our attention to inertial particle accelerations in figure 4.8(b). The

observed trend for inertial particles is analogous to that for fluid particles: at each value of St considered, the particle acceleration variance (normalized by Kolmogorov units) monotonically increases with R_λ (cf. [12]). As St increases, the acceleration variance decreases, presumably as a result of both biased sampling of the flow field and inertial filtering.

We now seek to understand and model how inertia changes the accelerations of particles through the filtering and biased sampling effects. To do so, we rescale the inertial particle acceleration variance by that of fluid particles and plot the results in figure 4.9. In figure 4.9(a), we compare the rescaled acceleration variance to the model of [197], which only accounts for inertial filtering of the underlying flow. The model of [197] is able to capture all the qualitative trends in R_λ and St, and the model predictions provide remarkably good quantitative agreement with the DNS at the largest values of St, where filtering is the dominant mechanism. At lower values of St, the rescaled particle acceleration variance decreases with increasing R_λ. In this case, as R_λ increases, the underlying flow is subjected to increasingly intermittent acceleration events, and the inertial particles filter a larger fraction of these events. At the largest values of St, most intermittent accelerations are filtered, and a particle's acceleration variance is determined by its interaction with the largest turbulence scales. Since the range of available large scales increases with R_λ, the rescaled particle acceleration variance increases with R_λ for the largest values of St.

We now consider the effect of biased sampling on the acceleration variances. In figure 4.9(b), we plot the variance of both inertial particle accelerations and fluid accelerations along inertial particle trajectories (scaled by the acceleration variance of $St = 0$ particles). As expected, for $St \ll 1$, where biased sampling

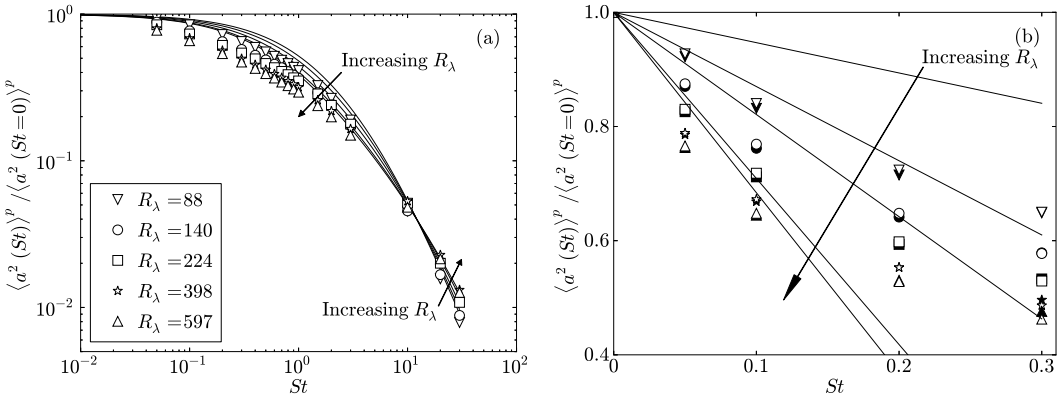

Figure 4.9: (a) Inertial particle acceleration variances scaled by the fluid particle acceleration variance (open symbols). The solid lines and arrows indicate the predictions from the filtering model of [197]. (b) The variance of the inertial particle accelerations (open symbols) and the fluid velocity accelerations along the particle trajectories (filled symbols), shown at low St to highlight the effect of biased sampling. The solid lines indicate the predictions from the biased sampling model given in Eq. (4.7).

is the dominant mechanism, inertial particle accelerations are almost equivalent to the accelerations of the underlying flow sampled along the particle trajectories. The model of [32] (Eq. (4.7)) is able to reproduce all the qualitative trends correctly in the limit of small St. The scaled variances decrease with increasing R_λ, and we expect that this trend is due to the fact that high vorticity regions are associated with high accelerations [20] and become increasingly efficient at ejecting particles (refer to §4.4.1).

We test this expectation in figure 4.10 by plotting the acceleration variance for fluid particles conditioned on $\mathcal{S}^2$ and $\mathcal{R}^2$, $\langle a^2\rangle^p_{\mathcal{S}^2,\mathcal{R}^2}$, and normalized by the unconditioned variance $\langle a^2\rangle^p$. We see that inertial particles are indeed ejected from high vorticity regions (both vortex sheets and vortex tubes) into lower vorticity regions (e.g., A into A' and C into C'), and that these high vorticity regions are marked by very large accelerations. Though some inertial particles

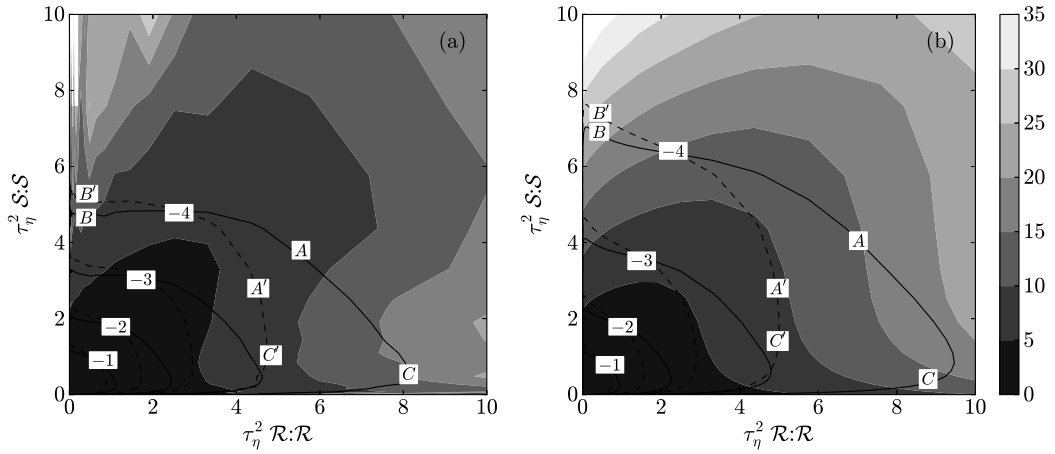

Figure 4.10: Filled contours of the variance of the fluid particle accelerations conditioned on $\mathcal{S}^2$ and $\mathcal{R}^2$, $\langle a^2\rangle^p_{\mathcal{S}^2,\mathcal{R}^2}$, normalized by the unconditioned fluid particle acceleration variance $\langle a^2\rangle^p$, at (a) $R_\lambda = 88$ and (b) $R_\lambda = 597$. Isocontours of particle concentration for $St = 0$ and $St = 0.1$ particles are included for reference, with the exponents of the decade indicated on the contour lines. Certain regions of the flow are labeled to aid in the discussion of the trends.

experience higher accelerations as they move into irrotational straining regions with higher strain rates (e.g., B into B'), this effect is relatively weak, and the overall trend is a decrease in the particle accelerations with increasing inertia.

To investigate the intermittency of inertial particle accelerations, we plot the kurtosis of the particle accelerations, $\langle a^4\rangle^p/(\langle a^2\rangle^p)^2$, in figure 4.11, where $\langle a^4\rangle^p \equiv \langle a_1^p(t)^4 + a_2^p(t)^4 + a_3^p(t)^4\rangle^p/3$. (Note that a Gaussian distribution has a kurtosis of 3, as indicated in figure 4.11 by a dotted line.) As expected, the particle accelerations are highly intermittent, with the degree of intermittency increasing with increasing R_λ. The kurtosis decreases very rapidly as St increases. Figure 4.11(b) indicates that the kurtosis of very small particles ($St = 0.05$) at the highest value of R_λ is over a factor of two smaller than that of fluid particles. The largest-St particles have kurtosis values approaching those of a Gaussian distri-

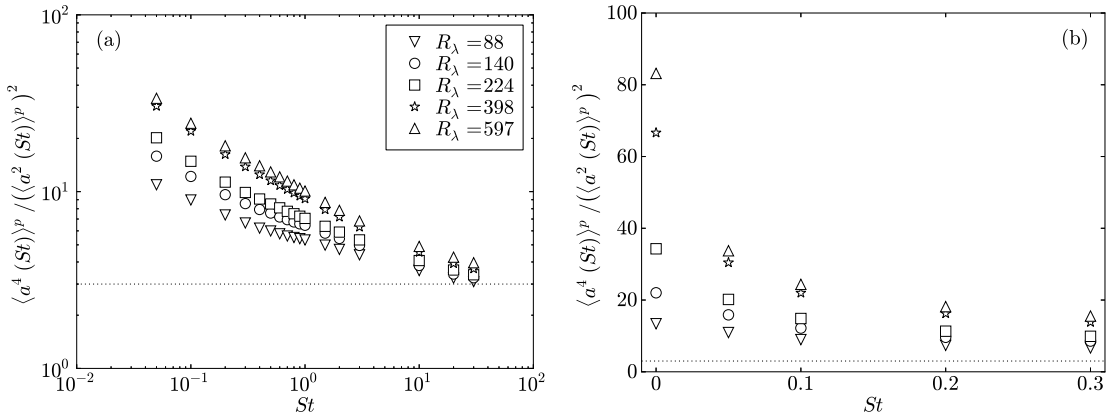

Figure 4.11: Particle acceleration kurtosis as a function of St for different values of R_λ. The dotted line indicates a kurtosis of 3, the value for a Gaussian distribution. Values over the whole range of non-zero St are shown in (a). (b) shows only small-St results on a linear plot to emphasize the rapid reduction in kurtosis as St increases from 0.

bution. These trends can be explained by the fact that both biased sampling and inertial filtering decrease the probability of high-intensity acceleration events. Standardized moments of up to order 10 (not shown) were also analyzed and found to exhibit the same trends.

We should note that the grid resolution study in [193] suggests that the acceleration moments from our DNS may be under-predicted. [193] showed that at $R_\lambda \approx 140$, increasing the grid resolution $k_{\max}\eta$ from 1.5 to 12 led to a 10% increase in the fluid acceleration variance and a 30% increase in the fluid acceleration kurtosis. It is unclear how these trends will change at higher R_λ, but it suggests that the quantitative results reported here should be interpreted with caution. (The velocity gradients presented earlier are likely reliable, however, since [193] found that such statistics are less dependent on the grid resolution.)

4.5 Two-particle statistics

We now consider two-particle statistics relevant for predicting inertial particle collisions. We analyze particle relative velocities in §4.5.1, clustering in §4.5.2, and use these data to compute the collision kernel in §4.5.3. (The mean-squared separation of inertial particle pairs was also studied from these data and is the topic of a separate publication [26].)

4.5.1 Particle relative velocities

We study particle relative velocities as a function of both St and R_λ. The relative velocities for inertial particles are defined by the relation

$$w^p_{\parallel,\perp}(t) \equiv \left[\boldsymbol{v}^p_2(t) - \boldsymbol{v}^p_1(t)\right] \cdot \boldsymbol{e}^p_{\parallel,\perp}(t). \tag{4.11}$$

Here, $\boldsymbol{v}^p_1$ and $\boldsymbol{v}^p_2$ indicate the velocities of particles 1 and 2, respectively, which are separated from each other by a distance $r^p(t) = |\boldsymbol{r}^p(t)|$. The subscripts $\parallel$ and $\perp$ indicate directions parallel (longitudinal) to the separation vector or perpendicular (transverse) to the separation vector, respectively, and $\boldsymbol{e}^p_{\parallel,\perp}$ denotes the unit vector in the corresponding direction. (We use the method discussed in [125] to compute the transverse components.)

We will also examine the velocity differences of the fluid at the particle locations, defined as

$$\Delta u^p_{\parallel,\perp}(t) \equiv \left[\boldsymbol{u}^p_2(t) - \boldsymbol{u}^p_1(t)\right] \cdot \boldsymbol{e}^p_{\parallel,\perp}(t), \tag{4.12}$$

where $\boldsymbol{u}^p_1$ and $\boldsymbol{u}^p_2$ are the velocities of the fluid underlying particles 1 and 2, respectively. Note that for uniformly-distributed fluid ($St = 0$) particles, the

particle velocity statistics are equivalent to the underlying fluid velocity statistics.

Following the nomenclature in [24, 25], we denote particle relative velocity moments of order n as

$$S^{p}_{n\parallel}(r) \equiv \left\langle \left[w^{p}_{\parallel}(t) \right]^{n} \right\rangle_{r}, \tag{4.13}$$

for the components parallel to the separation vector, and as

$$S^{p}_{n\perp}(r) \equiv \left\langle \left[w^{p}_{\perp}(t) \right]^{n} \right\rangle_{r}, \tag{4.14}$$

for components perpendicular to the separation vector. In these expressions $\langle \cdot \rangle_r$ denotes an ensemble average conditioned on $r^p(t) = r$.

For the purposes of computing the collision kernel (see §4.5.3), we are also interested in the mean inward relative velocity parallel to the separation vector, defined as

$$S^{p}_{-\parallel}(r) \equiv -\int_{-\infty}^{0} w_{\parallel} p(w_{\parallel}|r) dw_{\parallel}, \tag{4.15}$$

where $p(w_{\parallel}|r) = \langle \delta(w^{p}_{\parallel}(t) - w_{\parallel}) \rangle_r$ is the PDF for the longitudinal particle relative velocity conditioned on $r^p(t) = r$.

Finally, in some cases we are also interested in moments of the fluid velocity differences. We use a superscript fp to denote the moments of fluid velocity differences at the particle locations, and a superscript f to denote the moments of fluid velocity differences at fixed points with separation r. We therefore have

$$S^{fp}_{n\parallel}(r) \equiv \left\langle \left[\Delta u_{\parallel}(r^{p}(t), t) \right]^{n} \right\rangle_{r}, \tag{4.16}$$

and

$$S^{f}_{n\parallel}(r) \equiv \left\langle \left[\Delta u_{\parallel}(r, t) \right]^{n} \right\rangle. \tag{4.17}$$

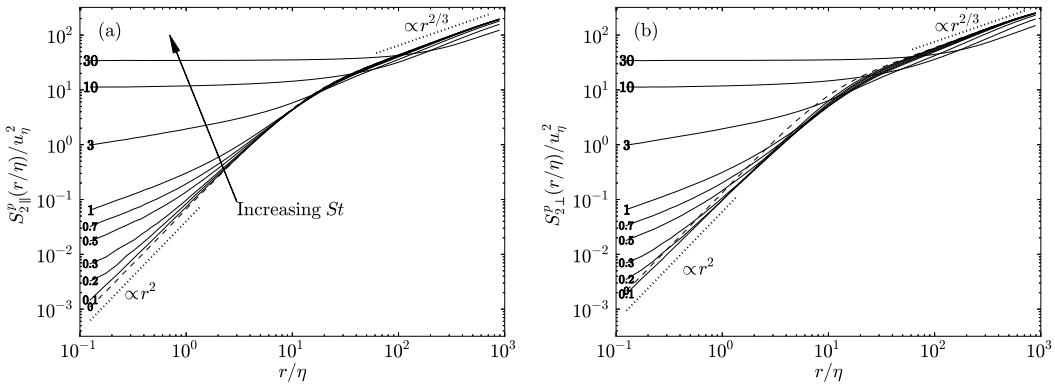

Figure 4.12: The particle relative velocity variances parallel to the separation vector (a) and perpendicular to the separation vector (b), plotted as a function of the separation r/η for $R_\lambda = 597$. The Stokes numbers are indicated by the line labels, and the $St = 0$ curves are shown with dashed lines for clarity. The expected dissipation and inertial range scalings (based on [94]) are included for reference.

The components perpendicular to the separation vector are defined analogously.

We first consider dissipation-range statistics, and then consider inertial-range statistics.

Dissipation range relative velocity statistics

In figure 4.12, we plot the relative velocity variances $S_{2\parallel}^p$ and $S_{2\perp}^p$ versus r/η at $R_\lambda = 597$. The mean inward relative velocity (not shown) has the same qualitative trends, and will be considered later in this section. For the purposes of the following discussion, we define the dissipation range as the region over which the fluid velocity variances follow r^2-scaling, which is seen to be $0 \leq r/\eta \lesssim 10$ in figure 4.12, in agreement with [87].

At small separations, the relative velocity variances parallel to the separation vector (figure 4.12(a)) increase monotonically with St and deviate from r^2-scaling, while the relative velocity variances perpendicular to the separation vector decrease for $St \lesssim 0.1$ and then increase monotonically with St for $St \gtrsim 0.1$ (figure 4.12(b)). We expect that the trends at small separations and small St are primarily due to biased sampling of the underlying flow, which also dictates much of the single-particle dynamics for small St (refer to §4.4).

To test this expectation, we compare the particle relative velocity variances to those of the fluid sampled by the particles in figure 4.13. In all cases, the velocity variances are normalized by those of $St = 0$ particles. At $St = 0.05$ and $St = 0.1$, the effect of biased sampling is dominant at all separations, as evidenced by the fact that $S_{2\parallel}^{fp}$ and $S_{2\perp}^{fp}$ are close to $S_{2\parallel}^{p}$ and $S_{2\perp}^{p}$, respectively. We note that for small St and small r/η, biased sampling leads to an increase in $S_{2\parallel}^{fp}$ with increasing St and to a decrease in $S_{2\perp}^{fp}$ with increasing St. This is consistent with the trends observed in figure 4.12 and with our argument (§4.4.1) that inertia causes particles to be ejected from vortex tubes. We expect that two particles which are rotating in a vortex tube will experience small (large) relative velocities parallel (perpendicular) to the particle separation vector, and that the parallel (perpendicular) relative velocities will increase (decrease) as particles are ejected from a vortex tube.

For $St \gtrsim 0.2$, the particle relative velocities are much larger than the underlying fluid velocity differences at small separations. This difference is due to path-history effects (see [24, 25]). That is, as inertial particles approach each other, they retain a memory of more energetic turbulence scales along their path histories, leading to relative velocities that exceed the local fluid velocity differ-

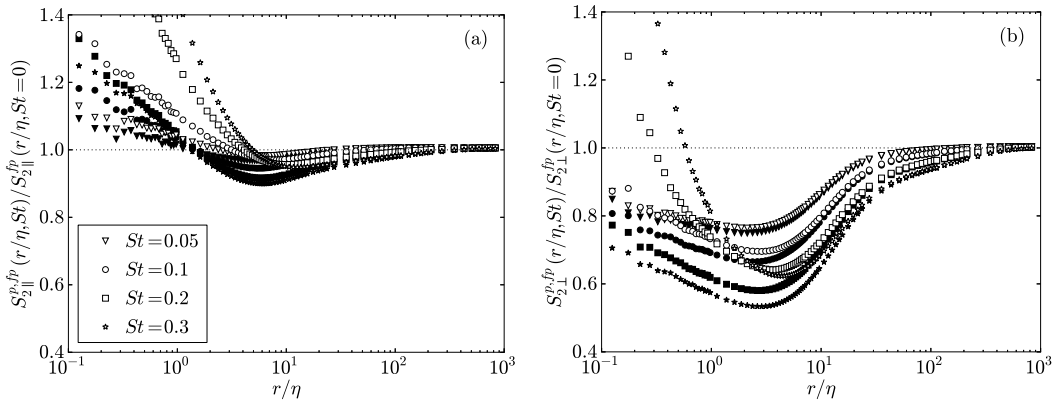

Figure 4.13: The parallel (a) and perpendicular (b) relative velocity variances of inertial particles ($S_{2\parallel}^{p}$ and $S_{2\perp}^{p}$, open symbols) and of the fluid at inertial particle positions ($S_{2\parallel}^{fp}$ and $S_{2\perp}^{fp}$, filled symbols) for $R_\lambda = 597$. All quantities are normalized by the relative velocity variances of $St = 0$ particles.

ence. These path-history effects imply that inertial particles can come together from different regions in the flow, occupy the same position in the flow at the same time, and yet have different velocities due to their differing path histories. This effect is referred to as 'caustics,' 'crossing trajectories,' or 'the sling effect,' causes a departure from r^2-scaling in the second-order structure functions at small separations, and can lead to large relative velocities [195, 55, 182, 183, 56]. (Also note that while caustics are instantaneous events, the statistical manifestation of caustics is known as 'random, uncorrelated motion' and is discussed in [80].) Since the timescale over which the particles retain a memory of their interactions with turbulence increases with increasing inertia, caustics become more prevalent as St increases.

One effect of caustics is to make the parallel and perpendicular relative velocity components nearly the same in the dissipation range, as can be seen in figure 4.12 for $St \gtrsim 0.3$. (Note that fluid particles do not experience caustics and have $2S_{2\parallel}^{p} = S_{2\perp}^{p}$ for $r/\eta \ll 1$ as a result of continuity (e.g., see [130]).) For $St \geq 10$,

the relative velocities are almost unaffected by the underlying turbulence in the dissipation range. As a result, the relative velocities are nearly independent of r/η in this range.

The effect of caustics can also be clearly seen in figure 4.14(a,b), where we plot the parallel relative velocities at a given separation as a function of St. From this figure, it is evident that the particle relative velocities at the smallest separation sharply increase as St exceeds about 0.2. The rapid increase in the particle relative velocities with St is consistent with the notion that caustics take an activated form [183] and that they are negligible below a critical value of St [144, 80]. Our data suggest a critical Stokes number for caustics of about 0.2 to 0.3, in agreement with [56] and [144]. The increase in the relative velocities occurs at higher values of St as the separation increases. In this case, the particles are subjected to larger-scale turbulence, and hence the particles must have more inertia for their motion to deviate significantly from that of the underlying flow.

We now examine the Reynolds-number dependence of the relative velocities, restricting our attention to the component parallel to the separation vector. The relative velocities of the largest particles ($St \gtrsim 10$) increase strongly with increasing R_λ in figure 4.14(a,b). There are two reasons for this trend. The first is that the effect of filtering on the larger turbulence scales decreases as R_λ is increased (see §4.4.2). The second is that u'/u_η increases with increasing R_λ, indicating that large-St particles in the dissipation range carry a memory of increasingly energetic turbulence (relative to the Kolmogorov scales) in their path history as R_λ is increased.

For smaller values of St ($St \leq 3$), the relative velocities in figure 4.14(a,b) are

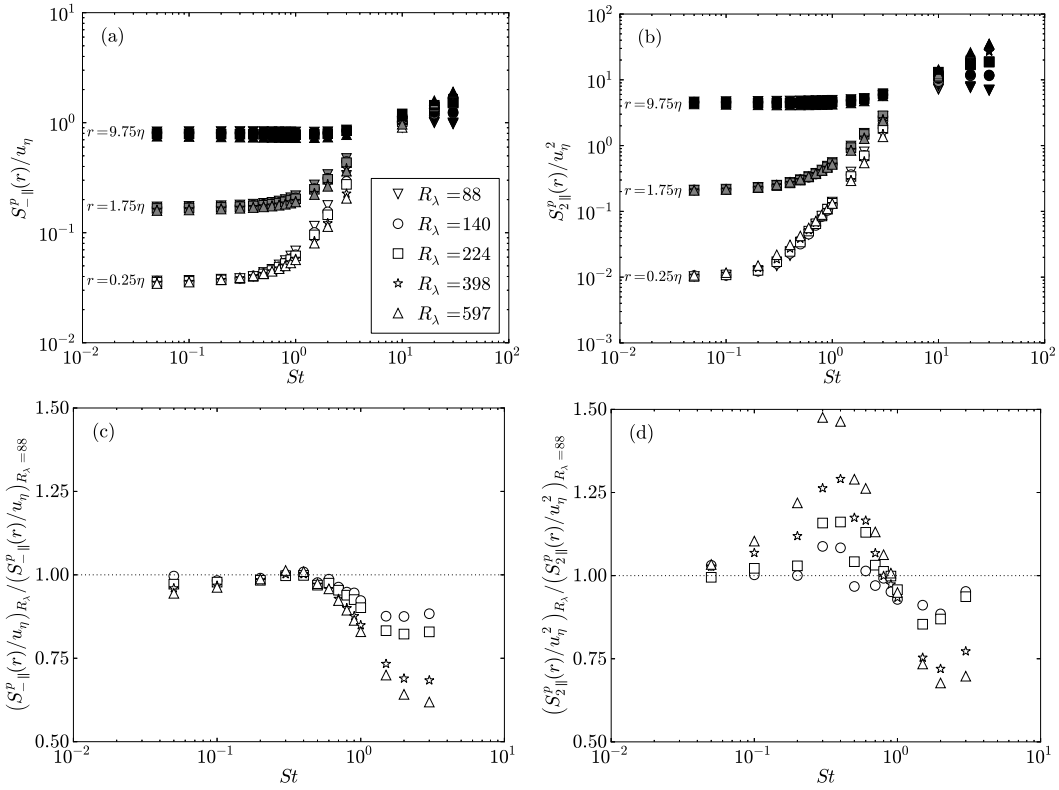

Figure 4.14: (a) The mean inward relative velocities and (b) the relative velocity variances, plotted as a function of St for small separations and different values of R_λ. Open symbols denote $r = 0.25\eta$, gray filled symbols denote $r = 1.75\eta$, and black filled symbols denote $r = 9.75\eta$. To emphasize any Reynolds-number dependencies for $St \leq 3$, we also plot (c,d) the ratio between the value of these quantities at a given Reynolds number to their value at $R_\lambda = 88$ at separation $r = 0.25\eta$.

only weakly dependent on R_λ, in agreement with previous DNS studies [178, 15, 141, 120, 121] and the model of [124]. To highlight any small Reynolds-number-effects in this range, we therefore divide the relative velocities at $r = 0.25\eta$ and a certain R_λ by their value at $R_\lambda = 88$ and plot the results in figure 4.14(c,d).

For $St \lesssim 1$, the relative velocity variances increase weakly with increasing R_λ (figure 4.14(d)). Since the dynamics of such particles are generally only affected by their memory of dissipation-range flow scales (e.g., see [136]), we do

not expect these trends with R_λ to be caused by the increase in u'/u_η described above. Instead, we expect that these larger relative velocities are due to the fact that the intermittency of the turbulence increases with increasing R_λ, which in turn slightly increases the particle relative velocity variances. We also note that this intermittency does not significantly alter the mean inward velocities (figure 4.14(c)), presumably because the mean inward velocity is a lower-order statistic that is less influenced by intermittent events.

For $1 \lesssim St \lesssim 3$, we also expect the increased intermittency of the turbulence to act to increase the relative velocities. However, we observe an overall *decrease* in the relative velocities here with increasing R_λ here, in agreement with [15, 141]. These reduced relative velocities are likely linked to the decrease in the Lagrangian rotation timescales $T^p_{\mathcal{R}\mathcal{R}}/\tau_\eta$ with increasing R_λ observed in §4.4.1. That is, as $T^p_{\mathcal{R}\mathcal{R}}/\tau_\eta$ decreases with increasing R_λ, the particles have a shorter memory of fluid velocity differences along their path histories, which in turn causes the relative velocities to decrease.

We now examine the behavior of the scaling exponents of $S^p_{-\parallel} \propto r^{\zeta^-_\parallel}$ and $S^p_{2\parallel} \propto r^{\zeta^2_\parallel}$ at small separations. (These scaling exponents will also be used in §4.5.2 to understand and predict the trends in the particle clustering.) We compute $\zeta^-_\parallel$ and $\zeta^2_\parallel$ using a linear least-squares regression for $0.75 \leq r/\eta \leq 2.75$ at different values of St and R_λ. Note that while using such a large range of r/η will necessarily introduce finite-separation effects, there is generally too much noise in the data to accurately compute the scaling exponents over smaller separations.

The scaling exponents are plotted in figure 4.15. We note that the scaling exponents are below those predicted by [94] (hereafter 'K41') for fluid ($St = 0$)

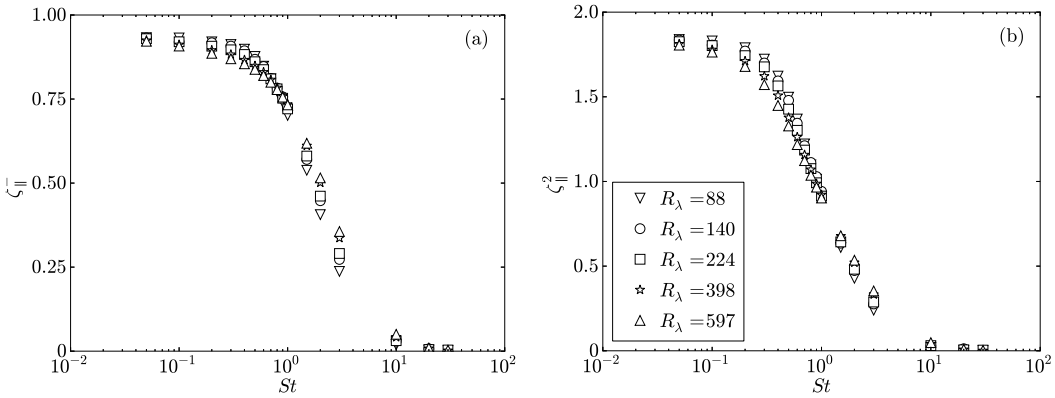

Figure 4.15: Dissipation-range scaling exponents for $S_{-\parallel}^{p}$ (a) and $S_{2\parallel}^{p}$ for various values of St and R_λ. The exponents are computed from linear least-squares regression for $0.75 \leq r/\eta \leq 2.75$.

particles ($\zeta_{\parallel}^{-} = 1$ and $\zeta_{\parallel}^{2} = 2$) and, like the relative velocities themselves, vary only slightly as R_λ changes.

For $St \geq 10$, the scaling exponents are about zero, indicating that the relative velocities are generally independent of r, as explained above. The scaling exponents for $1 \lesssim St \lesssim 3$ generally increase with increasing R_λ, since path-history interactions (which generally decrease the scaling exponents) become less important, as explained above. Finally, we note that $\zeta_{\parallel}^{2}$ decreases with increasing R_λ for $St \lesssim 1$, since intermittent path-history effects are expected to be more important here.

We next consider the PDFs of the relative velocities in the dissipation range. Figure 4.16 shows the PDFs for $0 \leq r/\eta \leq 2$ and $R_\lambda = 597$. In figure 4.16(a), we see that as St increases, the tails of the PDF of $w_{\parallel}^{p}/u_\eta$ become more pronounced, indicating that larger relative velocities become more frequent, in agreement with our observations above.

We show PDFs in standardized form in figure 4.16(b) to analyze the extent

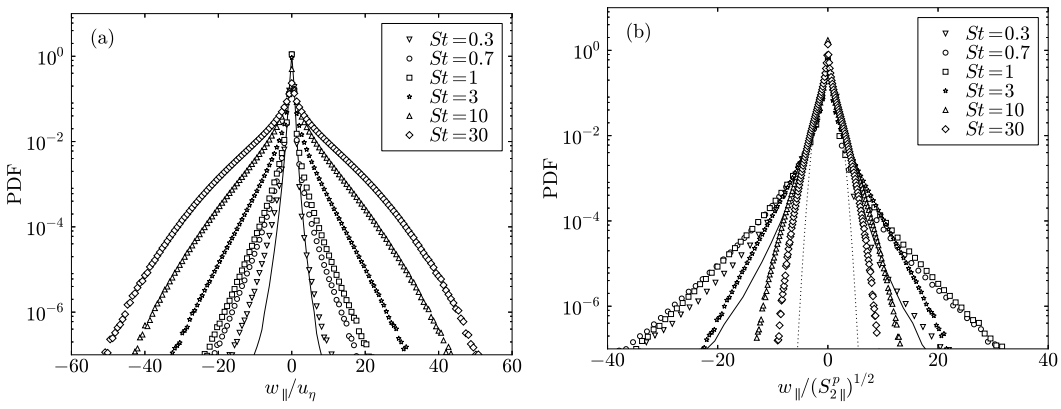

Figure 4.16: PDFs of the particle relative velocities $w_\parallel^p$ for separations $0 \leq r/\eta \leq 2$ and $R_\lambda = 597$. The relative velocities are normalized by both u_η (a) and $(S^p_{2\parallel})^{1/2}$ (b). The solid lines denote the relative velocity PDFs for $St = 0$ particles, and the dotted line in (b) indicates a standard normal distribution.

to which they deviate from that of a Gaussian distribution. It is evident that the degree of non-Gaussianity peaks for $St \sim 1$ and becomes smaller as St increases. The physical explanation for this intermittency at $St \sim 1$ is that the motion of these particles is affected by both the small-scale underlying turbulence and by the particles' memory of large-scale turbulent events in their path histories. This combination of contributions from both large- and small-scale events leads to strong intermittency. We also see that the underlying fluid is itself quite intermittent at this small separation, as expected (e.g., see [68]).

We now use three statistical measures to quantify the shape of the PDFs. The first is the ratio between the mean inward relative velocities and the standard deviation of the relative velocities, $S^p_{-\parallel}/(S^p_{2\parallel})^{1/2}$; the second is the skewness of the relative velocities, $S^p_{3\parallel}/(S^p_{2\parallel})^{3/2}$; and the third is the kurtosis of the relative velocities, $S^p_{4\parallel}/(S^p_{2\parallel})^2$. (Due to insufficient statistics, we will not consider data from these latter two quantities for $r/\eta < 1.75$.)

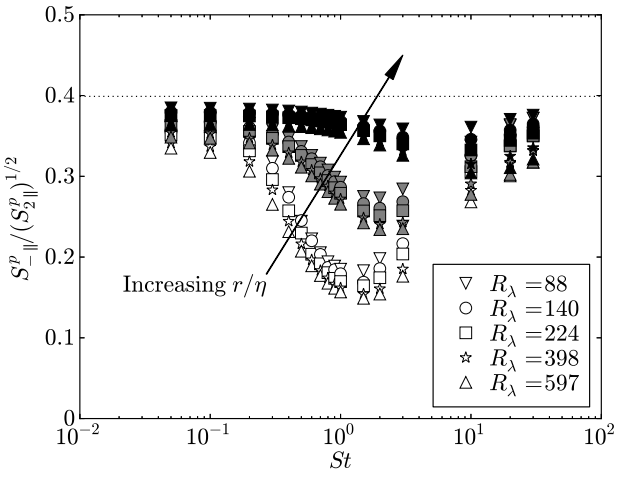

Figure 4.17: The ratio between mean inward relative velocities and the standard deviation of the relative velocities as a function of St for small separations and different values of R_λ. Open symbols denote $r = 0.25\eta$, gray filled symbols denote $r = 1.75\eta$, and black filled symbols denote $r = 9.75\eta$. The horizontal dotted line indicates that value of this quantity for a Gaussian distribution.

We show the ratio $S^p_{-\|}/(S^p_{2\|})^{1/2}$ in figure 4.17. One motivation for looking at this ratio is that existing theories (e.g., see [199, 124]) only predict the relative velocity variance, and by assuming the relative velocities have a Gaussian distribution, relate this variance to the mean inward relative velocity. For a Gaussian distribution, this ratio is approximately 0.4. At all values of St, R_λ, and r/η, our data indicate that the ratio is below 0.4 and thus that the particle relative velocities are intermittent (see also [178, 125]). The degree of intermittency peaks for order unity St, high R_λ, and small r/η, and using a Gaussian prediction in this regime would lead to predictions of the mean inward velocity which are in error by more than a factor of 2.

We next consider the skewness, $S^p_{3\|}/(S^p_{2\|})^{3/2}$, to provide information about the asymmetry of the relative velocities. Figure 4.18(a) indicates that the relative velocities are negatively skewed [178, 135]. This skewness is a result of

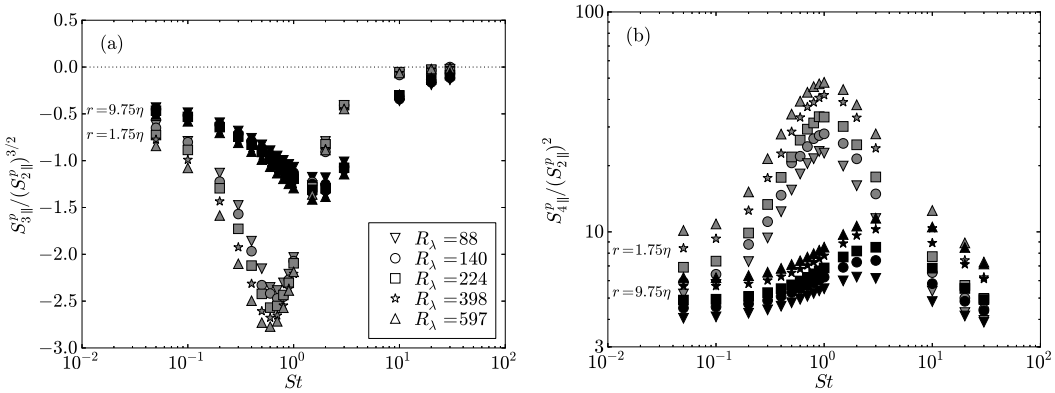

Figure 4.18: The (a) skewness and (b) kurtosis of the relative velocities as a function of St for separations in the dissipation range and different values of R_λ. Gray filled symbols denote $r = 1.75\eta$, and black filled symbols denote $r = 9.75\eta$.

two contributions. First, the velocity derivatives of the underlying turbulence are negatively skewed, a consequence of the energy cascade [164]. Second, additional skewness arises from the path-history effect described earlier (see also [25]). Figure 4.18(a) shows by implication that at $St \sim 1$ it is the latter effect that dominates the skewness behavior. At even larger values of St, the effect of both mechanisms decreases because, with increasing Stokes number, the particle velocity dynamics become increasingly decoupled from the small-scale fluid velocity field and their motion becomes increasingly ballistic in the dissipation range.

Finally, we consider the kurtosis of the relative velocities, $S^p_{4\|}/(S^p_{2\|})^2$, in figure 4.18(b) to quantify the contributions from intermittent events in the tails of the PDFs. The trends are similar to those in $S^p_{-\|}/(S^p_{2\|})^{1/2}$, as expected, indicating that contributions from intermittent events become strongest for intermediate St, the smallest separations, and the highest Reynolds numbers. In all cases, the kurtosis is above that for a Gaussian distribution ($S^p_{4\|}/(S^p_{2\|})^2 = 3$).

Inertial range relative velocity statistics

We finally consider the inertial-range statistics of the relative velocities. In figure 4.12, we see that the relative velocities in the inertial range generally decrease with increasing St. This implies that the filtering mechanism (which causes the velocities to decrease with increasing St) dominates the path-history mechanism (which causes the velocities to increase with increasing St), in contrast to their relative roles in the dissipation range. The role reversal occurs because the path-history effect weakens as the separation is increased, as explained in [25].

For $St \leq 10$, the relative velocity variances appear to scale with $r^{2/3}$, the same scaling predicted by K41 for $St = 0$ particles. However, we observe that at $St = 30$, no clear inertial-range scaling is present. The lack of inertial scaling suggests that these particles are affected by their memory of large-scale turbulence throughout the entire inertial range.

We now determine the scalings of the structure functions in the inertial range for $St \leq 10$ by computing the scaling exponents $\zeta_{\parallel}^{n}$ and $\zeta_{\perp}^{n}$. Following convention (e.g., see [87]), we consider the scaling exponents of the relative velocity magnitudes of $w_{\parallel}^{p}(t)$ and $w_{\perp}^{p}(t)$ here,

$$S^{p}_{|n|||}(r) = \left\langle \left| w_{\parallel}^{p}(t) \right|^{n} \right\rangle_{r} \propto r^{\zeta_{\parallel}^{n}} \tag{4.18}$$

and

$$S^{p}_{|n|||}(r) = \left\langle \left| w_{\perp}^{p}(t) \right|^{n} \right\rangle_{r} \propto r^{\zeta_{\perp}^{n}}. \tag{4.19}$$

According to K41, for $\eta \ll r \ll \ell$ and $St = 0$, $\zeta_{\parallel,\perp}^{n} = n/3$. It is well-known, however, that for fluid particles, the effect of intermittency leads to a nonlinear

relationship between $\zeta^n_{\parallel,\perp}$ and n (e.g., see [130]). Kolmogorov's refined similarity hypothesis ([95], hereafter 'K62') attempts to correct for the effect of intermittency, giving (for $St = 0$)

$$\zeta^n_{\parallel,\perp} = \frac{n}{3}\left[1 - \frac{\mu}{6}(n-3)\right], \tag{4.20}$$

where μ is typically taken to be 0.25 [130].

$\zeta^n_{\parallel,\perp}$ are shown in figure 4.19 at $R_\lambda = 88$ and $R_\lambda = 597$. For $R_\lambda = 88$, we have no clear inertial range and therefore used extended self-similarity ([18], hereafter 'ESS') to increase the scaling region for $\eta \ll r \ll \ell$. At $R_\lambda = 597$ we have nearly a decade of inertial range scaling ($50 \lesssim r/\eta \lesssim 500$), and thus we can compute the exponents directly over this range.

(To verify that any differences between the scaling exponents at $R_\lambda = 88$ and $R_\lambda = 597$ were in fact due to Reynolds-number effects and were not merely artifacts of ESS, we also computed the exponents for $R_\lambda = 597$ using ESS. Both methods of computing the exponents (directly and with ESS) gave similar results, with differences that were less than 8%, indicating the trends observed below are robust. We also note that while the inertial scaling region varies with St, we used the same fitting range for all values of St for consistency.)

For $St = 0$, Eq. (4.20) approximates the longitudinal scaling exponents excellently for $p \leq 8$ at $R_\lambda = 88$ (figure 4.19(a)), while it slightly under-predicts them at $R_\lambda = 597$ (figure 4.19(b)). By comparing figure 4.19(a) and figure 4.19(b), it is evident that $\zeta^n_\parallel$ increases with increasing R_λ. For $R_\lambda = 88$, the longitudinal scaling exponents decrease monotonically with increasing St, as was observed in [144]. However, for $R_\lambda = 597$, the exponents increase with St up to $St \approx 1$ before decreasing for higher values of St. The reason for these trends is unclear.

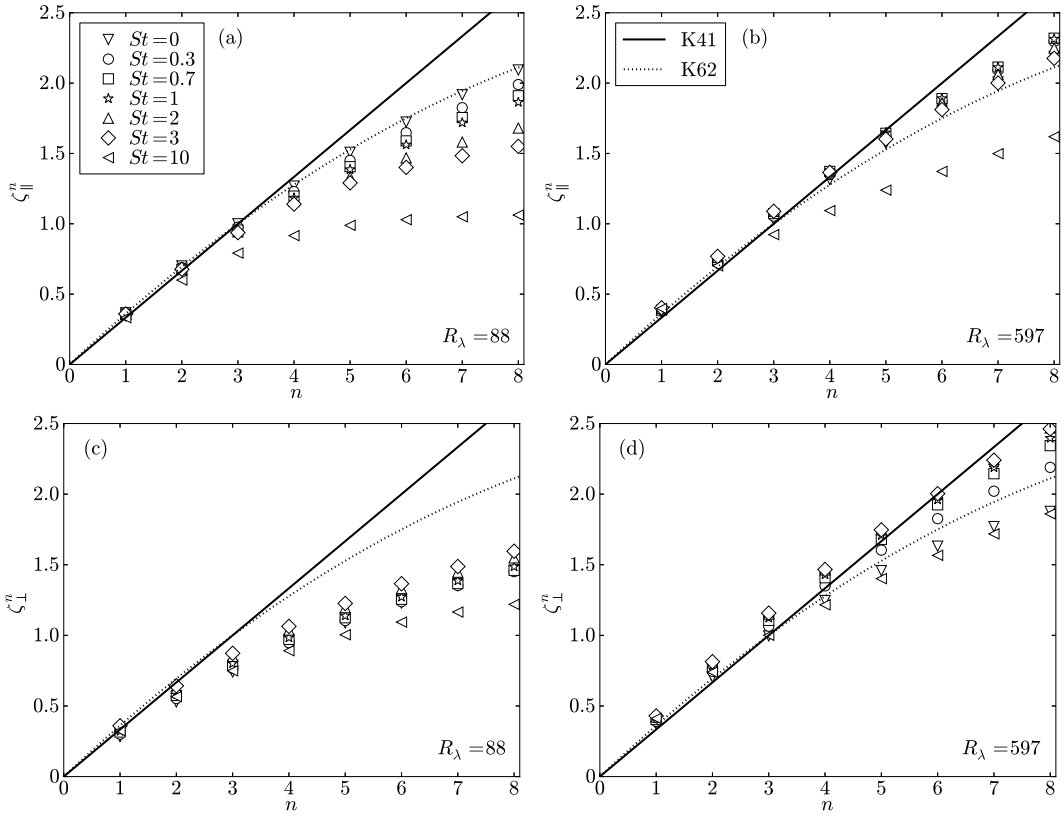

Figure 4.19: (a,b) Longitudinal and (c,d) transverse particle structure function scaling exponents in the inertial range for various values of St. (a,c) are for $R_\lambda = 88$, and (b,d) are for $R_\lambda = 597$. The exponents are computed from linear least-squares regression using ESS in (a,c) and directly in (b,d). The predicted scalings from from K41 and K62 (i.e., Eq (4.20) with $\mu = 0.25$) are indicated by the solid and dotted lines, respectively.

For most values of St, the transverse structure functions (figure 4.19(c,d)) are more intermittent than their longitudinal counterparts (figure 4.19(a,b)), in agreement with earlier observations (e.g., see [87]). The difference between the longitudinal and transverse structure functions seems to decrease as R_λ increases, however, suggesting that it may be a low-Reynolds-number artifact (see [92, 68, 150]).

4.5.2 Particle clustering

As discussed in §4.2, inertial particles form clusters when placed in a turbulent flow. We first consider a theoretical framework for understanding this clustering, and then analyze the clustering using DNS.

Theoretical framework for particle clustering

A variety of measures have been proposed to study particle clustering, including Voronoï diagrams [115], Lyapunov exponents [13], Minkowski functionals [31], and radial distribution functions (RDFs) [110]. The RDF has distinct advantages over these other methods. The RDF, unlike both Minkowski functionals [31] and Voronoï diagrams [163], is not biased by the number of particles simulated. Also, as [13] noted, the accurate computation of Lyapunov exponents is numerically unfeasible for high-Reynolds-number simulations, while computation of the RDF is relatively straightforward. Finally, the RDF, unlike the other measures, has a direct relevance to particle collisions, since it precisely corrects the collision kernel for particle clustering [161].

The RDF $g(r)$ is defined as the ratio of the number of particle pairs at a given separation r to the expected number of particle pairs in a uniformly distributed particle field,

$$g(r) \equiv \frac{N_i/V_i}{N/V}. \tag{4.21}$$

Here, N_i is the number of particle pairs that lie within a shell with an average radius r and a radial width Δr, V_i is the volume of the shell, and N is the total number of particle pairs located in the total volume V. An RDF of unity corresponds to uniformly distributed particles, while an RDF in excess of one

indicates a clustered particle field.

Based on the findings of [24] we use the model of [198] as a framework for understanding the physical mechanisms governing particle clustering. We will validate this model against DNS data in §4.5.2. In the following discussion, we non-dimensionalize all variables by Kolmogorov units and use $\hat{Y}$ to denote the non-dimensionalized form of a variable Y.

From [198], the equation describing $g(\hat{r})$ at steady-state for an isotropic system is

$$0 = -St\left(\hat{S}^{\,p}_{2\parallel} + \hat{\lambda}_{\parallel}\right)\nabla_{\hat{r}} g - St\, g\left(\nabla_{\hat{r}}\hat{S}^{\,p}_{2\parallel} + 2\hat{r}^{-1}\left[\hat{S}^{\,p}_{2\parallel} - \hat{S}^{\,p}_{2\perp}\right]\right), \tag{4.22}$$

where $\hat{\lambda}_{\parallel}$ is a diffusion coefficient describing the effect of the turbulence on the dispersion of the particle pairs (e.g., see [24]). We now consider Eq. (4.22) in the regimes of small St and large St in order to consider the effect of changes in R_λ within these regimes.

In the limit $St \ll 1$, Eq. (4.22) reduces to (see [24]),

$$0 = -15B_{nl}\hat{S}^{\,f}_{2\parallel}\nabla_{\hat{r}} g - \frac{St}{3}\hat{r} g\left(\langle\hat{\mathcal{S}}^2\rangle^p - \langle\hat{\mathcal{R}}^2\rangle^p\right), \tag{4.23}$$

where B_{nl} is a St-independent, non-local diffusion coefficient (see [32, 24]). The first term on the right-hand-side is associated with an outward particle diffusion which reduces clustering, while the second term on the right-hand-side is responsible for an inward particle drift which increases clustering.

$\hat{S}^{\,f}_{2\parallel}$ is independent of R_λ in the dissipation regime (based on our data and the findings in [68]), and so assuming that B_{nl} is also independent of R_λ, we expect the diffusion to be independent of R_λ. The drift is dependent on $\tau_\eta^2\langle\mathcal{S}^2\rangle^p - \tau_\eta^2\langle\mathcal{R}^2\rangle^p$ and we see from §4.4.1 that $\tau_\eta^2\langle\mathcal{S}^2\rangle^p - \tau_\eta^2\langle\mathcal{R}^2\rangle^p$ increases weakly with R_λ for $St \ll 1$.

We therefore expect the degree of clustering at low St to increase weakly as R_λ increases. We will test this expectation against DNS data in §4.5.2.

We next simplify Eq. (4.22) when St is large. As noted in §4.5.1, at sufficiently large St and small r/η, the relative particle velocities are dominated by caustics, and $S^p_{2\parallel} \approx S^p_{2\perp}$. Furthermore, $\lambda_\parallel \ll S^p_{2\parallel}$ in this regime (see [25]). Using these results we can simplify Eq. (4.22) in the dissipation range to the form,

$$0 \approx -St\hat{S}^p_{2\parallel}\nabla_{\hat{r}}g - Stg\nabla_{\hat{r}}\hat{S}^p_{2\parallel}. \tag{4.24}$$

The overall changes in the particle clustering at high St will therefore be determined by the extent to which the drift coefficient ($\nabla_{\hat{r}}\hat{S}^p_{2\parallel}$) and the diffusion coefficient ($\hat{S}^p_{2\parallel}$) are influenced by changes in R_λ. That is, if the ratio between the drift and diffusion coefficients increases (decreases) with increasing R_λ, the RDFs are expected to increase (decrease).

We therefore take the ratio between the drift and diffusion coefficients and obtain

$$\frac{\nabla_{\hat{r}}\hat{S}^p_{2\parallel}}{\hat{S}^p_{2\parallel}} = \frac{\zeta^2_\parallel}{\hat{r}}, \tag{4.25}$$

where $\zeta^2_\parallel$ is the scaling exponent of the longitudinal relative velocity variance. Eq. (4.25) implies that increases (decreases) in $\zeta^2_\parallel$ are fundamentally linked to increases (decreases) in the RDFs at high St. From §4.5.1, we see that $\zeta^2_\parallel$ increases with increasing R_λ for $1 \lesssim St \lesssim 3$, which suggests that $g(r/\eta)$ will increase with increasing R_λ here.

We also note that Eq. (4.24) is only applicable for high-St particles in the dissipation range, and is thus unable to predict the clustering for $St > 3$ particles, which is primarily dependent on inertial-range scales. We will examine the RDFs for $St > 3$ from DNS data below.

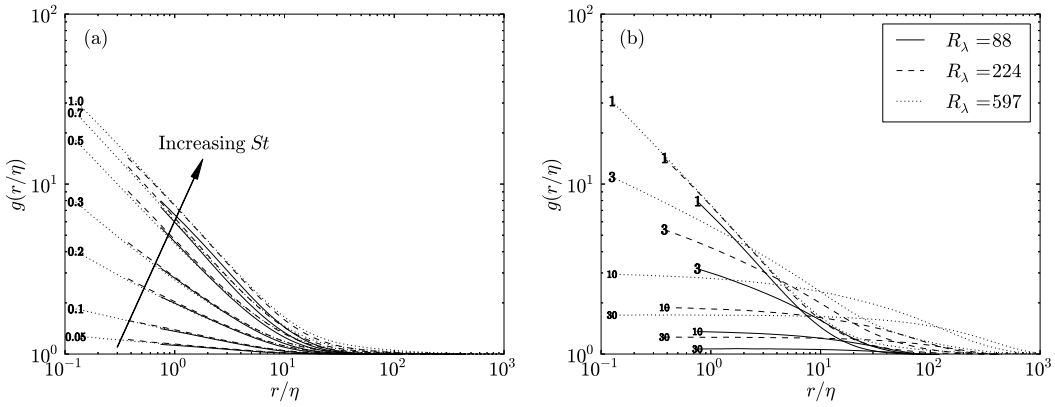

Figure 4.20: RDFs for (a) low-St particles and (b) high-St particles at three different values of R_λ, plotted as a function of the radial separation r/η. The Stokes numbers are indicated by the line labels.

In summary, at small St, clustering may increase with increasing R_λ depending upon whether B_{nl} varies with R_λ. At high St, the degree of clustering is determined by the influence of path-history effects on the scaling of the relative velocity variances, which in turn affects the relative strengths of the drift and diffusion mechanisms. Based on our relative velocity data in §4.5.1, we expect that clustering will increase with increasing R_λ here. We next consider DNS data to test these predictions.

Particle clustering results

In figure 4.20, we plot the RDFs for the different values of St considered at three different Reynolds numbers. Note that as the size of the simulation (and thus R_λ) increases, we are able to calculate $g(r/\eta)$ statistics accurately at progressively smaller values of r/η.

In agreement with past studies (e.g., see [175, 161, 9]), we see that particle

clustering peaks for $St \sim 1$ at all Reynolds numbers shown. Figure 4.20 also indicates that the largest particles ($St \geq 10$) exhibit clustering outside of the dissipation range of turbulence, and that the degree of clustering is independent of separation in the dissipation range. This is because large-St particles are unresponsive to the dissipative range scales and so move almost ballistically at these separations. The clustering that is observed for these particles is due almost entirely to eddies in the inertial range with timescales similar to the particle response time [67, 16]. If we make that assumption, along with the standard K41 approximations for the inertial range, we expect the clustering will depend only on ϵ and r, and will occur at lengthscales on the order of $\eta St^{3/2}$ [51, 16]. We test this in figure 4.21 by plotting the RDFs for $St = 20$ and $St = 30$ particles as a function of $r/\left(\eta St^{3/2}\right)$ at the three highest Reynolds numbers. (The two lower Reynolds numbers do not have a well-defined inertial range, as noted in §4.3.1, and hence the above argument would not hold.) We see that the RDFs decrease rapidly near $r/\left(\eta St^{3/2}\right) \sim 1$, suggesting that the particles are indeed clustering due to the influence of turbulent eddies in the inertial range with a timescale on the order of τ_p.

We now discuss how the RDFs change with the Reynolds number. In §4.5.2, we argued that $g(r/\eta)$ might increase weakly with R_λ for $St \ll 1$, since $\tau_\eta^2\langle\mathcal{S}^2\rangle^p - \tau_\eta^2\langle\mathcal{R}^2\rangle^p$ increases with R_λ in this limit. In figure 4.20(a), however, we observe that $g(r/\eta)$ is essentially independent of R_λ for $St \lesssim 1$, which implies that the non-local correction coefficient B_{nl} in Eq. (4.23) must increase weakly with R_λ in a compensating way. Several authors have also found the level of particle clustering to be independent of R_λ at small St (without gravity), including [34] (from data at $65 \leq R_\lambda \leq 152$), [14] ($65 \leq R_\lambda \leq 185$), [15] ($185 \leq R_\lambda \leq 400$), [135] ($95 \leq R_\lambda \leq 227$), and [141] ($28 \leq R_\lambda \leq 304$). Our data confirms this point up

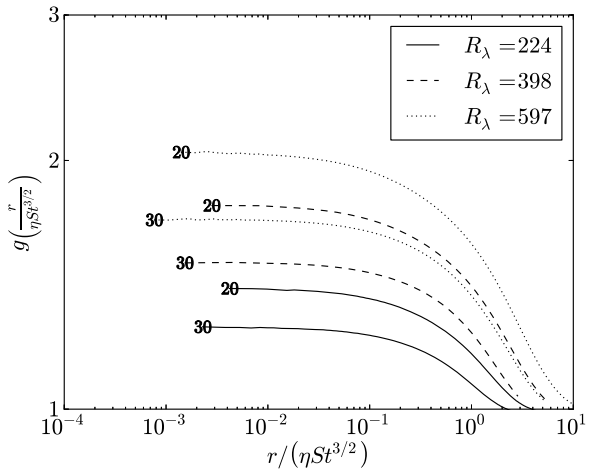

Figure 4.21: RDFs for $St = 20$ and $St = 30$ particles at the three highest values of R_λ. The separations are scaled by $\eta St^{3/2}$ to test for inertial range scaling. The Stokes numbers are indicated by the line labels.

to $R_\lambda = 597$. The fact that $g(r/\eta)$ is independent of R_λ for small Stokes numbers implies that the clustering mechanism is driven almost entirely by the small-scale turbulence, independent of any intermittency in the turbulence that occurs at higher Reynolds numbers. At higher values of St, the RDFs increase with increasing R_λ, in agreement with our expectations in §4.5.2.

We note, however, that two recent studies [120, 121] found that $g(r/\eta)$ decreases weakly with increasing R_λ over the range $81 \leq R_\lambda \leq 527$ at $St = 0.4$ and $St = 0.6$. Our results do not indicate such a trend, possibly because we are unable to analyze $g(r/\eta)$ at separations as low as those considered in [120] and [121]. It is also possible that the differences in the observed trends stem from differences in the underlying numerical methods, since [120] and [121] use a finite-difference method, while our study and most of the other literature use a pseudospectral method. In any case, the trends with R_λ at low St reported here, in [120] and [121], and in the rest of the literature are at most very weak.

It is important to note, however, that just because $g(r/\eta)$ is invariant with R_λ for low-St particles does not necessarily imply that higher-order moments of clustering are also independent of R_λ. For example, $g(r/\eta)$ is related to the variance of the particle density field [149]. Higher-order moments or PDFs of the particle density field (e.g., see [126]) could also be compared at different values of R_λ. However, we found that the number of particles in our simulations was insufficient to compute such statistics accurately at small separations. We would likely need about an order of magnitude more particles to test the Reynolds-number dependence of these higher-order clustering moments. Refer to [194] for a more complete discussion on the number of particles necessary for accurate higher-order clustering statistics.

Following [137], we fit the RDFs by a power law of the form

$$g(r/\eta) \approx c_0 \left(\frac{\eta}{r}\right)^{c_1}. \tag{4.26}$$

(Note that c_1 is related to the correlation dimension $\mathcal{D}_2$ [14] by the relation $c_1 = 3 - \mathcal{D}_2$.) This allows us to compare the DNS data to several theoretical predictions in figure 4.22. For each value of R_λ, we computed c_0 and c_1 by fitting $g(r/\eta)$ in the range $0.75 \leq r/\eta \leq 2.75$ using linear least-squares regression. For $St \geq 10$, we do not observe power-law scaling for the RDF, and thus no values of c_0 and c_1 are plotted here.

To verify the arguments presented above, we compare the DNS values of c_0 and c_1 to the predicted values from [198] at $R_\lambda = 597$. The comparisons are performed in two ways. In the first way (which we denote as 'ZT'), we use the model of [198] to compute the relative velocities, and then use these predicted relative velocities in Eq. (4.22) to solve for the RDFs. In this manner, we can test the quantitative predictions of the model when no additional inputs are used. In

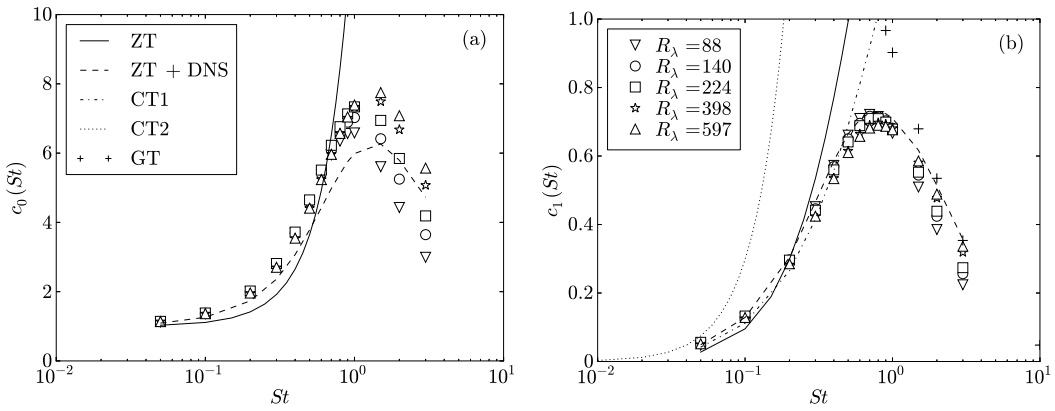

Figure 4.22: Power-law fits for $g(r/\eta)$ from Eq. (4.26). (a) shows the coefficient c_0, and (b) shows the exponent c_1. DNS data are shown with symbols, and the theoretical predictions from [198] ('ZT' and 'ZT + DNS'), [32] ('CT1' and 'CT2'), and [71] ('GT') at $R_\lambda = 597$ are shown with lines and plus signs. The details of each of the theoretical models are discussed in the text.

the second approach (which we denote as 'ZT + DNS'), we solve Eq. (4.22) with the particle velocities and the strain rate timescales along particle trajectories specified using DNS data. (The strain rate timescales are used in computing the dispersion tensor $\boldsymbol{\lambda}$. To maintain consistency in the model, we also adjusted the inertial range timescales through Eq. (18) in [196].) In both cases, we used the non-local diffusion correction discussed in [24], with $B_{nl} = 0.056$.

As expected, 'ZT' is only able to provide a reasonable prediction for c_0 and c_1 for $St \lesssim 0.3$. Above this point, inaccuracies in the predicted relative velocities lead to inaccurate clustering predictions, as discussed in [24]. However, 'ZT + DNS' predicts c_1 almost perfectly, with only slight discrepancies at $St \sim 1$, in agreement with the findings of [24] at a lower Reynolds number. We expect that these discrepancies are due to an additional drift term that was omitted in [198], as discussed in [24]. 'ZT + DNS' also provides reasonable predictions for c_0, though the agreement is not as good as that for c_1, possibly because c_0

is influenced by the inertial-range scales, which are generally more difficult to model. From these comparisons, we see that the model presented above is accurate, validating its use in interpreting the physical mechanisms responsible for particle clustering.

We next compare our results for c_1 against two relations derived in [32] in the limit of small St. The first (which we denote as 'CT1') uses DNS data for the strain and rotation rates sampled along inertial-particle trajectories to compute c_1, giving

$$c_1 = \frac{St\tau_\eta^2}{3B_{nl}}\left(\langle \mathcal{S}^2\rangle^p - \langle \mathcal{R}^2\rangle^p\right). \tag{4.27}$$

The second (which we denote as 'CT2') requires only DNS data for quantities sampled along fluid-particle trajectories and predicts,

$$\begin{aligned} c_1 = \frac{St^2}{12B_{nl}}\Big[&\frac{(\sigma^p_{\mathcal{S}^2})^2}{(\langle \mathcal{S}^2\rangle^p)^2}\frac{T^p_{\mathcal{S}^2\mathcal{S}^2}}{\tau_\eta} - \rho^p_{\mathcal{S}^2\mathcal{R}^2}\frac{\sigma^p_{\mathcal{S}^2}}{\langle \mathcal{S}^2\rangle^p}\frac{\sigma^p_{\mathcal{R}^2}}{\langle \mathcal{R}^2\rangle^p}\left(\frac{T^p_{\mathcal{S}^2\mathcal{R}^2}}{\tau_\eta} + \frac{T^p_{\mathcal{R}^2\mathcal{S}^2}}{\tau_\eta}\right) \\ &+ \frac{(\sigma^p_{\mathcal{R}^2})^2}{(\langle \mathcal{R}^2\rangle^p)^2}\frac{T^p_{\mathcal{R}^2\mathcal{R}^2}}{\tau_\eta}\Big]. \end{aligned} \tag{4.28}$$

'CT1' agrees well with the DNS up to $St \approx 0.5$, while 'CT2' only agrees well for $St = 0.05$, in agreement with [32, 24]. At higher values of St, both models from [32] over-predict c_1. As explained in [24], this over-prediction is because the theory of [32] fails to account for the contribution of the path-history effects on the drift and diffusion mechanisms that govern the clustering.

Finally, we compare our DNS values for c_1 against the theory from [71], here denoted as 'GT.' The theory in [71] predicts that in the limit of small r/η,

$$S^p_{n\|} \propto r^{c_1}, \tag{4.29}$$

for $n > c_1$. (Note that the predictions of [198] and [71] are equivalent when St is large, as explained in [24].) It therefore follows that for sufficiently small r/η,

$c_1 = \zeta_{\|}^2$, where $\zeta_{\|}^2$ is the scaling exponent of the relative velocity variance in the dissipation range, as computed in §4.5.1.

We include the prediction $c_1 = \zeta_2^{\|}$ in figure 4.22, and see that while 'GT' is in excellent agreement with the DNS for $St = 2, 3$, significant discrepancies exist at low St, as explained in [24].

4.5.3 Collision kernel

We now consider the kinematic collision kernel K for inertial particles, which has been shown to depend on both the radial distribution function and the radial relative velocities,

$$K(d) = 4\pi d^2 S^p_{-\|}(r = d) g(r = d), \tag{4.30}$$

where d is the particle diameter (see [161, 177]). While we simulate only point-particles (refer to §4.3.2), we compute d from St by assuming a given ρ_p/ρ_f. To study the dependence of $K(d)$ on ρ_p/ρ_f, we consider three different values for this parameter: 250, 1000, and 4000. (Note that for droplets in atmospheric clouds, $\rho_p/\rho_f \approx 1000$.)

In general, we do not have adequate statistics to calculate $g(r)$ or $S^p_{-\|}(r)$ at $r = d$ at low values of St ($St \leq 3$ for $\rho_p/\rho_f = 250$ and 1000, and $St \leq 10$ for $\rho_p/\rho_f = 4000$) and so we extrapolate from the power-law fits in §4.5.1 and §4.5.2 down to these separations, as was also done in [141]. For larger St ($St \geq 10$ for $\rho_p/\rho_f = 250$ and 1000, and $St \geq 20$ for $\rho_p/\rho_f = 4000$), the particle diameters are sufficiently large such that we can compute $g(d)$ and $S^p_{-\|}(d)$ by interpolating between data at smaller and larger separations.

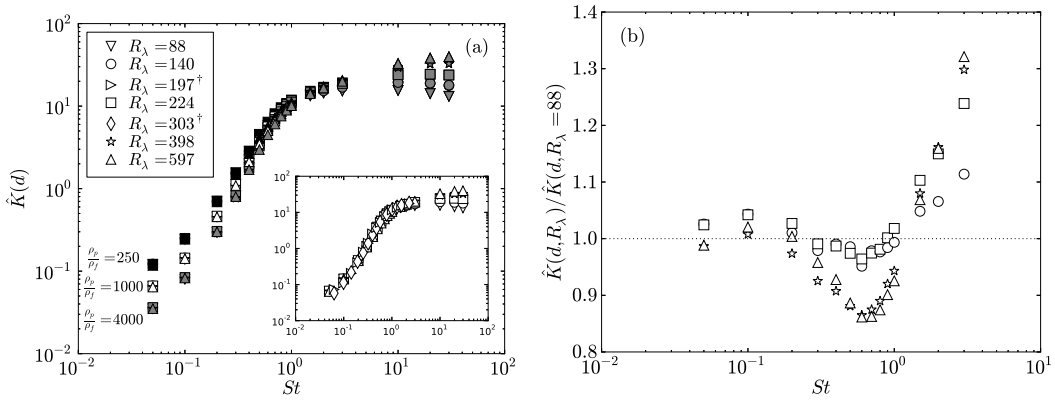

Figure 4.23: (a) The non-dimensional collision kernel $\hat{K}(d)$ as a function of St for different values of R_λ. Data are shown for $\rho_p/\rho_f = 250$ (filled black symbols), $\rho_p/\rho_f = 1000$ (open symbols), and $\rho_p/\rho_f = 4000$ (filled gray symbols). Legend entries marked with † indicate data taken from [141] (deterministic forcing scheme, no gravity) at $\rho_p/\rho_f = 1000$. These data are only included in the inset, where they are compared with our results at $\rho_p/\rho_f = 1000$. (b) The ratio between $\hat{K}(d)$ at a given value of R_λ to that at $R_\lambda = 88$, to highlight any Reynolds-number effects for $St \leq 3$. All data correspond to $\rho_p/\rho_f = 1000$.

Following [172], we compute the non-dimensional collision kernel $\hat{K}(d) \equiv K(d)/(d^2 u_\eta) = 4\pi g(d) S^p_{-\|}(d)/u_\eta$. Figure 4.23(a) shows $\hat{K}(d)$ for different values of ρ_p/ρ_f. Results from [141] (deterministic forcing scheme, no gravity, $\rho_p/\rho_f = 1000$) are included in the inset to Figure 4.23(a).

For $St \geq 10$, the collision kernels increase strongly with increasing R_λ, since both the relative velocities and the RDFs increase with R_λ here (see §4.5.1 and §4.5.2). $\hat{K}(d)$ is also independent of ρ_p/ρ_f here. The physical explanation is that while changes in ρ_p/ρ_f lead to changes d, $S^p_{-\|}(d)/u_\eta$ and $g(d)$ are largely independent of d here (see §4.5.1 and §4.5.2).

Such particles, however, are generally above the size range of droplets in atmospheric clouds (e.g., see [6]), and thus our primary focus is on the collision

rates of smaller ($St \lesssim 3$) particles. $\hat{K}(d)$ is independent of ρ_p/ρ_f for $1 \lesssim St \leq 3$, in agreement with the findings of [172]. In this case, while both $g(d)$ and $S^p_{-\|}/u_\eta$ are dependent on d, these two quantities have opposite scalings (see §4.5.2), causing their product to be independent of d (and thus of ρ_p/ρ_f).

For $St \lesssim 3$, our data show very little effect of R_λ on the collision rates, and are in good agreement with the collision statistics from [141] at $\rho_p/\rho_f = 1000$ (shown in the inset to figure 4.23(a)). However, since the Reynolds numbers in clouds ($R_\lambda \sim 10,000$) are at least an order of magnitude larger than those in the DNS, it is important to discern even weak trends in the collision kernel with the Reynolds number. We therefore plot the ratio of $\hat{K}(d)$ at a given Reynolds number to that at $R_\lambda = 88$ for $St \leq 3$ in figure 4.23(b).

At $St \lesssim 0.2$, the collision statistics are almost completely independent of R_λ, since both $S^p_{-\|}/u_\eta$ and g are independent of R_λ here (refer to §4.5.1 and §4.5.2). For larger St, the collision kernel very weakly decreases with increasing R_λ, since the mean inward relative velocities decrease with increasing R_λ here (see §4.5.1). Finally, for $1 < St \leq 3$, the collision kernel increases weakly as R_λ increases. In this case, the increase in the RDFs with increasing R_λ (§4.5.2) overwhelms the decrease in the relative velocities (§4.5.1), causing the collision kernel to increase weakly.

These findings suggest that lower-Reynolds-number studies may in fact capture the essential physics responsible for droplet collisions in highly turbulent clouds. However, the results must be interpreted with caution for two reasons. First, the collision rates at low and moderate St were computed by extrapolating power-law fits to very small separations, and it is not known if the functional form of the relative velocities and the RDFs remains the same at these separa-

tions. Second, even the highest Reynolds numbers in this study are still at least an order of magnitude smaller than those in atmospheric clouds. It is thus possible that the turbulence could exhibit different characteristics at much higher Reynolds numbers, or that the above trends in the Reynolds number, though weak, could lead to substantially different collision rates when R_λ is increased by another order of magnitude.

4.6 Conclusions

We have studied the effect of particle inertia and the flow Reynolds number on particle dynamics at the highest Reynolds number ($R_\lambda \approx 600$) and largest number of particles (~ 2.5 billion) to date. These simulations have provided new insights into both single- and two-particle statistics in homogeneous isotropic turbulence.

We first analyzed the statistics of individual inertial particles. At large St, the particle motions were seen to be influenced primarily by inertial filtering. The theoretical models of [2] and [197] were able to quantify the effect of filtering on kinetic energies and particle accelerations, respectively, in this limit, and provided us with a clear physical understanding of the effect of Reynolds number on these quantities.

In the opposite limit ($St \ll 1$), the particle motions were influenced primarily by preferential sampling, and we used the theoretical model of [32] to understand and predict the statistics here. For $St \ll 1$, the mean rotation rate sampled by the particles decreased with increasing St and R_λ, since intense rotation regions became more prevalent and more efficient at ejecting particles (see [34]).

As R_λ increased, intense rotation regions tended to occur together with intense strain regions in 'vortex sheets,' in agreement with [191], and particles were also ejected from these regions, decreasing the mean strain rate sampled by the particles. In agreement with [144], the particle kinetic energy increased with St for $St \ll 1$ due to biased sampling of the flow field. However, since ejections from vortex sheets tend to reduce the particle kinetic energy, this trend was reduced as the Reynolds number was increased. Fluid particle accelerations were seen to be extremely intermittent at high R_λ, and the trends in the acceleration variance were well-captured by the model of [147]. The particle acceleration variances decreased rapidly with increasing St, as inertial particles tended to be ejected from vortex tubes and vortex sheets, which were both characterized by very high fluid accelerations.

We then studied the relative velocity, clustering, and collision statistics of inertial particles. For $St \ll 1$, biased sampling led to an increase in the longitudinal relative velocities and to a decrease in the transverse relative velocities, and the relative velocities were generally independent of R_λ for $St \lesssim 0.1$. At higher values of St, the particle motions were influenced more by path-history interactions, leading to a sharp increase in the relative velocities with increasing St. While the mean inward relative velocities were generally independent of R_λ for $0.2 \lesssim St \lesssim 1$, the relative velocity variances increased weakly with increasing R_λ here, a trend we attributed to the increased intermittency of the turbulence at higher Reynolds numbers. For intermediate St ($1 \lesssim St \lesssim 3$), the relative velocities decreased with increasing R_λ, which we argued was related to the decrease in the Lagrangian rotation timescales with increasing R_λ. We observed that the relative velocities of particles with $St \gtrsim 10$ increased with increasing R_λ, since inertial filtering effects diminish and u'/u_η increases as the Reynolds number

increases.

We also analyzed the dissipation-range scaling exponents of the relative velocities, and found that particles with higher relative velocities generally had lower scaling exponents, since the particles were more influenced by path-history effects. Relative velocities in the dissipation range were seen to be strongly non-Gaussian, with the degree of non-Gaussianity being largest for $St \sim 1$, $r/\eta \to 0$, and high R_λ, suggesting that theories which assume a Gaussian distribution to relate the velocity variances to the mean inward velocities provide poor predictions for the mean inward relative velocities at particle contact. Higher-order inertial range structure functions were also examined and were observed to follow similar trends to those reported in [144].

We then used these trends in the relative velocities to predict the degree of clustering through the model of [198], and compared the results to DNS data. The trends in the RDFs at low St were tied to preferential sampling effects, which increased the inward particle drift, as was found in [32]. The RDFs were independent of R_λ here, in agreement with [34, 135, 141], suggesting that the non-local coefficient B_{nl} (see [32, 24]) must weakly increase as R_λ increases. (We were unable to test higher-order measures of clustering to determine if they were affected by changes in R_λ due to the limitations in the number of particles that could be simulated.)

At high St, the degree of clustering was tied to the influence of path-history effects on the particle drift and diffusion, as explained in [24]. By simplifying the model of [198] in this limit, we showed that changes in the scaling exponents of the relative velocity variances directly affected the drift and diffusion mechanisms, which in turn altered the clustering. The scaling exponents gen-

erally increased with increasing R_λ (suggesting that path-history effects became less important), which in turn led to increased levels of clustering. For $St \geq 10$ and $R_\lambda \geq 224$, particles were seen to cluster in the inertial range of turbulence, and the separation at which clustering decreased was predicted accurately by inertial-range scaling arguments.

For $St \lesssim 3$, the RDFs exhibited power-law scaling, consistent with [137]. The full model of [198] (without any inputs from the DNS) was able to predict the power-law coefficient c_0 and power-law exponent c_1 accurately only for $St \lesssim 0.4$ due to errors in the predicted relative velocities. However, when these relative velocities (and the associated Lagrangian timescales) were specified from the DNS, the model in [198] provided excellent predictions for c_1 and reasonable predictions for c_0, as was also found in [24] at a lower Reynolds number. We also tested the DNS against two model predictions from [32], one which required only fluid particle statistics from the DNS, and one which required strain and rotation statistics along particle trajectories. The former prediction was in acceptable agreement with the DNS only for $St = 0.05$, while the latter prediction was in good agreement up to $St \approx 0.5$, in agreement with [32, 24]. Finally, we found that the theory of [71] was able to predict c_1 well for $St = 2, 3$.

We used the relative velocity and RDF data to compute the kinematic collision kernel for inertial particles [161], and found that this quantity varied only slightly with Reynolds number (under 50% when R_λ changed by a factor of 7) for $0 \leq St \leq 3$. Our collision kernels were in good agreement with those computed by [141].

As mentioned in §4.2, one of the primary motivations for this study was to determine the extent to which turbulence-induced collisions are responsi-

ble to the rapid growth rate of droplets observed in warm, cumulus clouds. Our observations indicate that the collision rates of like particles are generally unaffected by changes in the Reynolds number, which suggests that relatively low-Reynolds-number simulations may allow us to study the essential physics of droplet collisions in highly turbulent atmospheric clouds. One promising avenue of future work would be to determine the droplet growth rates predicted by these collision kernels, either by solving an associated kinetic equation [187, 174] or by simulating the particle collision and coalescence process directly [138].

Finally, we note that it is unclear to what extent these conclusions would be altered if gravity were incorporated in the particle dynamics, since the introduction of gravity will likely cause particles to preferentially sample certain regions of the flow, and will alter the residence time of particles around certain flow features (e.g., see [175, 42, 66]). We will analyze the effect of gravity on inertial particle motion in turbulence in Part II [82].

Acknowledgments

The authors gratefully acknowledge Parvez Sukheswalla for helpful discussions regarding this work. This work was supported by the National Science Foundation through CBET grants 0756510 and 0967349, and through a graduate research fellowship awarded to PJI. Additional funding was provided by Cornell University. We would also like to acknowledge high-performance computing support from Yellowstone (ark:/85065/d7wd3xhc) provided by NCAR's Computational and Information Systems Laboratory through grants ACOR0001 and

P35091057, sponsored by the National Science Foundation.

CHAPTER 5

THE EFFECT OF REYNOLDS NUMBER ON INERTIAL PARTICLE DYNAMICS IN ISOTROPIC TURBULENCE. PART II: SIMULATIONS WITH GRAVITATIONAL EFFECTS.†

5.1 Abstract

In Part I [81], we analyzed the motion of inertial particles in isotropic turbulence in the absence of gravity using direct numerical simulations (DNSs). Here, in Part II, we introduce gravity and study its effect of single-particle and particle-pair dynamics over a wide range of flow Reynolds numbers. We find that the dynamics of heavy particles falling under gravity can be artificially influenced by the finite domain size and the periodic boundary conditions, and we therefore perform our simulations on larger domains to reduce these effects. We see that gravity causes particles to sample the flow more uniformly and reduces the time particles can spend interacting with the underlying flow. These reduced interaction times tend to reduce the particle kinetic energies, and the model of [176] is able to accurately capture the trends with Reynolds number, particle inertia, and gravity in the strong gravity/weak turbulence limit. We also find that gravity tends to increase inertial particle accelerations and introduce a model to understand and predict these changes.

† P. J. Ireland, A. D. Bragg, and L. R. Collins. The effect of Reynolds number on inertial particle dynamics in isotropic turbulence. Part II: Simulations with gravitational effects. 2014. In preparation.

We then analyze the particle relative velocities and radial distribution functions (RDFs), which are generally seen to be independent of Reynolds number for low and moderate Kolmogorov-scale Stokes numbers St. We see that gravity causes particle relative velocities in the dissipation range to decrease by reducing the degree of preferential sampling and the importance of path-history interactions, and that the relative velocities have higher scaling exponents in both the dissipation and inertial ranges with gravity. We observe that gravity has a non-trivial effect on clustering, acting to decrease clustering at low St and to increase clustering at high St. By considering the effect of gravity on the clustering mechanisms described in the theory of [198], we provide an explanation for this non-trivial effect of gravity. We also show using DNS data that an extension of the theory of [198] which accounts for gravity is able to predict the quantitative effects of gravity on clustering, validating our proposed explanations. The relative velocities and RDFs exhibit considerable anisotropy at small separations, and this anisotropy is quantified using spherical harmonic decomposition. We use the relative velocities and the RDFs to compute the particle collision kernels, and find that the collision kernels are generally independent of Reynolds number for low and moderate St. We conclude by discussing practical implications of the results for the cloud physics and turbulence communities and suggesting possible avenues for future research.

5.2 Introduction

This is the second part of a two-part paper in which we consider the Reynolds-number dependence of inertial particle statistics using direct numerical simulations (DNSs). In Part I of this study [81], we used high-Reynolds-number

DNSs to explore the motion of inertial particles in the absence of gravity. We saw that particles with weak inertia congregated in certain regions of the turbulence (a phenomenon known as 'preferential sampling,' see [106, 159, 48]). By exploring the specific regions of the flow contributing to this preferential sampling and using the theory in [32], we were able to understand and model the resulting trends. Particles with strong inertia had a modulated response to the underlying turbulence (a phenomenon known as 'inertial filtering'), decreasing the particle kinetic energies and accelerations, and we found our DNS data for these quantities to be in excellent agreement the model predictions of [2] and [197]. Such particles also exhibited increased relative velocities and 'caustics' [182, 183], which occur as a result of the particles' memory of their path-history interactions with the turbulence.

A primary goal of our analysis in Part I was to determine the effect of Reynolds number on particle collision rates. It is well-known that that droplet growth and precipitation in warm, cumulus clouds occurs faster than current microphysical models can predict, and the discrepancies are generally linked to turbulent effects (see [148, 45, 69]). We explored droplet motions in turbulence at the highest Reynolds numbers to date, and used the results to extrapolate to Reynolds numbers representative of those in atmospheric clouds. A secondary motivation to understand the extent to which protoplanetary nebulae formation (which depends on the collision and coalescence of small dust grains) is affected by turbulence. (A more complete explanation of the physical processes involved in cloud and protoplanetary nebulae formation is provided in Part I.)

To determine the collision rates, we computed particle radial distributions and relative velocities and used the theory of [161] to calculate the kinematic

collision kernel from these quantities. We observed that the collision rates of weakly inertial particles (such as those that would be present in the early stage of cloud formation) are almost entirely insensitive to the flow Reynolds number. This suggests that particle collisions are determined by the small-scale turbulence, and that DNS at low Reynolds numbers is able to capture the essential physics responsible for particle collisions in highly turbulent clouds.

One major simplification in Part I, however, was the neglect of gravitational forces on the particles, which (1) allowed us to clearly discern the effect of inertia on particle motions, (2) reduced the parameter space we must consider, (3) ensured that the particle phase was isotropic, and (4) limited artificial periodicity effects associated with the finite domain sizes. However, as noted in Part I, gravity is not negligible for many particle-laden environmental flows. For example, in warm cumulus clouds, the gravitational settling speeds of droplets may be an order of magnitude larger than the Kolmogorov velocity, suggesting that such droplets fall quickly through the turbulence and may therefore have a substantially modified response to the underlying flow [6]. Therefore, in Part II of our study, we systematically explore the effect of gravity on inertial particle statistics. To do so, we must consider how gravity introduces additional complexity to our analysis, in particular with regard to the four points listed above.

First, when gravitational forces are present, it becomes difficult to decouple the effects of inertia and gravity on particle motion. We must therefore repeatedly compare our data with gravity to comparable data from Part I without gravity, noting and explaining any changes in the results.

Second, the addition of gravity extends the dimensionality of the param-

eter space we must consider. In Part I, where gravity was ignored, we were able to consider only the effect of the Taylor-scale Reynolds number R_λ and the small-scale Stokes number St on the particle statistics. However, here in Part II, we must introduce an additional non-dimensional parameter to account for the gravitational acceleration. One way to do so is through a Froude number Fr, which compares the turbulent Kolmogorov acceleration to the gravitational acceleration (e.g., see [17]). Even for terrestrial atmospheric clouds (in which the gravitational acceleration may be regarded as fixed) the turbulent acceleration may vary by orders of magnitude (see [134]), leading to significant variations in Fr. To properly understand the role of gravity, therefore, we must consider particle statistics over a wide range of St, R_λ, and Fr.

Third, gravity may cause the particle distributions and motions to become anisotropic, even if the underlying turbulence is itself isotropic [6, 185, 17, 73]. This is because gravity acts along a given direction, reducing the symmetry of the particle phase from isotropic to axisymmetric. We now must consider how single-particle motions vary based on their direction relative to gravity, and also how particle-pair dynamics depend on the orientation of the particle separation vector relative to the direction of gravity.

Fourth, when gravity is strong, a particle may traverse the length of the domain more rapidly than the flow field decorrelates temporally. With periodic boundary conditions, a particle may encounter the same turbulence multiple times, artificially affecting its motion [185]. The domain size must be increased to prevent this from occurring, and thus larger simulations and more computational resources are needed.

Previous DNSs of inertial particles subjected to gravity have primarily fo-

cused on how turbulence alters particle settling velocities [175, 188, 190, 83, 17, 66] and collision rates [59, 6, 185, 119, 141, 17]. Our work here extends the knowledge gained from these studies by performing simulations on larger domains, over a wider-Reynolds-number range, and with more particle classes. We also consider the effect of gravity on additional particle statistics (such as velocity gradients, Lagrangian timescales, and accelerations), and specifically address the influence of anisotropy on these and other statistics. To understand the trends in many of these statistics, we introduce theoretical models and compare these models with the DNS data.

The organization of this paper is similar to that of Part I. In §5.3, we discuss the numerical methods and parameters for our simulations. Single-particle statistics are presented in §5.4, and particle-pair statistics in §5.5. We conclude in §5.6 by summarizing our findings and suggesting some practical implications for the cloud physics and turbulence communities.

5.3 Overview of simulations

5.3.1 Fluid phase

As in Part I, the flow fields here are from pseudospectral DNSs of isotropic turbulence on cubic, tri-periodic domains of length $\mathcal{L}$ with N^3 grid points, subject to the continuity and momentum equations for an incompressible flow,

$$\nabla \cdot \boldsymbol{u} = 0, \tag{5.1}$$

$$\frac{\partial \boldsymbol{u}}{\partial t} + \boldsymbol{\omega} \times \boldsymbol{u} + \nabla \left(\frac{p}{\rho_f} + \frac{u^2}{2} \right) = \nu \nabla^2 \boldsymbol{u} + \boldsymbol{f}, \tag{5.2}$$

where $\boldsymbol{u}$ is the fluid velocity, $\boldsymbol{\omega} \equiv \nabla \times \boldsymbol{u}$ is the vorticity, p is the pressure, ρ_f is the fluid density, ν is the kinematic viscosity, and $\boldsymbol{f}$ is a large-scale forcing term that is added to make the flow field statistically stationary. In these simulations, deterministic forcing is applied to wavenumbers with magnitude $\kappa = \sqrt{2}$. More details of the numerical methods are given in [84].

In Part I, $\mathcal{L} = 2\pi$ for all the simulations performed. To reduce artificial periodicity effects in these simulations with gravity, the domain lengths are here extended to $\mathcal{L} = 16\pi$ (for $R_\lambda = 90$), $\mathcal{L} = 8\pi$ (for $R_\lambda = 147$), and $\mathcal{L} = 4\pi$ (for $R_\lambda = 230$). ($R_\lambda \equiv 2k\sqrt{5/(3\nu\epsilon)}$ denotes the Taylor-scale Reynolds number, where k is the kinetic energy and ϵ is the turbulent energy dissipation rate.) The grid spacing is kept the same as the domain size is increased, and so the small-scale resolution $\kappa_{\max}\eta$ is approximately constant between the different domain sizes (where $\kappa_{\max}$ is the maximum resolved wavenumber and $\eta \equiv (\nu^3/\epsilon)^{1/4}$ is the Kolmogorov length scale). In increasing the domain size, we also keep the viscosity and forcing parameters the same, and thus both small-scale and large-scale flow parameters are held approximately constant. At the two highest Reynolds numbers, we expect periodicity effects to be minimal, and the domain sizes are the same ($\mathcal{L} = 2\pi$) both with and without gravity. Refer to Appendix A for a detailed examination of the effect of the domain size on fluid and particle statistics.

The simulation parameters are given in table 5.1. In all cases, the parameters are very close to those given in Part I, and based on the results in Appendix A, we can safely assume (with the exception of the acceleration kurtosis statistics–see §5.4.3) that the differences in the particle statistics between these simulations and those in Part I are due entirely to gravitational effects and not to any differences in the underlying flow. For simplicity, we will refer to all fields (both with

Table 5.1: Simulation parameters for the DNS study. All dimensional parameters are in arbitrary units, and all quantities are defined in the text in §5.3.1 and §5.3.2.

Simulation	I	II	III	IV	V	IIIb
R_λ	90	147	230	398	597	227
$\mathcal{L}$	16π	8π	4π	2π	2π	2π
ν	0.005	0.002	0.0008289	0.0003	0.00013	0.0008289
ϵ	0.257	0.244	0.239	0.223	0.228	0.246
ℓ	1.47	1.44	1.49	1.45	1.43	1.43
ℓ/η	55.6	107	213	436	812	206
u'	0.912	0.914	0.914	0.915	0.915	0.915
u'/u_η	4.82	6.15	7.70	10.1	12.4	7.65
$\kappa_{\max}\eta$	1.61	1.63	1.68	1.60	1.70	1.67
N	1024	1024	1024	1024	2048	512

and without gravity) by nominal Reynolds numbers which correspond to those in table 5.1. The Reynolds numbers for the simulations in Part I are within 5% of these values in all cases.

To perform a more complete parametric study of the effects of inertia and gravity on particle statistics, we also conducted a simulation with similar flow parameters to simulation III, but with a smaller domain size (due to computational limitations). The parameters for this simulation (referred to as IIIb) are also given in table 5.1.

5.3.2 Particle phase

We simulate the motion of spherical particles with finite inertia and gravitational forces. The magnitude of a particle's inertia is expressed as a non-dimensional Stokes number $St \equiv \tau_p/\tau_\eta$, where $\tau_p \equiv \rho_p d^2/\left(18\rho_f \nu\right)$ is the response time of the particle, and the Kolmogorov timescale $\tau_\eta \equiv (\nu/\epsilon)^{1/2}$.

The gravitational forces on a particle can be parameterized in a number of different ways (e.g., see [66]), with the two most commonly used non-dimensional parameters being the Froude number $Fr \equiv u_\eta/(\mathfrak{g}\tau_\eta)$ (which compares the Kolmogorov-scale turbulent acceleration u_η/τ_η to the gravitational acceleration $\mathfrak{g}$) and the settling parameter $Sv \equiv \tau_p \mathfrak{g}/u_\eta$ (which compares a particle's settling velocity $\tau_p \mathfrak{g}$ to the Kolmogorov velocity of the turbulence $u_\eta \equiv (\nu\epsilon)^{1/4}$). Note that these two non-dimensional parameters can be related through the Stokes number, $Fr = St/Sv$, and that the Froude number Fr is independent of τ_p.

Since a primary aim of this paper is to study the effect of gravity at conditions representative of those in cumulus clouds, we calculate Fr and Sv by assuming a dissipation rate $\epsilon = 10^{-2}$ m^2/s^3 [148], a kinematic viscosity $\nu = 1.5\times10^{-5}$ m^2/s, and a gravitational acceleration $\mathfrak{g} = 9.8$ m/s^2. This gives us $Fr = 0.052$ or $Sv = 19.3St$. Simulations I, II, III, and IV were therefore run with particles with $0 \leq St \leq 3$ and $Fr = 0.052$. Due to computational limitations, simulation V was only run with $0 \leq St \leq 0.3$ and $Fr = 0.052$.

However, while the gravitational parameters were selected to be representative of those in a cumulus cloud, experimental observations have suggested that cloud dissipation rates can vary by orders of magnitude (e.g., see [134]),

resulting in large variations in Fr and Sv. For example, a strongly turbulent cumulonimbus cloud with $\epsilon \sim 10^{-1}$ m^2/s^3 will give $Fr \approx 0.3$ and $Sv \approx 3.4St$, while a weakly turbulent stratiform cloud with $\epsilon \sim 10^{-3}$ m^2/s^3 will yield $Fr \approx 0.01$ and $Sv \approx 100St$ [129]. To study a larger St-Sv parameter space, therefore, we analyzed 513 different combinations of St and Sv in simulation IIIb, with $0 \leq St \leq 56.2$ and $0 \leq Sv \leq 100$. The results from this simulation will be used to study detailed trends in particle accelerations, clustering, relative velocities, and collision rates for different values of particle inertia and gravity. (The trends in the particle kinetic energies and settling velocities obtained from this data set are discussed in detail in [66].)

To model the dynamics of inertial particles, we make the following simplifying assumptions. The particles are assumed to be small ($d/\eta \ll 1$, where d is the particle diameter) and dense ($\rho_p/\rho_f \gg 1$, where ρ_p is the particle density), and subject to only linear drag forces. The last assumption is reasonable when the particle Reynolds number $Re_p \equiv |\boldsymbol{u}(\boldsymbol{x}^p(t),t) - \boldsymbol{v}^p(t)|/\nu < 0.5$ [49]. ($\boldsymbol{u}(\boldsymbol{x}^p(t),t) = \boldsymbol{u}^p(t)$ denotes the undisturbed fluid velocity at the center of the particle at position $\boldsymbol{x}^p$, and $\boldsymbol{v}^p$ denotes the velocity of the particle. As in Part I, we will use the superscript p on $\boldsymbol{x}$, $\boldsymbol{u}$, and $\boldsymbol{v}$ to denote time-dependent, Lagrangian variables defined along particle trajectories. Phase-space positions and velocities will be denoted without the superscript p.) While the linear drag model clearly breaks down for particles with large slip velocities (as would be the case for strong inertia or gravitational acceleration), the study of [66] suggests that existing nonlinear drag models provide only a poor approximation to the complex effects of drag on large, heavy particles. We have therefore restricted our attention to the case of linear drag, with the understanding that the results are likely in quantitative error when inertia and gravity are strong.

Under these assumptions, the governing equations for the inertial particles are [109],

$$\frac{d^2\boldsymbol{x}^p}{dt^2} = \frac{d\boldsymbol{v}^p}{dt} = \frac{\boldsymbol{u}\left(\boldsymbol{x}^p(t),t\right) - \boldsymbol{v}^p(t)}{\tau_p} + \mathfrak{g}, \tag{5.3}$$

where $\mathfrak{g} = (0, 0, -\mathrm{g})$ is the gravitational acceleration vector. To compute $\boldsymbol{u}(\boldsymbol{x}^p(t), t)$, we employ an eight-point B-spline interpolation from the Eulerian grid [169].

As in Part I, we began computing particle statistics once the particle distributions and velocities became statistically stationary and independent of their initial condition. For a subset N_{tracked} of the total number of particles in each class N_p, we stored particle positions, velocities, and velocity gradients every $0.1\tau_\eta$ for a duration of about $100\tau_\eta$. These data are used to compute Lagrangian correlations, accelerations, and timescales. Due to limitations in the available hard-disk space, these statistics were only stored for particles with $0 \leq St \leq 3$ and $Fr = 0.052$.

5.4 Single-particle statistics

As in Part I, we first study the statistics of individual inertial particles. We present small-scale velocity gradient statistics in §5.4.1, large-scale velocity statistics in §5.4.2, and acceleration statistics in §5.4.3.

5.4.1 Velocity gradient statistics

We denote the velocity gradients sampled by inertial particles as $\boldsymbol{A}(\boldsymbol{x}^p(t), t) \equiv \nabla \boldsymbol{u}(\boldsymbol{x}^p(t), t)$. We first consider the diagonal components of $\boldsymbol{A}$. In isotropic turbulence without gravity, these components are statistically equivalent, and for particles which uniformly sample the flow, their variances are given by $\langle [A_{11}(\boldsymbol{x}^p(t), t)]^2 \rangle = \langle [A_{22}(\boldsymbol{x}^p(t), t)]^2 \rangle = \langle [A_{33}(\boldsymbol{x}^p(t), t)]^2 \rangle = 1/(15\tau_\eta^2)$.

We expect that with the introduction of gravity, however, the particle phase will be anisotropic, and thus these components may no longer be statistically equivalent. Since gravity is applied along the x_3-direction, we expect that the statistics along this direction will differ from those in the x_1- and x_2-directions, and that the particle statistics along the x_1- and x_2-directions will be equivalent. For the remainder of the paper, the x_3-direction will be denoted as the vertical direction. The x_1- and x_2-directions will hereafter be referred to as the horizontal directions, and data along these two directions will be averaged together whenever possible and denoted with the subscript '1.'

We first consider vertical longitudinal velocity gradients (A_{33}) and horizontal longitudinal velocity gradients (A_{11}). We plot the variance of $A_{11}(\boldsymbol{x}^p(t), t)$ and $A_{33}(\boldsymbol{x}^p(t), t)$ in figure 5.1 at different values of R_λ, both with gravity ($Fr = 0.052$) and without gravity ($Fr = \infty$). Without gravity, the velocity gradients decrease with increasing St for $St \lesssim 0.3$. This is closely related to the trend in the strain rates observed in Part I, which was attributed to the fact that inertia causes particles to be ejected from vortex sheets. With gravity, the velocity gradients in the horizontal direction also decrease with increasing St for $St \lesssim 0.3$, as seen in figure 5.1(b). In addition, they are quite close to the corresponding values without gravity here, suggesting that gravity does not lead to significant changes in pref-

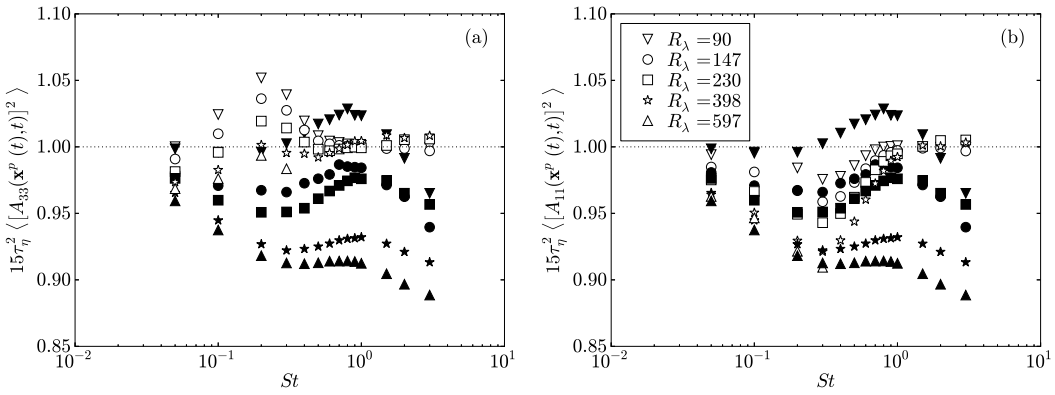

Figure 5.1: The normalized variance of the longitudinal velocity gradients sampled by inertial particles for different values of R_λ and St. Open symbols denote data with gravity (Fr = 0.052), and filled symbols denote data without gravity. The horizontal dotted line indicates the expected value for uniformly distributed particles in isotropic turbulence. The gradients in the vertical and horizontal directions are shown in (a) and (b), respectively.

erential sampling in the horizontal direction at low St. We see in figure 5.1(a), however, that gravity causes low-St particles to sample regions of larger vertical velocity gradients, and that these gradients are considerably different from those when gravity is absent. These results suggest that gravity has a stronger effect on the degree of preferential sampling in the vertical direction. Finally, we observe that gravity also tends to reduce the degree of preferential sampling at high St, causing the gradients to approach the values predicted for uniformly distributed particles in isotropic turbulence when $St \gtrsim 1$.

To further study the degree of preferential sampling, we decompose $\boldsymbol{A}(\boldsymbol{x}^p(t),t)$ into a symmetric strain rate tensor $\boldsymbol{\mathcal{S}}(\boldsymbol{x}^p(t),t) \equiv [\boldsymbol{A}(\boldsymbol{x}^p(t),t) + \boldsymbol{A}^\intercal(\boldsymbol{x}^p(t),t)]/2$ and an anti-symmetric rotation rate tensor $\boldsymbol{\mathcal{R}}(\boldsymbol{x}^p(t),t) \equiv [\boldsymbol{A}(\boldsymbol{x}^p(t),t) - \boldsymbol{A}^\intercal(\boldsymbol{x}^p(t),t)]/2$. We denote the average of the second invariants of the strain and rotation rates sampled by the particles as $\langle \mathcal{S}^2 \rangle^p \equiv \langle \boldsymbol{\mathcal{S}}(\boldsymbol{x}^p(t),t) : \boldsymbol{\mathcal{S}}^\intercal(\boldsymbol{x}^p(t),t) \rangle$ and $\langle \mathcal{R}^2 \rangle^p \equiv \langle \boldsymbol{\mathcal{R}}(\boldsymbol{x}^p(t),t) : \boldsymbol{\mathcal{R}}^\intercal(\boldsymbol{x}^p(t),t) \rangle$, respectively.

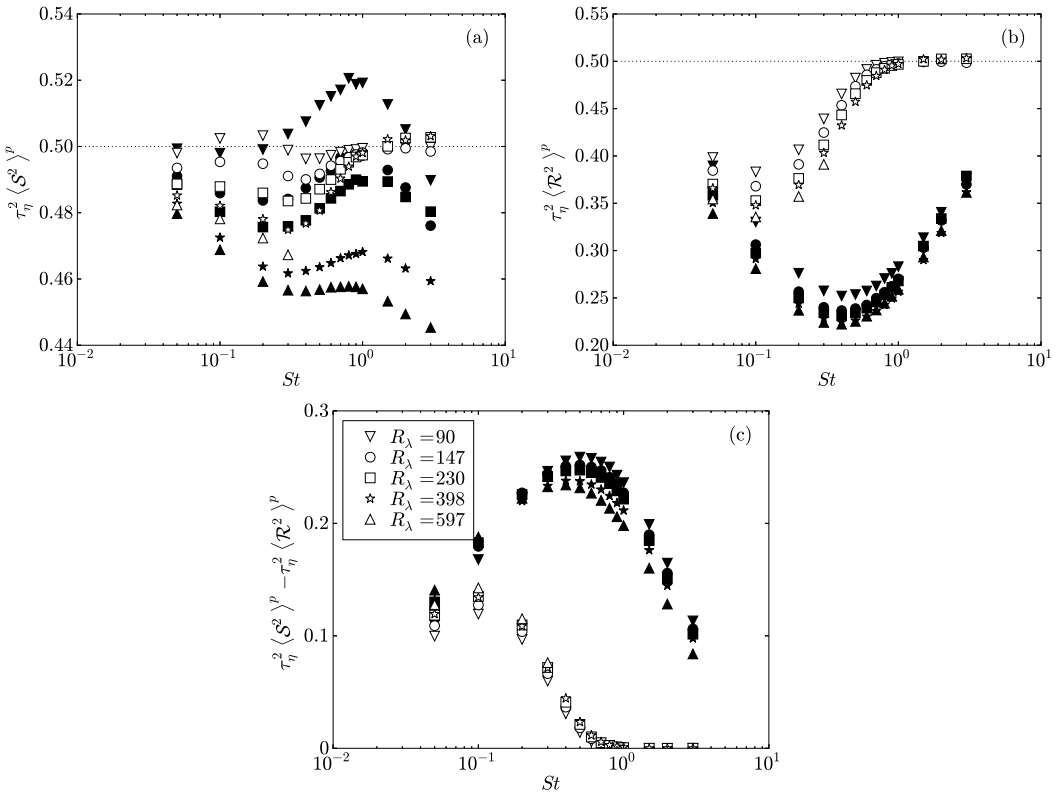

Figure 5.2: $\langle\mathcal{S}^2\rangle^p$ (a), $\langle\mathcal{R}^2\rangle^p$ (b), and $\langle\mathcal{S}^2\rangle^p - \langle\mathcal{R}^2\rangle^p$ (c) as function of St for different values of R_λ. Open symbols denote data with gravity ($Fr = 0.052$), and filled symbols denote data without gravity.

In figure 5.2, we plot $\tau_\eta^2\langle\mathcal{S}^2\rangle^p$, $\tau_\eta^2\langle\mathcal{R}^2\rangle^p$, and $\tau_\eta^2\langle\mathcal{S}^2\rangle^p - \tau_\eta^2\langle\mathcal{R}^2\rangle^p$, for particles which are subject to gravity ($Fr = 0.052$) and for particles which are not subject to gravity ($Fr = \infty$). As noted in Part I, when preferential sampling effects are absent, $\tau_\eta^2\langle\mathcal{S}^2\rangle^p = \tau_\eta^2\langle\mathcal{R}^2\rangle^p = 0.5$. We see from figure 5.2 that gravity reduces the degree of preferential sampling, causing $\tau_\eta^2\langle\mathcal{S}^2\rangle^p$, $\tau_\eta^2\langle\mathcal{R}^2\rangle^p$, and $\tau_\eta^2\langle\mathcal{S}^2\rangle^p - \tau_\eta^2\langle\mathcal{R}^2\rangle^p$ to be closer to the corresponding values for uniformly distributed particles. We also note that preferential sampling effects are eliminated altogether for $St \gtrsim 1$, which consistent with our observations above. The trends in the mean strain and rotation rates with R_λ are similar both with and without gravity, and are discussed in Part I.

To explain the reduction in preferential sampling with gravity, we note that gravity, by causing particles to downward through the underlying flow, reduces the interaction times between the particles and the turbulent eddies. As a result, particles have less time to be affected by straining and rotating regions of the flow, and therefore experience less preferential sampling (see also [73]).

We test this argument by computing Lagrangian strain and rotation timescales along inertial particle trajectories, both with and without gravity. These timescales will also be used in §5.5.2 to model the degree of particle clustering. We first consider the averaged strain timescale $T^p_{\mathcal{SS}}$ and the averaged rotation timescale $T^p_{\mathcal{RR}}$. As in Part I, $T^p_{\mathcal{SS}}$ is defined as the average of $T^p_{\mathcal{S}_{11}\mathcal{S}_{11}}$, $T^p_{\mathcal{S}_{11}\mathcal{S}_{22}}$, $T^p_{\mathcal{S}_{11}\mathcal{S}_{33}}$, $T^p_{\mathcal{S}_{12}\mathcal{S}_{12}}$, $T^p_{\mathcal{S}_{13}\mathcal{S}_{13}}$, $T^p_{\mathcal{S}_{22}\mathcal{S}_{22}}$, $T^p_{\mathcal{S}_{22}\mathcal{S}_{33}}$, $T^p_{\mathcal{S}_{23}\mathcal{S}_{23}}$, and $T^p_{\mathcal{S}_{33}\mathcal{S}_{33}}$, while $T^p_{\mathcal{RR}}$ is taken to be the average of $T^p_{\mathcal{R}_{12}\mathcal{R}_{12}}$, $T^p_{\mathcal{R}_{13}\mathcal{R}_{13}}$, and $T^p_{\mathcal{R}_{23}\mathcal{R}_{23}}$. As noted in Part I, these components of the strain and rotation timescales are statistically equivalent in isotropic turbulence in the absence of gravity. Here, we define

$$T^p_{\mathcal{S}_{ij}\mathcal{S}_{km}} \equiv \frac{\int_0^\infty \left\langle \mathcal{S}_{ij}(\boldsymbol{x}^p(0),0)\mathcal{S}_{km}(\boldsymbol{x}^p(s),s)\right\rangle ds}{\left\langle \mathcal{S}_{ij}(\boldsymbol{x}^p(t),t)\mathcal{S}_{km}(\boldsymbol{x}^p(t),t)\right\rangle}, \tag{5.4}$$

and we define the rotation timescales $T^p_{\mathcal{R}_{ij}\mathcal{R}_{km}}$ analogously.

Figure 5.3 shows DNS results for $T^p_{\mathcal{SS}}$ and $T^p_{\mathcal{RR}}$, both with and without gravity. We see that gravity does indeed reduce these timescales, in agreement with our explanations above. We note that both with and without gravity, the strain timescales are almost entirely insensitive to the flow Reynolds number. Also, while the rotation timescales without gravity weakly vary with R_λ (as noted in Part I) the rotation timescales with gravity appear to be Reynolds-number independent.

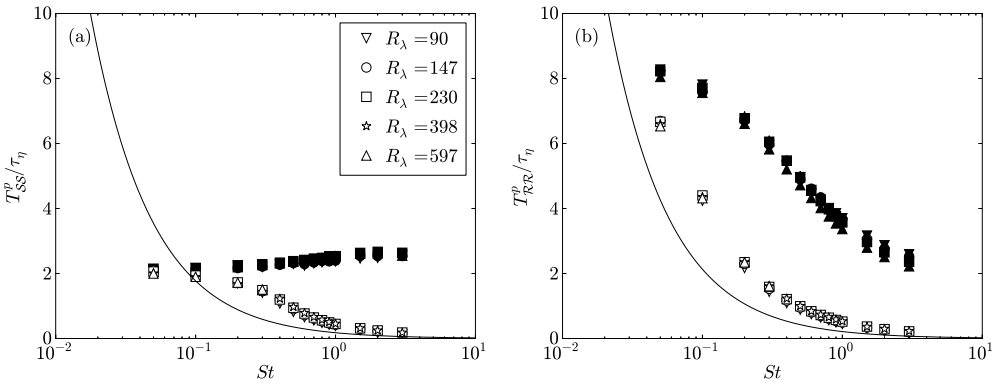

Figure 5.3: $T^p_{\mathcal{SS}}$ (a) and $T^p_{\mathcal{RR}}$ (b) plotted as a function of St for different values of R_λ. Open symbols denote data with gravity (Fr = 0.052), and filled symbols denote data without gravity. The theoretical predictions for $Sv \gg u'/u_\eta$ from Eq. (5.8) and Eq. (5.9) are indicated by solid lines in (a) and (b), respectively.

We now develop a theoretical model to understand and quantify these timescales when gravitational forces are strong ($Sv \gg u'/u_\eta$). In this limit, the particle motion is predominantly downward, and a particle's displacement over a time s is approximately equal to $\tau_p \mathbf{g} s$. We therefore model the Lagrangian timescale of $\mathcal{S}_{ij}\mathcal{S}_{km}$ as

$$T^p_{\mathcal{S}_{ij}\mathcal{S}_{km}} = \frac{1}{\left\langle \mathcal{S}_{ij}(\mathbf{0},0)\mathcal{S}_{km}(\mathbf{0},0)\right\rangle} \int_0^\infty \int_{\boldsymbol{X}} \left\langle \mathcal{S}_{ij}(\boldsymbol{X},s)\mathcal{S}_{km}(\mathbf{0},0)\right\rangle \varrho(\boldsymbol{X},s)\, d\boldsymbol{X} ds, \tag{5.5}$$

where $\varrho(\boldsymbol{X},s) \equiv \delta(\boldsymbol{X} - \tau_p \mathbf{g} s)$. Note that Eq. (5.5) is constructed by assuming that the Lagrangian and Eulerian timescales are equivalent (i.e., 'Corrsin's hypothesis,' see [36]). In the limit $Sv \gg u'/u_\eta$, Corrsin's hypothesis is expected to be exact, since the particle motions are almost independent of the underlying flow field here.

Taking the integral of Eq. (5.5), we obtain

$$T_{\mathcal{S}^p_{ij}\mathcal{S}^p_{km}} = \frac{1}{\left\langle \mathcal{S}_{ij}(\mathbf{0},0)\mathcal{S}_{km}(\mathbf{0},0)\right\rangle} \int_0^\infty \left\langle \mathcal{S}_{ij}(\tau_p \mathbf{g} s,0)\mathcal{S}_{km}(\mathbf{0},0)\right\rangle ds. \tag{5.6}$$

In deriving Eq. (5.6), we have assumed that the particles fall so quickly that the spatial decorrelation of the flow along their trajectories dominates the temporal decorrelation of the turbulence.

To derive an analytical expression for the timescales, we assume that $\langle \mathcal{S}_{ij}(\tau_p \mathfrak{g} \mathfrak{s}, 0) \mathcal{S}_{km}(\mathbf{0}, 0) \rangle$ decorrelates exponentially, which gives us

$$T^p_{\mathcal{S}_{ij}\mathcal{S}_{km}} = \ell_{\mathcal{S}_{ij}\mathcal{S}_{km},3} / \left(\tau_p \mathfrak{g} \right). \tag{5.7}$$

$\ell_{\mathcal{S}_{ij}\mathcal{S}_{km},3}$ is the integral lengthscale of $\mathcal{S}_{ij}\mathcal{S}_{km}$ evaluated along the x_3-direction. We express Eq. (5.7) in non-dimensional form,

$$\hat{T}^p_{\mathcal{S}_{ij}\mathcal{S}_{km}} = \frac{\hat{\ell}_{\mathcal{S}_{ij}\mathcal{S}_{km},3}}{S v}, \tag{5.8}$$

where we have used the top-hat symbol to denote a variable normalized by Kolmogorov units. The rotation timescales $T^p_{\mathcal{R}_{ij}\mathcal{R}_{km}}$ are defined analogously,

$$\hat{T}^p_{\mathcal{R}_{ij}\mathcal{R}_{km}} = \frac{\hat{\ell}_{\mathcal{R}_{ij}\mathcal{R}_{km},3}}{S v}. \tag{5.9}$$

Eq. (5.8) and Eq. (5.9) indicate that when $S v \gg u'/u_\eta$, the Lagrangian integral timescales of the flow experienced by the particles are directly proportional to the Eulerian integral lengthscales of the strain and rotation fields. Furthermore, we see that as $S v$ increases (i.e., gravitational forces become stronger), these timescales become smaller, in agreement with our explanation above.

We use Eq. (5.8) and Eq. (5.9) to predict the averaged timescales $T^p_{\mathcal{SS}}$ and $T^p_{\mathcal{RR}}$, and include comparisons with the DNS data in figure 5.3. We see that as $S t$ (and thus $S v$) increases, our modeled timescales approach those from the DNS. The differences between the DNS and theory are likely caused by the fact that we are not able to reach sufficiently large values of $S v$ for the model to hold, though it

is possible some of the discrepancies are due to the assumed exponential form of the correlations and slight periodicity effects (see Appendix A).

We next consider the anisotropy in the timescales. Based on the symmetries in the system, we divide the strain timescales into six groups:

1. $T^p_{\mathcal{S}_{11}\mathcal{S}_{11}}$, $T^p_{\mathcal{S}_{22}\mathcal{S}_{22}}$,
2. $T^p_{\mathcal{S}_{11}\mathcal{S}_{22}}$,
3. $T^p_{\mathcal{S}_{12}\mathcal{S}_{12}}$,
4. $T^p_{\mathcal{S}_{13}\mathcal{S}_{13}}$, $T^p_{\mathcal{S}_{23}\mathcal{S}_{23}}$,
5. $T^p_{\mathcal{S}_{11}\mathcal{S}_{33}}$, $T^p_{\mathcal{S}_{22}\mathcal{S}_{33}}$,
6. $T^p_{\mathcal{S}_{33}\mathcal{S}_{33}}$,

and the rotation timescales into two groups:

1. $T^p_{\mathcal{R}_{12}\mathcal{R}_{12}}$.
2. $T^p_{\mathcal{R}_{13}\mathcal{R}_{13}}$, $T^p_{\mathcal{R}_{23}\mathcal{R}_{23}}$,

with each of the elements in a group being statistically equivalent. These timescales are plotted in figure 5.4 at $R_\lambda = 398$. Any statistically equivalent timescales are averaged together, and the timescales are denoted by the first (or only) item in the groups above.

We can explain the directional dependence of the timescales when gravity is strong through Eq. (5.8) and Eq. (5.9). By using tensor invariance theory and the properties of the strain rate tensor in an isotropic, incompressible flow, we can

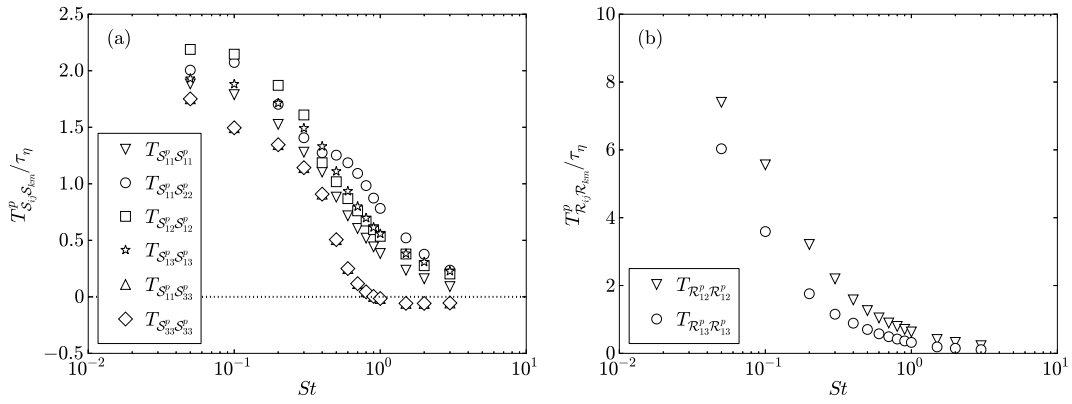

Figure 5.4: The Lagrangian strain (a) and rotation (b) timescales in different directions at $R_\lambda = 398$, plotted as a function of St, for particles with gravity ($Fr = 0.052$).

show that

$$2\ell_{\mathcal{S}_{11}\mathcal{S}_{11},3} = \ell_{\mathcal{S}_{11}\mathcal{S}_{22},3},$$

$$\ell_{\mathcal{S}_{11}\mathcal{S}_{33},3} = \ell_{\mathcal{S}_{33}\mathcal{S}_{33},3} = 0,$$

$$4\ell_{\mathcal{S}_{11}\mathcal{S}_{11},3} = 3\ell_{\mathcal{S}_{12}\mathcal{S}_{12},3},$$

$$\ell_{\mathcal{S}_{12}\mathcal{S}_{12},3} = \ell_{\mathcal{S}_{13}\mathcal{S}_{13},3}.$$

These relations imply that $T^p_{\mathcal{S}_{11}\mathcal{S}_{33}} = T^p_{\mathcal{S}_{33}\mathcal{S}_{33}} < T^p_{\mathcal{S}_{11}\mathcal{S}_{11}} < T^p_{\mathcal{S}_{12}\mathcal{S}_{12}} = T^p_{\mathcal{S}_{13}\mathcal{S}_{13}} < T^p_{\mathcal{S}_{11}\mathcal{S}_{22}}$. We similarly find that $2\ell_{\mathcal{R}_{13}\mathcal{R}_{13},3} = \ell_{\mathcal{R}_{12}\mathcal{R}_{12},3}$ in this limit, which implies that $2T^p_{\mathcal{R}_{13}\mathcal{R}_{13}} = T^p_{\mathcal{R}_{12}\mathcal{R}_{12}}$ here.

The trends in the relative magnitudes of the timescales are in agreement with the predictions above at high St, indicating that the Lagrangian timescales here are dictated by the Eulerian integral lengthscales of the strain and rotation fields. While comparisons between the DNS and theory for each of the components are not shown here, we found that the theory tends to under-predict the DNS timescales for $St \leq 3$, in agreement with our observations above. Two exceptions are the timescales $T^p_{\mathcal{S}_{11}\mathcal{S}_{33},3}$ and $T^p_{\mathcal{S}_{33}\mathcal{S}_{33},3}$, which our model predicts to be zero, but the DNS show to be slightly negative at large St (indicating that the

negative correlations are more significant than the positive correlations here). The physical explanation for these negative timescales is unknown.

5.4.2 Large-scale particle velocity statistics

We next consider the large-scale particle velocity statistics, focusing our attention on both the mean particle settling velocities (§5.4.2) and the particle velocity variances (§5.4.2). A discussion of these statistics over a large range of values of St and Sv can be found in [66]. Here, we discuss the large-scale velocity statistics of particles with $0 \leq St \leq 3$ with gravity ($Fr = 0.052$) and without gravity.

Mean particle settling velocities

We are interested in analyzing the effect of turbulence on the mean settling speed of inertial particles. These settling speeds are indirectly related to the collision rates of different-sized particles, though this relationship is in general more complex than the simplified treatment used in some models (e.g., those of [42, 64]). (Refer to [69] for a discussion of the relationship between the mean settling velocity and the particle relative velocities.)

In [66], we showed that turbulence causes particles with low and intermediate St to settle more quickly than they would in a quiescent flow. This finding was also documented in several other DNS [175, 188, 83, 17] and experimental [4, 189, 190, 66] studies. From Eq. (5.3), we can show that

$$\langle \boldsymbol{u}(\boldsymbol{x}^p(t), t) \rangle = \langle \boldsymbol{v}^p(t) \rangle - \tau_p \mathfrak{g} \equiv -\langle \boldsymbol{\Delta v} \rangle^p, \tag{5.10}$$

where $\tau_p \mathfrak{g} = (0, 0, -\tau_p \mathfrak{g})$ is the gravitational settling velocity in a quiescent flow.

We therefore see that settling velocities are enhanced ($\langle \Delta v_3 \rangle^p > 0$) when particles preferentially sample downward-moving flow. This phenomenon has been referred to as both 'preferential sweeping' [175] and 'fast-tracking' [118]. (Note that we have defined $\langle \Delta v_3 \rangle^p$ such that positive values indicate turbulence-enhanced settling, to follow the standard convention in the literature (e.g., see [175]).)

At larger values of St, a number of experimental studies have indicated that turbulence acts to reduce the particle settling speed [118, 189, 91]. In [66], we performed DNSs over a large range of different particle classes and concluded that these reduced settling velocities are only possible in isotropic turbulence when particles experience nonlinear drag forces. With nonlinear drag forces, particles spend more time in upward-moving flow (due to the higher drag coefficients) and less time in downward-moving flow (due to lower drag coefficients), leading to reduced settling speeds. However, we found that DNSs with a simple nonlinear drag model (e.g., see [33]) are in considerable quantitative disagreement with experiments, suggesting that more sophisticated treatments of the nonlinearities are necessary.

The DNSs in this study are performed using only a linear drag model (see §5.3.2), and thus our settling speeds at the largest values of St are likely in both qualitative and quantitative error. However, the results in [66] suggest that the settling rates at low and intermediate St ($St \lesssim 1$) are reasonably accurate, and the larger Reynolds-number range of this study allows us to analyze how the setting speeds of these particles are affected by changes in the flow Reynolds number.

In figure 5.5(a) we plot the settling velocity enhancement $\langle \Delta v_3 \rangle^p$ normalized

by the Kolmogorov velocity u_η. In agreement with [66], the DNS with linear drag shows no statistically significant indication of reduced settling speeds at any Reynolds number simulated. We see that the mean settling speeds are independent of R_λ for $St \leq 0.1$, indicating that the settling speeds in this limit are determined entirely by the small-scale turbulence, in agreement with [17]. [17] also argue that for $St \gg R_\lambda^{1/2} Fr$ and $Fr \ll R_\lambda^{1/2}$, the particles will fall so quickly that they sample the underlying turbulence as if it were a white-noise velocity field, and the particle settling velocities will scale as

$$\frac{\langle \Delta v_3 \rangle^p}{u_\eta} \propto R_\lambda^{3/4} Fr^{2/3}/St. \tag{5.11}$$

Our data in figure 5.5(b) support this scaling for small $R_\lambda^{3/4} Fr^{2/3}/St$, indicating that the settling velocities of these particles are dependent on both the small- and large-scale turbulence. However, the results must be interpreted with caution, since nonlinear drag effects (which are neglected in these simulations) are likely important when $R_\lambda^{3/4} Fr^{2/3}/St$ is small.

Particle velocity variances

We now consider the variance of the particle velocities. In Part I, we demonstrated that the theories of [32] and [2] approximate inertial particle velocity variances well in the limits of weak and strong inertia, respectively, in the absence of gravity. We now test the theory in [176], for the case where particles are subjected to strong gravitational forces ($Sv \gg u'/u_\eta$). Based on [176, 66], we model the vertical velocity variance $\langle v_3^2 \rangle^p \equiv \langle v_3^p(t) v_3^p(t) \rangle$ as

$$\frac{\langle v_3^2 \rangle^p}{u'^2} = \frac{1}{1 + StSv\left(\frac{\eta}{\ell}\right)}, \tag{5.12}$$

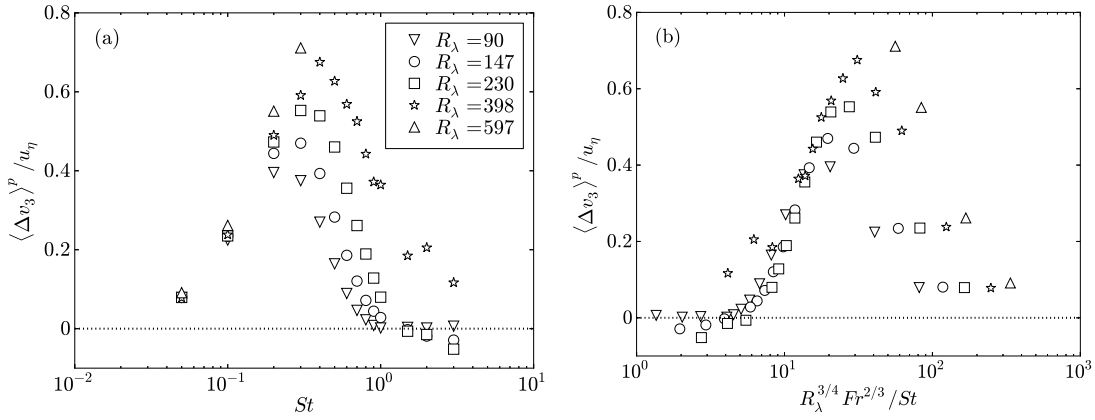

Figure 5.5: Turbulence-induced enhancements (positive) or reductions (negative) in the mean settling velocities of inertial particles with gravity ($Fr = 0.052$), normalized by the Kolmogorov velocity u_η. The symbols denote different values of R_λ. The data are plotted as a function of St in (a), and as a function of $R_\lambda^{3/4} Fr^{2/3}/St$ in (b) to test the scaling in Eq. (5.11).

and the horizontal velocity variance $\langle v_1^2 \rangle^p \equiv \langle v_1^p(t) v_1^p(t) \rangle$ as

$$\frac{\langle v_1^2 \rangle^p}{u'^2} = \frac{2 + StSv\left(\frac{\eta}{\ell}\right)}{2\left[1 + StSv\left(\frac{\eta}{\ell}\right)\right]^2}. \tag{5.13}$$

Eq. (5.12) and Eq. (5.13) imply that the particle velocity variances decrease with increasing St and increasing Sv. The physical explanation is that for large St or large Sv, the particles have a diminished response to the underlying flow, either because they filter out high frequency velocity modes as a result of their inertia (for large St) or because they fall quickly through the flow and have less time to respond to velocity fluctuations (for large Sv). We also observe from Eq. (5.12) and Eq. (5.13) that the particle velocity variances increase with increasing R_λ (since η/ℓ decreases). In this case (as explained in Part I), more velocity modes are present with timescales greater than the particle response time, causing the filtering effect to be minimized.

By taking the ratio of Eq. (5.12) and Eq. (5.13), we obtain

$$\frac{\langle v_3^2 \rangle^p}{\langle v_1^2 \rangle^p} = \frac{2 + 2StSv\left(\frac{\eta}{\ell}\right)}{2 + StSv\left(\frac{\eta}{\ell}\right)}, \tag{5.14}$$

which implies that the vertical velocity variance exceeds the horizontal velocity variance. The physical explanation is provided in [195, 37, 66] and is summarized below. As the particles fall, the fluid velocity along the particle trajectories decorrelates both spatially and temporally. In the limit of strong gravity, the particles traverse the lengthscales of the flow in a time which is much shorter than the temporal correlation of the flow field. Consequently, the fluid velocity field may be approximated as being 'frozen,' and it is the spatial correlations of the fluid velocity experienced by the particles that govern the particle velocity behavior. In the limit of strong gravity, the dominant particle motion is in the vertical direction. Since in isotropic turbulence the longitudinal integral lengthscale is twice the transverse integral lengthscale, the particles falling under gravity will experience vertical fluid velocities which are more significantly correlated over the timescale τ_p than are horizontal fluid velocities. This then leads to larger particle velocity variances in the vertical direction. Following [37], we will hereafter refer to this as the 'continuity effect.'

In figure 5.6, we show comparisons between the theory (Eq. (5.12) and Eq. (5.13)) and the DNS. The theory is in excellent agreement with the DNS at large St, as expected. We note that as R_λ increases, the agreement between the theory and DNS begins at increasingly larger values of St. This is because the theory is expected to hold for $Sv = St/Fr \gg u'/u_\eta$, and thus as R_λ increases (increasing u'/u_η), larger values of St are required.

We finally analyze the velocity variances when St is small. In this case, we expect the particle motion to be primarily determined by preferential sampling.

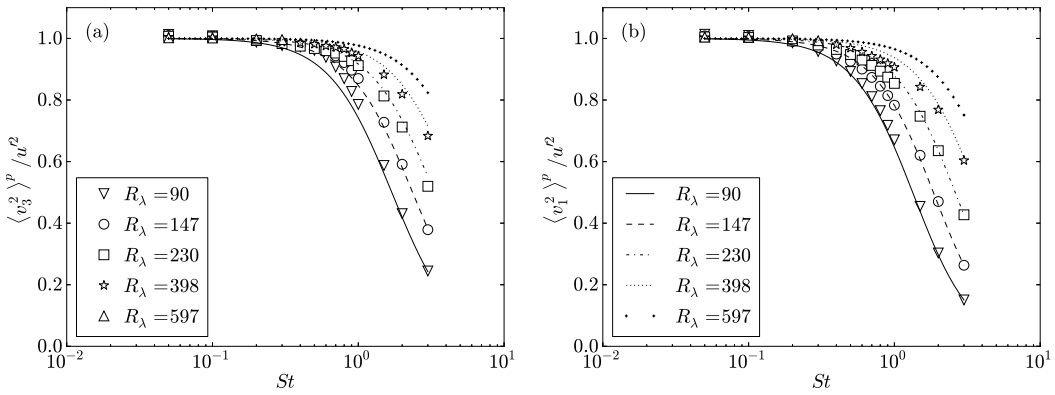

Figure 5.6: The variance of the particle velocities in the vertical (a) and horizontal (b) directions. The symbols denote the DNS data with gravity (Fr = 0.052), and the lines and plus signs in (a) and (b) indicate the predictions from Eq. (5.12) and Eq. (5.13) for the different Reynolds numbers simulated.

In Part I, we demonstrated that small-St particles preferentially sample high energy regions in the absence of gravity, causing them to have larger velocity variances than corresponding fluid particles. Figure 5.7 compares the variances of inertial particles to the variance of the fluid sampled by these particles for low St and Fr = 0.052. As expected, for low St (and hence low Sv), the particle velocity variances exceed u'^2 and are almost equal to the variances of the fluid velocity sampled by the particles. For $St > 0.1$, the particle velocity variances begin to deviate from those of the underlying fluid, indicating that preferential sampling is less significant here.

5.4.3 Particle accelerations

We now move from particle velocity statistics to particle acceleration statistics. In §5.4.3, we consider the expected acceleration behavior for different values of St and Sv, discuss DNS data for the acceleration variances, and introduce two

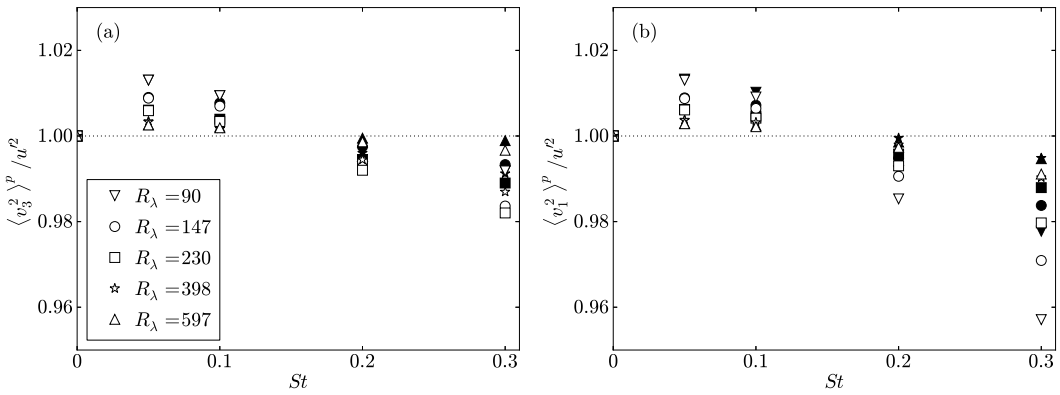

Figure 5.7: DNS data for the variance of the particle velocities with gravity ($Fr = 0.052$) at low St for different values of R_λ. Variances in the vertical and horizontal directions are shown in (a) and (b), respectively. Open symbols denote the variance of the particle velocities, and filled symbols denote the variance of fluid velocities at the particle locations.

theoretical models to understand and quantify the accelerations when gravitational forces are strong. We then examine higher-order acceleration statistics from the DNS in §5.4.3.

Particle acceleration variances

We first consider the particle acceleration variances, which we expect to be strongly dependent on both St and Sv. For $St \ll 1$ and $Sv = 0$ (weakly inertial particles without gravity), preferential sampling is the dominant mechanism (as discussed in Part I), the particle acceleration $\boldsymbol{a}^p(t) \equiv d\boldsymbol{v}^p(t)/dt$ is approximately equal to the fluid acceleration at the particle locations $\boldsymbol{a}^{fp}(t)$, and we therefore have (e.g., see [12]),

$$\boldsymbol{a}^p(t) \approx \boldsymbol{a}^{fp}(t) = \frac{\partial \boldsymbol{u}(\boldsymbol{x}^p(t),t)}{\partial t} + \boldsymbol{u}(\boldsymbol{x}^p(t),t) \cdot \nabla \boldsymbol{u}(\boldsymbol{x}^p(t),t). \tag{5.15}$$

In Part I, we showed that the trends in the accelerations at low St without gravity can be well-modeled by the preferential-sampling theory in [32].

As Sv is increased, but St still remains small, the particles will still respond almost instantaneously to the underlying flow, but the imposed gravitational forces will induce a downward particle motion. The particles will therefore encounter different regions of the turbulence over a short duration, increasing their accelerations. We refer to this phenomenon as the 'gravitational trajectory effect.' (Note that [195] used the term the 'effect of crossing trajectories' to refer to this mechanism. Since current literature generally uses the term 'crossing trajectories' to denote the fact that the particle velocity can take on multiple values at a single point in the absence of gravity (e.g., see [58, 113, 144]), we use an alternate term, the 'gravitational trajectory effect,' to avoid any ambiguity.) The particle acceleration in this case can be approximated by the derivative of the fluid velocity along an inertial particle trajectory (denoted here as $d\boldsymbol{u}^p/dt$), giving (see [12]),

$$\boldsymbol{a}^p(t) \approx \frac{d\boldsymbol{u}^p}{dt} = \frac{\partial \boldsymbol{u}(\boldsymbol{x}^p(t),t)}{\partial t} + \boldsymbol{v}^p(t)\cdot\nabla\boldsymbol{u}(\boldsymbol{x}^p(t),t). \tag{5.16}$$

We expect that for $St \ll 1$ and $Sv \ll 1$, $\boldsymbol{u}(\boldsymbol{x}^p(t),t) \approx \boldsymbol{v}^p(t)$, and thus $\boldsymbol{a}^p(t)$, $\boldsymbol{a}^{fp}(t)$, and $d\boldsymbol{u}^p/dt$ will be equivalent.

As St (and thus Sv) increases, the particles will fall more rapidly through the flow, causing $d\boldsymbol{u}^p/dt$ to become larger. However, large-St particles will no longer respond quickly to changes in the underlying flow (due to the inertial filtering effect, as discussed in Part I), and we expect that $\boldsymbol{a}^p(t)$ will eventually decrease with increasing St.

We test these arguments in figure 5.8(a,b) by plotting DNS data for the variance of $\boldsymbol{a}^p(t)$, $\boldsymbol{a}^{fp}(t)$, and $d\boldsymbol{u}^p/dt$ in the vertical and horizontal directions for

$St \leq 3$. (The vertical and horizontal variances of $\boldsymbol{a}^p(t)$ are denoted as $\langle a_3^2 \rangle^p$ and $\langle a_1^2 \rangle^p$, respectively; the vertical and horizontal variances of $\boldsymbol{a}^{fp}(t)$ are denoted as $\langle a_3^2 \rangle^{fp}$ and $\langle a_1^2 \rangle^{fp}$, respectively; and the vertical and horizontal variances of $d\boldsymbol{u}^p/dt$ are denoted as $\langle (du_3/dt)^2 \rangle^p$ and $\langle (du_1/dt)^2 \rangle^p$, respectively.) The data are also shown in figure 5.8(c,d) for $St \leq 0.3$ to highlight the trends when St is small.

At the smallest Stokes number ($St = 0.05$, corresponding to $Sv = 0.96$), inertial and gravitational effects are small, and all three quantities are almost identical, indicating that the preferential-sampling effect is dominant. The accelerations increase with increasing R_λ, since the fluid acceleration field becomes increasingly intermittent (refer to Part I). For $St > 0.05$ (corresponding to $Sv > 0.96$), gravitational effects are important, and $\langle a_{1,3}^2 \rangle^p$ increases due to the gravitational trajectory effect and deviates from $\langle a_{1,3}^2 \rangle^{fp}$. For $St \lesssim 0.2$, the $\langle a_{1,3}^2 \rangle^p \approx \langle (du_{1,3}^2/dt) \rangle^p$, demonstrating that Eq. (5.16) holds here. $\langle (du_1/dt)^2 \rangle^p$ and $\langle (du_3/dt)^2 \rangle^p$ continue to increase with increasing St, as expected, while $\langle a_1^2 \rangle^p$ and $\langle a_3^2 \rangle^p$ begin to decrease with increasing St for $St \gtrsim 0.7$ (due to the inertial filtering effect). All of these trends are in agreement with our physical explanations above.

By comparing the DNS data with gravity here to the data without gravity in Part I, we see that gravity can lead to particle acceleration variances which are orders of magnitude larger than those without gravity. The physical explanation is that with gravity, preferential sampling effects (which tend to decrease the accelerations, as explained in Part I) are reduced, and gravitational trajectory effects (which tend to increase the accelerations, as explained above) are introduced.

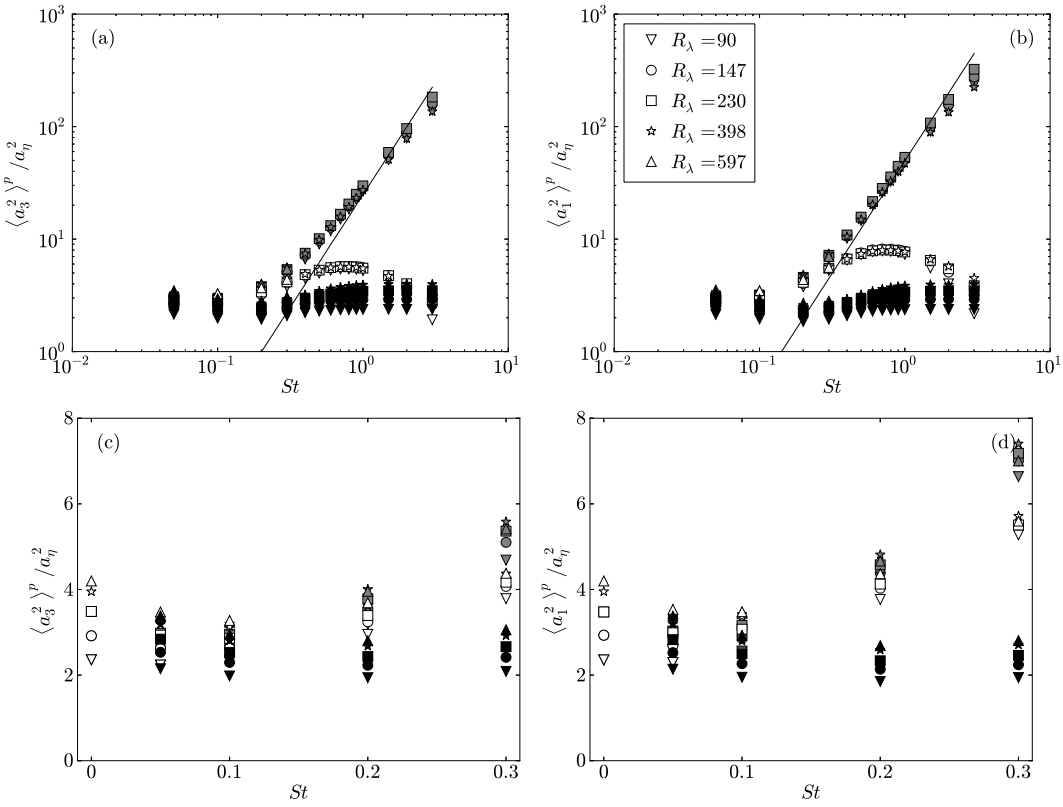

Figure 5.8: Inertial particle acceleration variances in the vertical direction (a,c) and horizontal directions (b,d) for different values of St and R_λ. All data are with gravity included (Fr = 0.052). Open symbols denote $\langle a_{1,3}^2 \rangle^p$, filled black symbols denote $\langle a_{1,3}^2 \rangle^{fp}$, and filled gray symbols denote $\langle (du_{1,3}/dt)^2 \rangle^p$. (a) and (b) show data over the full range of non-zero St on logarithmic axes, and (c) and (d) show data for $St \leq 0.3$ on linear axes to highlight the trends here. The lines in (a) and (b) are the predictions from Eq. (5.19) and Eq. (5.20), respectively.

We now develop two theoretical models to predict these quantities when gravitational forces are strong ($Sv \gg u'/u_\eta$). The first predicts the variance of $d\boldsymbol{u}^p/dt$, while the second predicts the variance of $\boldsymbol{a}^p(t)$.

For $Sv \gg u'/u_\eta$, the convective velocity $\boldsymbol{v}^p(t)$ is about equal to the gravitational settling velocity $\tau_p \mathfrak{g}$, and $d\boldsymbol{u}^p/dt$ is approximated as

$$\frac{d\boldsymbol{u}^p}{dt} \approx \frac{\partial \boldsymbol{u}(\boldsymbol{x}^p(t),t)}{\partial t} - \tau_p \mathfrak{g} \frac{\partial \boldsymbol{u}(\boldsymbol{x}^p(t),t)}{\partial x_3}. \tag{5.17}$$

$\langle (du_3/dt)^2 \rangle^p$ is therefore approximated as

$$\begin{aligned}\left\langle \left(\frac{du_3}{dt} \right)^2 \right\rangle^p \approx & \left\langle \left(\frac{\partial u_3(\boldsymbol{x}^p(t),t)}{\partial t} \right)^2 \right\rangle \\ & - 2\tau_p \mathcal{G} \left\langle \left(\frac{\partial u_3(\boldsymbol{x}^p(t),t)}{\partial t} \right) \left(\frac{\partial u_3(\boldsymbol{x}^p(t),t)}{\partial x_3} \right) \right\rangle \\ & + \tau_p^2 \mathcal{G}^2 \left\langle \left(\frac{\partial u_3(\boldsymbol{x}^p(t),t)}{\partial x_3} \right)^2 \right\rangle .\end{aligned} \tag{5.18}$$

We computed each of the terms on the right-hand-side of Eq. (5.18) from DNS data to test their relative magnitudes. The first term was seen to be highly intermittent and generally independent of St. [165] attributed this intermittency to the large-scale advection of dissipation-range eddies (which causes the velocity at a fixed point to vary rapidly in time), and proposed that this quantity scales with $R_\lambda a_\eta^2$. A linear least-squares regression from our DNS suggests that it scales approximately with $R_\lambda^{1.3} a_\eta^2$, though presumably the linear scaling with R_λ may be recovered at larger Reynolds numbers. We therefore expect the first term to be large at high Reynolds numbers, though for the Reynolds numbers simulated in our study, it is always less than $50 a_\eta^2$.

DNS indicate that the second term is negligible, since the partial temporal and partial spatial derivatives are generally uncorrelated. (The correlation coefficients are always less than 5%.) One possible explanation is that $\partial u_3^p(\boldsymbol{x}^p(t),t)/\partial t$ is influenced by large-scale advection, while $\partial u_3^p(\boldsymbol{x}^p(t),t)/\partial x_3$ is affected almost entirely by small-scale motions. These terms are therefore expected to be uncorrelated given a sufficient separation between the large and small scales of the turbulence.

Based on our results in §5.4.1, the third term is given as $\tau_p^2 \mathcal{G}^2/(15\tau_\eta^2)$ for $St \gtrsim 1$, which is equivalent to $a_\eta^2 Sv^2/15$. For large Sv, this term is much larger than the

other terms, and we therefore have

$$\left\langle \left(\frac{du_3}{dt} \right)^2 \right\rangle^p \approx a_\eta^2 \frac{S\nu^2}{15}. \tag{5.19}$$

We apply similar arguments in the horizontal directions, yielding

$$\left\langle \left(\frac{du_1}{dt} \right)^2 \right\rangle^p \approx \tau_p^2 \mathcal{G}^2 \left\langle \left(\frac{\partial u_1(\boldsymbol{x}^p(t),t)}{\partial x_3} \right)^2 \right\rangle \approx 2a_\eta^2 \frac{S\nu^2}{15}. \tag{5.20}$$

Eq. (5.19) and Eq. (5.20) indicate that $\langle (du_1/dt)^2 \rangle^p = 2\langle (du_3/dt)^2 \rangle^p$. The physical explanation is that, since the particle motion is mostly downward, the horizontal acceleration components will involve transverse velocity derivatives, and these are larger than the longitudinal velocity derivatives since they include the effect of rotation.

The predictions from Eq. (5.19) and Eq. (5.20) are included in figure 5.8, and are in good agreement with the DNS for $St \gtrsim 1$. The DNS also indicates that at large St, the variance of $d\boldsymbol{u}^p/dt$ is larger (smaller) in horizontal (vertical) direction, as explained above.

We now develop a model for the particle acceleration variances in the limit $S\nu \gg u'/u_\eta$. Following [12], we write the formal solution for the particle acceleration as

$$\boldsymbol{a}^p(t) = \frac{1}{\tau_p^2} \int_{-\infty}^{t} \exp\left[\frac{s-t}{\tau_p} \right] [\boldsymbol{u}(\boldsymbol{x}^p(t),t) - \boldsymbol{u}(\boldsymbol{x}^p(s),s)]\, ds. \tag{5.21}$$

Without loss of generality, we take $t = 0$ and write the particle acceleration covariance tensor $\langle \boldsymbol{a}^p(0)\boldsymbol{a}^p(0) \rangle$ as

$$\begin{aligned} \langle \boldsymbol{a}^p(0)\boldsymbol{a}^p(0) \rangle =& \frac{1}{\tau_p^4} \left\langle \boldsymbol{u}(\boldsymbol{x}^p(0),0)\boldsymbol{u}(\boldsymbol{x}^p(0),0) \int_{-\infty}^{0}\int_{-\infty}^{0} \exp\left[\frac{s}{\tau_p}\right] \exp\left[\frac{S}{\tau_p}\right] ds dS \right\rangle \\ &- \frac{2}{\tau_p^4} \left\langle \boldsymbol{u}(\boldsymbol{x}^p(0),0) \int_{-\infty}^{0}\int_{-\infty}^{0} \exp\left[\frac{s}{\tau_p}\right] \exp\left[\frac{S}{\tau_p}\right] \boldsymbol{u}(\boldsymbol{x}^p(s),s) ds dS \right\rangle \\ &+ \frac{1}{\tau_p^4} \left\langle \int_{-\infty}^{0}\int_{-\infty}^{0} \exp\left[\frac{s}{\tau_p}\right] \exp\left[\frac{S}{\tau_p}\right] \boldsymbol{u}(\boldsymbol{x}^p(s),s)\boldsymbol{u}(\boldsymbol{x}^p(S),S) ds dS \right\rangle. \end{aligned} \tag{5.22}$$

The first term on the right-hand-side of Eq. (5.22) is

$$\tau_p^{-2}\Big\langle \boldsymbol{u}(\boldsymbol{x}^p(0),0)\boldsymbol{u}(\boldsymbol{x}^p(0),0)\Big\rangle = \frac{u'^2}{\tau_p^2}\boldsymbol{I} + \frac{\langle \boldsymbol{\Delta v}\rangle^p\langle \boldsymbol{\Delta v}\rangle^p}{\tau_p^2} \approx \frac{u'^2}{\tau_p^2}\boldsymbol{I}. \tag{5.23}$$

In deriving Eq. (5.23), we have used the fact that $\langle \boldsymbol{u}(\boldsymbol{x}^p(t),t)\rangle = \langle \boldsymbol{v}^p(t)\rangle - \tau_p \boldsymbol{g} \equiv -\langle \boldsymbol{\Delta v}\rangle^p$ and that $|\langle \boldsymbol{\Delta v}\rangle^p|/u' \ll 1$ (see §5.4.2). Based on PDF theory [139], the second term on the right-hand-side of Eq. (5.22) is equivalent to the particle velocity covariance multiplied by $-2\tau_p^{-2}$, while the third term equivalent to the particle velocity covariance multiplied by τ_p^{-2}.

Using these relationships and the expressions for the velocity variances in Eq. (5.12) and Eq. (5.13), we write the vertical and horizontal particle acceleration variances as

$$\frac{\langle a_3^2\rangle^p}{a_\eta^2} = \left[\frac{u'}{u_\eta}\right]^2 \left[\frac{Sv}{St}\right]\left[\frac{1}{StSv + \frac{\ell}{\eta}}\right], \tag{5.24}$$

and

$$\frac{\langle a_1^2\rangle^p}{a_\eta^2} = \left[\frac{u'}{u_\eta}\right]^2 \left[\frac{Sv}{St}\right]\left[\frac{2StSv + 3\left(\frac{\ell}{\eta}\right)}{2\left(StSv + \frac{\ell}{\eta}\right)^2}\right], \tag{5.25}$$

respectively. By taking the ratio of Eq. (5.24) and Eq. (5.25), we see that

$$\frac{\langle a_3^2\rangle^p}{\langle a_1^2\rangle^p} = \frac{2StSv + 2\left(\frac{\ell}{\eta}\right)}{2StSv + 3\left(\frac{\ell}{\eta}\right)}. \tag{5.26}$$

This implies that the acceleration variances, in contrast to the velocity variances, are larger in the horizontal than in the vertical direction. There are two reasons for this trend. The first is that the variance of $d\boldsymbol{u}^p/dt$ is larger in the horizontal direction, as explained above. The second is because of the continuity effect described in §5.4.2. That is, the spatial correlation of the fluid velocity along the particle trajectories is shorter for horizontal velocity components. As a result, the horizontal fluid velocities will change more rapidly, leading to larger particle accelerations in these directions.

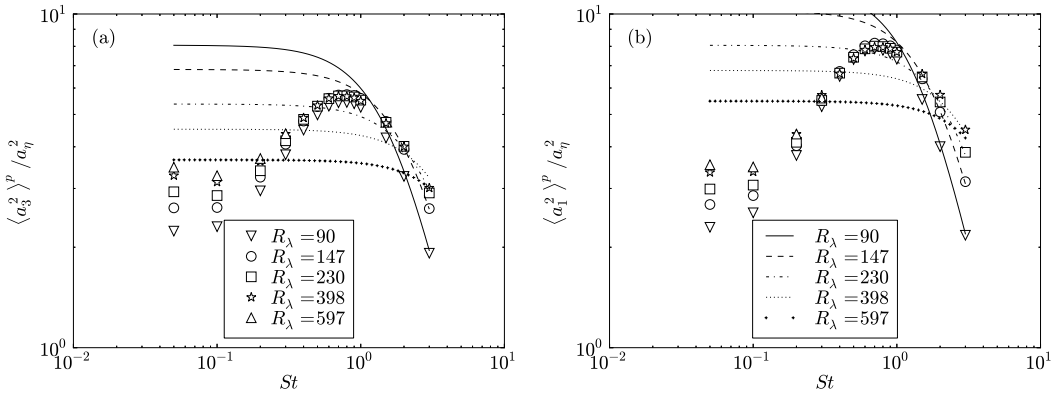

Figure 5.9: The variance of the particle accelerations in the vertical (a) and horizontal (b) directions. Open symbols denote DNS data with gravity (Fr = 0.052), and the lines and plus signs in (a) and (b) indicate the predictions from Eq. (5.24) and Eq. (5.25) for the different Reynolds numbers simulated.

In figure 5.9, we compare the predictions from Eq. (5.24) and Eq. (5.25) to DNS data. The results are in excellent agreement at large St. For large St, the theory is able to capture the trends with R_λ, the decrease in the variances with increasing St, and the fact that the variances are larger in the horizontal directions than in the vertical direction.

To further explore the trends in the accelerations for particles with varying levels of inertia and gravity, we plot in figure 5.10 inertial particle acceleration variances for $0 < St \leq 56.2$, $0 < Sv \leq 100$, and $R_\lambda = 227$. (It is important to recognize, however, that the statistics at large Sv are likely in significant quantitative error and should be treated with caution. Refer to Appendix A for more information on the effects of periodicity.) As expected, the particle acceleration variances are the largest for $St \ll 1$ and $Sv \gg 1$, due to the gravitational trajectory effect, as suggested by Eq. (5.24) and Eq. (5.25). For sufficiently large St, particles filter out nearly all of the large-scale turbulence, and so acceleration variances are small. For intermediate St and Sv, the particle accelerations are

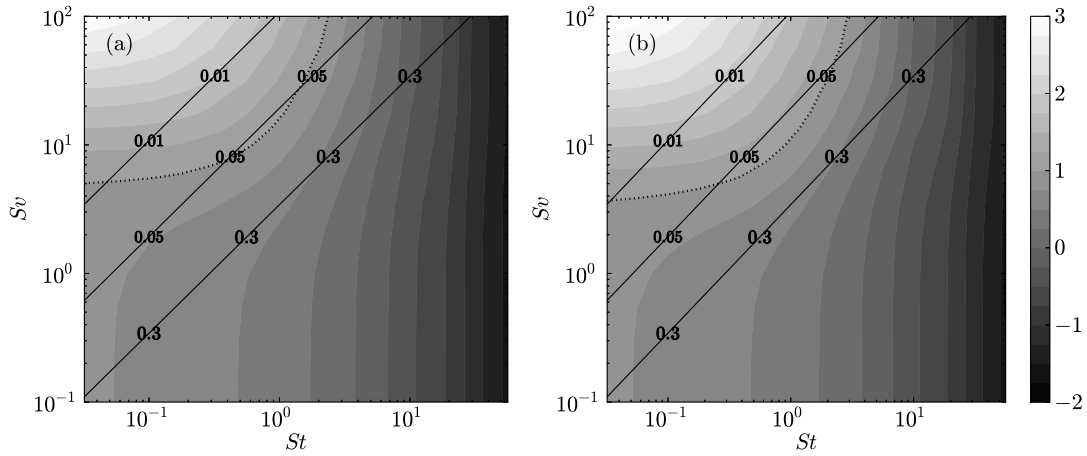

Figure 5.10: Filled contours of the particle acceleration variances, $\langle a_3^2 \rangle^p$ (a) and $\langle a_1^2 \rangle^p$ (b), normalized by the Kolmogorov acceleration variance a_η^2, for $R_\lambda = 227$. The contours are logarithmically scaled, and the labels on the colorbar denote exponents of the decade. The diagonal lines denote three different values of Fr, corresponding to conditions representative of stratiform clouds ($Fr = 0.01$), cumulus clouds ($Fr = 0.05$), and cumulonimbus clouds ($Fr = 0.3$). The dotted line corresponds to $\langle a_{1,3}^2 \rangle^p = a_\eta^2$.

determined by a combination of preferential-sampling, gravitational-trajectory, and inertial-filtering effects. We also observe from this figure that the particle acceleration variances are the largest in conditions representative of stratiform clouds (i.e., $Fr = 0.01$) and the smallest in conditions representative of cumulonimbus clouds (i.e., $Fr = 0.3$).

Higher-order particle acceleration statistics

Having considered the acceleration variances, we now examine higher-order statistics of the particle accelerations. In figure 5.11, we plot PDFs of the particle acceleration, both with and without gravity, at $R_\lambda = 398$. We observe that as St increases (both with and without gravity), the tails of the acceleration PDFs

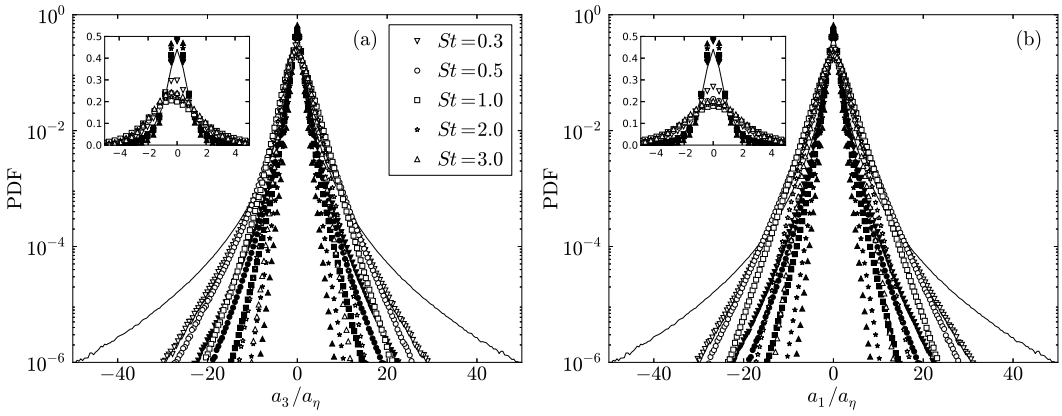

Figure 5.11: PDFs of the vertical (a) and horizontal (b) acceleration components at $R_\lambda = 398$. The open symbols denote data with gravity ($Fr = 0.052$), the filled symbols denote data without gravity, and the solid line denotes data for fluid ($St = 0$) particles. The insets show the central region of the PDFs on a linear scale.

become less pronounced, indicating that the particles are less likely to experience very strong accelerations [12, 143]. However, in the presence of gravity, this reduction in the tails is less apparent, suggesting that the particles sample more high intensity accelerations than they would without gravity. As shown in the insets in figure 5.11, gravity also leads to an increased probability of moderate acceleration events and a decreased probability of low acceleration events, causing the increased variances discussed in §5.4.3.

The PDFs in figure 5.11(a) have a slight positive skewness for moderate St with gravity, indicating a preference for strongly positive accelerations (i.e., accelerations opposite to gravity) over strongly negative ones (i.e., accelerations in the same direction as gravity). The PDFs without gravity and in the horizontal directions exhibit no skewness, as expected. We quantify the skewness in the vertical direction (denoted as $\langle a_3^3 \rangle^p / (\langle a_3^2 \rangle^p)^{3/2}$) at different values of R_λ in figure 5.12, where we see that it peaks for $St \sim 1$. From Eq. (5.3), we can show that the positive skewness in the particle accelerations corresponds to a positive

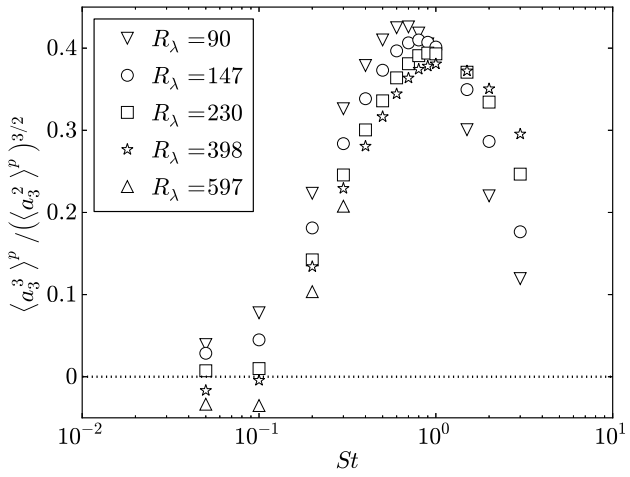

Figure 5.12: Skewness of the particle accelerations parallel to gravity as a function of St at different values of R_λ. The symbols denote DNS data with gravity (Fr = 0.052).

skewness in the slip velocity $u_3^p - v_3^p$, and that the mean slip velocity of a statistically stationary system must equal $\tau_p \mathfrak{g}$. The skewness in the vertical particle accelerations therefore indicates an asymmetry in the slip velocities at the particle positions. Specifically, it indicates that the slip velocities which are farthest from the mean are associated with a small fraction of particles which reside in regions where $u_3^p - v_3^p \gg \tau_p \mathfrak{g}$. This skewness in the acceleration diminishes as St increases, since the particles tend to sample the flow more uniformly here (see §5.4.1), causing their slip velocities to become more symmetric.

Finally, in figure 5.13, we examine the kurtosis of the particle accelerations (denoted as $\langle a_{1,3}^4 \rangle^p / (\langle a_{1,3}^2 \rangle^p)^2$) with and without gravity. We see that gravity decreases the kurtosis of the largest particles (as compared to the case without gravity) and that the kurtosis values are almost identical in both vertical and horizontal directions. By analyzing the PDFs in figure 5.11, we notice that while gravity increases the tails of the PDFs, it also increases the central region, causing an overall increase in the variance and a subsequent decrease in the kurtosis.

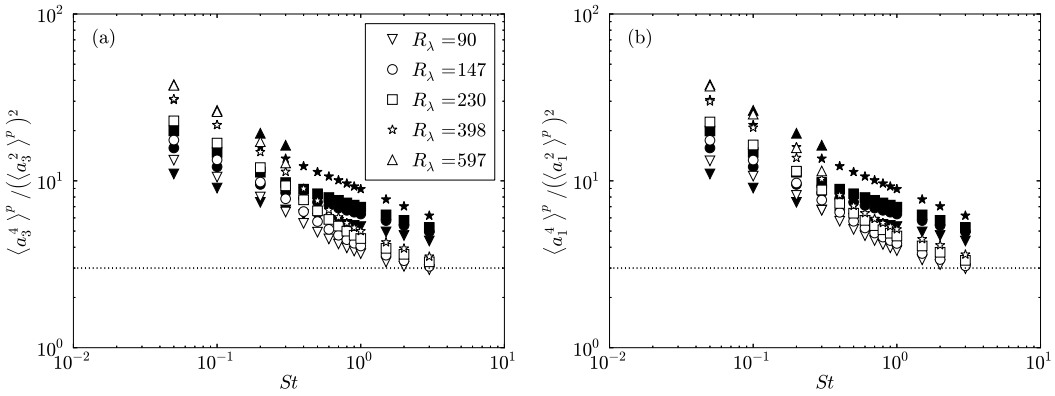

Figure 5.13: Kurtosis of the particle accelerations in the vertical (a) and horizontal directions (b) as a function of St at different values of R_λ. The open symbols denote DNS data with gravity (Fr = 0.052), and the filled symbols denote DNS data without gravity.

We also observe that at the lowest values of St and the three lowest Reynolds numbers, the acceleration kurtosis values with gravity are slightly larger than those without gravity. This, however, is a numerical artifact of the differences in the box size between the cases with and without gravity (refer to §5.3.1), and no such deviations are seen if the box sizes are kept the same. (Refer to Appendix A for a more complete discussion.)

In closing this section, we note that our study is, to the best of our knowledge, the first study to analyze the accelerations of particles with non-negligible gravitational forces in homogeneous turbulence. Previous studies which considered particle accelerations in channel flows demonstrated that the coupling between particle inertia, gravity, and shear can lead to strong accelerations in the near-wall region [63, 98]. Here, we demonstrate that even in a homogeneous and isotropic turbulence, the coupling between particle inertia and gravity is sufficient to lead to large particle acceleration variances under certain conditions.

The large particle accelerations observed here are particularly relevant to collisions between particles with different sizes. As explained in [32], the relative velocity between two particles of different sizes is related to their accelerations. It is thus possible that increased particle accelerations could lead to larger relative velocities and more frequent collisions between different-sized particles.

5.5 Two-particle statistics

We now consider two-particle statistics with gravity, in particular, particle relative velocities (§5.5.1), clustering (§5.5.2), and collision kernels (§5.5.3). In each case, we compare our results to those without gravity (from Part I) to highlight the role gravity plays on each statistic.

5.5.1 Particle relative velocities

In this section, we examine the effect of gravity on the relative velocities of inertial particles. These data will help us to model and explain the trends in particle clustering in §5.5.2. We first discuss the expected effect of gravity on the relative velocities from a theoretical framework (§5.5.1), and then analyze DNS results for separations in the dissipation (§5.5.1) and inertial (§5.5.1) ranges. Finally, in §5.5.1, we study the anisotropy in the relative velocities induced by gravity.

Theoretical framework for particle relative velocities

We define $\boldsymbol{w}^p(t)$ as the relative velocity between two particles at time t, and $\boldsymbol{\Delta u}(\boldsymbol{r}^p(t), t)$ as the difference in the fluid velocities at the particle locations at that time. Following the nomenclature in Part I, we define the second-order particle relative velocity structure function tensor as

$$\boldsymbol{S}_2^p(\boldsymbol{r}) = \left\langle \boldsymbol{w}^p(t)\boldsymbol{w}^p(t) \right\rangle_{\boldsymbol{r}},$$

where $\langle\cdot\rangle_{\boldsymbol{r}}$ denotes an ensemble average conditioned on $\boldsymbol{r}^p(t) = \boldsymbol{r}$. ($\boldsymbol{r}^p(t)$ is the particle separation vector at time t.)

To construct an exact integral solution for $\boldsymbol{S}_2^p(\boldsymbol{r})$, we first rewrite Eq. (5.3) as an equation for the relative motion between two identical particles,

$$\frac{d\boldsymbol{w}^p(t)}{dt} = \frac{\boldsymbol{\Delta u}(\boldsymbol{r}^p(t), t) - \boldsymbol{w}^p(t)}{\tau_p}. \tag{5.27}$$

It is thus clear that gravity does not explicitly affect the relative motion of like particles; indeed, gravity only features implicitly in Eq. (5.27) through its effect on $\boldsymbol{\Delta u}(\boldsymbol{r}^p(t), t)$.

The formal solution of Eq. (5.27) can then be used to construct the exact expression for $\boldsymbol{S}_2^p(\boldsymbol{r})$ (see [124]),

$$\hat{\boldsymbol{S}}_2^p(\hat{\boldsymbol{r}}) = \frac{1}{S\,t^2} \int_{-\infty}^{0} \int_{-\infty}^{0} \left\langle \boldsymbol{\Delta}\hat{\boldsymbol{u}}(\hat{\boldsymbol{r}}^p(\hat{s}), \hat{s}) \boldsymbol{\Delta}\hat{\boldsymbol{u}}(\hat{\boldsymbol{r}}^p(\hat{S}), \hat{S}) \right\rangle_{\hat{\boldsymbol{r}}} \exp\left[S\,t^{-1}(\hat{s} + \hat{S}) \right] d\hat{s} d\hat{S}. \tag{5.28}$$

In this equation, we have used $\hat{Y}$ to denote a variable Y normalized by Kolmogorov units.

We first consider Eq. (5.28) in the absence of gravity. From Eq. (5.28), we observe that particle relative velocities are affected by the fluid velocity difference $\boldsymbol{\Delta u}(\boldsymbol{r}^p(t), t)$ along their trajectories. For small values of $S\,t$, the exponential

term in Eq. (5.28) causes contributions to the integral from times in the past (i.e. $\hat{s} < 0$, $\hat{S} < 0$) to be negligible, and the particle relative velocities become equivalent to the fluid velocity differences at the particle positions, indicating that preferential sampling is the dominant mechanism affecting relative particle motion. As shown in Part I, preferential sampling causes inertial particles to experience larger (smaller) fluid velocity differences than those of fluid particles in directions parallel (perpendicular) to the particle separation vector.

As St increases (but gravitational forces are still absent or negligible), the exponential term is no longer small for times in the past. These particles retain a memory of their interactions with the turbulence, and it is the fluid velocities at larger separations along their path histories that dominate the contribution to the particle velocity dynamics, leading to particle relative velocities which are greater than those of the local fluid. This phenomenon has been referred to as 'caustics' (e.g., see [182, 183]). Refer to [25] for a more complete theoretical discussion of the relative velocities of inertial particles in the absence of gravity, and to Part I for a detailed examination of relative velocity statistics here.

We now discuss how these relative velocities will be modified by the presence of gravity. We saw in §5.4.1 that gravity generally reduces the degree of preferential sampling. With gravity, we therefore expect the relative velocities of small-St particles to be affected less by preferential sampling, and therefore to be closer to those of $St = 0$ particles.

At higher values of St, gravity is expected to alter the inertial particle relative velocities through its influence on the path-history mechanism. We observed in §5.4.1 that gravity reduces the correlation timescales of the flow along particle trajectories. This implies that gravity causes the fluid velocity differ-

ences in Eq. (5.28) to become decorrelated more rapidly, and thus it reduces the correlation radius over which the relative velocities are influenced by their path-history interactions with the fluid. We therefore expect the particle relative velocities here to be reduced with gravity.

To summarize, particles with weak inertial ($St \ll 1$) and gravitational ($Sv \ll 1$) forces are subject to preferential sampling effects, which tend to increase (decrease) their relative velocities parallel (perpendicular) to the separation vector. As gravitational forces are increased, however, this preferential sampling effect is reduced, causing the relative velocities to approach those of fluid particles. Particles with strong inertia ($St \gtrsim 1$) and weak gravitational forces ($Sv \ll 1$) retain a memory of path-history interactions with the turbulence, which increases their relative velocities. However, as Sv increases, the influence of these path-history interactions is reduced, decreasing the relative velocities. We now test these arguments using DNS data for different values of St and Sv.

Dissipation range relative velocity statistics

We first consider DNS data for separations in the dissipation range, which is taken to extend from $0 \leq r \lesssim 10\eta$, as in Part I and [87]. We define the relative velocities parallel to the separation vector (i.e., the longitudinal relative velocities) as $w_{\parallel}^{p}$, and the relative velocities perpendicular to the separation vector (i.e., the transverse relative velocities) as $w_{\perp}^{p}$.

Before examining different moments of the relative velocity statistics, we first consider PDFs of $w_{\parallel}^{p}$ to gain an understanding of the overall effect of grav-

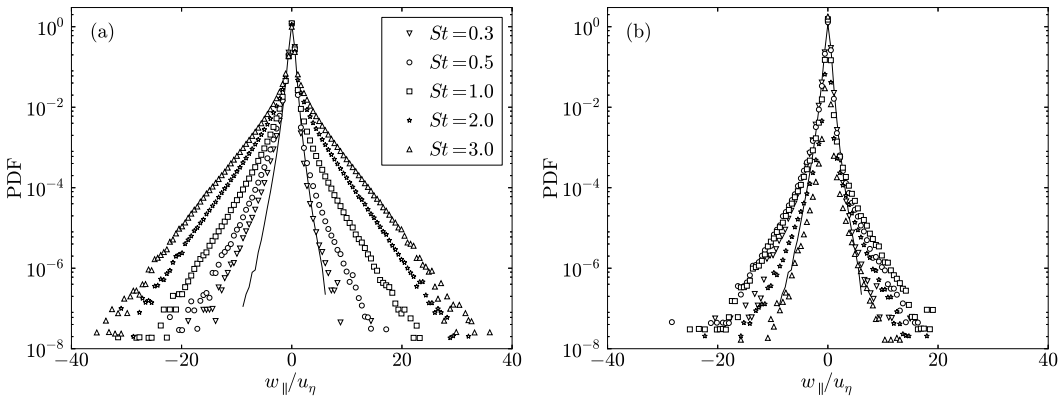

Figure 5.14: PDFs of the radial relative velocities without gravity (a) and with gravity ($Fr = 0.052$) (b) at $R_\lambda = 398$ and $0 \le r/\eta \le 2$. The solid line denotes data for fluid ($St = 0$) particles.

ity on the distribution of the relative velocities. We see from figure 5.14 that gravity has a dramatic effect on the relative velocities at large St and leads to strong reductions in the tails of the PDFs here. This is in agreement with our explanation above, where we argue that gravity suppresses path-history effects and thereby reduces the relative velocities.

We now quantify the effect of gravity at both low and high St by examining the longitudinal and transverse relative velocity variances. As in Part I, we define the longitudinal relative velocity variance as

$$S^p_{2\parallel}(r) \equiv \left\langle \left[w^p_\parallel(t) \right]^2 \right\rangle_r, \tag{5.29}$$

and the transverse relative velocity variance as

$$S^p_{2\perp}(r) \equiv \left\langle \left[w^p_\perp(t) \right]^2 \right\rangle_r, \tag{5.30}$$

where $\langle \cdot \rangle_r$ denotes an ensemble average conditioned on $|\boldsymbol{r}^p(t)| = r$.

In figure 5.15, we plot the relative velocity variances $S^p_{2\parallel}$ and $S^p_{2\perp}$. For $St \ge 1$ (corresponding to $Sv \ge 19.3$), we observe that gravity strongly decreases the

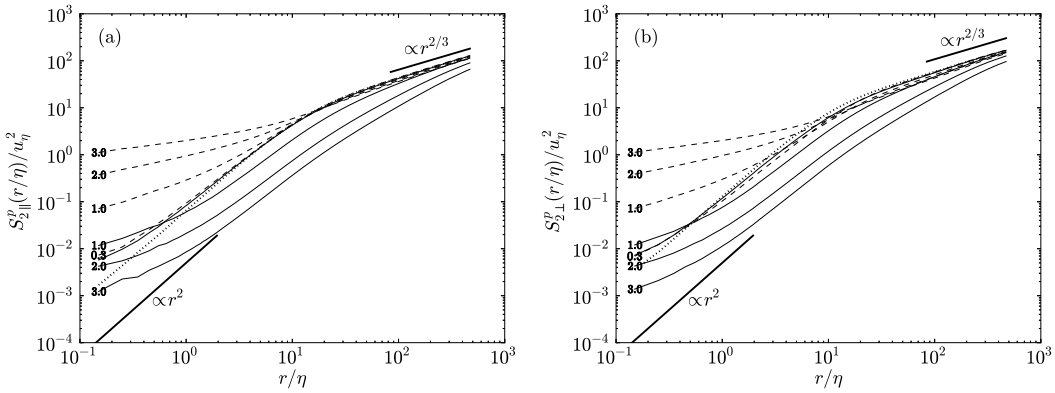

Figure 5.15: The variance of the particle relative velocities parallel to the separation vector (a) and perpendicular to the separation vector (b) for $R_\lambda = 398$, plotted as a function of r/η for different St. The thin solid lines indicate data with gravity ($Fr = 0.052$), the dashed lines indicate data without gravity, and the thick dotted line indicates fluid ($St = 0$) particles. The Stokes numbers are indicated by the line labels, and the fluid velocity scalings are indicated by thick solid lines.

relative velocities, in some cases causing them to be orders of magnitude smaller than their values without gravity. This indicates that gravity reduces the effect of path-history interactions on the relative velocities, as explained above.

For $St = 0.3$ and very small separations ($r/\eta \lesssim 1$), the relative velocities show evidence of path-history effects (see also Part I), causing the relative velocities to exceed those of $St = 0$ particles in both the parallel and perpendicular directions. At larger separations ($1 \lesssim r/\eta \lesssim 10$), however, we observe the expected increase (decrease) in the longitudinal (transverse) relative velocities as a result of preferential sampling. We also see that gravity causes the relative velocities here to be closer to those of the underlying fluid, since it decreases preferential sampling effects. These trends are consistent with our explanations above. (Note that since particles with $St < 0.3$ have only weak gravitational forces ($Sv < 5.79$), the effect of gravity on the relative velocities is less apparent, and

data from these particle classes are therefore not shown.)

The decreased influence of path-history interactions is also apparent in the scaling of the relative velocity variances in figure 5.15. In the dissipation range the fluid relative velocity variances scale with r^2. In the absence of gravity, the relative velocities for $St \geq 1$ do not exhibit r^2-scaling over any of the dissipation range, as was noted in Part I. However, with the addition of gravity, we see a clear r^2-scaling for $1 \lesssim r/\eta \lesssim 10$. Compared to the case without gravity, one has to go to smaller separations to observe deviations from r^2 scaling, since the reduction in the path-history contribution means that one needs to go to regions where $\Delta \boldsymbol{u}$ is much smaller before the history contribution becomes important.

While our efforts to this point have primarily been focused on understanding the relative velocity variance, we are primarily interested in the mean inward relative velocity, since this quantity is directly proportional to the particle collision kernel (see §5.5.3). We define the longitudinal mean inward relative velocity as

$$S^{p}_{-\parallel}(r) \equiv -\int_{-\infty}^{0} w^{p}_{\parallel} p(w^{p}_{\parallel}|r) dw^{p}_{\parallel}, \tag{5.31}$$

where $p(w^{p}_{\parallel}|r)$ is the probability density function of the relative velocity conditioned on a separation magnitude r. The mean inward relative velocity is more difficult to model than the relative velocity variance, but we expect both statistics to follow many of the same trends. In figure 5.16, we show $S^{p}_{-\parallel}(r)$ at $R_\lambda = 398$, both with and without gravity.

We see that the mean inward velocities, like the variances, decrease with the addition of gravity at large (small) St due to the reduced influence of the path-history (preferential-sampling) mechanisms. Interestingly, with gravity, the mean inward relative velocities (in contrast to the relative velocity variances)

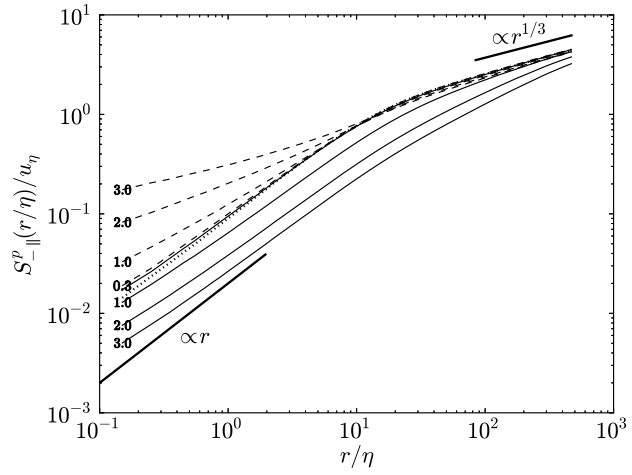

Figure 5.16: The mean inward particle relative velocity for $R_\lambda = 398$, plotted as a function of r/η for different St. The thin solid lines indicate data with gravity ($Fr = 0.052$), the dashed lines indicate data without gravity, and the thick dotted line indicates fluid ($St = 0$) particles. The Stokes numbers are indicated by the line labels, and the fluid velocity scalings are shown by thick solid lines.

follow the local fluid scaling almost perfectly throughout the entire dissipation range. This result was also noted in [17]. One plausible explanation is that since the mean inward velocity is a lower-order statistic than the velocity variance, it is less affected by path-history interactions, which generally tend to decrease the scaling (see Part I).

To further verify our arguments above, it is helpful to decouple the effects of gravity and inertia by varying each independently. We do so in figure 5.17, where we show $S^p_{-\|}(r)$ and $S^p_{2\|}(r)$ for $0 < St \leq 56.2$, $0 < Sv \leq 100$, and $R_\lambda = 227$. While the results at high Sv are likely artificially affected by the periodic boundary conditions, we can nevertheless use these data to discuss the qualitative trends in the relative velocities at different values of St and Sv.

We see that $S^p_{-\|}(r)$ and $S^p_{2\|}(r)$ have similar qualitative trends, as expected. For

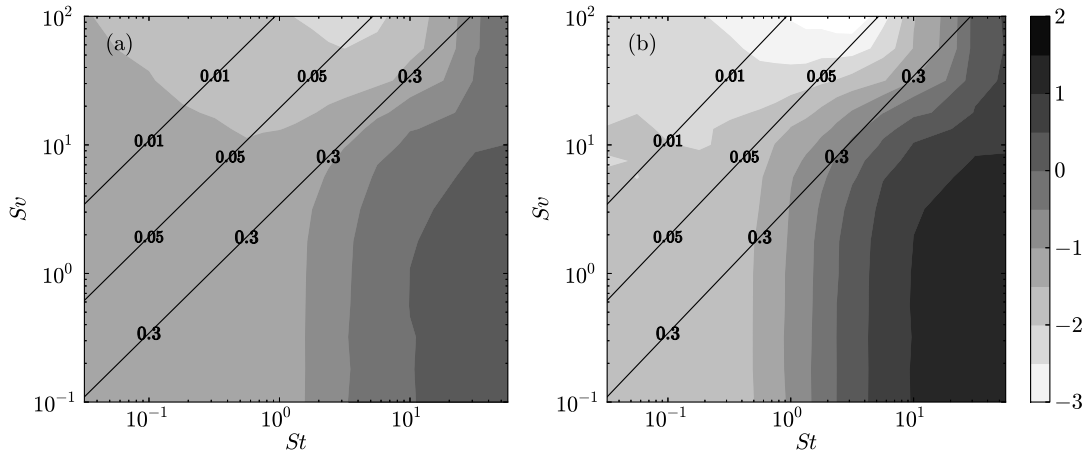

Figure 5.17: Filled contours of $S^p_{-\|}(r)/u_\eta$ (a) and $S^p_{2\|}(r)/u_\eta^2$ (b) evaluated at $r/\eta = 0.25$ and $R_\lambda = 227$ for different values of St and Sv. The contours are logarithmically scaled, and the colorbar labels indicate the exponents of the decade. The diagonal lines denote three different values of Fr, corresponding to conditions representative of stratiform clouds ($Fr = 0.01$), cumulus clouds ($Fr = 0.05$), and cumulonimbus clouds ($Fr = 0.3$).

$Sv \lesssim 10$, both quantities increase with increasing St, either due to preferential-sampling effects (at low St) or path-history effects (at high St). The relative velocities also decrease with increasing Sv, since gravity causes both effects to be less significant, as explained in §5.5.1. Finally, we observe that the relative velocities are the smallest for the largest values of Sv and $St \sim 1$. At smaller (larger) St, preferential-concentration (path-history) effects are more significant, leading to an increase in the relative velocities. One implication of these results is that for a given value of St, droplets in stratiform clouds ($Fr = 0.01$) will generally have smaller relative velocities than droplets in cumulonimbus clouds ($Fr = 0.3$).

We have thus far examined and explained relative velocity statistics for fixed Reynolds numbers. We now consider how these statistics are affected by changes in R_λ. In figure 5.18, we show both $S^p_{-\|}/u_\eta$ and $S^p_{2\|}/u_\eta^2$. For $0 \leq St \leq 3$,

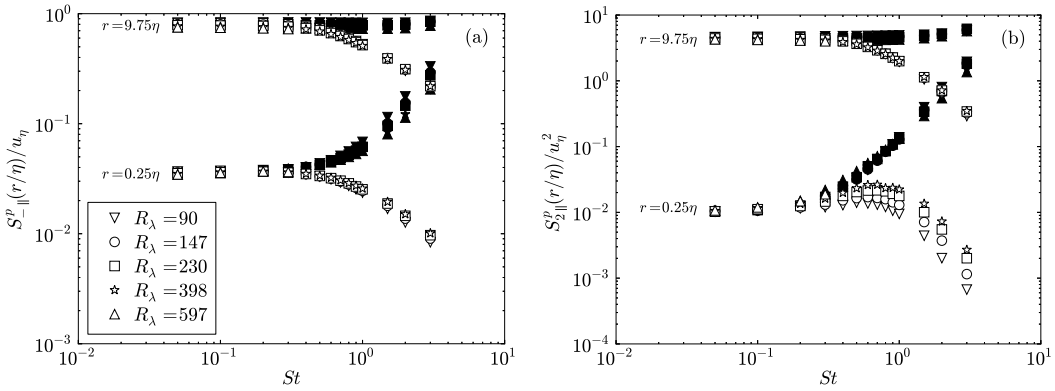

Figure 5.18: The normalized mean inward radial relative velocities (a) and relative velocity variances (b) plotted as a function of St for different values of R_λ. The open symbols denote the case with gravity ($Fr = 0.052$), and the filled symbols denote the case without gravity. Data are shown for particles with separations $r = 0.25\eta$ and $r = 9.75\eta$.

the longitudinal relative velocities have a very weak dependence on R_λ, both with and without gravity. In Part I, we noted that $S^p_{2\|}/u^2_\eta$ increases weakly with increasing R_λ in the absence of gravity for $0.3 \lesssim St \lesssim 1$, and attributed this trend to the increase in the intermittency of the turbulence with increasing R_λ. While we expected the increased intermittency of the turbulence to also increase the relative velocities for higher-St particles, we instead found that the relative velocities decreased with increasing R_λ for $1 \lesssim St \lesssim 3$. We argued that this trend was caused by a corresponding decrease in the rotation timescales $T^p_{\mathcal{RR}}/\tau_\eta$, which in turn reduced the influence of path-history effects and decreased the relative velocities. However, with gravity, we find that $T^p_{\mathcal{RR}}/\tau_\eta$ is generally independent of R_λ (see §5.4.1), and thus we expect the increased intermittency of the turbulence to cause $S^p_{2\|}/u^2_\eta$ to uniformly increase with increasing R_λ for $St \gtrsim 0.3$. Our results in figure 5.18 confirm this expectation. We also see that $S^p_{-\|}/u_\eta$ is generally unaffected by changes in R_λ, since it is less influenced by the intermittency of the flow (as explained in Part I).

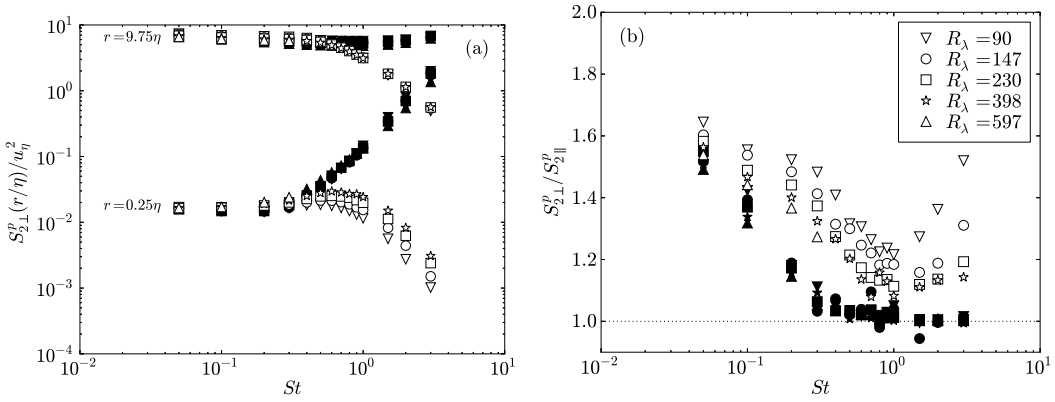

Figure 5.19: (a) The transverse relative velocity variances, plotted as a function of St for different values of R_λ. Data are shown for particles with separations $r = 0.25\eta$ and $r = 9.75\eta$. (b) The ratio between the transverse and longitudinal relative velocity variances $S^p_{2\perp}/S^p_{2\parallel}$, evaluated at $r/\eta = 0.25$. In both plots, the open symbols denote the case with gravity ($Fr = 0.052$), and the filled symbols denote the case without gravity.

We are also interested in the effect of the Reynolds number on the transverse relative velocities. Figure 5.19(a) shows the transverse relative velocity variances $S^p_{2\perp}$ for different values of St, r/η, and R_λ. We see that the trends with R_λ are identical to those in the longitudinal direction.

In Part I, we found that without gravity, the longitudinal and transverse relative velocities became equivalent at small separations for $St \gtrsim 0.3$. The physical explanation is that the path-history contribution to their relative velocities decreases the coherence of the pair motion, and in the ballistic limit where the pairs move independently of each other, the longitudinal and transverse components are equal. However, with gravity, path-history effects are weaker, and thus the longitudinal and transverse velocities may not be the same in this regime. We compare these two quantities in figure 5.19(b) by plotting $S^p_{2\perp}/S^p_{2\parallel}$ at $r/\eta = 0.25$.

From figure 5.19(b) we see that both with and without gravity, the ratio

$S^p_{2\perp}/S^p_{2\parallel}$ approaches 2, the value for fluid particles (e.g., see [130]), at low values of St. Figure 5.19(b) also indicates that for $St \gtrsim 0.3$ without gravity, $S^p_{2\perp}$ and $S^p_{2\parallel}$ are equivalent, as expected. At high values of St with gravity, however, the longitudinal and transverse components are not equivalent, since path-history effects are less significant. As R_λ increases, the particle relative velocities are affected by increasingly intermittent turbulence along their path histories. As a result, the relative velocities and larger and the particles move more ballistically, causing the ratio $S^p_{2\perp}/S^p_{2\parallel}$ to decrease with increasing R_λ.

We now examine the effects of Reynolds number on the scaling of the relative velocities. As in Part I, we compute the scaling exponents of the mean inward relative velocity ($\zeta^-_\parallel$) and the relative velocity variance ($\zeta^2_\parallel$) by performing linear least-squares power-law fits over separations $0.75 \leq r/\eta \leq 2.75$. While our observations from figure 5.15 suggest that the power-law exponent may vary considerably over this range, we are forced to use this relatively large range due to insufficient statistics at smaller separations. Thus, while these scaling exponents allow us to assess the qualitative trends in the scaling as we change R_λ and add gravity, they only provide an indication of the average scaling behavior between $0.75 \leq r/\eta \leq 2.75$, and do not necessarily suggest that the velocities follow the same scaling throughout this entire region.

The scaling exponents are shown in figure 5.20. The trends at a given value of R_λ are in agreement with our observations from figure 5.15 and figure 5.16, which are explained above. We also see that with gravity, the scaling exponents tend to decrease with increasing R_λ, since the particles are more influenced by their memory of increasingly intermittent turbulence, and therefore tend to move ballistically, as noted above.

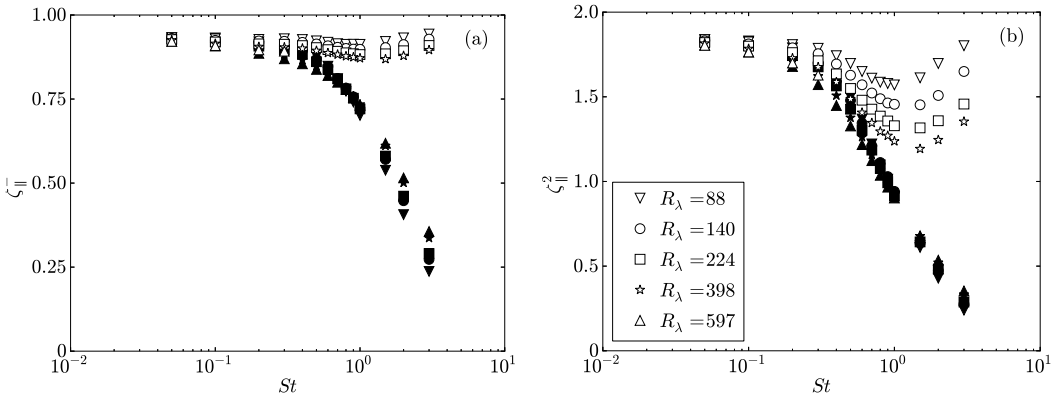

Figure 5.20: The scaling exponents of the longitudinal mean inward relative velocities (a) and relative velocity variances (b) plotted as a function of St for different values of R_λ. The open symbols denote the case with gravity (Fr = 0.052), and the filled symbols denote the case without gravity. The scaling exponents are computed using linear least-squares regression over the range $0.75 \leq r/\eta \leq 2.75$.

Finally, in closing this section, we note that we also examined higher-order moments of the relative velocities in the dissipation range and found them to follow very similar trends both with and without gravity. The higher-order statistics with gravity are not shown here due to space considerations, but these statistics without gravity are shown and discussed in detail in Part I.

Inertial-range relative velocity statistics

We now consider the scaling of the inertial particle relative velocity statistics for separations in the inertial range. Following convention (e.g., see [87]), we consider the scaling exponents of the velocity magnitudes here,

$$S^p_{|n|||} = \left\langle \left| w^p_{||}(t) \right|^n \right\rangle_r \propto r^{\zeta^n_{||}}, \tag{5.32}$$

where n is the order of the structure function considered.

[94] (hereafter 'K41') predicts that $\zeta_{\|}^n = n/3$, while Kolmogorov's refined similarity hypothesis ([95], hereafter 'K62') suggests the scaling,

$$\zeta_{\|}^n = \frac{n}{3}\left[1 - \frac{\mu}{6}(n-3)\right], \tag{5.33}$$

where μ is generally taken as 0.25 [130].

In Part I, we analyzed these statistics in the absence of gravity. We expect that for sufficiently large separations, the large relative velocities induced by the turbulence will overwhelm any gravitational effects, and thus the relative velocity statistics here will be equal to those in the absence of gravity. However, for the values of R_λ simulated and all but the smallest-St particles, the finitude of the scale separation prevents us from attaining such large separations, suggesting that gravity will influence the particle relative velocity statistics over the entire inertial range.

We plot the scaling exponents in figure 5.21 at $R_\lambda = 88$ and $R_\lambda = 398$. At $R_\lambda = 88$, we have no clear inertial range and therefore used extended self-similarity (hereafter 'ESS', see [18]) to compute the scaling exponents. We computed the scaling exponents at $R_\lambda = 398$ both directly and through ESS, and the two methods gave results which varied by under 6% in all cases. The exponents shown in figure 5.21 at $R_\lambda = 398$ are those computed through ESS.

Our data suggest that the scaling exponents are only weakly dependent of R_λ for the Reynolds numbers simulated. We also observe that for $St \lesssim 0.3$ (corresponding to $Sv \lesssim 5.8$), the effect of gravity is negligible in the inertial range, the scaling exponents are almost identical with and without gravity, and K62 is able to model these exponents well. However, while the scaling exponents generally decrease with increasing St in the absence of gravity, they increase with increasing St when gravity is present, and in some cases are larger than even

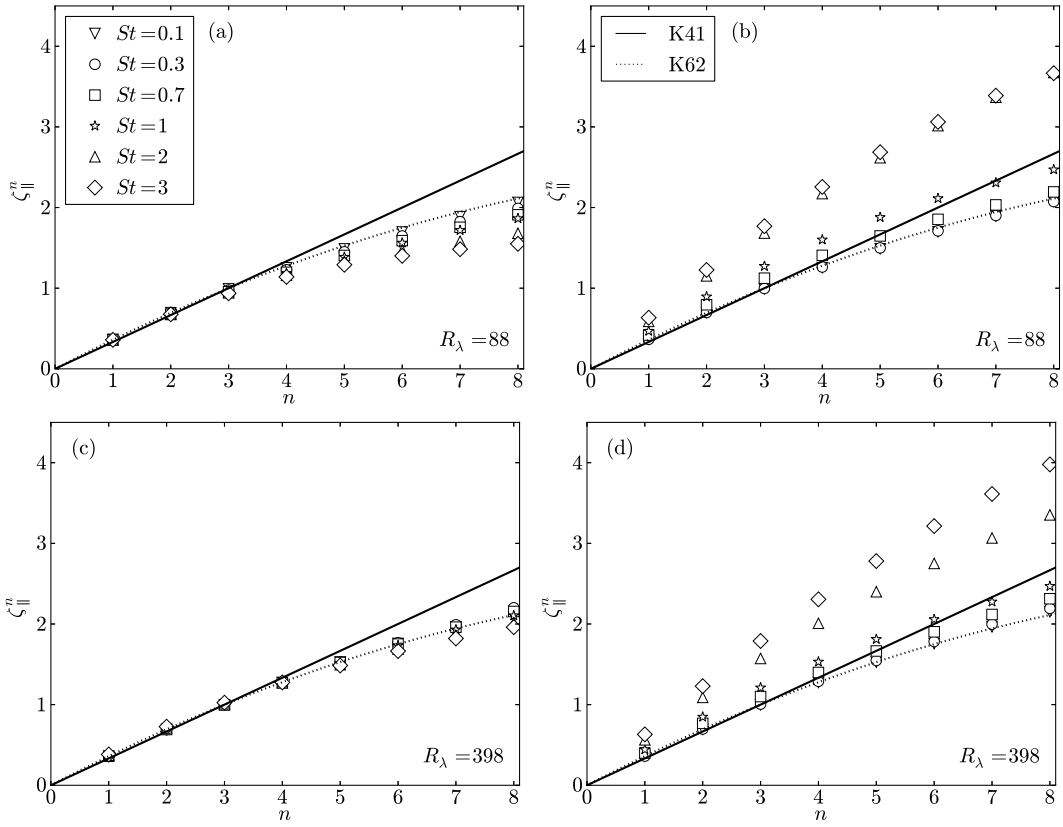

Figure 5.21: Longitudinal particle structure function scaling exponents in the inertial range for various values of St. (a,b) are for R_λ = 88, and (c,d) are for R_λ = 398. The data without gravity are shown on the left (a,c), and the data with gravity are shown on the right (b,d). The exponents are computed from linear least-squares regression using ESS. The predicted scalings from K41 and K62 are indicated by the solid and dotted lines, respectively.

K41 predicts.

We provide a possible explanation for these larger scaling exponents with gravity by using K62-type arguments. In §5.4.1, we found that gravity reduces the time particles spend interacting with the turbulence. One consequence of this is that the relative motion of particles will be unaffected by eddies with timescales below a certain value. In this case, we can define an effective fluid

dissipation rate experienced by a particle, which we denote as ϵ_p. Based on dimensional arguments, we can write

$$S^{p}_{|n|||}(r) \propto \left(r\epsilon_p\right)^{n/3}, \tag{5.34}$$

If the particle separation is small, the relative motion of particles will be due to small turbulence scales. If gravity is strong, the particles will fall through these scales in a time much less than their response time τ_p, and thus they will be unresponsive to these small-scale motions. In this case, the particle separation will be unaffected by the turbulence, suggesting that $\epsilon_p \to 0$.

As the particle separation increases, however, the particle relative motion will be determined by larger turbulence scales, and it will take settling particles longer to fall through these scales. As a result, the particles will be more responsive to the underlying turbulence, causing their relative velocities to increase. In this case, we expect ϵ_p to increase from its value at small separations, since turbulence now has an effect on the particle motions. At sufficiently large separations, the time it takes a particle to fall through the corresponding large scales will greatly exceed τ_p. As a result, the particles will have sufficient time to respond to nearly all of the turbulence at these separations, and thus $\epsilon_p \to \epsilon$.

These observations suggest that ϵ_p will increase with increasing r, and thus that $(\epsilon_p)^n \propto r^{\alpha^n_{\|}}$, where $\alpha^n_{\|} > 0$. We can therefore rewrite Eq. (5.34) as

$$S^{p}_{|n|||}(r) \propto r^{n/3+\alpha^n_{\|}}, \tag{5.35}$$

where $\alpha^n_{\|} > 0$. This indicates that scaling exponents for sufficiently strong gravity may exceed those predicted by K41, as was observed in figure 5.21.

Finally, we note that while we only consider longitudinal structure functions in this section, the transverse structure functions were also examined and were

seen to be affected by gravity in a similar manner. Refer to Part I for a detailed discussion of trends in the transverse velocity components without gravity.

Anisotropy in the relative velocity statistics

We finally consider the directional dependence of the relative velocity statistics. We here define the directionally dependent mean inward relative velocity as

$$S^{p}_{-\|}(\boldsymbol{r}) = S^{p}_{-\|}(r,\theta,\phi) \equiv -\int_{-\infty}^{0} w^{p}_{\|}\, p(w^{p}_{\|}|r,\theta,\phi) dw^{p}_{\|}, \tag{5.36}$$

where $p(w^{p}_{\|}|r,\theta,\phi)$ is the probability density function of the relative velocity conditioned on a separation magnitude r, a polar axis θ, and an azimuthal angle ϕ. The polar axis is taken to coincide with the orientation of gravity.

Figure 5.22 shows $S^{p}_{-\|}(r,\theta,\phi)/S^{p}_{-\|}(r)$ on a unit sphere for different values of St, $R_\lambda = 398$, and $r < \eta$. We see that the asymmetry in the relative velocities follows opposite trends at small and large St.

At small St, the relative velocities are largest for particles which are separated in the vertical direction. The physical explanation is as follows. At small separations, particle pairs which are separated vertically will have longitudinal relative velocities which are proportional to $A_{33}(\boldsymbol{x}^p(t),t)$, the longitudinal velocity gradient in the vertical direction as sampled by inertial particles (see §5.4.1). Particle pairs which are separated along the horizontal direction, however, will have longitudinal relative velocities which are proportional to $A_{11}(\boldsymbol{x}^p(t),t)$, the longitudinal velocity gradient in the horizontal direction. In §5.4.1, we observed that particles tend to preferentially sample flow where the vertical (horizontal) velocity gradients are larger (smaller). As a result, the relative velocities are

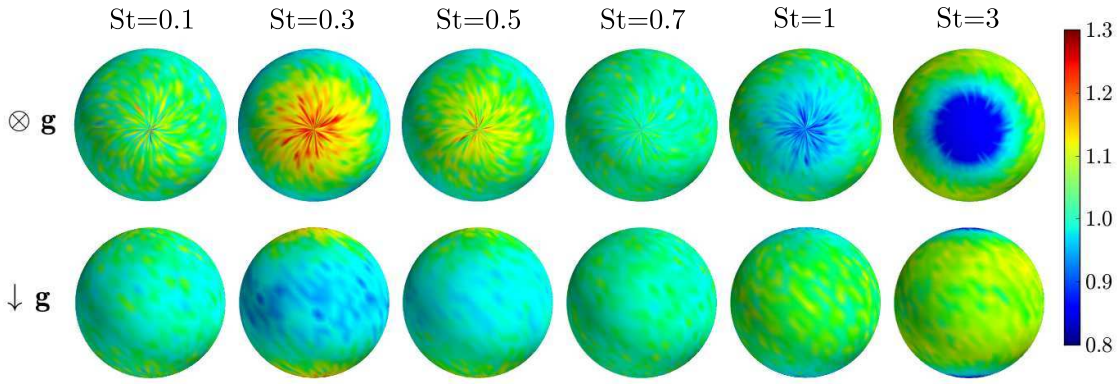

Figure 5.22: The directionally dependent mean inward relative velocity $S^p_{-\|}(r,\theta,\phi)$, normalized by the spherically averaged mean inward relative velocity $S^p_{-\|}(r)$, shown on a unit sphere for $R_\lambda = 398$ and $r < \eta$ with gravity ($Fr = 0.052$). The different columns correspond to different values of St. The top row shows the projection where gravity is directed into the page, and the bottom row shows the projection where gravity is directed downward.

larger (smaller) for particles which are separated in the vertical (horizontal) directions.

At large St, however, the relative velocities are smallest for particles which are separated vertically. The physical explanation is that the correlation timescales of the flow along this direction are the smallest (see §5.4.1), causing fluid velocity differences here to decorrelate the most rapidly, leading to lower particle relative velocities.

Figure 5.22 indicates that the relative velocity statistics are axisymmetric, as expected. We therefore represent them as a combination of axisymmetric spherical harmonic functions,

$$S^p_{-\|}(r,\theta,\phi) = \sum_{\ell=0}^{\infty} c^0_{2\ell}(r) Y^0_{2\ell}(\theta,\phi), \tag{5.37}$$

where $c^0_{2\ell}$ are the spherical harmonic coefficients and $Y^0_{2\ell}$ are the spherical har-

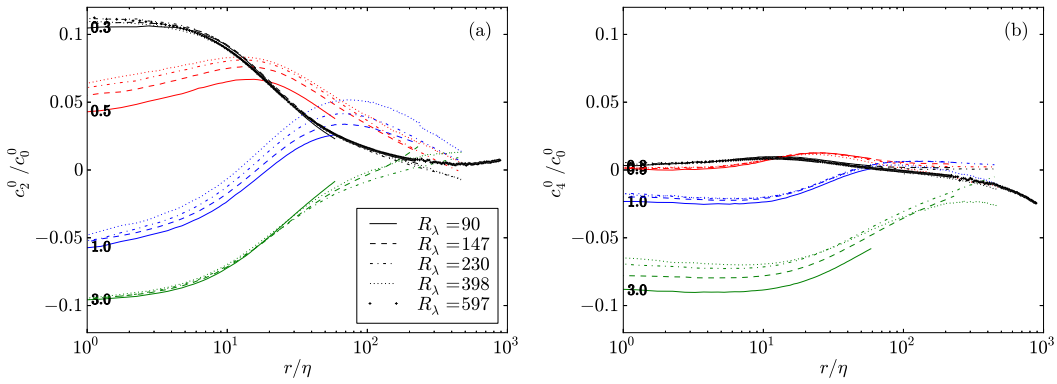

Figure 5.23: The second (a) and fourth (b) spherical harmonic coefficients of $S^p_{-||}(r,\theta,\phi)$, normalized by the zeroth spherical harmonic coefficient, plotted as a function of r/η for different St and R_λ with gravity ($Fr = 0.052$). The different values of St considered (0.3, 0.5, 1, 3) are shown in black, red, blue and green, respectively, and the Stokes numbers are indicated by the line labels.

monic functions. The spherical harmonic coefficients of order 2 and 4 are plotted in figure 5.23. (Coefficients above order 4 are comparatively small and are thus not shown.)

We see that the anisotropy in the relative velocities generally decreases with increasing separation. The physical explanation is that at large separations, the motion of particle pairs will generally be influenced by large, isotropic turbulent eddies, and the relative velocities induced by these eddies will generally be larger than any anisotropic velocities induced by gravity. At small separations, however, the turbulence-induced relative velocities are small, and therefore gravitational effects are expected to be more significant.

For small (large) values of St, c_2^0 and c_4^0 are positive (negative), indicating that the particle relative velocities are strongest for particles which are separated vertically (horizontally). These observations are in agreement with the trends shown in figure 5.22. We also see that c_2^0 and c_4^0 tend to become more (less)

isotropic at high (low) St as R_λ increases. While the physical explanation for the trend at low St is unclear, at high St, we expect that this increase in isotropy is linked to the increase in the relative velocities with increasing R_λ. That is, as the overall relative velocities increase, the anisotropic velocities induced by gravity will be comparatively weaker, and thus the particle relative velocities will be more isotropic.

5.5.2 Particle clustering

It is well-known that particles with inertia cluster in a turbulent flow field, both with and without gravity. In this section, we consider how gravity affects this clustering process. We first provide a theoretical explanation for the clustering (§5.5.2) and then compare our theory to DNS results (§5.5.2).

Theoretical framework for particle clustering

We use the angular distribution function $g(\boldsymbol{r})$ (hereafter 'ADF,' see [70]) to quantify the degree and orientation of particle clustering. We define $g(\boldsymbol{r})$ as

$$g(\boldsymbol{r}) = g(r,\theta,\phi) \equiv \frac{N(r,\theta,\phi)/V(r,\theta,\phi)}{N/V}. \tag{5.38}$$

In this equation, $N(r,\theta,\phi)$ denotes the number of particle pairs in a truncated spherical cone with nominal radius r, polar angle θ, and azimuthal angle ϕ. The volume of the truncated spherical cone $V(r,\theta,\phi)$ is given by

$$V(r,\theta,\phi) \equiv \sin(\theta)\Delta\theta\Delta\phi\left[(r+\Delta r)^3 - (r-\Delta r)^3\right]/3,$$

where Δr is the radial width, $\Delta\theta$ is the extent of the polar angle, and $\Delta\phi$ is the extent of the azimuthal angle.

By integrating the ADF over θ and ϕ and averaging, we recover the spherically symmetric radial distribution function ('RDF') $g(r)$ [110, 161], defined as

$$g(r) \equiv \frac{N(r)/V(r)}{N/V}, \tag{5.39}$$

where $N(r)$ is the number of particle pairs in a spherical shell with radius r and radial width Δr, $V(r) = 4\pi/3\left[(r+\Delta r)^3 - (r-\Delta r)^3\right]$ is the volume of the shell, N is the total number of particle pairs, and V is the total volume (refer to Part I for a more complete discussion).

As shown in §5.5.1, the equation governing the relative motion of like particles (Eq. (5.27)) is the same with and without gravity. A consequence of this is that theories describing the positions and relative velocities of like particles are identical in form for systems with and without gravity. We therefore consider the effect of gravity on the theoretical model of [198] (which was developed for systems without gravity) to predict the behavior of $g(\boldsymbol{r})$ in the presence of gravity. From [198, 24], the equation describing $g(\boldsymbol{r})$ at steady-state is

$$\mathbf{0} = -St\tau_\eta\left(\boldsymbol{S}_2^p + \boldsymbol{\lambda}\right) \cdot \boldsymbol{\nabla}_r g - St\tau_\eta g \boldsymbol{\nabla}_r \cdot \boldsymbol{S}_2^p, \tag{5.40}$$

where $\boldsymbol{\lambda}$ is a dispersion tensor describing the influence of the fluid velocity difference field on the dispersion of the particles (see [24]).

Since §5.5.1 indicates that the particle phase is anisotropic with gravity, to predict the ADF $g(\boldsymbol{r})$ from Eq. (5.40), we would first need to compute the full tensor $\boldsymbol{S}_2^p$ for every possible orientation of $\boldsymbol{r}$, and then solve for $g(\boldsymbol{r})$ over these different orientations. To simplify, however, we take the spherical average of Eq. (5.40) and use the resulting equation to predict the RDF $g(r)$. (Note that a similar approach was adopted in [3] to model particle clustering based on Eq. (5.40) in a homogeneous turbulent shear flow.) We will test the accuracy of this method in §5.5.2.

The isotropic form of Eq. (5.40) is

$$0 = -St\left(\hat{S}^{p}_{2\parallel} + \hat{\lambda}_{\parallel}\right)\nabla_{\hat{r}}g - Stg\left(\nabla_{\hat{r}}\hat{S}^{p}_{2\parallel} + 2\hat{r}^{-1}\left[\hat{S}^{p}_{2\parallel} - \hat{S}^{p}_{2\perp}\right]\right), \tag{5.41}$$

where $\hat{Y}$ denotes a variable Y normalized by Kolmogorov units. $\lambda_{\parallel}$ denotes the projection of the dispersion tensor $\boldsymbol{\lambda}$ along a direction parallel to the particle separation vector.

In [24], it was shown that for $St \ll 1$, Eq. (5.41) simplifies to

$$0 = -15B_{nl}\hat{S}^{f}_{2\parallel}\nabla_{\hat{r}}g - \frac{St}{3}\hat{r}g\left(\langle\hat{\mathcal{S}}^{2}\rangle^{p} - \langle\hat{R}^{2}\rangle^{p}\right), \tag{5.42}$$

where B_{nl} is the non-local coefficient, as defined in [32], and $\hat{S}^{f}_{2\parallel}$ is the second-order longitudinal relative velocity structure function at fixed points in an Eulerian reference frame with separation r. We noted that the first term on the right-hand-side is associated with an outward particle diffusion (which acts to decrease the RDF) and the second term on the right-hand-side is associated with an inward particle drift (which acts to increase the RDF).

We expect the first term to unaffected by gravity (since it depends only on the Eulerian velocity field). Based on §5.4.1, however, we see that gravity reduces the drift term by reducing $\langle\mathcal{S}^{2}\rangle^{p} - \langle\mathcal{R}^{2}\rangle^{p}$. We therefore expect the clustering at low St to decrease with gravity.

We also note that at low St, the trends in the strain and rotation rates with R_{λ} are very weak and are the same both with and without gravity. In Part I, we showed that these trends caused the clustering at low St to be independent of R_{λ} without gravity. We therefore expect the degree of clustering at low St to also be independent of R_{λ} when gravity is present.

We next use Eq. (5.41) to understand clustering at larger values of St. In Part I, we argued that without gravity, $\hat{S}^{p}_{2\parallel} \approx \hat{S}^{p}_{2\perp}$ for $St \gtrsim 0.3$, and we were thus able

to neglect the term $2\hat{r}^{-1}(\hat{S}^p_{2\parallel} - \hat{S}^p_{2\perp})$ in Eq. (5.41) at high St. However, with the addition of gravity, the longitudinal and transverse relative velocity variances are generally not equal (as discussed in §5.5.1), and this term must be retained in the analysis here. We are still able to neglect $\hat{\lambda}_\parallel$ at small separations and high St, however, since this term is inversely proportional to St and decreases as the timescales of the fluid velocity field seen by the particle decrease (see [24]).

The simplified form of Eq. (5.41) at high St is then

$$0 = -St\hat{S}^p_{2\parallel}\nabla_{\hat{r}}g - Stg\left(\nabla_{\hat{r}}\hat{S}^p_{2\parallel} + 2\hat{r}^{-1}\left[\hat{S}^p_{2\parallel} - \hat{S}^p_{2\perp}\right]\right). \tag{5.43}$$

We take the ratio of the drift and diffusion coefficients to analyze the trends in the clustering. Changes in this ratio as we go to a new state (e.g., by changing gravity or the Reynolds number) indicate that the drift and diffusion mechanisms are unequally affected, which in turns alters the degree of clustering. In particular, an increase (decrease) in this ratio will correspond to an increase (decrease) in clustering. We therefore have

$$\frac{\nabla_{\hat{r}}\hat{S}^p_{2\parallel} + 2\hat{r}^{-1}\left[\hat{S}^p_{2\parallel} - \hat{S}^p_{2\perp}\right]}{\hat{S}^p_{2\parallel}} = \frac{1}{\hat{r}}\left(\zeta^2_\parallel + 2 - 2\hat{S}^p_{2\perp}/\hat{S}^p_{2\parallel}\right), \tag{5.44}$$

where $\zeta^2_\parallel$ is the scaling exponent of the longitudinal relative velocity variance (see §5.5.1). Eq. (5.44) implies that that increases (decreases) in the RDFs at high St are linked to increases (decreases) in $\zeta^2_\parallel - 2\hat{S}^p_{2\perp}/\hat{S}^p_{2\parallel}$.

We now use Eq. (5.44) and DNS relative velocity statistics to predict how $g(r)$ will be affected by changes in gravity and R_λ at high St. From §5.5.1, we see that when gravity is added, $\zeta^2_\parallel$ increases very strongly, while $2\hat{S}^p_{2\perp}/\hat{S}^p_{2\parallel}$ increases weakly. We attributed these trends to the fact that gravity reduces the influence of path-history effects. We expect that $\zeta^2_\parallel - 2\hat{S}^p_{2\perp}/\hat{S}^p_{2\parallel}$ will therefore increase with gravity, leading to an increase in the clustering.

Note that this reversal in the effect of gravity on clustering at high and low St is a consequence of the fact that gravitational effects are stronger on the drift mechanism at low St than they are on the diffusion mechanism, but that the opposite occurs at higher St when the caustic contribution to the particle relative velocities dominates [24]. In other words, at low St, gravity causes the ratio between the drift and diffusion to decrease (and thus decreasing the clustering), while at higher St, gravity causes the ratio between the drift and diffusion to increase (and thus increasing the clustering). Without this reversal in the relative effect of gravity on the ratio between the drift and diffusion, the clustering would be uniformly affected by gravity for all St.

We also see from §5.5.1 that with gravity, increasing R_λ generally leads to a decrease in both $\zeta_\parallel^2$ and $\hat{S}^p_{2\perp}/\hat{S}^p_{2\parallel}$, due to the increased influence of path-history effects at higher Reynolds numbers. While both quantities seem to be decreased by about the same amount as R_λ increases, the latter quantity has a greater effect on the clustering, since it is multiplied by a factor of two in Eq. (5.44). We therefore expect the ratio between the drift and diffusion to increase as R_λ increases, leading to a decrease in the clustering.

In summary, we expect that gravity will reduce the inward particle drift by reducing the effect of preferential concentration at low St and will thereby decrease the clustering here. The RDFs at low St are also expected to be independent of R_λ. At high St, gravity will increase the ratio between the drift and the diffusion by making path-history effects less important, causing the clustering to increase. We also predict that the clustering at high St will increase with increasing R_λ.

We now compare our arguments regarding the effect of gravity on cluster-

ing to existing explanations in the literature. At low St, our explanation for the trends in the clustering is similar to the one proposed by [59, 6, 185, 119, 141]; namely, that gravity causes particles to have shorter interaction times with the underlying turbulence and thereby reduces particle clustering. At high St, however, several authors have argued that gravity facilitates interactions with large-scale turbulent eddies, which in turn leads to increased particle clustering [59, 185, 141]. We argue, however, that gravity reduces the importance of path-history interactions, and therefore causes particles to be *less* affected by their interactions with larger-scale turbulence. In fact, our explanations suggest that this reduced path-history interaction is the cause of the increased clustering at high St with gravity.

Another recent explanation for the increased clustering at high St with gravity is given in [127], where the authors argue that this enhanced clustering is linked to the skewness of the vertical velocity gradients of the underlying fluid. Our results, however, indicate that for $St \gtrsim 1$, the particle velocities are strongly affected by non-local, path-history effects at small separations (see §5.5.1), and thus we expect that the local fluid velocity gradients will have a weak or negligible effect on the particle clustering. In addition, [73] observed qualitatively similar strong clustering of high-St particles in the presence of gravity, and their studies were conducted in a Gaussian flow field (whose velocities by definition have no skewness). Our findings and those of [73] therefore cast doubt upon any causal connection between particle clustering at high St with gravity and the skewness of the underlying flow field.

Particle clustering results

Before using DNS to quantify the degree of particle clustering, it is helpful to examine instantaneous snapshots of particle positions in the simulations in figure 5.24. From these visualizations, it is evident that gravity alters both the degree and orientation of the clusters, and generally causes them to be aligned with the gravity vector. We emphasize that this clustering at large St with gravity is unrelated to the centrifuging mechanism explained in [106]. For example, while figure 5.24 indicates that clustering is strong with gravity for $St \geq 1$, figure 5.2 indicates that such particles uniformly sample the underlying strain and rotation fields. This is consistent with recent theoretical explanations for clustering which argue that when $St \ll 1$, the centrifuge mechanism gives way to a non-local clustering mechanism that does not depend upon preferential sampling of the turbulent velocity field [72, 24].

We first consider RDFs to provide a leading-order measure of the clustering, and later consider ADFs to investigate the anisotropy and directional dependence of the clusters. In figure 5.25, we plot the RDFs for $St = 0.3$ and $St = 3$ both with gravity ($Fr = 0.052$) and without gravity at $R_\lambda = 398$. Our DNS shows that when gravity is included, the RDFs decrease (increase) at low (high) values of St, in agreement with our arguments in §5.5.2 and the findings of [59, 6, 185, 119, 141, 17, 73]. For sufficiently large separations, the RDFs with and without gravity become equivalent.

To test the theory above quantitatively, we compute $g(r)$ from Eq. (5.41). We do so by prescribing DNS data for the relative velocities $S^p_{2\parallel}$ and $S^p_{2\perp}$. In addition, we use the directionally averaged strain timescales $T_{S^pS^p}$ from the DNS (see §5.4.1) and the non-local closure proposed in [24] to compute the dispersion

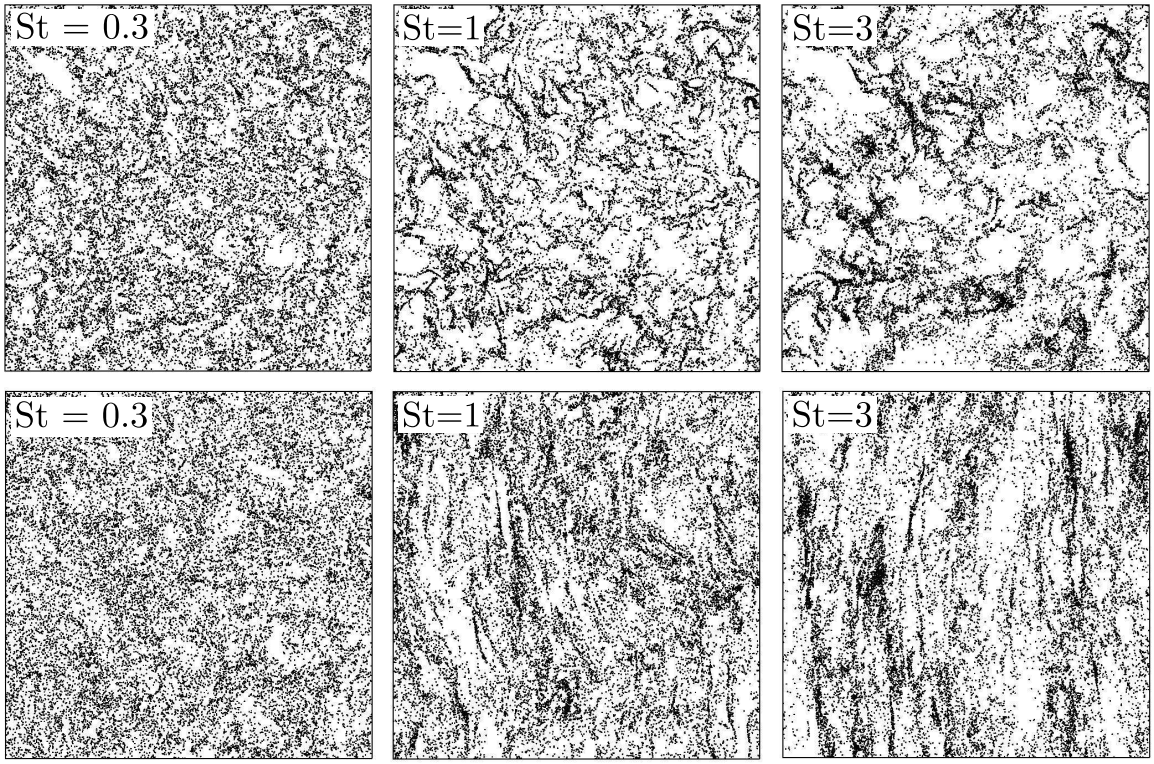

Figure 5.24: Instantaneous particle locations in $1000\eta \times 1000\eta \times 10\eta$ slices of the domain for different values of St and $R_\lambda = 398$. The top row is for the case without gravity, and the bottom row is for the case with gravity ($Fr = 0.052$), with the gravitational vector pointing downward.

tensor. This allows us to test the formulation of Eq. (5.41) and the theoretical arguments above. Figure 5.25 shows that the theory captures the quantitative results in the DNS well, indicating Eq. (5.41) is an accurate model even with an anisotropic particle phase, and thus verifying our physical explanations in §5.5.2.

Next, we consider the dependence of the RDFs on R_λ in figure 5.26. As was the case without gravity (see Part I), the RDFs are largely independent of R_λ for $St \lesssim 1$ with gravity (figure 5.26(a)). This is in agreement with our arguments above and implies that small-St clustering is a small-scale phenomenon (both

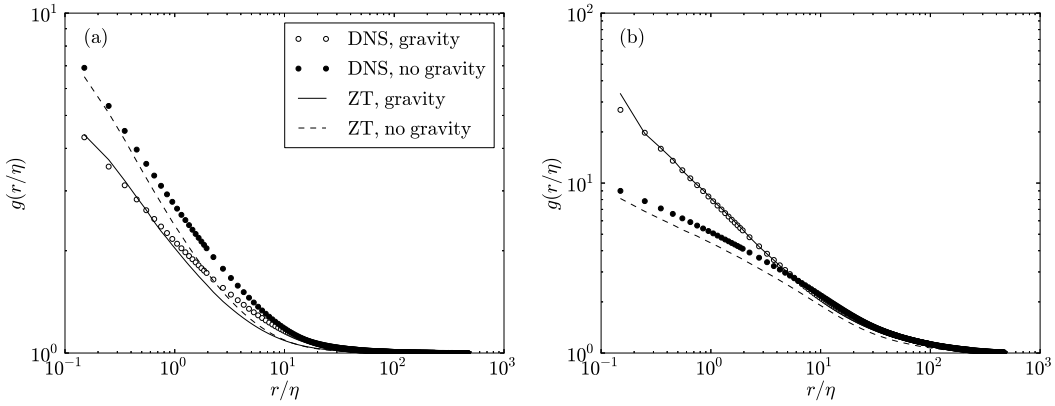

Figure 5.25: DNS (symbols) and theoretical (lines) data for the RDFs g plotted as a function of r/η at $R_\lambda = 398$ both with gravity (open symbols and solid lines) and without gravity (filled symbols and dashed lines). (a) shows RDFs for $St = 0.3$, and (b) for $St = 3$. The theoretical predictions are calculated from the equations in [198] with the non-local correction from [24], using our DNS data to specify $T_{\mathcal{SS}}$, $S^p_{2\parallel}$, and $S^p_{2\perp}$.

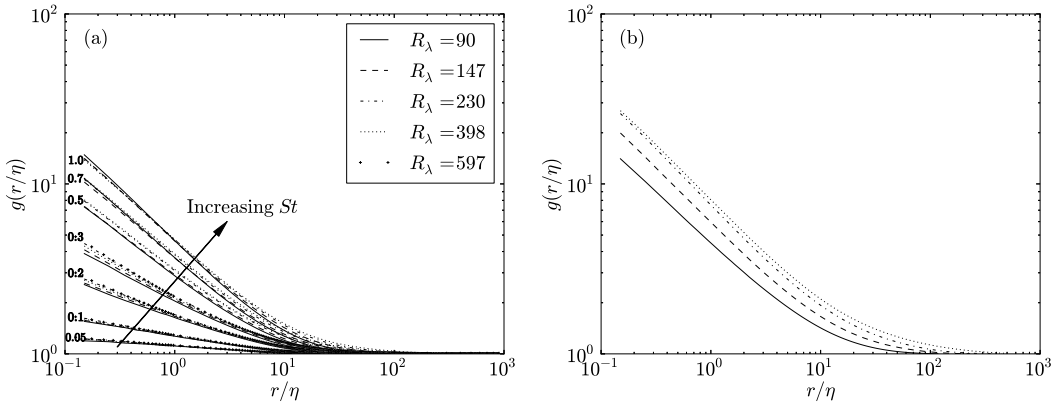

Figure 5.26: The RDFs g plotted as a function of r/η for different R_λ for $St \leq 1$ (a) and for $St = 3$ (b). The Stokes numbers in (a) are indicated by the line labels.

with and without gravity) that is generally unaffected by the intermittency of the turbulence. At larger St (figure 5.26(b)) the RDFs increase monotonically with increasing R_λ, since the ratio between the drift and diffusion increases, as explained above.

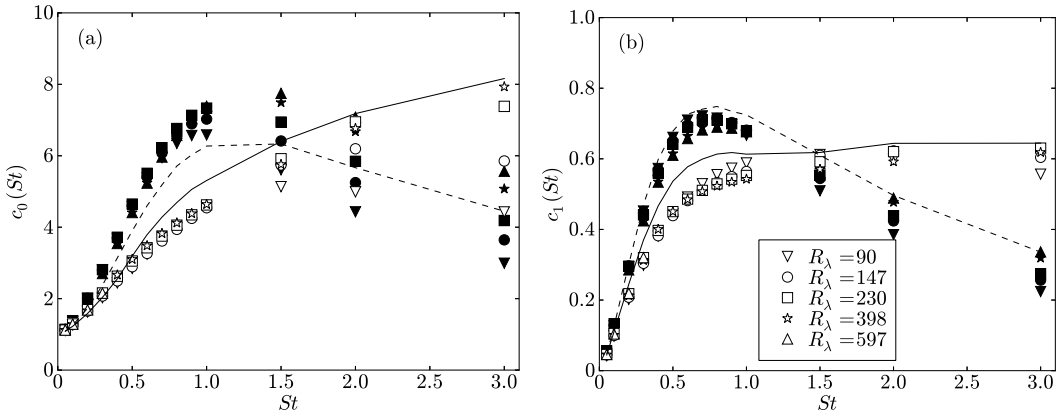

Figure 5.27: The prefactor c_0 (a) and the exponent c_1 (b) of the power-law fits of the RDFs using Eq. (5.45). Open symbols denote data with gravity ($Fr = 0.052$), and filled symbols denote data without gravity. The predictions from [198] for $R_\lambda = 398$ (where DNS data are used to specify the relative velocities and the strain timescales here) are shown with solid lines (gravity) and dashed lines (no gravity).

We can also quantify the degree of small-scale clustering by performing a power-law fit of the RDFs [137] at small separations,

$$g(r) \approx c_0 \left(\frac{\eta}{r}\right)^{c_1}, \tag{5.45}$$

as was discussed in Part I. The power-law fits are performed over the range $0.75 \leq r/\eta \leq 2.75$, and the calculated values of c_0 and c_1 are plotted in figure 5.27. We observe that both the power-law coefficient c_0 and the exponent c_1 decrease when gravity is introduced for $St \lesssim 1.5$ and increase when gravity is introduced for $St \gtrsim 1.5$, consistent with our explanations above. The theoretical model for $g(r/\eta)$ from Eq. (5.41) (with the relative velocities and strain timescales specified from the DNS) is in good agreement with the DNS data, both with and without gravity. We also note that our DNS results for the exponent c_1 agree well with those of [141] and [17] (not shown).

To further investigate the two-parameter space of particle inertia and grav-

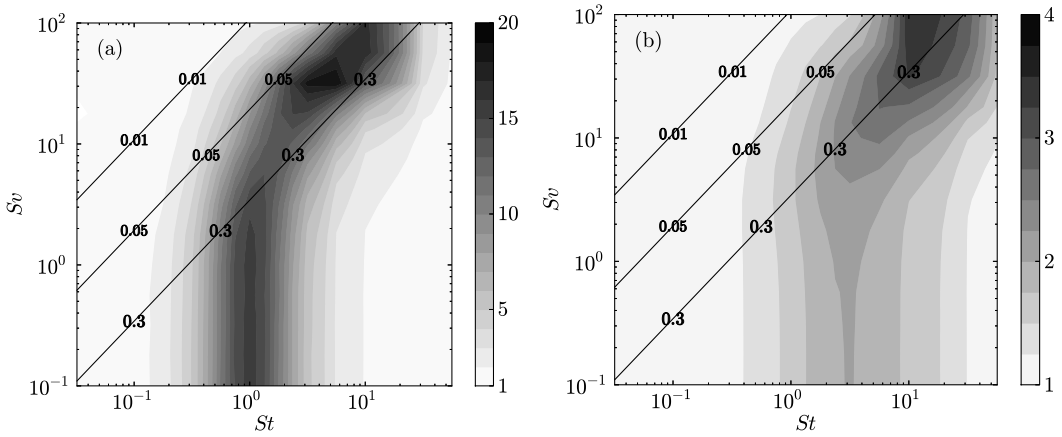

Figure 5.28: Filled contours of the RDF evaluated at $r/\eta = 0.25$ (a) and $r/\eta = 9.75$ (b) for different values of St and Sv, for $R_\lambda = 227$. The diagonal lines denote three different values of Fr, corresponding to conditions representative of stratiform clouds ($Fr = 0.01$), cumulus clouds ($Fr = 0.05$), and cumulonimbus clouds ($Fr = 0.3$).

ity, we consider the RDFs at $R_\lambda = 227$ for $0 < St \leq 56.2$ and $0 < Sv \leq 100$ in figure 5.28. While the particle clustering behavior here is generally complex and varies strongly with St and Sv, we are able to provide physical explanations for some of the observed trends. For $St \gg 1$, the RDFs generally decrease with increasing St, since the particles become unresponsive to almost all of the underlying turbulence, as expected. Also, for $St < 1$, the RDFs tend to decrease with increasing Sv, since preferential sampling effects tend to be reduced by gravity (see §5.4.1). We also see that for $1 < St < 10$, the RDFs generally increase with increasing Sv, as expected, since gravity increases the ratio between the drift and the diffusion, as explained above.

It is important to note, however, the results presented in figure 5.28 are likely in considerable quantitative error for large values of St and Sv and only are meant to provide a qualitative picture of particle clustering here, since the assumption that these particles are infinitesimal points subjected to linear drag

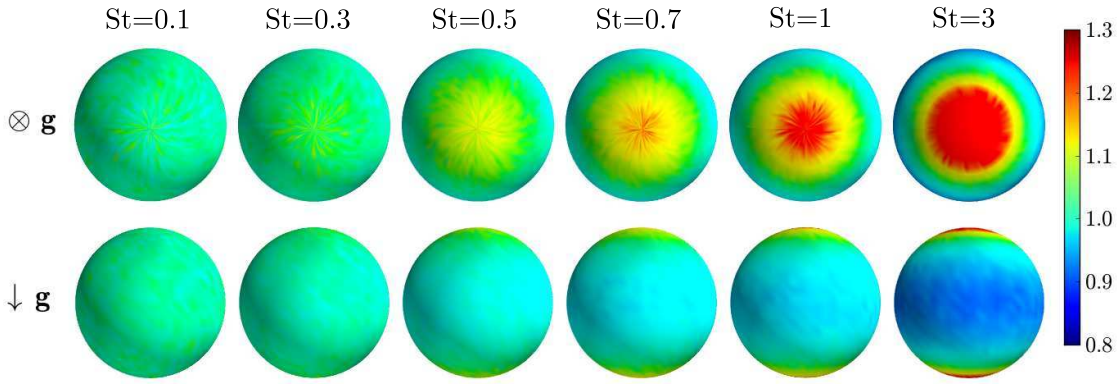

Figure 5.29: The ADF $g(r, \theta, \phi)$ (normalized by the RDF $g(r)$) shown on a unit sphere for $R_\lambda = 398$ and separations $r < \eta$ with gravity ($Fr = 0.052$). The different columns correspond to different values of St. The top row shows the projection where gravity is directed into the page, and the bottom row shows the projection where gravity is directed downward.

(refer to §5.3.2) breaks down (see [66]) and the effects of the domain periodicity are likely severe (see Appendix A).

We now consider the full ADFs $g(r, \theta, \phi)$, where the polar axis is taken to coincide with the gravitational direction. We plot the three-dimensional ADFs (normalized by the spherically symmetric RDFs) in figure 5.29 for various values of St with gravity ($Fr = 0.052$) at $R_\lambda = 398$.

In accord with our qualitative observations from figure 5.24, we see that particle clustering is strongest along the vertical direction, in agreement with the findings of [44, 17, 127]. At low St, the anisotropic clustering is caused by the fact that particles tend to preferentially sample downward-moving flow (see §5.4.2). [17] showed that this preferential sampling causes particles to form vertical clusters when St is small.

When St is large, the effects of preferential sampling vanish, and the

anisotropy is related to the way gravity influences path-history effects. In §5.5.1, we saw that at high St, gravity causes the relative velocities of vertically separated particles to be smaller than the relative velocities of horizontally separated particles. Since our arguments in §5.5.2 are only developed to describe the spherically averaged clustering, we are unable to use them to predict these trends. However, we note that Eq. (5.40) implies the reduced vertical relative velocities are evidently causing the ratio between the drift and the diffusion to be larger in the vertical direction.

We also note that the anisotropy tends to increase with increasing St. The physical explanation is that as St (and thus Sv) increases, gravitational forces become more significant, causing the particle motion to be more anisotropic. We expect that at some point, the particles will become so large that they are unaffected by underlying turbulence, and thus the clustering and clustering anisotropy will vanish.

Since the ADFs are axisymmetric about the vertical direction, we quantify the anisotropy of particle clustering by decomposing the ADFs into a series of axisymmetric spherical harmonic functions,

$$g(r,\theta,\phi) = \sum_{\ell=0}^{\infty} c_{2\ell}^{0}(r) Y_{2\ell}^{0}(\theta,\phi), \tag{5.46}$$

where $c_{2\ell}^{0}$ are the spherical harmonic coefficients and $Y_{2\ell}^{0}$ are the spherical harmonic functions.

The spherical harmonic coefficients c_2^0 and c_4^0 are plotted in figure 5.30 (coefficients above order four are much smaller and are not shown). In agreement with figure 5.24, we see that the anisotropy increases with increasing St. We also observe that as r/η increases, the anisotropy goes to zero, since both the clustering and the clustering anisotropy vanish as the separation increases.

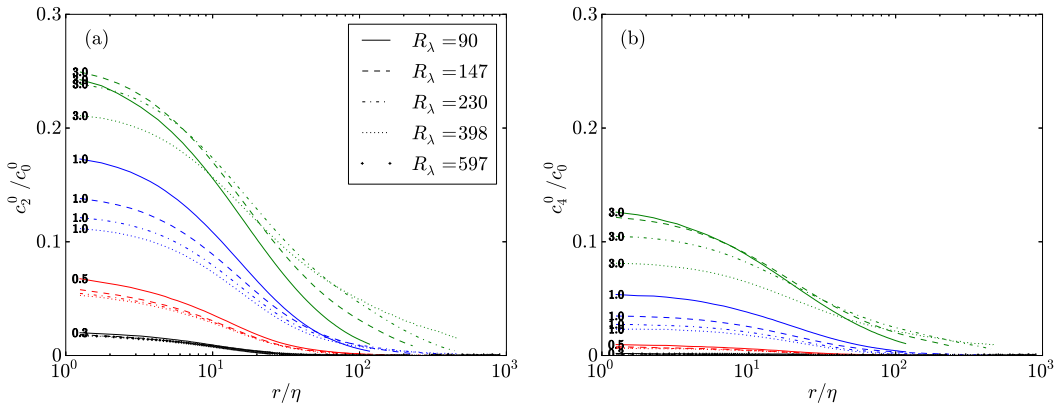

Figure 5.30: The second (a) and fourth (b) spherical harmonic coefficients of the angular distribution function, normalized by the zeroth spherical harmonic coefficient, plotted as a function of r/η, for different St and R_λ with gravity ($Fr = 0.052$). The different values of St considered (0.3, 0.5, 1, 3) are shown in black, red, blue and green, respectively, and the Stokes numbers are indicated by the line labels.

The degree of anisotropy is also Reynolds-number-dependent and decreases with increasing R_λ for larger values of St. Since the relative velocities of high-St particles generally also tend to become more isotropic as R_λ increases (see §5.5.1), it is likely that the reduction in the anisotropy of the relative velocities will cause a similar reduction in the anisotropy of the clustering.

5.5.3 Particle collision kernels

The final two-particle statistic we consider is the kinematic collision kernel K for inertial particles. [161, 178] showed that for an isotropic particle field, K is proportional to the product between the spherically averaged RDF and mean inward radial relative velocity,

$$K(d) = 4\pi d^2 g(d) S^p_{-\|}(d), \tag{5.47}$$

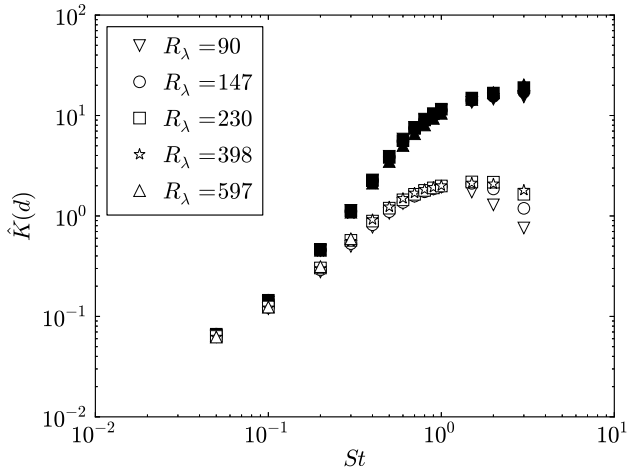

Figure 5.31: The non-dimensional collision kernel $\hat{K}(d)$ plotted as a function of St for different values of R_λ. The open symbols denote data with gravity ($Fr = 0.052$), and the filled symbols denote data without gravity.

where d is the particle diameter. In Appendix B, we show mathematically that Eq. (5.47) holds even for an anisotropic particle phase. As in Part I, we plot the non-dimensional collision kernel $\hat{K}(d) = K(d)/(d^2 u_\eta)$ in figure 5.31 (see also [172]). Note that while we simulate only point particles, we calculate d from St by prescribing the density ratio $\rho_p/\rho_f = 1000$. Since our statistics are generally not sufficient to compute the RDFs and relative velocities at separations on the order of the particle diameter, we fit both quantities using linear least-squares power-law regression and extrapolate the resulting power-law fits to $r = d$ (refer to [141]).

Figure 5.31 indicates that the collision kernel is reduced with gravity. At low St, the RDFs and the relative velocities both decrease with gravity, thereby decreasing the collision kernel. At higher St, the strong decreases in the relative velocity with gravity (see §5.5.1) overwhelm the slight increases in clustering here (see §5.5.2), causing the collision kernel to decrease. Finally, we note that at

large St with gravity, the collision rates increase with increasing R_λ, since both the relative velocities and RDFs are larger at higher Reynolds numbers.

We found in Part I that $\hat{K}(d)$ is independent of ρ_p/ρ_f for $St \gtrsim 1$ without gravity, in agreement with [172]. The physical explanation is that $g(d)$ and $S^p_{-\|}(d)/u_\eta$ are either independent of d (for $St \geq 10$) or have opposite scalings with d (for $1 \lesssim St \leq 3$). With gravity, however, path-history effects are suppressed, and these quantities have different scaling behaviors (see §5.5.1 and §5.5.2). We therefore find (not shown) that with gravity, $\hat{K}(d)$ depends strongly on ρ_p/ρ_f at all values of St considered.

Next, we expand our parameter space to consider the collision kernel for $0 < St \leq 56.2$ and $0 < Sv \leq 100$ at $R_\lambda = 227$ in figure 5.32. We note that these results should be treated with caution, especially at large St and Sv, since the statistics are likely artificially affected by the periodicity of the domain (see Appendix A), and the linear drag model used (refer to §5.3.2) is likely inaccurate here (e.g., see [66]). In addition, we calculated the collision kernels by assuming that the RDFs and relative velocity statistics can be extrapolated to separations $r = d$ using power-law fits, an assumption which is questionable for $St > 3$ (as discussed in Part I). Nevertheless, we can use the data in figure 5.32 to discern the qualitative trends in the collision kernel for different degrees of inertia and gravity.

In agreement with our observations above, we see that the collision kernel generally increases with increasing St and generally decreases with increasing gravity (i.e., increasing Sv and decreasing Fr). One practical implication is that at a given value of St, cumulonimbus clouds ($Fr \approx 0.3$) will have more frequent droplet collisions and growth than stratiform clouds ($Fr \approx 0.01$).

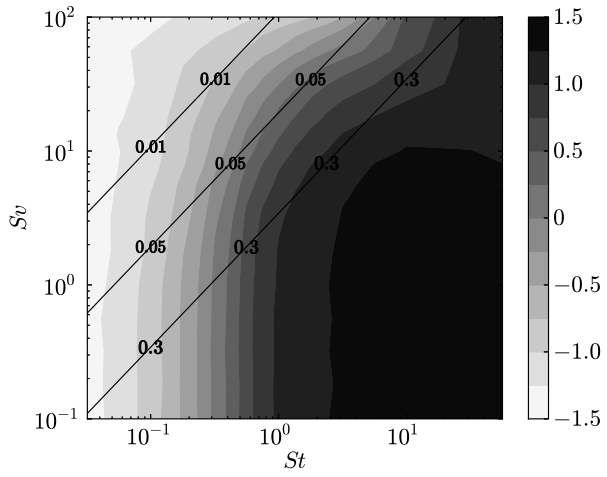

Figure 5.32: Filled contours of $\hat{K}(d)$ for different values of St and Sv at $R_\lambda = 227$. The contours are logarithmically scaled, and the colorbar labels indicate the exponents of the decade. The diagonal lines denote three different values of Fr, corresponding to conditions representative of stratiform clouds ($Fr = 0.01$), cumulus clouds ($Fr = 0.05$), and cumulonimbus clouds ($Fr = 0.3$).

We now consider the anisotropic collision kernel, $K(r, \theta, \phi)$, defined as

$$K(r, \theta, \phi) \equiv 4\pi r^2 g(r, \theta, \phi) S^p_{-\|}(r, \theta, \phi). \tag{5.48}$$

$K(r = d, \theta, \phi)$ provides a measure of the rate at which particles with diameter d collide along an orientation defined by the radial angle θ and azimuthal angle ϕ. We plot the ratio between $K(r, \theta, \phi)$ and its spherical average in figure 5.33 at $R_\lambda = 398$. (We are unable to show the anisotropic collision kernel at $r = d$ due to inadequate statistics at these small separations. We instead show data at $0 \leq r < \eta$, the smallest separation range over which adequate statistics are available.)

At low St, the collision kernel is approximately isotropic, since gravitational effects are weak. Interestingly, the collision kernel also tends toward isotropy at large St, due to the opposing trends in anisotropy of the relative velocities (see figure 5.22) and ADFs (see figure 5.29). For St between 0.1 and 1, particles are

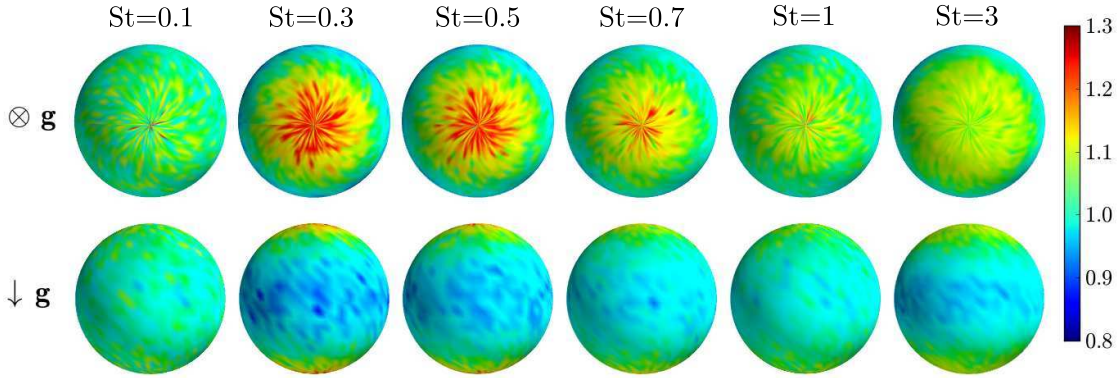

Figure 5.33: The anisotropic collision kernel $K(r, \theta, \phi)$ (normalized by the spherical average $K(r)$) shown on a unit sphere for $R_\lambda = 398$ and separations $r < \eta$ with gravity ($Fr = 0.052$). The different columns correspond to different values of St. The top row shows the projection where gravity is directed into the page, and the bottom row shows the projection where gravity is directed downward.

more likely to collide along the vertical direction, since both the ADFs and the relative velocities are strongest in the vertical direction for these values of St.

As we did in §5.5.1 and §5.5.2, we quantify the anisotropy by decomposing the collision kernel into a series of axisymmetric spherical harmonic functions,

$$K(r, \theta, \phi) = \sum_{\ell=0}^{\infty} c_{2\ell}^0(r) Y_{2\ell}^0(\theta, \phi). \tag{5.49}$$

We plot the second harmonic coefficient c_2^0 (normalized by the zeroth harmonic coefficient c_0^0) for different values of r in figure 5.34. (Coefficients above order two are very close to zero and are therefore not shown.) Note that, for a given particle class, the collision kernel is only strictly defined when $r = d$ (i.e., when the particles are in contact). Due to limitations in the number of particles that can be simulated, however, we are generally only able to consider values of $r > d$. We therefore plot c_2^0 as a function of r to discern the trends in this quantity and to help us extrapolate to smaller separations where particle contact occurs.

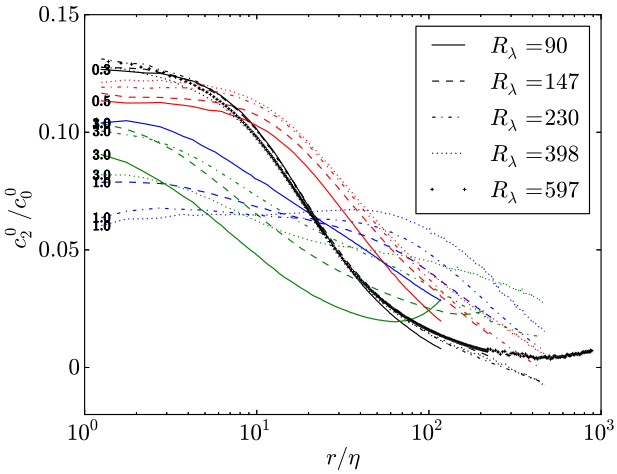

Figure 5.34: The second spherical harmonic coefficient of the collision kernel, normalized by the zeroth spherical harmonic coefficient, plotted as a function of r/η for different St and R_λ with gravity ($Fr = 0.052$). The different values of St considered (0.3, 0.5, 1, 3) are shown in black, red, blue and green, respectively, and the Stokes numbers are indicated by the line labels.

In agreement with figure 5.33, we see that the maximum anisotropy occurs around $St \approx 0.3$, and then decreases at higher values of St. The collision kernel anisotropy, unlike the collision kernel itself, seems to be dependent of the Reynolds number, since the anisotropy of both the ADFs and the relative velocities varies with R_λ.

Before closing this section, we emphasize two practical implications of these collision results for the cloud physics community. The first is that since the DNS indicates that the collision rates of particles with low and moderate St are independent of R_λ, it is likely that the collision kernels computed here will be useful for predicting droplet collisions in high-Reynolds-number atmospheric clouds. The second is that gravity significanly reduces the collision kernels for $St \gtrsim 0.1$. This implies that simulations without gravity can significantly overpredict the collision rates of droplets in atmospheric clouds, and highlights the need to in-

clude gravity in any analysis of collisional droplet growth in turbulent clouds.

5.6 Conclusions

In this study, we explored the influence of gravity on inertial particle statistics in isotropic turbulence. The simulations were performed over the largest Reynolds-number range ($90 \leq R_\lambda \leq 597$), domain lengths ($\mathcal{L}/\ell \lesssim 40$), and range of particle classes ($0 \leq St \leq 56.2$, $0 \leq Sv \leq 100$) to date. We showed that such large domain sizes are necessary to obtain accurate statistics of heavy particle motion, suggesting that that results of several published DNSs may be in quantitative error, and that accurate analysis of particle-laden turbulence with gravitational forces requires more computationally intensive simulations (see Appendix A).

Our results indicate that preferential sampling affects the dynamics of particles with $St \ll 1$, both with and without gravity, and that the particle velocity and acceleration variances at small St are equivalent to those of the fluid sampled by the particles. Gravity, however, decreases the degree of preferential sampling by limiting the interaction between the particles and the underlying turbulence, which in turn decreases the Lagrangian strain and rotation timescales along particle trajectories. We introduced and verified a model for these timescales, which were seen to be independent of R_λ.

As gravitational forces were increased, the particles fell rapidly through the flow, leading to smaller velocities and larger accelerations than in the case without gravity. We used the theory in [176] to model the velocity variances in the limit of strong gravity/weak turbulence, and developed a similar model for the

acceleration variances in this limit. Our model predictions were in excellent agreement with the DNS when $Sv \gg u'/u_\eta$. We also observed that the mean settling velocities in our DNS scaled according to the predictions in [17]. These mean settling velocity results, however, must be interpreted with caution at large St, since [66] showed that the settling behavior predicted by a linear drag particle model is qualitatively incorrect here.

We then used this knowledge of single-particle statistics with gravity to understand the effect of gravity on two-particle statistics relevant for predicting the collision kernel. At high St, we observed that gravity reduced the particle relative velocities from their values without gravity by limiting the influence of both path-history interactions. At low St, gravity acts primarily to reduce the degree of preferential sampling, causing the relative velocities at small separations to be closer to those of fluid particles.

Next, we related the trends in the relative velocities to the trends in the particle clustering by considering the effect of gravity on the model of [198]. With gravitational effects included, this model was able to predict the RDFs very accurately when DNS data was used to prescribe the relative velocities and the Lagrangian strain timescales. By analyzing this model at low St, we saw that the predominant effect of gravity is to decrease in the inward particle drift, leading to a decrease in the RDFs. At high St, however, gravity caused the ratio between the inward drift and the outward particle diffusion to increase by limiting the effect of path-history interactions. This led to an increase in clustering with gravity. We also found that the degree of clustering was generally independent of R_λ at low St, and increased with increasing R_λ at high St. The model of [198] was able predict these trends by relating them to the effect of path-history

interactions on the particle relative velocities.

We also quantified the degree and orientation of anisotropy in these two-particle statistics through spherical harmonic decompositions. Our results indicate that the particle angular distribution functions and radial relative velocities can have anisotropies on the order of 25%, with the degree of anisotropy generally peaking at small r/η. At larger separations, the relative velocities induced by turbulence become comparatively stronger, limiting the effect of gravity on particle dynamics.

We used these data for the RDFs and relative velocities to compute the particle collision kernel. As in Part I, we found that the collision kernel is generally independent of R_λ at low St, while it increases with increasing R_λ at high St. We analyzed the collision kernel using spherical harmonic decompositions, and found that the collision kernel is generally more isotropic than the ADFs and the mean inward relative velocities, since the anisotropies in the ADFs and the relative velocities have opposing trends at large St.

We conclude by highlighting some practical implications of this work for the cloud physics and turbulence communities and suggesting promising research directions. As in Part I, the fact that the collision rates are generally independent of R_λ for droplet sizes representative of those in warm, cumulus clouds suggests that the collision rates predicted here (for $R_\lambda \lesssim 600$) may agree well with those in atmospheric clouds ($R_\lambda \sim 10,000$). Of course, more simulations will be needed to verify this point at even higher Reynolds numbers. Also, as noted in §5.5.3, we observed that collision rates with gravity are considerably lower than those without gravity. This implies that many earlier studies which do not account for gravity are likely to substantially overpredict the collision rates.

While our study has primarily focused on the dynamics of like-sized particles, our results suggest that gravity may have a substantial effect of the collisions of different-sized particles. For example, we observed that gravity tends to enhance the settling speeds of particles with low and intermediate values of St. The coupling between turbulence and gravity may thereby increase the relative velocities of different-sized particles, leading to more frequent collisions. In addition, we found that gravity causes inertial particles in turbulence to experience large accelerations. [32] found that large accelerations can contribute to higher relative velocities between different-sized particles, thereby leading to more frequent collisions.

Finally, one especially promising finding of this study was that by extending the model of [198] and using DNS data to specify the Lagrangian strain timescales and relative velocities, we were able to accurately predict the RDFs both without gravity (as was also found in [24]) and with gravity. As noted in [25], however, this model provides poor approximations to the relative velocities of particles with moderate and large inertia. Future work should therefore be directed at improving these relative velocity predictions. In addition, while we developed a model for the strain and rotation timescales in the limit of large St with gravity, we generally require a model for all values of St. If accurate models can be developed for the relative velocities and the strain and rotation timescales over the entire range of St in atmospheric clouds, we will be able to use the theory of [198] to predict the RDFs without any inputs from the DNS, and will thereby be able to model the collision kernel accurately, both with and without gravity.

Acknowledgments

The authors gratefully acknowledge Garrett Good, Stephen Pope, and Parvez Sukheswalla for helpful discussions regarding this study. This work was supported by the National Science Foundation through CBET grants 0756510 and 0967349, and through a graduate research fellowship to PJI. Additional funding was provided by Cornell University. Computational simulations were performed on Yellowstone (ark:/85065/d7wd3xhc) at the U.S. National Center for Atmospheric Research [35] under grants ACOR0001 and P35091057, and on resources at the Max Planck Institute for Dynamics and Self-Organization. We are grateful to Denny Flieger for assistance with the computational resources at the Max Planck Institute.

CHAPTER 6

CONCLUSIONS

6.1 Summary

1. In §2 [84], we discussed the code we developed for the simulation of particle-laden turbulence. The code is the most efficient and general multiphase code of its kind and enables highly parallel simulations of high-Reynolds-number turbulence.

   (a) We implemented a two-dimensional domain decomposition to increase the granularity of the parallelization. The fluid solver was parallelized based on the P3DFFT library [128], and the particle solver was parallelized using efficient, ghost-cell communication.

   (b) We embedded a number of different interpolation methods for computing the particle velocities, and analyzed the computational expense and numerical accuracy of each.

   (c) We introduced an exponential integrator scheme for the particle update, which improves the accuracy of the particle solver, particularly when the characteristic timescales of the flow and particles differ by orders of magnitude.

2. In §3 [83], we performed the first computational study of the dynamics of inertial particles across a shearless turbulence mixing layer, which is arguably the simplest inhomogeneous turbulent flow. This study was designed to mimic wind-tunnel experiments performed at Cornell [62, 65] and to provide insight into the mixing of water droplets near the boundaries of clouds.

(a) We observed that particle mixing was controlled by the large scales of the flow, independent of the Reynolds number. This suggests that low-Reynolds-number simulations may be able to accurately represent the mixing processes at the edges of highly turbulent atmospheric clouds.

(b) The degree of particle mixing was stronger for the turbulent–turbulent interface (TTI) and weaker for the turbulent–non-turbulent interface (TNI). This provides a physical understanding for the observation that the boundaries of turbulent clouds are generally sharp and well-defined.

(c) Under certain conditions, the mean profiles of the particle concentrations and particle velocities are self-similar. Given a relation for the growth of the mixing layer half-width, we can therefore predict these profiles at earlier and later stages in the flow evolution.

(d) The particles in the non-injection region were clustered on scales on the order of the integral lengthscale of the turbulence. This clustering resulted from the mixing and transport of the particles by large eddies and was seen to be unrelated to the commonly observed small-scale clustering of inertia particles in homogeneous turbulence.

(e) Gravity (unlike particle inertia) had a strong effect on the particle dynamics, and changes in the orientation of gravity relative to the interface led to substantial changes in the mean concentration profiles.

3. In §4 [81], we studied the effects of Reynolds number on inertial particle dynamics in isotropic turbulence when gravity was absent. We did so by performing simulations at the highest Reynolds number ever studied for inertial-particle-laden DNS.

(a) We analyzed the characteristics of the different regions of the flow sampled by inertial particles. We used this analysis and the model of [32] to understand the trends in the fluid strain and rotation rates, fluid kinetic energies, and fluid accelerations sampled by the particles at different Stokes numbers St and Reynolds numbers R_λ.

(b) We found that the models of [2] and [199] were able to accurately represent the effects of inertial filtering on particle kinetic energies and accelerations, respectively, when St was large. We used these models to explain the trends in these statistics with St and R_λ.

(c) The relative velocities of small-St particles are largely independent of R_λ in the dissipation range. The weak trends in the relative velocities with R_λ at higher values of St are due to the intermittency of the turbulence, non-local/path-history effects, and the role of inertial filtering.

(d) The radial distribution functions (RDFs) of particles with weak and moderate inertia are independent of R_λ, suggesting that small-scale clustering is driven almost entirely by the small-scale turbulence. The RDFs of higher-St particles increased with increasing R_λ, since the particle clustering here was affected by inertial-range scales and the size of the inertial range.

(e) We used the model of [198] to understand and predict the trends in the particle radial distribution functions (RDFs) with varying R_λ. The model provided excellent qualitative and quantitative predictions of the RDFs for $St \lesssim 3$ when DNS data was used to specify the particle relative velocities. We also tested two models from [32] against the DNS data, and the models (which do not account for path-history

effects) were seen to break down at much lower values of St than that of [198].

(f) The particle collision kernel is largely insensitive to the flow Reynolds number. This suggests that relatively low-Reynolds-number simulations may provide accurate representations of droplet collision processes in highly turbulent atmospheric clouds.

4. In §5 [82], we studied the effect of gravity on the dynamics of inertial particles in turbulence at various Reynolds numbers.

   (a) We observed that with gravity, the periodic boundary conditions can artificially affect the interactions between particles and underlying turbulence, which can in turn alter the particle kinetic energies, accelerations, strain and rotation timescales, relative velocities, and RDFs. We therefore performed the simulations on extended domain lengths to minimize these issues.

   (b) We found that gravity reduced the time particles spend interacting with straining and rotating regions of the flow, and hence lowered the degree of preferential sampling.

   (c) At high values of St, gravity acted to reduce the particle velocity variances, and the model of [176] was able to accurately predict the trends here.

   (d) The coupling between particle inertia, gravity, and turbulence can lead to large particle accelerations. We introduced two models to predict and understand these accelerations.

   (e) At high St, gravity led to a decrease in the particle relative velocities, which we attributed to the reduced influence of path-history interac-

tions. The particle relative velocities were generally independent of R_λ at low St and increased weakly with increasing R_λ at higher St.

(f) The RDFs, as in the case without gravity, were independent of R_λ at low St and increased with increasing R_λ at high St. We extended the model of [198] to account for gravitational effects, and found that this extended model was able to predict and quantify the trends in the RDFs with St and R_λ.

(g) Both the relative velocities and the RDFs were strongly anisotropic. We considered this anisotropy both visually and through spherical harmonic decomposition, and provided an explanation for many of the trends in the anisotropy of these statistics.

(h) We found that the particle collision kernel was generally independent of R_λ for $St \lesssim 1$, suggesting that (as in the case without gravity) low-Reynolds-number simulations may accurately capture the essential physics responsible for droplet collisions in clouds.

6.2 Conclusions and future research directions

When taken together, these studies indicate that relatively low-Reynolds-number simulations may provide accurate predictions of both large-scale particle mixing and small-scale particle collisions in atmospheric clouds. As computational capabilities evolve, larger simulations at higher Reynolds numbers should be used to verify that the mixing and collision processes are indeed independent of R_λ at conditions more representative of those in cumulus clouds ($R_\lambda \sim 10,000$).

Such large simulations, however, are impractical for use in global climate models, in which cloud growth and precipitation are treated as sub-grid processes. The cloud physics community is thus in need of accurate, computationally efficient models for predicting particle growth. One promising model is that of [198], which was used extensively in [81] and [82] to predict and understand the RDFs. However, we found (in agreement with [25]) that this model provides only poor predictions for the particle relative velocities. Future work should therefore be aimed at improving these predictions.

One important finding of these studies is that gravity can significantly impact the dynamics of inertial particles, and that neglecting gravity may cause leading-order errors in the predicted particle motions. Since much of the research to date in particle mixing and collisions has been done by assuming gravity is negligible, future work is needed to better understand and model the effect of gravity on particle distributions, velocities, and collision rates.

While this dissertation has mostly focused on the statistics of monodisperse populations of particles, some of the findings in §5 suggest that bidisperse and polydisperse particle populations may exhibit large collision rates and rapid droplet growth, which in turn could partially explain the rapid growth of the droplet size distribution in warm, cumulus clouds. Specifically, the findings in [82] indicate that gravity can increase droplet settling speeds and accelerations under certain conditions, which may in turn lead to higher relative velocities (see [69, 32]). The datasets generated in [82] could therefore be used to systematically explore the relative velocities and collision rates of polydisperse particle populations.

As noted at the start of this dissertation, a primary motivation of this work

was to analyze the mechanisms responsible for droplet growth in warm, cumulus clouds. While these studies indicate that turbulence can enhance collision rates, and that the degree of enhancement is generally independent of R_λ, it is as yet unclear how these enhanced collision rates will quantitatively alter the coagulation and growth rates of droplets in cloud-like conditions. One way to investigate these questions would be to explicitly simulate these droplet collisions and the resulting growth of the droplet size distribution. Such an approach was taken about 15 years ago in [138], and the subsequent advances in computing capabilities now allow for simulations with more particles, with a broader range of particle classes, and with Reynolds numbers which are closer to those in atmospheric clouds.

APPENDIX A

PERIODICITY EFFECTS

As noted in [185], particle statistics in DNS may be artificially influenced by the periodicity of the domain when gravitational forces are strong. In particular, [185] estimated that periodicity effects become significant when the time it takes a particle to fall through the domain ($\sim \mathcal{L}\tau_p^{-1}g^{-1}$) is less than the large-eddy turnover time $T_L \equiv \ell/u'$, or equivalently, when

$$Sv = \frac{St}{Fr} \gtrsim \frac{\mathcal{L}}{\ell}\frac{u'}{u_\eta}. \tag{A.1}$$

In this case, particle can artificially encounter the same large eddy multiple times due to the finite domain length. We define St_{crit} as the value of St at which $St/Fr = \mathcal{L}u'/(\ell u_\eta)$. This roughly corresponds to the largest Stokes number at which we can expect the results to be unaffected by periodicity.

To study the effects of periodicity, we systematically increased the domain size for the cases at the three lowest Reynolds numbers, while keeping the large scales, small scales, and the forcing parameters the same. The simulation parameters are summarized in table A.1. For convenience, we will hereafter refer to the simulations from groups I, II, and III by their nominal Reynolds numbers of $R_\lambda \approx 90$, 147, and 230, respectively. In all cases, $0 \leq St \leq 3$ and $Fr = 0.052$.

The resulting energy spectra are shown in figure A.1. In all cases, forcing is applied deterministically to wavenumbers with magnitude $\kappa = \sqrt{2}$, and thus the location of the peak in the spectra is approximately the same for all domain sizes. The spectra are nearly identical to the right of the peak, indicating that the inertial- and dissipation-range flow scales remain unchanged. We notice that as the domain size increases, larger-scale (i.e., lower-wavenumber) flow features

Table A.1: Simulation parameters for the periodicity study.

	I				II			III	
R_λ	88	90	90	90	140	145	147	226	230
N	128	256	512	1024	256	512	1024	512	1024
$\mathcal{L}$	2π	4π	8π	16π	2π	4π	8π	2π	4π
$S\,t_{\text{crit}}$	1.06	2.06	4.26	8.55	1.39	2.69	5.55	1.78	3.39
ℓ	1.46	1.52	1.47	1.47	1.40	1.49	1.44	1.40	1.49
ℓ/η	55.8	57.7	55.7	55.6	106	111	107	202	213
u'	0.914	0.912	0.912	0.912	0.914	0.916	0.914	0.915	0.914
u'/u_η	4.77	4.81	4.82	4.82	6.01	6.12	6.15	7.60	7.70

become present. These features, however, account for very little of the overall energy, and thus they do not significantly affect the fluid statistics.

We first consider the effect of the domain size on the strain and rotation rates along particle trajectories. $\langle \mathcal{S}^2 \rangle^p$ and $\langle \mathcal{R}^2 \rangle^p$ (not shown) are generally invariant with changes in the domain size, since they are small-scale, single-time quantities. The Lagrangian strain and rotation timescales in figure A.2, however, appear to be over-predicted on the smaller domain sizes at large $S\,t$. The explanation is that these timescales involve integrals of the autocorrelations of the strain and rotation components (see Eq. (5.4)), and artificially high correlations can result when a particle is wrapped around a domain boundary, increasing the timescales. At the highest values of $S\,t$, our results suggest that the strain and rotation timescales have not yet converged to a grid-independent result, even though our scaling argument in Eq. (A.1) indicates that the Stokes numbers considered are generally well-below $S\,t_{\text{crit}}$. Since these timescales are very small ($\sim 0.1\tau_\eta$), their values can be significantly affected by very weak corre-

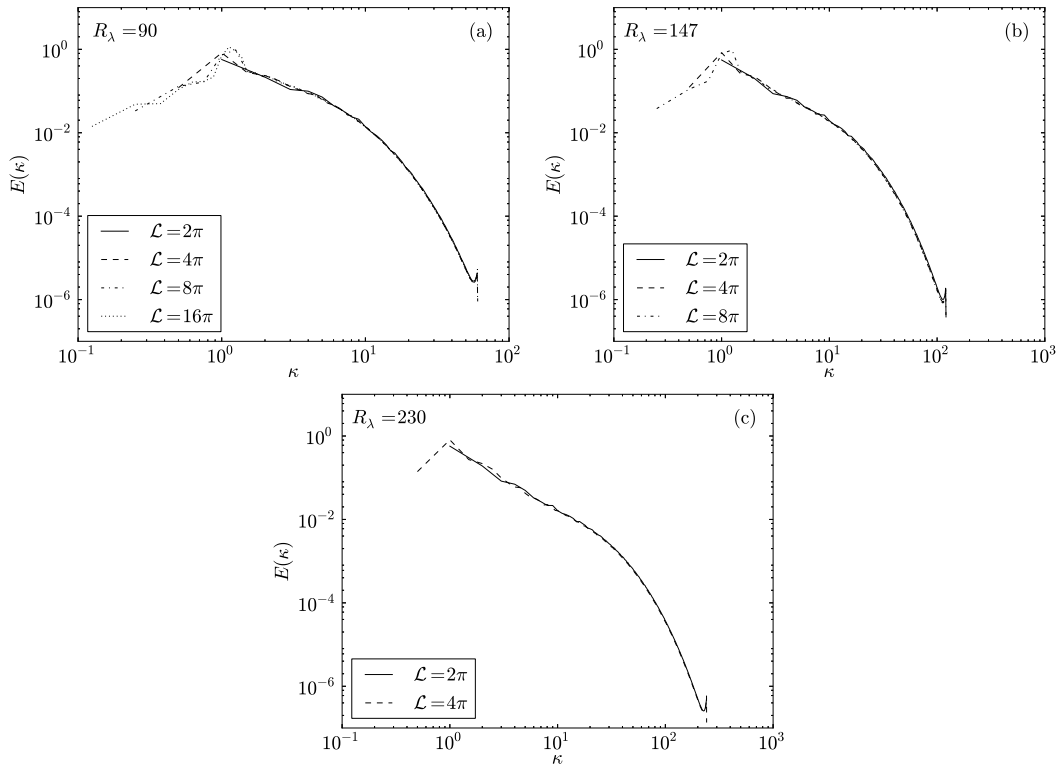

Figure A.1: Energy spectra for different domain lengths $\mathcal{L}$ and nominal Reynolds numbers R_λ = 90 (a), R_λ = 147 (b), and R_λ = 230 (c). All values are in arbitrary units.

lations induced by periodicity, and thus extremely large domain sizes may be necessary for these artificial correlations to vanish. We also see that our DNS timescales are considerably larger than the theoretical predictions from §5.4.1. While part of this discrepancy at large St is due to periodicity effects, it is also possible that the theory in §5.4.1 requires larger values of Sv than we are able to simulate here.

We next consider the effect of periodicity on large-scale velocity statistics. The turbulence-induced changes in the mean particle settling speeds (not shown) are independent of the domain size to within statistical noise. This is presumably because the turbulence-induced settling speed modifications of

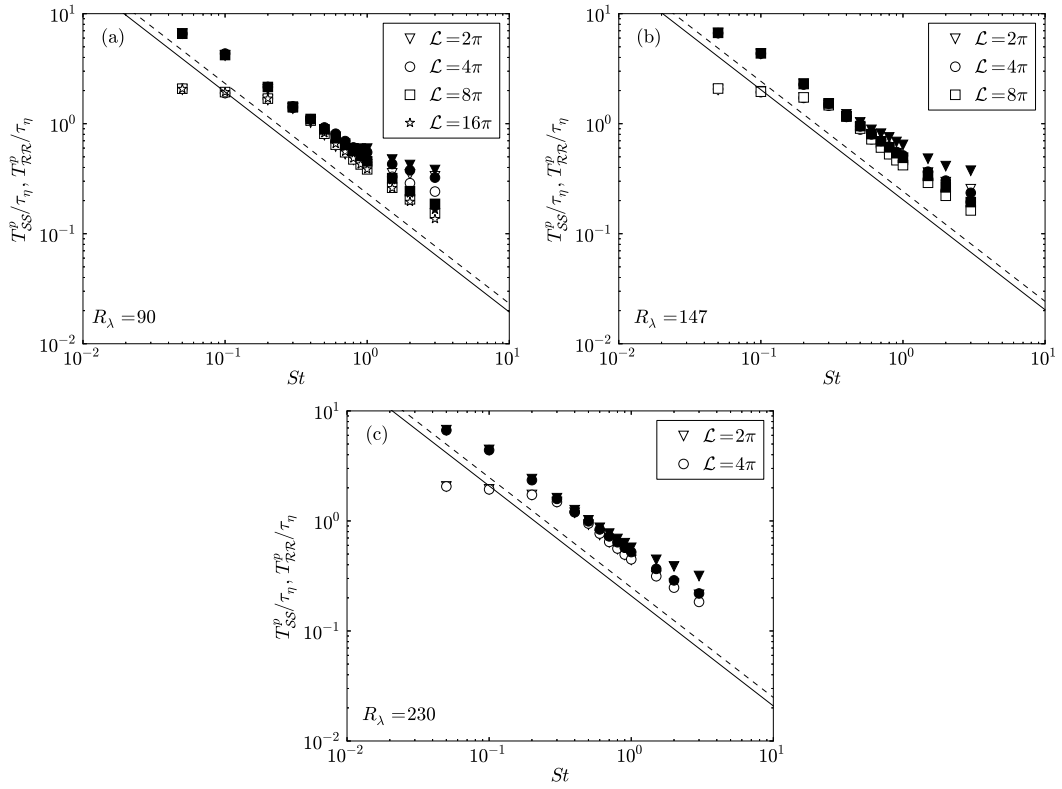

Figure A.2: The Lagrangian strain (open symbols) and rotation (filled symbols) timescales for different domain lengths $\mathcal{L}$ and nominal Reynolds numbers $R_\lambda = 90$ (a), $R_\lambda = 147$ (b), and $R_\lambda = 230$ (c). The theoretical predictions for the strain and rotation timescales for $Sv \gg u'/u_\eta$ are shown with solid and dashed lines, respectively.

large-St particles (which experience the strongest periodicity effects) are negligible, and thus the domain periodicity will not lead to significant changes in this statistic. It is possible, however, that the settling speeds with a nonlinear drag model (which are reduced at large St, see [66]) will be affected by the domain size.

The velocity variance statistics, however, are strongly affected by changes in the domain size, as is evident in figure A.3. For example, at the lowest Reynolds number and smallest domain size, the velocity variances may be in error by

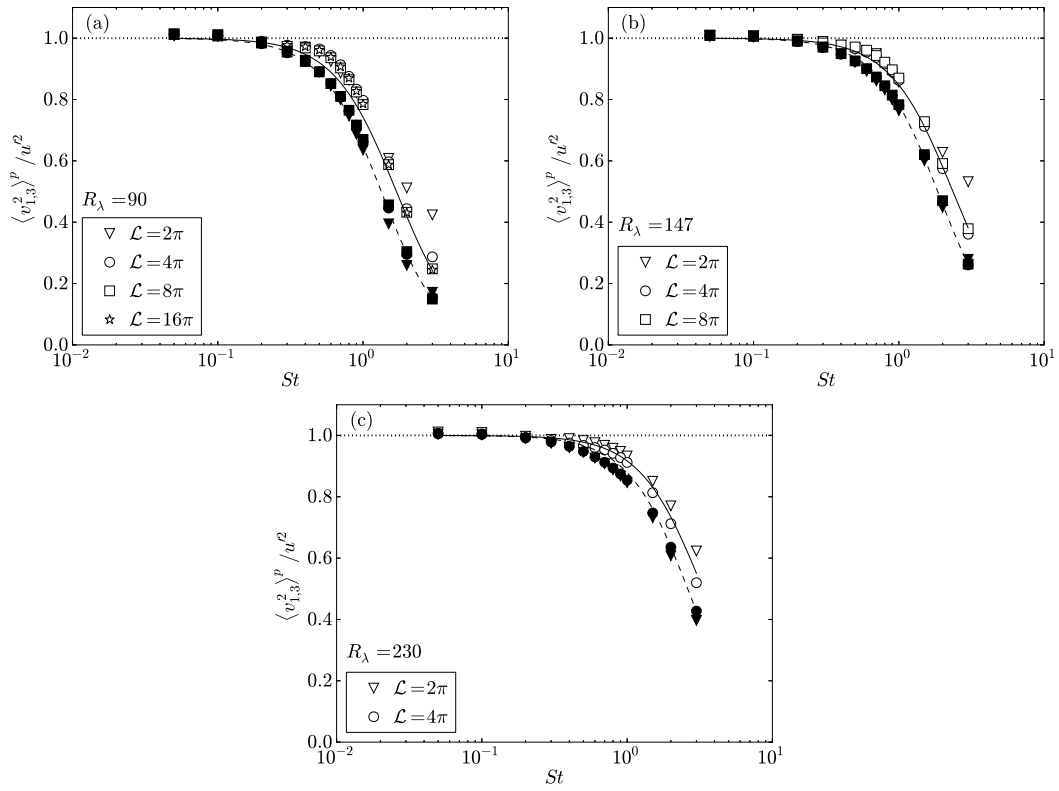

Figure A.3: DNS data for the ratio between the particle velocity variance and the underlying fluid velocity variance in the vertical (open symbols) and horizontal (filled symbols) directions for different domain lengths $\mathcal{L}$ and nominal Reynolds numbers R_λ = 90 (a), R_λ = 147 (b), and R_λ = 230 (c). The theoretical predictions for the vertical (Eq. (5.12)) and horizontal (Eq. (5.13)) components for $Sv \gg u'/u_\eta$ are shown with solid and dashed lines, respectively.

nearly a factor of two. We also observe that the vertical velocity variances are more sensitive to changes in the domain size than the horizontal velocity variances. The physical explanation is that the vertical velocity variances are correlated over longer lengthscales (see §5.4.2), and are thus expected to be more susceptible to artificial periodicity effects. As the domain size is increased, the DNS results for both components at high St converge to our theoretical predic-

tions from §5.4.2, as expected.

We show acceleration variance statistics in figure A.4 and figure A.5, respectively. The acceleration variances are under-predicted at the smallest domain sizes, and converge to the theoretical predictions at high St (see §5.4.3) as the domain size is increased. As with the velocity variances, the vertical acceleration variances are more affected by the periodic boundary conditions than the horizontal acceleration variances, since the vertical velocities are correlated over longer lengthscales.

We next consider acceleration kurtosis statistics in figure A.5. Interestingly, we see that the acceleration kurtosis increases as the domain size increases for *small* St. (No significant differences are seen between the kurtosis of components parallel and perpendicular to gravity, and so we do not show these components separately.) The increased kurtosis at small St suggests that increasing the domain size causes the underlying fluid accelerations to become more intermittent. For a fixed domain size, [193] observed a 30% increase in the fluid acceleration kurtosis when the grid resolution $k_{\max}\eta$ increased from 1.5 to 12. Our results suggest that a similar increase in the acceleration kurtosis occurs for a fixed grid resolution when the domain size is increased.

We conclude this section by examining the relative velocity statistics and the RDFs. Figure A.6 and figure A.7 show the longitudinal mean inward relative velocities and relative velocity variances, respectively. These statistics are only weakly sensitive to the domain size for all St and converge to a grid-independent result. The relative velocity variances appear to be slightly more sensitive to the domain size than the mean inward relative velocities, presumably because the former are higher-order statistics and are thus sensitive to

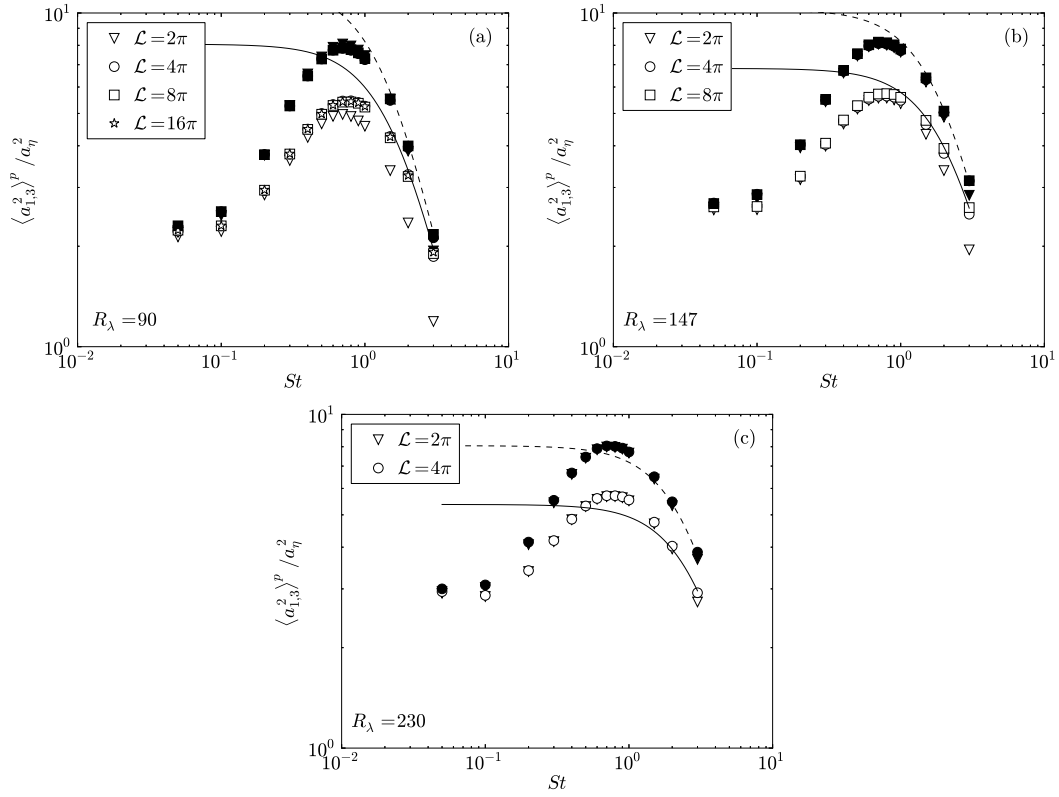

Figure A.4: DNS data for the particle acceleration variance in the vertical direction (open symbols) and horizontal direction (filled symbols) for different domain lengths $\mathcal{L}$ and nominal Reynolds numbers $R_\lambda = 90$ (a), $R_\lambda = 147$ (b), and $R_\lambda = 230$ (c). The theoretical predictions for components parallel to gravity (Eq. (5.24)) and perpendicular to gravity (Eq. (5.25)) for $Sv \gg u'/u_\eta$ are shown with solid and dashed lines, respectively.

larger and more intermittent flow features.

Figure A.8 indicates that the RDFs are almost entirely unaffected by the finite domain sizes at low St. At $St = 3$ (figure A.9), however, the RDFs are evidently quite sensitive to the domain size, and do not converge to a grid-independent result. It is possible that these RDFs are influenced by the small fraction of larger-scale features which appear as grid size is increased (see figure A.1), or that the scaling argument in Eq. (A.1) is not sufficiently stringent for the RDF

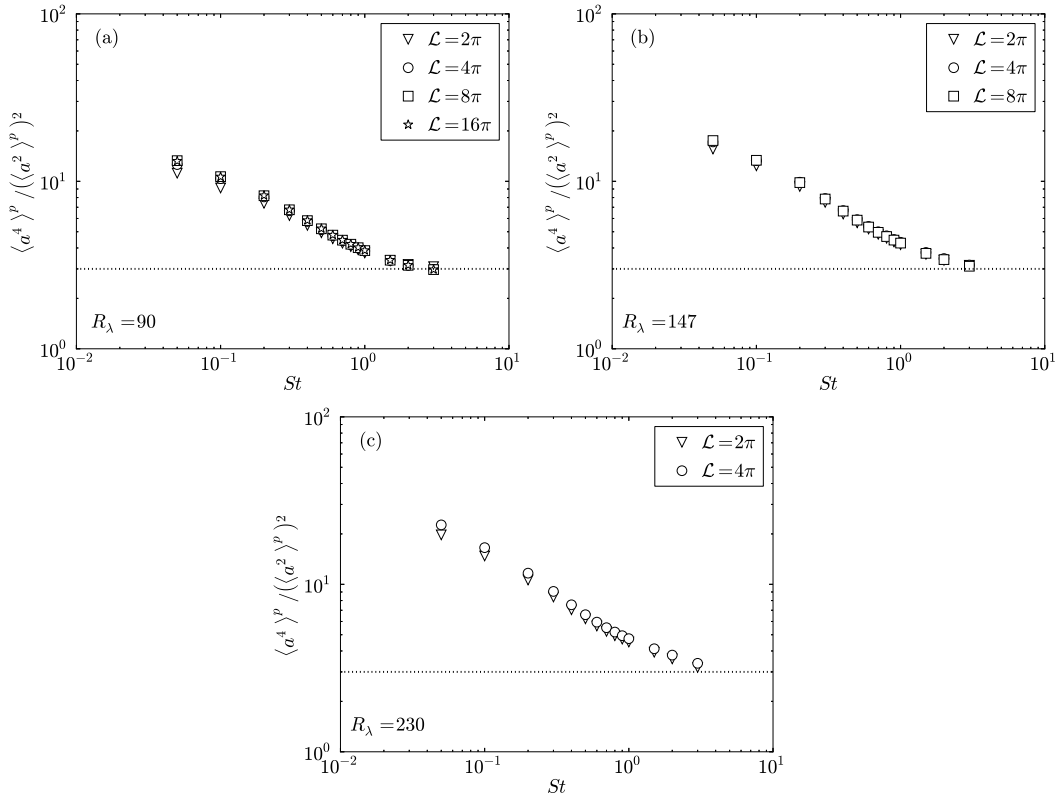

Figure A.5: DNS data for the particle acceleration kurtosis for different domain lengths $\mathcal{L}$ and nominal Reynolds numbers $R_\lambda = 90$ (a), $R_\lambda = 147$ (b), and $R_\lambda = 230$ (c). The dotted line indicates the kurtosis of a Gaussian distribution (3).

statistics. In any case, the results at large St should be interpreted with caution, since the linear drag model and the point-particle approximation are less accurate here (see §5.3.2).

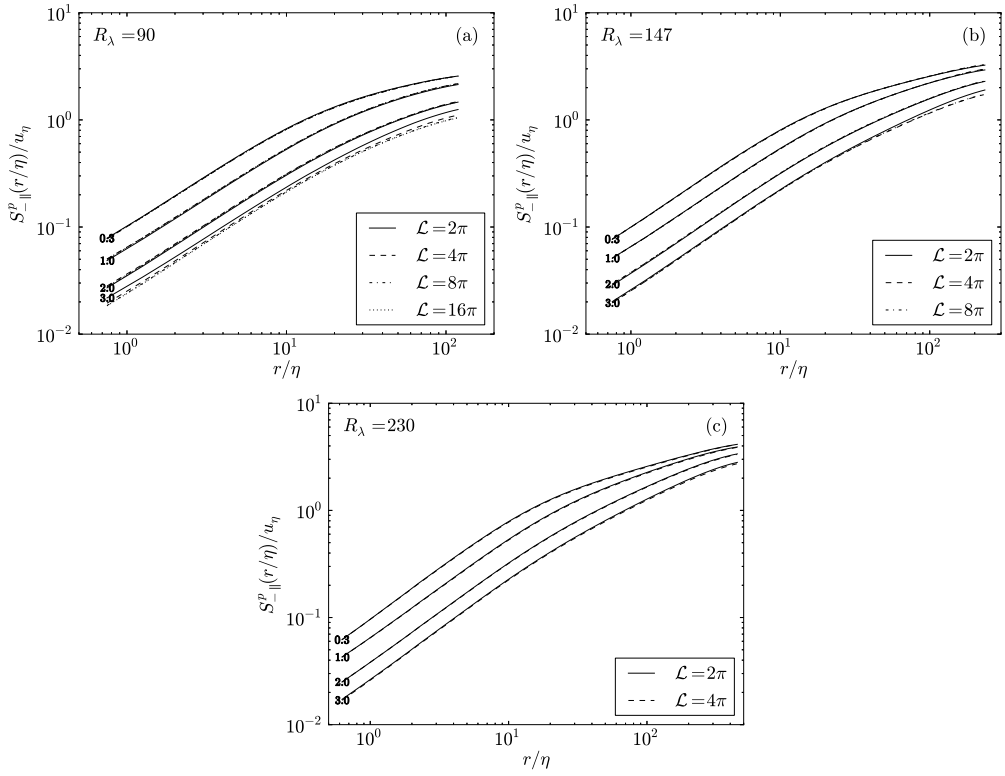

Figure A.6: The longitudinal mean inward relative velocities (normalized by u_η) for different domain lengths $\mathcal{L}$ for nominal Reynolds numbers R_λ = 90 (a), R_λ = 147 (b), and R_λ = 230 (c). The different Stokes numbers (St = 0.3, 1, 2, 3) are indicated by the line labels.

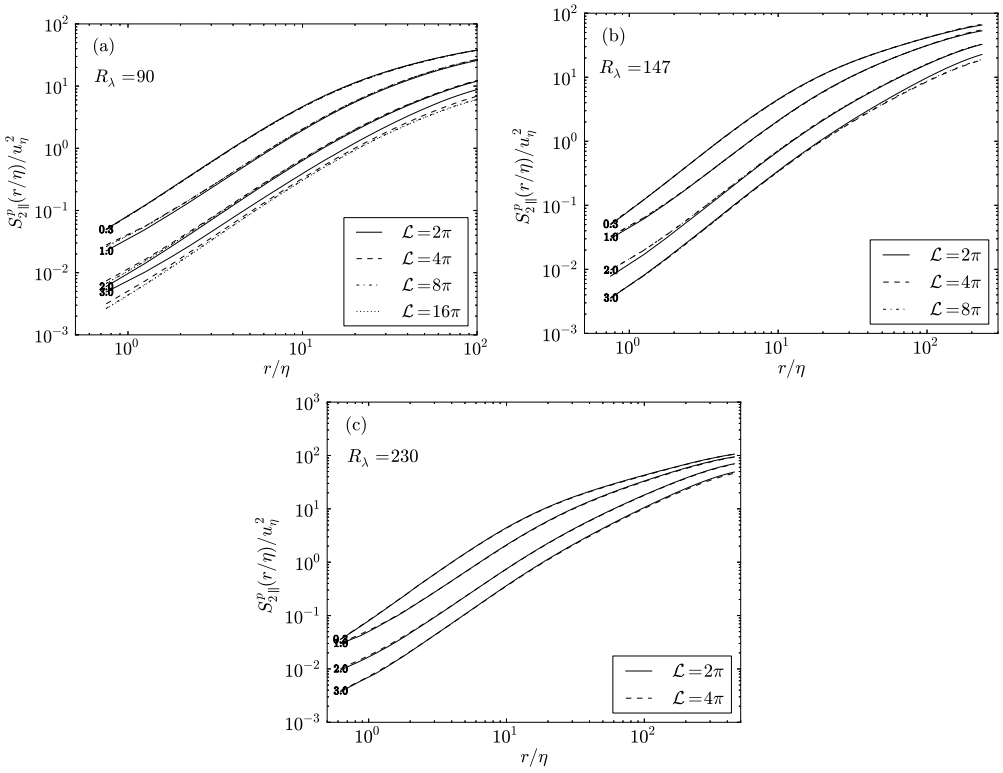

Figure A.7: The longitudinal relative velocity variances (normalized by u_η^2) for different domain lengths $\mathcal{L}$ for nominal Reynolds numbers R_λ = 90 (a), R_λ = 147 (b), and R_λ = 230 (c). The different Stokes numbers (St = 0.3, 1, 2, 3) are indicated by the line labels.

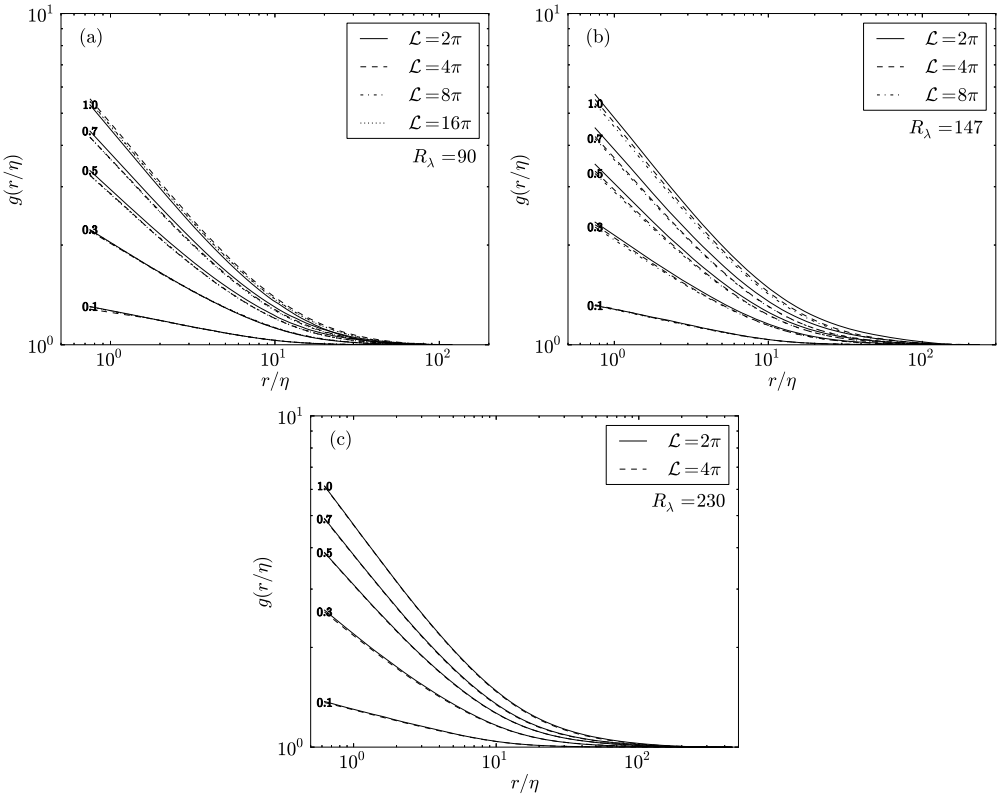

Figure A.8: RDFs for different domain lengths $\mathcal{L}$ for nominal Reynolds numbers $R_\lambda = 90$ (a), $R_\lambda = 147$ (b), and $R_\lambda = 230$ (c). Data are shown for $St \leq 1$, with the Stokes numbers indicated by the line labels.

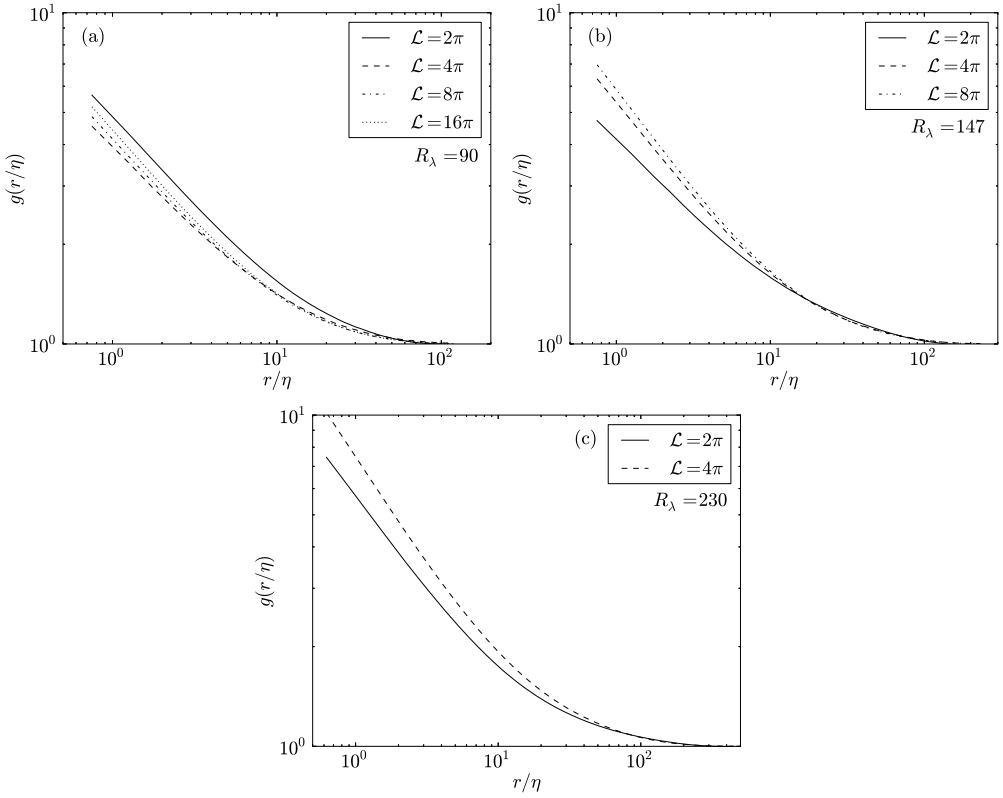

Figure A.9: RDFs for different domain lengths $\mathcal{L}$ for nominal Reynolds numbers $R_\lambda = 90$ (a), $R_\lambda = 147$ (b), and $R_\lambda = 230$ (c). Data are shown for $St = 3$.

APPENDIX B

KINEMATIC COLLISION KERNEL FOR AN ANISOTROPIC PARTICLE PHASE

In this section, we extend the derivation of [161] to determine the kinematic collision kernel formulation for an anisotropic particle phase. From [161], we write the average number of collisions per unit volume over a time period τ as

$$Z_c(\tau) = \frac{n^2}{2} \int_{\boldsymbol{w}} \int_{\boldsymbol{r}} \Phi(\boldsymbol{r}, \boldsymbol{w}, \tau) p(\boldsymbol{r}, \boldsymbol{w}) d\boldsymbol{r} d\boldsymbol{w}, \tag{B.1}$$

where n is the particle-number density, $\Phi(\boldsymbol{r}, \boldsymbol{w}, \tau)$ is the collision operator, and $p(\boldsymbol{r}, \boldsymbol{w})$ is the joint PDF of the particle-pair separation and relative velocity. At this stage, it is simpler to leave the PDF as is rather than split it into a conditional average and the RDF as was done in [161]. The collision kernel is given as

$$K(d) = \frac{2}{n^2} \lim_{\tau \to 0} \frac{Z_c(\tau)}{\tau} = \frac{2}{n^2} \frac{d}{d\tau} Z_c(0), \tag{B.2}$$

or equivalently,

$$\begin{aligned} K(d) &= \int_{\boldsymbol{w}} \int_{\boldsymbol{r}} -\frac{\boldsymbol{r} \cdot \boldsymbol{w}}{r(0)} H(t^*) \delta[d - r(0)] p(\boldsymbol{r}, \boldsymbol{w}) d\boldsymbol{r} d\boldsymbol{w} \\ &= \int_{\boldsymbol{r}} -H(t^*) \delta[d - r(0)] \frac{\boldsymbol{r}}{r(0)} \cdot \int_{\boldsymbol{w}} \boldsymbol{w} p(\boldsymbol{r}, \boldsymbol{w}) d\boldsymbol{w} d\boldsymbol{r} \\ &= \int_{\boldsymbol{r}} -H(t^*) \delta[d - r(0)] \frac{\boldsymbol{r}}{r(0)} \cdot \varrho \langle \boldsymbol{w}^p(t) \rangle_{\boldsymbol{r}} d\boldsymbol{r}. \end{aligned} \tag{B.3}$$

In the above equations, t^* denotes the time required to reach the minimum particle separation, H is the Heaviside function, δ is the Dirac delta function, and ϱ is the particle-pair PDF.

From the definition of t^* in [161], we require $\boldsymbol{r} \cdot \boldsymbol{w} \leq 0$ for $H(t^*) \geq 0$. Since

$$\boldsymbol{r} \cdot \langle \boldsymbol{w}^p(t) \rangle_{\boldsymbol{r}} = \langle \boldsymbol{r}^p(t) \cdot \boldsymbol{w}^p(t) \rangle_{\boldsymbol{r}}, \tag{B.4}$$

then in order to satisfy $H(t^*) \geq 0$, we replace

$$\frac{\boldsymbol{r}}{r(0)} \cdot \varrho \langle \boldsymbol{w}^{p}(t) \rangle_{r}, \tag{B.5}$$

with

$$-\frac{\boldsymbol{r}}{r(0)} \cdot \varrho \langle \boldsymbol{w}^{p-}(t) \rangle_{r}, \tag{B.6}$$

where

$$\varrho \langle \boldsymbol{w}^{p-}(t) \rangle_{r} = -\int_{-\infty}^{0} \boldsymbol{w} p(\boldsymbol{r}, \boldsymbol{w}) d\boldsymbol{w}. \tag{B.7}$$

Furthermore, since

$$\frac{\boldsymbol{r}}{r(0)} \cdot \varrho \langle \boldsymbol{w}^{p-}(t) \rangle_{r} = \frac{1}{r(0)} \varrho \langle \boldsymbol{r}^{p}(t) \cdot \boldsymbol{w}^{p-}(t) \rangle_{r} = \frac{r}{r(0)} \varrho S^{p}_{-\|}(\boldsymbol{r}), \tag{B.8}$$

and we are considering the limit $\tau \to 0$ (in which $r(0) \to r$), we have

$$K(d) = \int_{r} \delta[d - r] \varrho S^{p}_{-\|}(\boldsymbol{r}) d\boldsymbol{r}. \tag{B.9}$$

Since we are interested in collisions on a sphere, we write Eq. (B.9) in spherical coordinates by replacing $\boldsymbol{r}$ with (r, θ, ϕ) and $d\boldsymbol{r}$ with $r^2 \sin\theta dr d\theta d\phi$. This gives us

$$\begin{aligned} K(d) &= \int_{r} \int_{0}^{2\pi} \int_{0}^{\pi} \delta[d - r] \varrho S^{p}_{-\|}(r, \theta, \phi) r^2 \sin\theta d\theta d\phi, \\ &= d^2 \int_{0}^{2\pi} \int_{0}^{\pi} g(d, \theta, \phi) S^{p}_{-\|}(d, \theta, \phi) \sin\theta d\theta d\phi. \end{aligned} \tag{B.10}$$

For an isotropic particle phase, we recover the expected result,

$$K(d) = 4\pi d^2 g(d) S^{p}_{-\|}(d), \tag{B.11}$$

where

$$g(d) = \frac{1}{4\pi} \int_{0}^{2\pi} \int_{0}^{\pi} g(d, \theta, \phi) \sin\theta d\theta d\phi, \tag{B.12}$$

and

$$S^{p}_{-\|}(d) = \frac{1}{4\pi} \int_{0}^{2\pi} \int_{0}^{\pi} S^{p}_{-\|}(d, \theta, \phi) \sin\theta d\theta d\phi. \tag{B.13}$$

For an anisotropic particle phase, however, Eq. (B.13) no longer holds. Note that $S^{p}_{-\|}(d)$ is an average over particle pairs on the entire surface of the sphere, while $S^{p}_{-\|}(d,\theta,\phi)$ is an average over particle pairs on a differential element of the sphere. When the particle phase is anisotropic, we must compute $S^{p}_{-\|}(d)$ by weighting each of the averages on the differential elements $S^{p}_{-\|}(d,\theta,\phi)$ by the number of particle pairs contributing to that average. In this case, we have

$$S^{p}_{-\|}(d) = \frac{1}{4\pi}\int_0^{2\pi}\int_0^{\pi} S^{p}_{-\|}(d,\theta,\phi)\frac{g(d,\theta,\phi)}{g(d)}\sin\theta d\theta d\phi, \tag{B.14}$$

which reduces to Eq. (B.13) for an isotropic particle phase. From Eq. (B.14), we can therefore show that

$$4\pi d^2 g(d) S^{p}_{-\|}(d) = d^2\int_0^{2\pi}\int_0^{\pi} g(d,\theta,\phi) S^{p}_{-\|}(d,\theta,\phi)\sin\theta d\theta d\phi, \tag{B.15}$$

which is precisely the result we derived in Eq. (B.10) for the anisotropic collision kernel. We have therefore demonstrated mathematically that Eq. (B.11) holds for both isotropic and anisotropic particle phases. This explains the empirical observations in [6], from which the authors argue that Eq. (B.11) holds even when the particle distribution is anisotropic.

APPENDIX C

LESSONS LEARNED FROM RUNNING LARGE-SCALE, MEMORY-INTENSIVE JOBS

In this section, we discuss some of the lessons we learned from running large-scale simulations. In §C.1, we discuss the computing challenges we faced, while in §C.2, we focus on issues related to the file system.

C.1 Large-scale-computing challenges

The largest simulations discussed in this dissertation were conducted on 16,384 cores (1024 nodes). We faced a number of challenges in running these simulations, including attaining the necessary CPU hours, debugging and verifying the code, dealing with frequent hardware failures, and queuing and restarting jobs.

C.1.1 Attaining CPU hours

In order to perform the largest simulations discussed ($R_\lambda = 597$, about 3 billion particles), we required about 20 million CPU hours. While we had several past computing allocations and considerable experience in running jobs at national supercomputing centers, our largest allocations at that time had been on the order of a few million CPU hours. We therefore had to prove that we were capable of running much larger jobs, and then attain access to a supercomputer on which we could run our largest simulations.

Our code was first developed on computing clusters at Cornell University,

and we were able to use these resources to test our code on up to 64 cores. We then applied for small computing grants to test and develop our code for use on larger numbers of processors. These grants were given on a number of different platforms: Bluefire (National Center for Atmospheric Research), Jaguar (Oak Ridge National Laboratory), Janus (National Center for Atmospheric Research), Kraken (National Institute for Computational Sciences), and Ranger (Texas Advanced Computing Center). We modified the compile commands and library linkages to enable to code to run on these platforms, and then ran a range of jobs with different numbers of processors and grid points to test and improve the parallel scaling of the code. In one case, on Bluefire (a machine with about 4000 cores), our scaling runs caused problems with the job scheduler, and we had to work with the computing staff to run the jobs at prescribed times when they would not adversely impact other users.

Having demonstrated the parallel performance of the code, we next needed to apply for about 20 million CPU hours. While many of our past allocations had been on XSEDE resources (sponsored the U.S. National Science Foundation), these resources tend to be over-subscribed, have long queuing times, and impose strict limitations on the number of CPU hours available to users. We therefore first considered working toward a large-scale INCITE grant through the U.S. Department of Energy. However, the long review cycle for computing awards (on the order of a year) discouraged us from applying for this opportunity. Through conversations with colleagues, we learned that the National Center for Atmospheric Research was building a new supercomputer (Yellowstone), and was planning to give a few users the opportunity to use this machine before it was released to the full atmospheric science community. We therefore submitted a proposal and were awarded 19 million CPU hours on the Yellow-

stone supercomputer.

C.1.2 Debugging and verifying the code

Extensive debugging and verification is necessary before the results from any complex code can be taken as reliable. Our initial debugging was performed using computing resources at Cornell. This allowed us to quickly submit and run small jobs, and then check that the code ran correctly.

To verify the results were correct, we compared the output from the code (two-dimensional parallel domain decomposition) to that from the original code (one-dimensional parallel domain decomposition). We used the same initial condition for both codes, and ensured that the fluid velocities, particle velocities, and particle positions between the different codes were identical to within working precision.

We then used national supercomputing resources to test the code on larger domains and larger processor counts. While our initial debugging on smaller problem sizes was able to catch most of the issues with the code, a few problems appeared as we began to run very large jobs. One particular problem was that integer variables became larger than their type allowed. To address this, we either increased the integer precision (i.e., changed from four-byte integers to eight-byte integers) or changed the order in which operations were performed.

We also encountered an issue on the Jaguar supercomputer which arose from a buggy MPI implementation. We include this example below to highlight the fact that errors in one's code can (on rare occasions) result from problems in the

external libraries used. On the supercomputer Jaguar, we found that the MPI calls in the particle-tracking portion of our code were deadlocking when we ran on more than about 1000 processors. To determine the cause of the deadlock, we used the Allinea parallel debugger and found that the two of the processors were stuck in a `MPI_SENDRECV` statement. Since this MPI call is by construction designed to avoid deadlocks, we contacted the computing staff, who determined that the issues were caused by an error in the MPI library. By reverting to an earlier MPI implementation, we were able to eliminate this issue and run the code successfully.

One of the most pernicious errors in our code, however, was not caught during the initial debugging phase of our project. Instead, it appeared during a production run on 16,384 processors. We include a description of this error to emphasize the importance of constantly monitoring the results from the simulations and checking for any irregularities.

As the run was under way on 16,384 processors, we checked fluid and particle statistics at fixed time intervals to make sure the results were as expected. The results seemed to be in agreement with our expectations, and we convinced ourselves the code was running correctly. We then began recording a time-series of the fluid and particle velocities for use in a paper we were putting together. While the other statistics looked reasonable, the particle-velocity time-series showed strange oscillations. Upon closer examination, these oscillations perfectly coincided with the times when the code was restarted. We then examined the code segment used in these restarts, and found that the particles were being assigned incorrect velocities here.

After fixing this segment of the code, we had to let the particle field evolve

for a longer period of time, and we had to ignore any particle results we had obtained to that point. While this meant that we were unable to run for as a long a time as we had hoped, we were able to run in a lower-priority and less-expensive queue to attain sufficient statistics for accurate time averages, and our run was still able to provide meaningful data. Had we not checked these statistics and found this problem during run-time, however, our simulation results would have been incorrect, and the entire simulation would have been wasted. It is therefore crucial to systematically analyze the data as the simulation progresses, especially on a newer codes which have not been tested by a large number of users.

Finally, we note that in order to systematically capture and correct these bugs, it was very helpful to use a version-control system for the code. We use Subversion for this, and it allowed us to quickly correct bugs and examine changes in the code when new versions were introduced.

C.1.3 Dealing with hardware failures

We were among the first users on NCAR Yellowstone, and the supercomputer experienced frequent hardware failures after it first became available. In many cases, however, it was unclear which of the errors in our code were due to hardware failures and which were due to problems in the code itself. For example, one constant concern was to make sure we specified the code parameters so as not to run out of available memory. Often, when the hardware would fail, it would give similar error messages to when we ran out of memory. We therefore had to work closely with NCAR staff to report times when our code failed,

along with information about the processors used at the time. In one humorous example, we encountered puzzling code failures over a period of two or three days. Finally, NCAR staff notified us that the failures were caused by a raccoon which broke a transformer, caused a power outage, and destabilized the supercomputer.

Other times, the code itself did not strictly fail, but it exhibited irregular performance. For example, one step of the fluid solver would take 15 seconds some times, and would take several minutes other times. We regularly reported these irregularities to NCAR, who found that they were caused by differences in the communication patterns between different sets of nodes. They responded by re-routing the InfiniBand cables until fast and consistent performance was attained.

Finally, one effect of the hardware failures was to disrupt the queuing and running of jobs, as discussed below. We therefore could often not rely on automated queuing tools, and had to constantly monitor existing jobs and submit new jobs accordingly.

C.1.4 Queuing and restarting jobs

On Yellowstone, we were only able to run a given job for about 12 hours at a time. In general, however, our jobs required long run times to reach a statistically stationary state and to provide us sufficient statistics for accurate time averages. We therefore had to restart our jobs frequently.

As early users on Yellowstone, we were granted high priority in the queues,

and therefore the jobs we submitted to the queue would initially run quite quickly. During this phase, however, the hardware was quite unstable, and it was rare for a job to run successfully for the full 12 hours allotted to it. In this case, we had to frequently output files for restarting the code, and revert back to the latest files before the job exited. This required considerable vigilance in managing the data (so as not to exceed disk quotas), as will be discussed in §C.2.

As the system became more mature, hardware failures became less frequent, and it became more common for the jobs to run successfully for their full duration. However, more users came on board the system during this time, and queue times increased. Yellowstone uses LSF for job scheduling, and this tool allows the user to submit a number of different dependent jobs. In periods where none of us would have access to the supercomputer, we could set up the scheduler so that a number of jobs could run sequentially. However, in general, it was preferable to monitor and submit jobs manually, as this allowed us to check the results and clean up the output data before continuing the simulation.

C.2 File-system challenges

Some of the toughest challenges faced involved managing and accessing the about 75 terabytes generated by our simulations. We discuss the file formats used, archival-storage demands, and file-system-bandwidth issues.

C.2.1 File formats used

An early version of our code output the particle and fluid data using the default Fortran unformatted writes. While these files provided a relatively compact representation of the data, they had a number of drawbacks. Using the default Fortran unformatted write command produces a binary file, and the storage format is system-specific (e.g., little endian or big endian). In some cases, it is therefore not possible to transfer these files to another supercomputer and have this supercomputer read in the data. In addition, these binary files contain arrays, and it is difficult to discern the sizes of the arrays in order to read them in. In our early implementation, we stored the sizes of the arrays in a separate ASCII file. We first read in this file, allocated the appropriate array sizes, and then read in the binary files. However, if the ASCII file became separated from the binary files, this approach became impossible, and the binary files were essentially inaccessible.

We therefore introduced the Hierarchical Data Format (HDF) into our code. This format has several advantages. First, it is not platform-specific, and thus data can be easily exchanged between supercomputers with different storage formats. Second, it provides information about the data as headers within the HDF files themselves, eliminating the need for additional files which describe the shape of the data. Third, it allows for different levels of compression to provide an optimization between file size and read speed. Fourth, it also allows multiple cores to write to different regions of a single file. While we did not take advantage of this last capability (and instead had each core write its own file), we suggest that future versions of the code be adapted to allow for this functionality.

C.2.2 Archival storage demands

Since we generated large amounts of data, we often needed move the data to a tape archive to avoid running over our hard-disk quota. The tape archive on Yellowstone (the High Performance Storage System or HPSS) has a tool called the HPSS Tape Archiver (HTAR) which allows users to compress and transfer the data using a single command. By using HTAR, we reduced the number of separate files stored on our tape archive. This led to faster transfers between the tape archive and the hard-disk. Generally, we tried to post-process this data as much as possible before moving to a tape archive.

One open question, however, is what to do with these data over the next 5-10 years. Ideally, we would like to make them accessible to a large community of researchers. To do so, we would need a dedicated place to store about 75 terabytes of data, and an interface through which the researchers could query the data. We are unsure how to handle this issue, which seems to be an increasingly pressing one for researchers in high-performance computing.

C.2.3 File-system-bandwidth issues

One of the ways we unintentionally destabilized Yellowstone was through reading in large amounts of data at a given time. This issue arose was when we were running a post-processing script on Yellowstone to calculate Lagrangian correlations of statistics along particle trajectories over long times. To run this script, we had to read in about 50 terabytes of data. Our initial naive implementation had all 16,384 cores reading their portion of the data simultaneously (i.e., each core was reading in about 3 gigabytes of the data). While our processing script

was able to execute successfully, this enormous read essentially ground the file system to a halt, making other users to be unable to read in data, and causing some unrelated jobs to crash.

An ideal solution would be to have the file system recognize the threat posed by such a large read, throttle the read-rates to the program, and thus keep the system stable for other users. However, the file system on Yellowstone (the Globally Accessible Data Environment or GLADE) does not currently have this capability. Instead, we worked with NCAR staff to insert `do` loops and `MPI_BARRIER`s into the code to manually control the read rates. While doing so increased the time to run our processing script by an order of magnitude, it kept the system stable for other users and prevented their jobs from crashing.

We include this last example to highlight the fact that users should be very careful in their use of the file system, and should consider ways their file access patterns could have unintended consequences for other users.

BIBLIOGRAPHY

[1] Engineering and scientific subroutine library (ESSL) and parallel ESSL, October 2012.

[2] J. Abrahamson. Collision rates of small particles in a vigorously turbulent fluid. *Chem. Eng. Sci.*, 30:1371–1379, 1975.

[3] V. M. Alipchenkov and A. I. Beketov. On clustering of aerosol particles in homogeneous turbulent shear flows. *J. Turbul.*, 14(5):1–9, 2013.

[4] A. Aliseda, A. Cartellier, F. Hainaux, and J. C. Lasheras. Effect of preferential concentration on the settling velocity of heavy particles in homogeneous isotropic turbulence. *J. Fluid Mech.*, 468:77–105, 2002.

[5] W. T. Ashurst, A. R. Kerstein, R. M. Kerr, and C. H. Gibson. Alignment of vorticity and scalar gradient with strain rate in simulated Navier-Stokes turbulence. *Phys. Fluids*, 30(8):2343–2353, 1987.

[6] O. Ayala, B. Rosa, L.-P. Wang, and W. W. Grabowski. Effects of turbulence on the geometric collision rate of sedimenting droplets. part 1. results from direct numerical simulation. *New J. Phys.*, 10:075015, 2008.

[7] S. Ayyalasomayajula, Z. Warhaft, and L. R. Collins. Modeling inertial particle acceleration statistics in isotropic turbulence. *Phys. Fluids*, 20:094104, 2008.

[8] Sathyanarayana Ayyalasomayajula, Armann Gylfason, Lance R. Collins, Eberhard Bodenschatz, and Zellman Warhaft. Lagrangian measurements of inertial particle accelerations in grid generated wind tunnel turbulence. *Phys. Rev. Lett.*, 97:144507, 2006.

[9] S. Balachandar and J. K. Eaton. Turbulent dispersed multiphase flow. *Annu. Rev. Fluid Mech.*, 42:111–133, 2010.

[10] S. Balachandar and M. R. Maxey. Methods for evaluating fluid velocities in spectral simulations of turbulence. *J. Comput. Phys.*, 83:96–125, 1989.

[11] R. G. Batt. Turbulent mixing of passive and chemically reacting species in a low-speed shear layer. *J. Fluid Mech.*, 82:53–95, 1977.

[12] J. Bec, L. Biferale, G. Boffetta, A. Celani, M. Cencini, A. S. Lanotte, S. Musacchio, and F. Toschi. Acceleration statistics of heavy particles in turbulence. *J. Fluid Mech.*, 550:349–358, 2006.

[13] J. Bec, L. Biferale, G. Boffetta, M. Cencini, S. Musacchio, and F. Toschi. Lyapunov exponents of heavy particles in turbulence. *Phys. Fluids*, 18:091702, 2006.

[14] J. Bec, L. Biferale, M. Cencini, A. S. Lanotte, S. Musacchio, and F. Toschi. Heavy particle concentration in turbulence at dissipative and inertial scales. *Phys. Rev. Lett.*, 98:084502, 2007.

[15] J. Bec, L. Biferale, M. Cencini, A. S. Lanotte, and F. Toschi. Intermittency in the velocity distribution of heavy particles in turbulence. *J. Fluid Mech.*, 646:527–536, 2010.

[16] J. Bec, L. Biferale, A. S. Lanotte, A. Scagliarini, and F. Toschi. Turbulent pair dispersion of inertial particles. *J. Fluid Mech.*, 645:497–528, 2010.

[17] J. Bec, H. Homann, and S. S. Ray. Gravity-driven enhancement of heavy particle clustering in turbulent flow. *Phys. Rev. Lett.*, 112:184501, 2014.

[18] R. Benzi, S. Ciliberto, R. Tripiccione, C. Baudet, F. Massaioli, and S. Succi. Extended self-similarity in turbulent flows. *Phys. Rev. E*, 48:R29–R32, 1993.

[19] J. P. Berrut and L. N. Trefethen. Barycentric Lagrange interpolation. *Siam Rev.*, 46:501–517, 2004.

[20] L. Biferale, G. Boffetta, A. Celani, A. Lanotte, and F. Toschi. Particle trapping in three-dimensional fully developed turbulence. *Phys. Fluids*, 17:021701, 2005.

[21] David K. Bisset, Julian C. R. Hunt, and Michael M. Rogers. The turbulent/non-turbulent interface bounding a far wake. *J. Fluid Mech.*, 451:383–410, 2002.

[22] A. M. Blyth. Entrainment in cumulus clouds. *J. Appl. Meteor.*, 32:626–641, 1993.

[23] Thorsten Bosse, Leonhard Kleiser, and Eckart Meiburg. Small particles in homogeneous turbulence: Settling velocity enhancement by two-way coupling. *Phys. Fluids*, 18:027102, 2006.

[24] A. D. Bragg and L. R. Collins. New insights from comparing statistical theories for inertial particles in turbulence: I. Spatial distribution of particles. *New J. Phys.*, 16:055013, 2014.

[25] A. D. Bragg and L. R. Collins. New insights from comparing statistical theories for inertial particles in turbulence: II: Relative velocities. *New J. Phys.*, 16:055014, 2014.

[26] A. D. Bragg, P. J. Ireland, and L. R. Collins. Forward and backward in time mean square separation of inertial particles in isotropic turbulence. *Phys. Fluids*, 2014. In preparation.

[27] R. Breidenthal. Structure in turbulent mixing layers and wakes using a chemical reaction. *J. Fluid Mech.*, 109:1–24, 1981.

[28] D. A. Briggs, J. H. Ferziger, J. R. Koseff, and S. G. Monismith. Entrainment in a shear-free turbulent mixing layer. *J. Fluid Mech.*, 310:215–241, 1996.

[29] J. E. Broadwell and R. E. Breidenthal. A simple model of mixing and chemical reaction in a turbulent shear layer. *J. Fluid Mech.*, 125:397–410, 1982.

[30] K. A. Brucker, J. C. Isaza, T. Vaithianathan, and L. R. Collins. Efficient algorithm for simulating homogeneous turbulent shear flow without remeshing. *J. Comp. Phys.*, 225:20–32, 2007.

[31] E. Calzavarini, M. Kerscher, D. Lohse, and F. Toschi. Dimensionality and morphology of particle and bubble clusters in turbulent flow. *J. Fluid Mech.*, 607:13–24, 2008.

[32] J. Chun, D. L. Koch, S. Rani, A. Ahluwalia, and L. R. Collins. Clustering of aerosol particles in isotropic turbulence. *J. Fluid Mech.*, 536:219–251, 2005.

[33] R. Clift, J. R. Grace, and M. E. Weber. *Bubbles, Drops, and Particles*. Academic Press, 1978.

[34] L. R. Collins and A. Keswani. Reynolds number scaling of particle clustering in turbulent aerosols. *New J. Phys.*, 6:119, 2004.

[35] Computational and Information Systems Laboratory. Yellowstone: IBM iDataPlex System (University Community Computing). http://n2t.net/ark:/85065/d7wd3xhc, 2012.

[36] S. Corrsin. Estimates of the relations between Eulerian and Lagrangian scales in large Reynolds number turbulence. *J. Atmos. Sci.*, 20:115–119, 1963.

[37] G. T. Csanady. Turbulent diffusion of heavy particles in the atmosphere. *J. Atmos. Sci.*, 20:201–208, 1963.

[38] J. N. Cuzzi, S. S. Davis, and A. R. Dobrovolskis. Blowing in the wind II. Creation and redistribution of refractory inclusions in a turbulent protoplanetary nebula. *Icarus*, 166:385–402, 2003.

[39] J. N. Cuzzi and R. C. Hogan. Blowing in the wind I. Velocities of chondrule-sized particles in a turbulent protoplanetary nebula. *Icarus*, 164:127–138, 2003.

[40] J. N. Cuzzi, R. C. Hogan, J. M. Paque, and A. R. Dobrovolskis. Size-selective concentration of chrondrules and other small particles in protoplanetary nebula turbulence. *Astrophysical J.*, 546:496–508, 2001.

[41] W. J. A. Dahm and P. E. Dimotakis. Measurements of entrainment and mixing the turbulent jets. *AIAA J.*, 25:1216–1223, 1987.

[42] J. Dávila and J. C. R. Hunt. Settling of small particles near vortices and in turbulence. *J. Fluid Mech*, 440:117–145, 2001.

[43] J. de Jong, J. P. L. C. Salazar, L. Cao, S. H. Woodward, L. R. Collins, and H. Meng. Measurement of inertial particle clustering and relative velocity statistics in isotropic turbulence using holographic imaging. *Int. J. Multiphase Flow*, 36:324–332, 2010.

[44] A. Dejoan and R. Monchaux. Preferential concentration and settling of heavy particles in homogeneous turbulence. *Phys. Fluids*, 25:013301, 2013.

[45] B. J. Devenish, P. Bartello, J.-L. Brenguier, L. R. Collins, W. W. Grabowski, R. H. A. IJzermans, S. P. Malinowski, M. W. Reeks, J. C. Vassilicos, L.-P. Wang, and Z. Warhaft. Droplet growth in warm turbulent clouds. *Q. J. R. Meteorol. Soc.*, 138:1401–1429, 2012.

[46] O. A. Druzhinin and S. Elghobashi. On the decay rate of isotropic turbulence laden with microparticles. *Phys. Fluids*, 11:602–610, 1999.

[47] W. M. Durham, E. Climent, M. Barry, F De Lillo, G. Boffetta, M. Cencini,

and R. Stocker. Turbulence drives microscale patches of motile phytoplankton. *Nat. Commun.*, 4(2148):1–7, 2013.

[48] J. K. Eaton and J. R. Fessler. Preferential concentration of particles by turbulence. *Int. J. Multiphase Flow*, 20:169–209, 1994.

[49] S. E. Elghobashi and G. C. Truesdell. Direct simulation of particle dispersion in a decaying isotropic turbulence. *J. Fluid Mech.*, 242:655, 1992.

[50] S. E. Elghobashi and G. C. Truesdell. On the two-way interaction between homogeneous turbulence and dispersed particles. i: Turbulence modification. *Phys. Fluids A*, 5:1790–1801, 1993.

[51] A. ElMaihy and F. Nicolleau. Investigation of the dispersion of heavy-particle pairs and Richardson's law using kinematic simulation. *Phys. Rev. E*, 71:046307, 2005.

[52] V. Eswaran and S. B. Pope. Direct numerical simulations of the turbulent mixing of a passive scalar. *Phys. Fluids*, 31:506–520, 1988.

[53] V. Eswaran and S. B. Pope. An examination of forcing in direct numerical simulations of turbulence. *Comput. Fluids*, 16:257–278, 1988.

[54] G. M. Faeth. Spray combustion phenomena. *Int. Combust. Symp.*, 26(1):1593–1612, 1996.

[55] G. Falkovich, A. Fouxon, and M. G. Stepanov. Acceleration of rain initiation by cloud turbulence. *Nature*, 419:151–154, 2002.

[56] G. Falkovich and A. Pumir. Sling effect in collisions of water droplets in turbulent clouds. *J. Atm. Sci.*, 64:4497, 2007.

[57] P. Fede and O. Simonin. Numerical study of the subgrid fluid turbulence effects on the statistics of heavy colliding particles. *Phys. Fluids*, 18:045103–+, 2006.

[58] P. Février, O. Simonin, and K. D. Squires. Partitioning of particle velocities in gas– solid turbulent flows into a continuous field and a spatially uncorrelated random distribution: theoretical formalism and numerical study. *J. Fluid Mech.*, 533:1–46, 2005.

[59] C. N. Franklin, P. A. Vaillancourt, and M. K. Yau. Statistics and parameterizations of the effect of turbulence on the geometric collision kernel of cloud droplets. *J. Atmos. Sc.*, 64:938–954, 2007.

[60] M. Frigo and S. G. Johnson. The design and implementation of FFTW3. *Proceedings of the IEEE*, 93(2):216–231, February 2005.

[61] J. C. H. Fung and J. C. Vassilicos. Inertial particle segregation by turbulence. *Phys. Rev. E*, 68:046309, 2003.

[62] S. Gerashchenko, G. Good, and Z. Warhaft. Entrainment and mixing of water droplets across a shearless turbulent interface with and without gravitational effects. *J. Fluid Mech.*, 668:293–303, 2011.

[63] S. Gerashchenko, N. S. Sharp, S. Neuscamman, and Z. Warhaft. Lagrangian measurements of inertial particle accelerations in a turbulent boundary layer. *J. Fluid Mech.*, 617:255–281, 2008.

[64] S. Ghosh, J. Dávila, J. C. R. Hunt, A. Srdic, H. H. S. Fernando, and P. R. Jonas. How turbulence enhances coalescence of settling particles with applications to rain in clouds. *Proc. R. Soc. A*, 461:3059–3088, 2005.

[65] G. H. Good, S. Gerashchenko, and Z. Warhaft. Intermittency and inertial particle entrainment at a turbulent interface: the effect of the large-scale eddies. *J. Fluid Mech.*, 694:371–398, 2012.

[66] G. H. Good, P. J. Ireland, G. P. Bewley, E. Bodenschatz, L. R. Collins, and Z. Warhaft. Settling regimes of inertial particles in isotropic turbulence. *J. Fluid Mech.*, 2014. In review.

[67] S. Goto and J. C. Vassilicos. Self-similar clustering of inertial particles and zero-acceleration points in fully developed two-dimensional turbulence. *Phys. Fluids*, 18:115103, 2006.

[68] T. Gotoh, D. Fukayama, and T. Nakano. Velocity field statistics in homogeneous steady turbulence obtained using a high-resolution direct numerical simulation. *Phys. Fluids*, 14:1065–1081, 2002.

[69] W. W. Grabowski and L.-P. Wang. Growth of cloud droplets in a turbulent environment. *Annu. Rev. Fluid Mech.*, 45:293–324, 2013.

[70] P. Gualtieri, F. Picano, and C. M. Casciola. Anisotropic clustering of inertial particles in homogeneous shear flow. *J. Fluid Mech.*, 629:25–39, 2009.

[71] K. Gustavsson and B. Mehlig. Distribution of relative velocities in turbulent aerosols. *Phys. Rev. E*, 84:045304, 2011.

[72] K. Gustavsson and B. Mehlig. Ergodic and non-ergodic clustering of inertial particles. *Eur. Phys. Lett.*, 96:60012, 2011.

[73] K. Gustavsson, S. Vajedi, and B. Mehlig. Clustering of particles falling in a turbulent flow. *Phys. Rev. Lett.*, 112:214501, 2014.

[74] R. J. Hill. Scaling of acceleration in locally isotropic turbulence. *J. Fluid Mech.*, 452:361–370, 2002.

[75] M. Hochbruck and A. Ostermann. Exponential integrators. *Acta Numerica*, 19:209–286, 2010.

[76] G. L. Holtzer and L. R. Collins. Relationship between the intrinsic radial distribution function for an isotropic field of particles and lower-dimensional measurements. *J. Fluid Mech.*, 459:93–102, 2002.

[77] M. Holzner, A. Liberzon, N. Nikitin, W. Kinzelbach, and A. Tsinober. Small-scale aspects of flows in proximity of the turbulent/nonturbulent interface. *Phys. Fluids*, 19:071702, 2007.

[78] M. Holzner, A. Liberzon, N. Nikitin, B. Lüthi, W. Kinzelbach, and A. Tsinober. A Lagrangian investigation of the small-scale features of turbulent entrainment through particle tracking and direct numerical simulation. *J. Fluid Mech.*, 598:465–475, 2008.

[79] Wontae Hwang and John K. Eaton. Homogeneous and isotropic turbulence modulation by small heavy ($St \sim 50$) particles. *J. Fluid Mech.*, 564:361–393, 2006.

[80] R. H. A. IJzermans, E. Meneguz, and M. W. Reeks. Segregation of particles in incompressible random flows: singularities, intermittency and random uncorrelated motion. *J. Fluid Mech.*, 653:99–136, 2010.

[81] P. J. Ireland, A. D. Bragg, and L. R. Collins. Reynolds-number effects on inertial particle dynamics in isotropic turbulence. Part I: Simulations without gravitational effects. 2014. In preparation.

[82] P. J. Ireland, A. D. Bragg, and L. R. Collins. Reynolds-number effects on inertial particle dynamics in isotropic turbulence. Part II: Simulations with gravitational effects. 2014. In preparation.

[83] P. J. Ireland and L. R. Collins. Direct numerical simulation of inertial particle entrainment in a shearless mixing layer. *J. Fluid Mech.*, 704:301–332, 2012.

[84] P. J. Ireland, T. Vaithianathan, P. S. Sukheswalla, B. Ray, and L. R. Collins. Highly parallel particle-laden flow solver for turbulence research. *Comput. Fluids*, 76:170–177, 2013.

[85] J. C. Isaza and Lance R. Collins. On the asymptotic behaviour of large-scale turbulence in homogeneous shear flow. *J. Fluid Mech.*, 637:213–239, 2009.

[86] T. Ishihara, Y. Kaneda, M. Yokokawa, K. Itakura, and A. Uno. Small-scale statistics in high-resolution direct numerical simualtion of turbulence: Reynolds number dependence of one-point velocity gradient statistics. *J. Fluid Mech.*, 592:335–366, 2007.

[87] Takashi Ishihara, Toshiyuki Gotoh, and Yukio Kaneda. Study of high-Reynolds-number isotropic turbulence by direct numerical simulation. *Annu. Rev. Fluid Mech.*, 41:165–180, 2009.

[88] R. W. Johnson. *The Handbook of Fluid Dynamics*. CRC Press, 1998.

[89] Y. Kaneda, T. Ishihara, M. Yokokawa, K. Itakura, and A. Uno. Energy dissipation rate and energy spectrum in high resolution direct numerical simulations of turbulence in a periodic box. *Phys. Fluids*, 15:L21–L24, 2003.

[90] H. S. Kang and C. Meneveau. Experimental study of an active grid-generated shearless mixing layer and comparisons with large-eddy simulation. *Phys. Fluids*, 20:125102, 2008.

[91] K. Kawanisi and R. Shiozaki. Turbulent effects on the settling velocity of suspended sediment. *J. Hydrol. Eng.*, 134:261–266, 2008.

[92] R. M. Kerr, M. Meneguzzi, and T. Gotoh. An inertial range crossover in structure functions. *Phys. Fluids*, 13:1985–1994, 2001.

[93] B. Knaepen, O. Debliquy, and D. Carati. Direct numerical simulation and

large-eddy simulation of a shear-free mixing layer. *J. Fluid Mech.*, 514:153–172, 2004.

[94] A. N. Kolmogorov. The local structure of turbulence in an incompressible viscous fluid for very large Reynolds numbers. *Dokl. Akad. Nauk. SSSR*, 30:299–303, 1941.

[95] A. N. Kolmogorov. A refinement of previous hypotheses concerning the local structure of turbulence in a viscous incompressible fluid at high Reynolds number. *J. Fluid Mech.*, 13:82–85, 1962.

[96] M. M. Koochesfahani and P. E. Dimotakis. Mixing and chemical reactions in a turbulent liquid mixing layer. *J. Fluid Mech.*, 170:83–112, 1986.

[97] J. C. LaRue and P. A. Libby. Thermal mixing layer downstream of half-heated turbulence grid. *Phys. Fluids*, 24(4):597–603, apr 1981.

[98] V. Lavezzo, A. Soldati, S. Gerashchenko, Z. Warhaft, and L. R. Collins. On the role of gravity and shear on the acceleration of inertial particles in near-wall turbulence. *J. Fluid Mech.*, 658:229–246, 2010.

[99] F. Lekien and J. Marsden. Tricubic interpolation in three dimensions. *International Journal for Numerical Methods in Engineering*, 63(3):455–471, 2005.

[100] W. I. Li, M. Perzl, J. Heyder, R. Langer, J. D. Brain, K. H. Englemeier, R. W. Niven, and D. A. Edwards. Aerodynamics and aerosol particle deaggregation phenomena in model oral-pharyngeal cavities. *Journal of Aerosol Science*, 27(8):1269–1286, 1996.

[101] D. K. Lilly. Models of cloud-topped mixed layers under a strong inversion. *J. Fluid Mech.*, 94:292–309, 1968.

[102] B. K. Ma and Z. Warhaft. Some aspects of the thermal mixing layer in grid turbulence. *Phys. Fluids*, 29(10):3114–3120, oct 1986.

[103] E. Malkiel, J. N. Abras, E. A. Widder, and J. Katz. On the spatial distribution and nearest neighbor distance between particles in the water column determined from in situ holographic measurements. *Journal of Plankton Research*, 28(2):149–170, 2006.

[104] M. Mascagni and A. Srinivasan. Algorithm 806: SPRNG: a scalable li-

brary for pseudorandom number generation. *ACM Trans. Math. Softw.*, 26(3):436–461, September 2000.

[105] Joseph Mathew and Amit J. Basu. Some characteristics of entrainment at a cylindrical turbulence boundary. *Phys. Fluids*, 14:2065–2072, 2002.

[106] M. R. Maxey. The gravitational settling of aerosol particles in homogeneous turbulence and random flow fields. *J. Fluid Mech.*, 174:441–465, 1987.

[107] M. R. Maxey. The motion of small spherical particles in a celluar flow field. *Phys. Fluids*, 30:1915–1928, 1987.

[108] M. R. Maxey and S. Corrsin. Gravitational settling of aerosol particles in randomly oriented cellular flow fields. *J. Aerosol. Sci.*, 43:1112–1134, 1986.

[109] M. R. Maxey and J. J. Riley. Equation of motion for a small rigid sphere in a nonuniform flow. *Phys. Fluids*, 26:883–889, 1983.

[110] D. A. McQuarrie. *Statistical Mechanics*. Harper & Row, New York, 1976.

[111] R. Mei. Effect of turbulence on the particle settling velocity in the nonlinear drag range. *Int. J. Multiphase Flow*, 20:273–284, 1994.

[112] J. P. Mellado. The evaporatively driven cloud-top mixing layer. *J. Fluid Mech.*, 660:5–36, 2010.

[113] E. Meneguz and M. W. Reeks. Statistical properties of particle segregation in homogeneous isotropic turbulence. *J. Fluid Mech.*, 686:338–351, 2011.

[114] C. Meneveau. Lagrangian dynamics and models of the velocity gradient tensor in turbulent flows. *Annu. Rev. Fluid Mech.*, 43:219–245, 2011.

[115] R. Monchaux, M. Bourgoin, and A. Cartellier. Preferential concentration of heavy particles: A Voronoï analysis. *Phys. Fluids*, 22:103304, 2010.

[116] E. G. Moody and L. R. Collins. Effect of mixing on nucleation and growth of titania particles. *Aerosol Sci. Tech.*, 37:403–424, 2003.

[117] M. G. Mungal and P. E. Dimotakis. Mixing and combustion with low heat release in a turbulent shear layer. *J. Fluid Mech.*, 148:349–382, 1984.

[118] Peter Nielsen. Turbulence effects on the settling of suspended particles. *J. Sediment. Petrol.*, 63:835–838, 1993.

[119] R. Onishi, K. Takahashi, and S. Komori. Influence of gravity on collisions of monodispersed droplets in homogeneous isotropic turbulence. *Phys. Fluids*, 21:125108, 2009.

[120] R. Onishi, K. Takahashi, and J. C. Vassilicos. An efficient parallel simulation of interacting inertial particles in homogeneous isotropic turbulence. *J. Comput. Phys.*, 242:809–827, 2013.

[121] R. Onishi and J. C. Vassilicos. Collision statistics of inertial particles in two-dimensional homogeneous isotropic turbulence with an inverse cascade. *J. Fluid Mech.*, 745:279–299, 2014.

[122] S. A. Orszag and G. S. Patterson. Numerical simulation of three-dimensional homogeneous isotropic turbulence. *Phys. Rev. Lett.*, 28:76–79, 1972.

[123] S. A. Orszag and G. S. Patterson. *Numerical simulation of turbulence*. Springer-Verlag, New York, 1972.

[124] L. Pan and P. Padoan. Relative velocity of inertial particles in turbulent flows. *J. Fluid Mech.*, 661:73–107, 2010.

[125] L. Pan and P. Padoan. Turbulence-induced relative velocity of dust particles i: identical particles. *ApJ*, 776:12, 2013.

[126] L. Pan, P. Padoan, J. Scalo, A. G. Kritsuk, and M. L. Norman. Turbulent clustering of protoplanetary dust and planetesimal formation. *ApJ*, 740:6, 2011.

[127] Y. Park and C. Lee. Gravity-driven clustering of inertial particles in turbulence. *Phys. Rev. E*, 89:061004(R), 2014.

[128] D. Pekurovsky. P3DFFT: A framework for parallel computations of Fourier transforms in three dimensions. *SIAM J. Sci. Comput.*, 34(4):C192–C209, 2012.

[129] M. B. Pinsky, A. P. Khain, and M. Shapiro. Collisions of cloud droplets in a turbulent flow. Part IV: Droplet hydrodynamic interaction. *J. Atmos. Sci.*, 64:2462–2482, 2007.

[130] S. B. Pope. *Turbulent Flows*. Cambridge University Press, New York, 2000.

[131] Cedric Poulain, Nicolas Mazellier, Philippe Gervais, Yves Gagne, and Christophe Baudet. Spectral vorticity and Lagrangian velocity measurements in turbulent jets. *Flow Turb. Combust.*, 72:245–271, 2004.

[132] S. E. Pratsinis, W. Zhu, and S. Vemury. The role of gas mixing in flame synthesis of titania powders. *Powder Tech.*, 86:87–93, 1996.

[133] W. H. Press, S. A. Teukolsky, W. T. Vetterling, and B. P. Flannery. *Numerical Recipies in Fortran*. Cambridge University Press, Cambridge, 1999.

[134] H. R. Pruppacher and J. D. Klett. *Microphysics of Clouds and Precipitation*. Kluwer, Dordrecht, 1997.

[135] B. Ray and L. R. Collins. Preferential concentration and relative velocity statistics of inertial particles in Navier-Stokes turbulence with and without filtering. *J. Fluid Mech.*, 680:488–510, 2011.

[136] B. Ray and L. R. Collins. Investigation of sub-kolmogorov inertial particle pair dynamics in turbulence using novel satellite particle simulations. *J. Fluid Mech.*, 720:192–211, 2013.

[137] W. C. Reade and L. R. Collins. Effect of preferential concentration on turbulent collision rates. *Phys. Fluids*, 12:2530–2540, 2000.

[138] W. C. Reade and L. R. Collins. A numerical study of the particle size distribution of an aerosol undergoing turbulent coagulation. *J. Fluid Mech.*, 415:45–64, 2000.

[139] M. W. Reeks. On the constitutive relations for dispersed particles in nonuniform flows. I: Dispersion in a simple shear flow. *Phys. Fluids A*, 5:750–761, 1993.

[140] R. S. Rogallo. Numerical experiments in homogeneous turbulence. Technical Report 81315, NASA, 1981.

[141] B. Rosa, H. Parishani, O. Ayala, W. W. Grabowski, and L. P. Wang. Kinematic and dynamic collision statistics of cloud droplets from high-resolution simulations. *New J. Phys.*, 15:045032, 2013.

[142] P. G. Saffman and J. S. Turner. On the collision of drops in turbulent clouds. *J. Fluid Mech.*, 1:16–30, 1956.

[143] J. P. L. C. Salazar and L. R. Collins. Inertial particle acceleration statistics in turbulence: effects of filtering, biased sampling, and flow topology. *Phys. Fluids*, 24:083302, 2012.

[144] J. P. L. C. Salazar and L. R. Collins. Inertial particle relative velocity statistics in homogeneous isotropic turbulence. *J. Fluid Mech.*, 696:45–66, 2012.

[145] J. P. L. C. Salazar, J. de Jong, L. Cao, S. Woodward, H. Meng, and L. R. Collins. Experimental and numerical investigation of inertial particle clustering in isotropic turbulence. *J. Fluid Mech.*, 600:245–256, 2008.

[146] Ewe W. Saw, Raymond A. Shaw, Sathyanarayana Ayyalasomayajula, Patrick Y. Chuang, and Armann Gylfason. Inertial clustering of particles in high-Reynolds-number turbulence. *Phys. Rev. Lett.*, 100:214501, 2008.

[147] B. L. Sawford, P.-K. Yeung, M. S. Borgas, P. Vedula A. La Porta, A. M. Crawford, and E. Bodenschatz. Conditional and unconditional acceleration statistics in turbulence. *Phys. Fluids*, 15:3478–3489, 2003.

[148] R. A. Shaw. Particle-turbulence interactions in atmospheric clouds. *Annu. Rev. Fluid Mech.*, 35:183–227, 2003.

[149] R. A. Shaw, B. Kostinski, and M. L. Larsen. Towards quantifying droplet clustering in clouds. *Q. J. R. Meteorol. Soc.*, 128:1043–1057, 2002.

[150] X. Shen and Z. Warhaft. Longitudinal and transverse structure functions in sheared and unsheared wind-tunnel turbulence. *Phys. Fluids*, 14:370–381, 2002.

[151] S. S. Shy and R. E. Breidenthal. Laboratory experiments on the cloud-top entrainment instability. *J. Fluid Mech.*, 214:1–15, 1990.

[152] H. Siebert, K. Lehmann, and M. Wendisch. Observations of small-scale turbulence and energy dissipation rates in the cloudy boundary layer. *J. Atmos. Sci.*, 63:1451–1466, 2006.

[153] H. Siebert, R. A. Shaw, and Z. Warhaft. Statistics of small scale velocity fluctuations in marine stratocumulus clouds. *J. Atmos. Sci.*, 67:262–273, 2010.

[154] J. Soria, R. Sondergaard, B. J. Cantwell, M. S. Chong, and A. E. Perry. A study of the fine-scale motions of incompressible time-developing mixing layers. *Phys. Fluids*, 6(2):871–884, 1994.

[155] P. R. Spalart. Direct simulation of a turbulent boundary layer up to R_θ = 1410. *J. Fluid Mech.*, 187:61–98, 1988.

[156] C. G. Speziale. Analytical methods for the development of Reynolds-stress closures in turbulence. *Annu. Rev. Fluid Mech.*, 23:107–157, 1991.

[157] K. D. Squires and J. K. Eaton. Particle response and turbulence modification in isotropic turbulence. *Phys. Fluids A*, 2:1191–1203, 1990.

[158] K. D. Squires and J. K. Eaton. Measurements of particle dispersion from direct numerical simulations of isotropic turbulence. *J. Fluid Mech.*, 226:1–35, 1991.

[159] K. D. Squires and J. K. Eaton. Preferential concentration of particles by turbulence. *Phys. Fluids A*, 3:1169–1178, 1991.

[160] F. Stratmann, O. Moehler, R. Shaw, and H. Wex. *Clouds in the Perturbed Climate System*. MIT Press, Cambridge, 2009.

[161] S. Sundaram and L. R. Collins. Collision statistics in an isotropic, particle-laden turbulent suspension I. Direct numerical simulations. *J. Fluid Mech.*, 335:75–109, 1997.

[162] S. Sundaram and L. R. Collins. A numerical study of the modulation of isotropic turbulence by suspended particles. *J. Fluid Mech.*, 379:105–143, 1999.

[163] Y. Tagawa, J. M. Mercado, V. N. Prakash, E. Calzavarini, C. Sun, and D. Lohse. Three-dimensional Lagrangian Voronoï analysis for clustering of particles and bubbles in turbulence. *J. Fluid Mech.*, 693:201–215, 2012.

[164] S. Tavoularis, J. C. Bennett, and S. Corrsin. Velocity-derivative skewness in small Reynolds number, nearly isotropic turbulence. *J. Fluid Mech.*, 88:63–69, 1978.

[165] H. Tennekes. Eulerian and Lagrangian time microscales in isotropic turbulence. *J. Fluid Mech.*, 67:561–567, 1975.

[166] D. Tordella and M. Iovieno. Numerical experiments on the intermediate asymptotics of shear-free turbulent transport and diffusion. *J. Fluid Mech.*, 549:429–441, 2006.

[167] D. Tordella and M. Iovieno. Small-scale anisotropy in turbulent shearless mixing. *Phys. Rev. Lett.*, 107:194501, 2011.

[168] M. A. T. van Hinsberg, J. H. M. ten Thije Bookkkamp, F. Toschi, and H. J. H. Clercx. Optimal interpolation schemes for particle tracking in turbulence. *Phys. Rev. E*, 87:043307, 2013.

[169] M. A. T. van Hinsberg, J. H. M. Thije Boonkkamp, F. Toschi, and H. J. H. Clercx. On the efficiency and accuracy of interpolation methods for spectral codes. *SIAM J. Sci. Comput.*, 34(4):B479–B498, 2012.

[170] S. Veeravalli and Z. Warhaft. The shearless turbulence mixing layer. *J. Fluid Mech.*, 207:191–229, 1989.

[171] S. Veeravalli and Z. Warhaft. Thermal dispersion from a line source in the shearless turbulence mixing layer. *J. Fluid Mech.*, 216:35–70, 1990.

[172] M. Voßkuhle, A. Pumir, E. Lévêque, and M. Wilkinson. Prevalence of the sling effect for enhancing collision rates in turbulent suspensions. *J. Fluid Mech.*, 749:841–852, 2014.

[173] G. A. Voth, A. La Porta, A. M. Crawford, J. Alexander, and E. Bodenschatz. Measurement of particle accelerations in fully developed turbulence. *J. Fluid Mech.*, 469:121–160, 2002.

[174] L.-P. Wang and W. W. Grabowski. The role of air turbulence in warm rain initiation. *Atmos. Sci. Let.*, 10:1–8, 2009.

[175] L.-P. Wang and M. R. Maxey. Settling velocity and concentration distribution of heavy particles in homogeneous isotropic turbulence. *J. Fluid Mech.*, 256:27–68, 1993.

[176] L.-P. Wang and D. E. Stock. Dispersion of heavy particles by turbulent motion. *J. Atmos. Sci.*, 50:1897–1913, 1993.

[177] L.-P. Wang, A. S. Wexler, and Y. Zhou. Statistical mechanical descriptions of turbulent coagulation. *Phys. Fluids*, 10:2647–2651, 1998.

[178] L.-P. Wang, A. S. Wexler, and Y. Zhou. Statistical mechanical description and modeling of turbulent collision of inertial particles. *J. Fluid Mech.*, 415:117–153, 2000.

[179] Z. Warhaft. Laboratory studies of droplets in turbulence: towards understanding the formation of clouds. *Fluid Dyn. Res.*, 41:011201–+, 2009.

[180] J. Westerweel, C. Fukushima, J. M. Pedersen, and J. C. R. Hunt. Mechanics of the turbulent-nonturbulent interface of a jet. *Phys. Rev. Lett.*, 95:174501, 2005.

[181] J. Westerweel, T. Hofmann, C. Fukushima, and J. C. R. Hunt. The turbulent/non-turbulent interface at the outer bounary of a self-similar turbulent jet. *Exp. Fluids*, 33:873–878, 2002.

[182] M. Wilkinson and B. Mehlig. Caustics in turbulent aerosols. *Europhys. Lett.*, 71:186–192, 2005.

[183] M. Wilkinson, B. Mehlig, and V. Bezuglyy. Caustic activation of rain showers. *Phys. Rev. Lett.*, 97:048501, 2006.

[184] A. Witkowska, J. G. Brasseur, and D. Juvé. Numerical study of noise from isotropic turbulence. *J. Comput. Acoust.*, 5:317–336, 1997.

[185] E. J. P. Woittiez, H. J. J. Jonker, and L. M. Portela. On the combined effects of turbulence and gravity on droplet collisions in clouds: a numerical study. *J. Atmos. Sci.*, 66:1926–1943, 2009.

[186] A. M. Wood, W. Hwang, and J. K. Eaton. Preferential concentration of particles in homogeneous and isotropic turbulence. *Int. J. Multiphase Flow*, 31:1220–1230, 2005.

[187] Y. Xue, L.-P. Wang, and W. W. Grabowski. Growth of cloud droplets by turbulent collision-coalescence. *J. Atmos. Sci.*, 65:331–356, 2008.

[188] C. Y. Yang and U. Lei. The role of turbulent scales in the settling velocity of heavy particles in homogeneous isotropic turbulence. *J. Fluid Mech.*, 20:179–205, 1998.

[189] T. S. Yang and S. S. Shy. The settling velocity of heavy particles in an aqueous near-isotropic turbulence. *Phys. Fluids*, 15:868–880, 2003.

[190] T. S. Yang and S. S. Shy. Two-way interaction between solid particles and homogeneous air turbulence: particle settling rate and turbulence modification measurements. *J. Fluid Mech.*, 526:171–216, 2005.

[191] P. K. Yeung, D. A. Donzis, and K. R. Sreenivasan. Dissipation, enstrophy, and pressure statistics in turbulence simulations at high reynolds numbers. *J. Fluid Mech.*, 700:5–15, 2012.

[192] P. K. Yeung and S. B. Pope. Lagrangian statistics from direct numerical simulations of isotropic turbulence. *J. Fluid Mech.*, 207:531–586, 1989.

[193] P. K. Yeung, S. B. Pope, A. G. Lamorgese, and D. A. Donzis. Acceleration and dissipation statistics of numerically simulated isotropic turbulence. *Phys. Fluids*, 18(6):065103, 2006.

[194] H. Yoshimoto and S. Goto. Self-similar clustering of inertial particles in homogeneous turbulence. *J. Fluid Mech.*, 577:275–286, 2007.

[195] M. I. Yudine. Physical considerations on heavy-particle dispersion. *Adv. Geophys.*, 6:185–191, 1959.

[196] L. I. Zaichik and V. M. Alipchenkov. Pair dispersion and preferential concentration of particles in isotropic turbulence. *Phys. Fluids*, 15:1776–1787, 2003.

[197] L. I. Zaichik and V. M. Alipchenkov. Acceleration of heavy particles in isotropic turbulence. *Int. J. Multiphase Flow*, 34(9):865–868, 2008.

[198] L. I. Zaichik and V. M. Alipchenkov. Statistical models for predicting pair dispersion and particle clustering in isotropic turbulence and their applications. *New J. Phys.*, 11:103018, 2009.

[199] L. I. Zaichik, O. Simonin, and V. M. Alipchenkov. Two statistical models for predicting collision rates of inertial particles in homogeneous isotropic turbulence. *Phys. Fluids*, 15:2995–3005, 2003.

[200] Y. Zhou, A. S. Wexler, and L.-P. Wang. Modelling turbulent collision of bidisperse inertial particles. *J. Fluid Mech.*, 433:77–104, 2001.